University of Strathclyde

Department of Physics

Quantum Cascade Laser based Absorption Spectrometer for Trace Gas Molecular Detection and Nonlinear Optics

By

Michael Telfer M^{c}Culloch

A Thesis presented in the fulfilment of the requirements for the degree of Doctor of Philosophy

2006

BEST COPY

AVAILABLE

Variable print quality

© Copyright 2006

'The copyright of this thesis belongs to the author under the terms of the United Kingdom Copyright Acts as qualified by University of Strathclyde Regulation 3.49. Due acknowledgement must always be made of the use of any material contained in, or derived from, this thesis.'

Acknowledgements

After working for 3 years there are many people who have helped me along the way. Firstly I would like to thank my supervisor Prof. Geoff Duxbury for giving me the opportunity to work in such an interesting field of physics. I am also grateful for the time and effort he dedicated to helping me with my project. I would also like to thank my second supervisor Dr. Nigel Langford for his contribution to my studies. They were always enthusiastic and willing to help.

I would like to thank a very bright PhD student, Erwan Normand, whom I had the pleasure of overlapping in his final year during my first year. Our collaboration experiments gave me a great insight into the research I was lucky to be involved with.

I would like to thank Stephen Walker for his friendship during my PhD, and for creating a great atmosphere in the group especially when we were the only PhD students in the group. I am grateful to Stephen Wright, a talented and hard working PhD student who started in my final year. His questioning of what we were doing helped my own understanding of the work. I am thankful for the help of our technicians Ged Drinkwater, Mark Hutcheon, Bob Wylie and all the members of the electronic and mechanical workshops.

I would not have been able to undertake my work had it not been for the love and support of my family and friends. I would like to thank my parents and my gran for their backing. Last, but not least, I would like to thank Gill Macnaught for her love and understanding during my PhD.

Publications List

1) Les lasers à cascade quantique et leurs applications, E. Normand, C. Sirtori, M. Garcia, M. T. McCulloch, N. Langford and G. Duxbury, Revue de l'Electricité et de l'Electronique (REE) **9**, 36 (2002)

2) Highly Sensitive Detection of Trace Gases Using Pulsed Quantum Cascade Lasers, G. Duxbury, E. L. Normand, N. Langford, M. T. McCulloch and S. Walker, SPIE proceedings, **4817** (2003)

3) Fast, real-time spectrometer based on a pulsed quantum-cascade laser, E. L. Normand, M. T. McCulloch, G. Duxbury and N. Langford, Opt. Lett. **28**, 16-18 (2003)

4) Highly Sensitive Detection of Trace Gases Using The Time Resolved Frequency Down-chirp From Pulsed Quantum-Cascade Lasers, M. T. McCulloch, E. L. Normand, N. Langford, G.Duxbury and D. A. Newnham, J.Opt. Soc. Am. B, **20**, 1761-1768 (2003)

5) Real-time trace-level detection of carbon dioxide and ethylene in car exhaust gases, M. T. McCulloch, N. Langford and G.Duxbury, Appl. Opt. **44**, 2888-2894 (2005)

6) Quantum cascade semiconductor infared and far-infared lasers: from trace gas sensing to non-linear optics, G. Duxbury, N. Langford, M. T. McCulloch and S. Wright, Chem. Soc. Rev. **34**, 921-934 (2005)

7) Observation of Saturation and Rapid Passage Signals in the 10.25 micron spectrum of Ethylene Using a Frequency Chirped Quantum Cascade Laser, M. T. McCulloch, G.Duxbury and N. Langford, (submitted to Mol.Phys. February 21, 2006)

Contents

Publications List		**III**
Abstract		**VIII**
1.0	**Introduction**	**1**
2.1	**Laser Theory**	**3**
2.1.1	Introduction	4
2.1.2	Bipolar Semiconductor Lasers	4
2.1.3	Quantum Cascade Lasers	6
2.1.4	References	8
2.2	**Spectroscopy Theory**	**9**
2.2.1	Introduction	10
2.2.2	Molecular Classification	10
2.2.3	Rigid Rotor	11
2.2.4	Diatomic Rotation	12
2.2.5	Diatomic Vibration	13
2.2.6	Rotation Vibration	14
2.2.7	Morse Potential	15
2.2.8	Centrifugal Distortion	17
2.2.9	Polyatomic Molecular Vibration	17
2.2.10	Polyatomic Molecular Rotation	19
2.2.11	Polyatomic Molecular Vibration Rotation	20
2.2.12	Linear Absorption Spectroscopy	21
2.2.13	Lineshape Function	23
2.2.14	References	25

2.3	**Astigmatic Herriott Cell**	**26**
2.3.1	Introduction	27
2.3.2	Astigmatic Herriott cell Model	28
2.3.3	Astigmatic Herriott cell Solutions	30
2.3.4	Conclusions	37
2.3.5	References	38
3.1	**Spectrometer Design**	**39**
3.1.1	Introduction	40
3.1.2	Optical Setup	41
3.1.3	Detector	42
3.1.4	Amplifier	42
3.1.5	Digitiser	43
3.1.6	Evacuatable Astigmatic Herriott Cell	44
3.1.7	Electronics	45
3.1.8	Radio Frequency (RF) removal	47
3.1.9	Detection Scheme	48
3.1.10	Resolution	51
3.1.11	Software	53
3.1.12	Concentration Retrieval	63
3.1.13	Conclusions	71
3.1.14	References	72
3.2	**Laser Characterisation**	**74**
3.2.1	Introduction	75
3.2.2	Alpes Laser 10.24μm DFB Quantum Cascade Laser	75
3.2.3	Alpes Laser 7.8μm DFB Quantum Cascade Laser	78
3.2.4	Thales 9.46μm FP Quantum Cascade Laser	83
3.2.5	Discussion	86
3.2.6	References	87

4	**Nonlinear Optics**	**88**
4.1	Introduction	89
4.2	Rabi Frequency	89
4.3	Rapid Passage	91
4.4	Power Saturation and Rapid Passage	100
4.5	Nitrogen Broadening and Concentration Retrieval	113
4.6	Dicke Narrowing and Rapid Passage	115
4.7	Conclusions	118
4.8	References	119
5.1	**Atmospheric Experiments**	**121**
5.1.1	Introduction	122
5.1.2	Experimental Setup	122
5.1.3	Results - 10μm	123
5.1.4	Results - 8μm	125
5.1.5	Conclusions	129
5.1.6	References	130
5.2	**Breath Experiments**	**131**
5.2.1	Introduction	132
5.2.2	Exhaled Breath Components	132
5.2.3	Patients Studied	132
5.2.4	Experimental Setup	133
5.2.5	Results	134
5.2.6	Discussion	143
5.2.7	Conclusions	143
5.2.8	References	145
5.3	**Cigarette Smoke Experiments**	**146**
5.3.1	Introduction	147

5.3.2	Cigarette Smoke	147
5.3.3	Prior Art Cigarette Smoke work	148
5.3.4	Cigarettes Studied	148
5.3.5	Experimental Setup	149
5.3.6	Results - 10μm	152
5.3.7	Discussion - 10μm	159
5.3.8	Results - 8μm	161
5.3.9	Discussion - 8μm	197
5.3.10	Conclusions	199
5.3.11	References	200
5.4	**Vehicle Emissions Experiments**	**202**
5.4.1	Introduction	203
5.4.2	Vehicle Exhaust Components	203
5.4.3	Other Vehicle Exhaust Monitoring	204
5.4.4	Catalytic Converter	204
5.4.5	Vehicles Studied	205
5.4.6	Experimental Setup	206
5.4.7	Results - 10μm	207
5.4.8	Discussion - 10μm	217
5.4.9	Results – 8μm	219
5.4.10	Discussion - 8μm	233
5.4.11	Conclusions	234
5.4.12	References	235
6	**Future Work and Conclusions**	**236**
6.1	An Airplane based Instrument	237
6.2	An Open path Sensor	238
6.3	Nonlinear Optics	238
6.4	Conclusions	239

1.0 Introduction

Over the past decades the increasing concern over the condition of the Earths atmosphere has led to research into atmospheric monitoring. It is clear that mans influence on the atmosphere has increased as the industrialisation of society has increased. The concentrations of the trace gases in the atmosphere have been changing at an alarming rate, with some concentrations varying by as much as 1% per year. Evidence of this increasing rate of change can be found in densely populated areas of the planet where large local Carbon Monoxide concentrations can be found. This climate change is not only caused by the industrialisation. Intensive farming using Nitrogen based fertilisers is thought to add to the trace gases in the atmosphere. These atmospheric changes are thought to be responsible for two phenomena, ozone depletion and global warming.

Ozone is one of the key molecules in the atmosphere. It is important for the biological life on the planet that is protected from harmful UV radiation by the Ozone in the atmosphere. Decreases in Stratospheric Ozone have occurred since in 1970s. The discovery of the Ozone hole over the Antarctic was one of the events that has brought the subject of atmospheric pollution to the front of public awareness.

Global warming is an effect that occurs naturally. Approximately a third of the radiation from the sun is reflected back into space. Most of the rest of the radiation is absorbed by the water and land on the surface of the planet. The absorbed radiation is re-emitted by the planet, but at infrared wavelengths, rather than the shorter wavelength radiation produced by the sun. Some of the infrared radiation is absorbed in the atmosphere by naturally occurring greenhouse gases, such as Water, Methane and Carbon Dioxide. This keeps the atmosphere warmer than it otherwise would be. This is the natural greenhouse effect. If the concentrations of these natural greenhouse gases increases or if non natural greenhouse gases are introduced into the atmosphere then the radiation trapping will increase.

Several techniques have been developed to accurately and precisely measure the trace gases in the atmosphere. These techniques range from ground based observations to balloon, aircraft and satellite platforms. Measurements from these instruments have been used to develop theoretical models to predict the long term effects of gases in the atmosphere. These instruments are also helping the development of legislation designed to reduce the emissions of pollutant gases from industrial sources and motor vehicles. This has led to the need for the development of an instrument capable of long time unattended operation for atmospheric trace gas monitoring. Tunable diode laser absorption spectrometers (TDLAS) utilising semiconductor lasers have been widely used for this purpose. They have been shown to provide high sensitivities. Until recently near infrared lasers have been the lasers of choice, utilising a variety of detection schemes. With the development of Quantum Cascade lasers high sensitivity mid infrared spectrometers capable of running at near room temperature have been developed. The mid infrared region contains the fundamental absorption transitions of most molecular species, which should provide high sensitivities.

2.1 Laser Theory

2.1.1 Introduction

Since the laser [1, 2] was invented in 1960 by T. H. Maiman the applications of laser technology have become countless. Today there are several different types of lasers that impact our daily lives, including dye lasers, gas lasers, semiconductor lasers and others. These lasers range in size from a few microns to the size of buildings. In this chapter I will discuss semiconductor lasers, which are the basis for the work that I have done during my PhD.

Semiconductor lasers, which were first invented in 1962 [3], utilise one of two different processes in order to emit light. The first process is electron hole recombination, which is done in a bipolar device, involving a transition between the conduction band and the valence band. The second process involves only one type of charge carrier and is performed by unipolar devices. Semiconductor lasers can be made very small, typically on the millimeter scale, which makes them useful in applications where size and weight are a consideration. The first semiconductor lasers were constructed out of simple biased p-n junctions, which will be introduced at the start of this chapter. I will also discuss the technology behind a more complicated semiconductor laser, the Quantum Cascade Laser (QCL), which is an example of a unipolar semiconductor laser device.

2.1.2 Bipolar Semiconductor Lasers

The optical gain of this type of semiconductor laser is provided in the active region of a forward biased p-n junction. The p-n junction is formed from a single crystal semiconductor. The p region is doped with acceptor impurities and the n region is doped with donor impurities. The electrons from the n region diffuse into the p region and the holes in the p region diffuse into the n region. The electric field across the p-n junction limits the diffusion of carriers from the two regions. When the junction is biased the electric field is reduced, which allows further diffusion. The depletion region, where electrons and holes are both present, in the middle of the junction narrows. By reducing

the size of the depletion region carriers require less energy to cross this region. By applying a large enough voltage the p-n junction will begin to conduct. The electron hole pairs in the depletion region, or active region, can undergo recombination. This recombination can be radiative or nonradiative. Radiative recombination involves the emission of a photon with energy, $E_g = h\nu$, where E_g is the bandgap of the material.

When the current flowing across the depletion region reaches a critical level population inversion, which is one of the requirements for laser operation, occurs. The rate of emission exceeds the rate of absorption which causes the junction to provide optical gain to the system. The second requirement for a laser is that the output is coherent. Coherence is achieved be forming an optical cavity around the junction. By cleaving the two ends of the crystal two partially reflecting mirrors can be created. This forms a Fabry-Perot cavity, which provides positive feedback. This type of cavity provides a broad gain curve allowing several longitudinal modes to lase at the same time. This type of laser is known as a homojunction laser.

This structure can be improved by encasing the active region with a layer above and a layer below of material with a higher band gap. This reduces the amount of charge carriers that diffuse out of the active region and thus reduces the threshold current. This type of laser is called a double heterostructure laser.

These types of semiconductor laser can provide a tunable laser frequency output by changing the length of the laser cavity. This can be done by changing the temperature of the laser or the cavity length can be altered by external cavity feedback. This produces a tunable diode laser (TDL) which can either operate in pulsed or continuous wave modes. As the output laser wavelength is effectively set by the band gap of the materials chosen the range over which materials may be used is limited. In the near infrared (0.5μm - 3μm) Gallium Arsenide (GaAs) based lasers operate at room temperature and give output powers of up to several Watts. In the mid infrared (3μm -15μm) lead salt laser have been the laser of choice. These lasers tend to require cryogenic cooling and only produce a few μWatts of output power.

2.1.3 Quantum Cascade Lasers

The theory of Quantum Cascade lasers (QCL) was first proposed in 1971 by R. F. Kazarinov and R. A. Suris [4]. A working Quantum Cascade laser was first produced in 1994 [5]. Even though the QC laser is a semiconductor laser, the structure of a QC laser is very different to that of a bipolar semiconductor laser. A comparison of the band structure of a conventional semiconductor laser and a QC is shown in Figure 2.1.1.

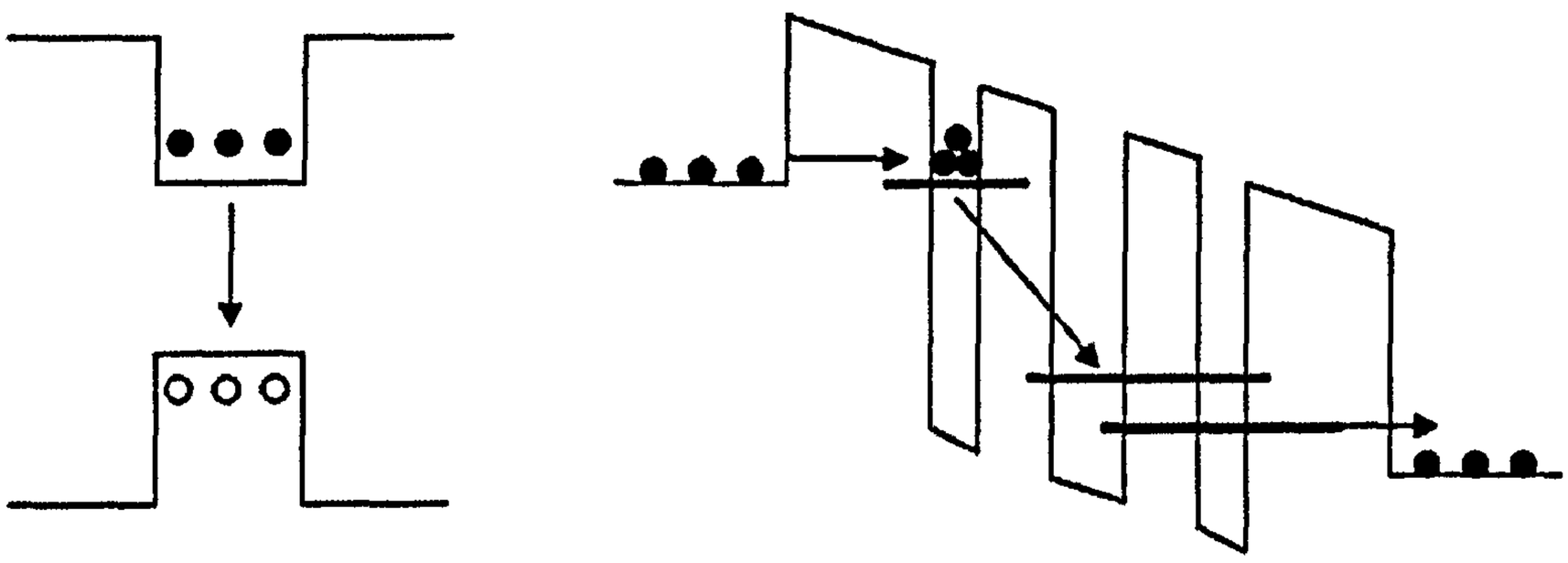

Figure 2.1.1 – *The left diagram shows the band structure of a conventional semiconductor laser. The right diagram shows the conduction band of a Quantum Cascade laser.*

Unlike in a conventional semiconductor laser where the radiation is generated by the recombination of charge carriers across the band gap a Quantum Cascade laser generates light by using only one type of charge carrier. This is why the QC laser is a unipolar device instead of a bipolar device. The QC laser is based upon the transitions of electrons between excited states in the conduction band. The pumping of the laser relies on the resonant tunneling of electrons into the upper laser level. The width of the quantum wells and the height of the barriers define the energy levels inside the wells. The energy gap between the upper laser level, n_3, and the lower laser level, n_2, defines the wavelength of the emitted light rather than the material band gap. By tailoring the width of these quantum wells the emission wavelength of the laser can be varied. The

maximum energy separation of $E_3 - E_2$ and thus the smallest wavelength possible is set by the conduction band discontinuity. This should allow wavelengths from the near infrared out to the far infrared (3.5μm-100μm) [6, 7], which allows these lasers to access the main molecular fingerprint region in the mid infrared (3μm-15μm). The population inversion in the system is achieved by tailoring the quantum wells such that the lifetime of the upper laser level is greater than the lifetime of the lower laser level. The active region of the laser is formed by the quantum wells. By cascading active regions alternatively with relaxation/injector regions a staircase effect can be created. The relaxation/injector takes the electrons from the previous active region in the cascade and quickly tunnels it into the upper laser level of the next active region. Each electron can emit one photon per active region, which leads to the term "electron recycling". This can lead to quantum yields of greater than one. In an ideal system each electron would produce a photon at each of the active regions, which would mean that the output power of the laser is proportional to the number of active regions. In a typical QC laser as many as 45 or more active regions are cascaded. The cascaded active regions are sandwiched between thick cladding layers of lower refractive index, which provides optical confinement. One of the advantages of Quantum Cascade lasers is that intersubband transitions produce a spectrally narrower output compared to a bipolar semiconductor laser due to the transitions between bands of the same curvature sign. Quantum Cascade lasers also have the advantage of being able to operate at room temperature while being much less sensitive to temperature fluctuations than Lead Salt lasers. Due to the cascade of active regions QC lasers can be made to produce optical output powers in the Watts range.

The typical optical output from a QC laser is multimode. In this case the device is known as a Fabry-Perot QC laser (FP). These modes are separated by the Free Spectral Range of the optical cavity. The ideal distribution of these modes is Gaussian. A Distributed Feedback Laser (DFB) uses a diffraction grating grown on the QC to force the device to be single mode. These types of devices tend to have a higher threshold current than their equivalent FP Laser.

2.1.4 References

1) Long-Wavelength Semiconductor Lasers, G. P. Agrawal and N. K. Dutta, Van Nostrand, (1986)

2) Laser Spectroscopy : Basic Concepts and Instrumentation 3rd edition, W. Demtröder, Springer, (2003)

3) Coherent light emission from GaAs junctions, R. N. Hall, G. E. Fenner, J. D. Kingsley, T. J. Soltys and R. O. Carlson, Phys. Rev. Lett., **9**, 9, 366-368, (1962)

4) R. F. Kazarinov and R. A. Suris, Sov. Phys. Semicond., **5**, 707, (1971)

5) Quantum Cascade Laser, J. Faist, F. Capasso, D. L. Sivco, C. Sirtori, A. L. Hutchinson and A. Y. Cho, Science, **264**, 553, (1994)

6) Demonstration of High-Performance 10.16μm Quantum Cascade Distributed Feedback lasers Fabricated without Epitaxial Regrowth, D. Hofstetter, J. Faist, M. Beck, A. Műller and U. Oesterie, App. Phys. Lett., **75**, 5, 665-667

7) Quantum Cascade Laser: The Quantum Technology for Semiconductor lasers in the mid-far-infrared, C. Sirtori and J. Nagle, C. R. Physique, **4**, (2003) 639-648

2.2 Spectroscopy Theory

2.2.1 Introduction

Spectroscopy is the monitoring of something by a process. There are many different types of spectroscopy for looking at various different things. In my case the absorption of light by a molecule is the tool used to study molecules. By better understanding the interaction of molecules and light the results of my experiments can be better interpreted. In this chapter I will cover some of the basic theory regarding the motion of molecules and their interaction with light.

2.2.2 Molecular Classification

The moments of inertia of a molecule can be used to make a classification. The moment of inertia, I, of any molecule through the centre of gravity about any axis is given by:

$$I = \sum_i m_i r_i^2$$

where m_i is the mass of atom i and r_i is the distance from the inertial axis of atom i. The inertial axis of largest moment is the c axis. The axis of least moment is the a axis and the third axis, which is labelled axis b, is perpendicular to both the c axis and the a axis such that:

$$I_c \geq I_b \geq I_a$$

The three rotation constants used later in this chapter A, B and C are derived from these three moments of inertia such that:

$$X = \frac{\hbar}{4\pi I_x c}$$

where X is either A, B or C (in cm^{-1}). Using the moments of inertia molecules can be grouped into the four distinct groups Linear, Spherical top, Symmetric top and Asymmetric top. The last two can be further subdivided into oblate and prolate symmetric tops and near oblate and near prolate asymmetric tops. The Ray asymmetry parameter, κ, can be used to determine how oblate or prolate a molecule is.

$$\kappa = \frac{2B - A - C}{A - C}$$

This parameter varies from -1 in the prolate limit to +1 in the oblate limit. In Table 2.2.1 the moments of inertia are related to their classifications.

Moment of Inertia	Classification
$I_c = I_b > I_a = 0$	Linear
$I_c = I_b = I_a$	Spherical top
$I_c > I_b = I_a$	Oblate Symmetric top
$I_c = I_b > I_a$	Prolate Symmetric top
$I_c > I_b \approx I_a$	Near Oblate Asymmetric top
$I_c \approx I_b > I_a$	Near Prolate Asymmetric top

2.2.3 Rigid Rotor

As molecules are made up of two or more nuclei the motion of these nuclei must be considered as well as that of the electrons. This means that the energy of a molecular system is the sum of the vibrational, rotational and electronic energies. Using the Born-Oppenheimer separation these energies can be treated independently. The wavefunction, ψ, for the system can be written:

$$\psi = \psi_e \psi_v \psi_r$$

where ψ_e is the electronic wavefunction, ψ_v is the vibrational wavefunction and ψ_r is the rotational wavefunction. By separating the three wavefunctions the energy levels associated with the three types of motion can be more easily calculated. It is transitions between different energy levels that leads to the absorption or emission of photons. In the infrared the rotational and vibrational energy levels provide the transitions observed. The energy required to make an electron move is not generated in the infrared and must come from visible or ultraviolet radiation.

2.2.4 Diatomic Rotation

The rigid rotor approximation is a useful model for the rotation of diatomic molecules. It assumes that the bond between the atoms is a rigid, weightless rod. The moment of inertia about the centre of gravity is [1]:

$$I = \frac{m_1 m_2}{m_1 + m_2} r^2 = \mu r^2$$

where m_1 and m_2 are the masses of the two atoms, r is the bond length and μ is the reduced mass. By using the Schrödinger equation the allowed rotational energy levels in the rigid rotor approximation can be found. The energy levels are given by [1]:

$$E_J = \frac{\hbar}{4\pi Ic} J(J+1) = BJ(J+1)$$

where J is the rotational quantum number that can take the value of any whole number. This means that the separation of the energy levels increases with J. The selection rules for these energy levels are:

$$\Delta J = \pm 1$$

By substituting J into the energy level equation and by obeying the selection rules it can be shown that a set of lines is generated that are spaced by 2B.

2.2.5 Diatomic Vibration

The vibration of diatomic molecules occurs when the bond length of the molecule varies. This variation can be treated in the same we as we think of the motion of a spring. The restoring force on the atoms can be examined with Hooke's law:

$$f = -k(r - r_0)$$

where k is the spring constant, r is the separation of the atoms and r_0 is the average bond length. The energy of the system forms a parabolic curve of the form:

$$E = \frac{1}{2}k(r - r_0)^2$$

This model for the vibration of diatomic molecules is called the simple harmonic oscillator model. The frequency of oscillation of this system is given by:

$$\omega = \frac{1}{2\pi c}\sqrt{\frac{k}{\mu}}$$

The vibrational energy levels of this system can be found by solving the Schrödinger equation for simple harmonic motion using the parabolic energy potential shown above. The solutions are given by:

$$E_v = h\nu\left(v+\tfrac{1}{2}\right) = \omega\left(v+\tfrac{1}{2}\right)$$

where v is the vibrational quantum number that can take the value of any whole number. The selection rules for these energy levels are:

$$\Delta v = \pm 1$$

In the simple harmonic oscillator model the vibrational energy levels are equally spaced.

2.2.6 Rotation Vibration

In the separation of the wavefunction into the three components we have treated the three motions separately. Transitions are permitted that alter the vibration and the rotation of the molecule simultaneously. These rotation vibration transitions follow the selection rules that govern the individual transitions such that $\Delta J = 0, \pm 1$ and $\Delta v = \pm 1$ must be satisfied. The energies of these transitions are the sum of the individual energies of the vibration and rotation components. This is due to the Born-Oppenheimer approximation. These types of transitions give rise to a spectrum of lines of spacing 2B centred about a frequency ω. An example of a Fourier Transform Spectrum of a typical Linear molecule, Carbon Dioxide, is shown in Figure 2.2.1.

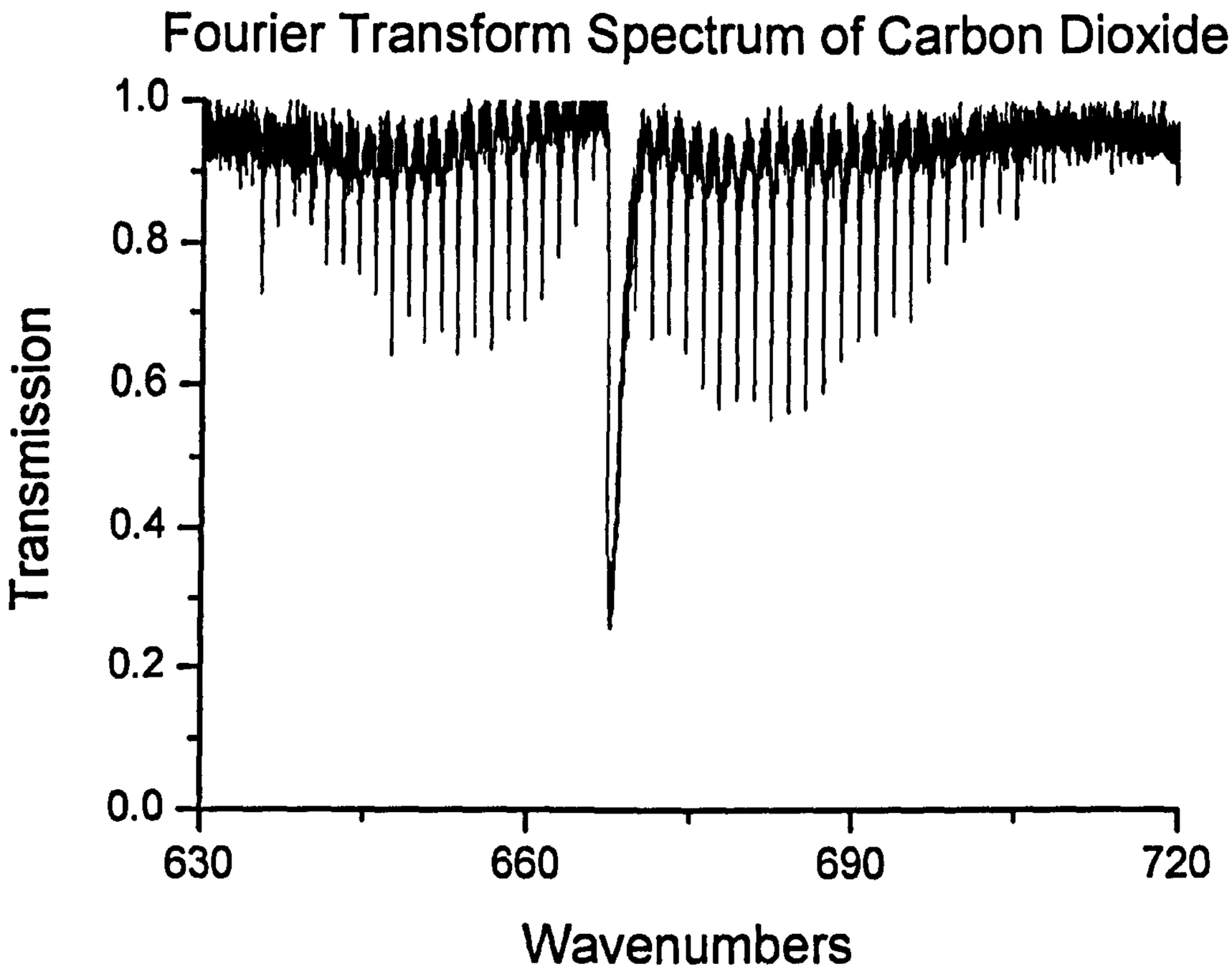

Figure 2.2.1 – *The Fourier Transform Spectrum of Carbon Dioxide.*

2.2.7 Morse Potential

A real molecule does not follow the simple harmonic motion model. When a molecular bond is stretched it will reach a point where it will break. Also as the bond length is decreased the intermolecular repulsion will increase forcing the atoms apart. These two things which lead to anharmonicity are taken into account by the Morse potential [2]:

$$V(r) = D^e\left[1 - e^{-\alpha(r-r_0)}\right]^2$$

where D^e is the dissociation energy of the molecule, r_0 is as above and α is given by:

$$\alpha = \sqrt{\frac{k}{2D^e}}$$

Where k is the force constant and is analogous to the force constant in the simple harmonic oscillator model. By solving the Schrödinger equation with a Morse potential the vibrational energy levels become:

$$E_v = \omega\left(v+\tfrac{1}{2}\right) - \omega\chi\left(v+\tfrac{1}{2}\right)^2$$

where ω is the oscillation frequency and ωχ is the anharmonicity constant. χ is given by:

$$\chi = \frac{\alpha^2\hbar}{\mu\omega} = \frac{\omega\hbar}{4D^e}$$

The reduced mass of the system is given by μ. This gives a solution of energy levels with a decreasing separation with increasing v. A different set of selection rules is required for the anharmonic case:

$$\Delta v = \pm 1, \pm 2, \pm 3, \ldots.$$

The transitions governed by the $\Delta v = \pm 2, \pm 3$ selection rules are known as the first and second overtones. The probability of these transitions decreases by about a factor of a hundred for each overtone above the fundamental transition. The transitions of the first and second overtones will occur at approximately 2ω and 3ω respectively. At room temperature almost all molecules will be in the ground vibrational state.

2.2.8 Centrifugal Distortion

As the rotational velocity of a molecule increases the rigid rotor approximation begins to fail. In real molecules the bond length increases with increasing with increasing quanta of rotation. The increase in the moment of inertia experienced by the molecule is the centrifugal distortion. This increased moment of inertia leads to a decrease in the rotation constants and the energy levels of the system are less far apart at high J than expected. The effect of the centrifugal distortion on the energy levels is found by solving the Schrödinger equation for non rigid rotation:

$$E_J = BJ(J+1) - DJ^2(J+1)$$

where D is the centrifugal distortion term and is given by:

$$D = \frac{\hbar^3}{4\pi I^2 r^2 kc}$$

The selection rules for the non rigid rotor case are the same as the rigid case.

2.2.9 Polyatomic Molecular Vibration

The treatment of molecular movement so far has concentrated on diatomic molecules. The effect of rotation and vibration on polyatomic molecules must be considered. For a nonlinear molecule made up of N atoms there are the 3N-6 different possible vibrations. For linear molecules there are 3N-5 different possible vibrations. These vibrations occur because there are 3N degrees of freedom. Three of these degrees are required to specify the translational movement of the system and a further three are required to specify the perpendicular rotation of the system. In the linear molecule case only two angles are

required for the perpendicular rotation. In some cases some of these vibrations may be degenerate with each other. An example of three different vibrations in a linear molecule is shown in Figure 2.2.2.

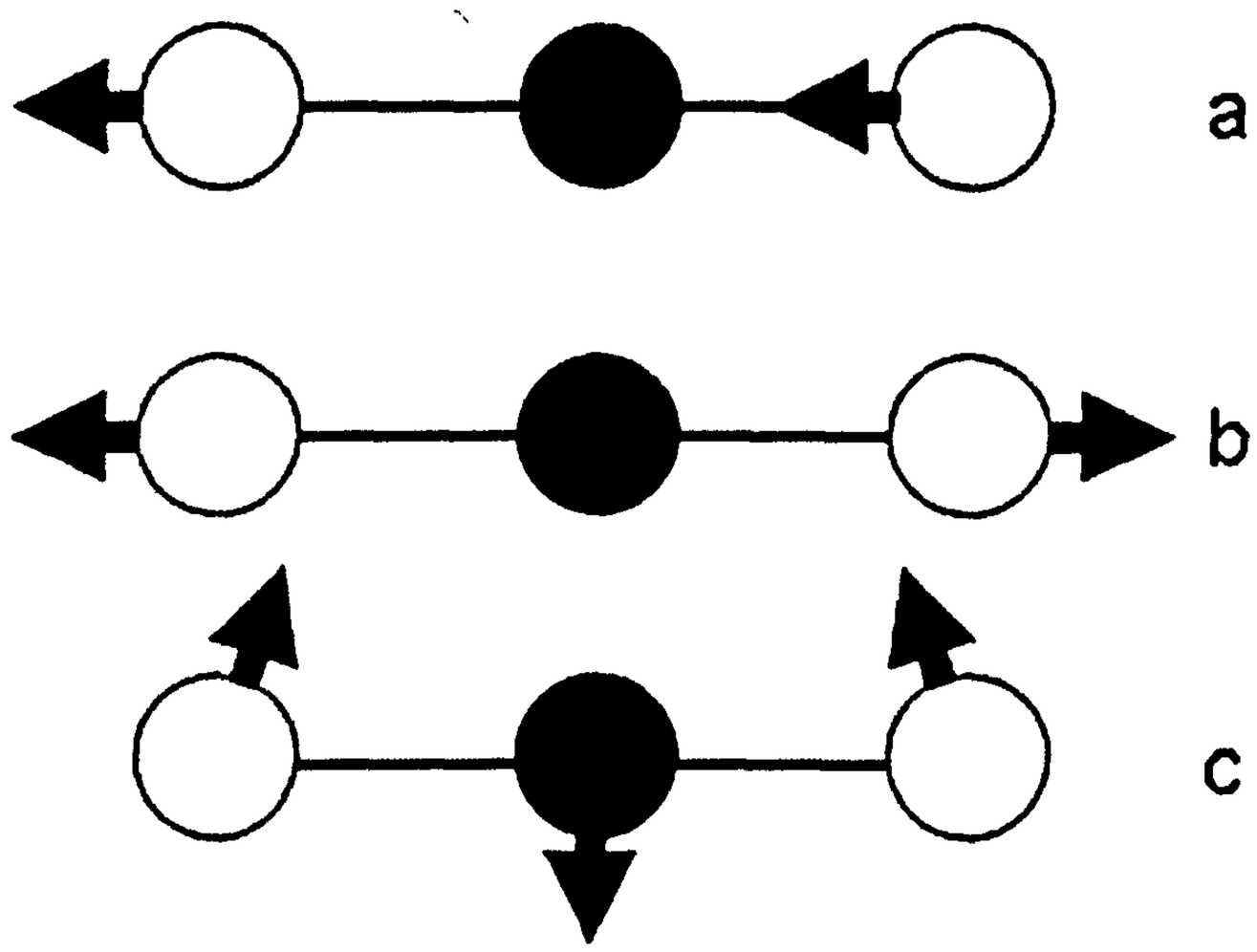

Figure 2.2.2 – *Three examples of vibration. (a) antisymmetric stretch. (b) symmetric stretch. (c) orthogonal bending vibration.*

The change in the electric dipole of the molecule during a transition can be used to classify the type of vibration. If the change in dipole moment is along the symmetry axis the vibration is parallel and if the change in dipole moment is at right angles to the symmetry axis the vibration is a perpendicular vibration. Vibrations that cause a change in dipole moment are said to be infrared active as they can contribute to the vibrational absorption spectrum. The selection rules for a polyatomic molecule are altered such that combinations and differences of vibrations are permitted. This allows bands to be produced of the form: v_1-v_2 and $2v_2$+v_1. These bands are normally very weak compared to fundamental vibrations.

2.2.10 Polyatomic Molecular Rotation

Linear polyatomic molecules rotate in a similar way to diatomic molecules. The energy levels associated with these rotations are given by the same expression. Due to the generally larger masses in linear polyatomic molecules the spectra lines will tend to be closer together than in the diatomic molecule case. In the case of a symmetric top molecule the energy levels associated with rotation are more complex. This arises from the fact that the molecule can rotate in two directions at the same time. This means that two quantum numbers are required to represent the rotations. The total angular momentum is represented by J and the rotation about the top axis is denoted by K. The energy levels for a symmetric top are given by:

$$E_{J,K} = AK^2 + B\left[J(J+1) - K^2\right] - D_J J^2 (J+1)^2 - D_{JK} J(J+1) K^2 - D_K K^4$$

where the centrifugal distortion constants are given by D_J, D_{JK} and D_K. A and B are the rotational constants for the two inertial axes a and b. The quantum number J takes any whole number as before and K can take any value in the range:

$$K = -J, -(J-1), -(J-2), ..., 0, ..., J-2, J-1, J$$

The selection rules for this type of molecule are:

$$\Delta J = \pm 1, \Delta K = 0$$

The spectrum associated with these transitions is similar to the diatomic molecule case except that for each of the rotational transitions there are J+1 additional lines created by K.

2.2.11 Polyatomic Molecular Vibration Rotation

For the rotational vibrational transitions the selection rules are different depending on the type of vibration. For a parallel vibration in a linear molecule the selection rules are:

$$\Delta J = \pm 1, \Delta \mathrm{v} = \pm 1, \pm 2, \pm 3, \ldots.$$

For a perpendicular vibration in a linear molecule the selection rules are:

$$\Delta J = 0, \pm 1, \Delta \mathrm{v} = \pm 1, \pm 2, \pm 3, \ldots.$$

For the case of the perpendicular vibration a transition can occur between the vibrational levels that preserves the rotation of the system. These transitions are known as Q branch transitions. For the parallel vibration of a symmetric top the selection rules are:

$$\Delta J = 0, \pm 1, \Delta \mathrm{v} = \pm 1, \Delta \mathrm{K} = 0$$

For a perpendicular vibration in a symmetric top the selection rules are:

$$\Delta J = 0, \pm 1, \Delta \mathrm{v} = \pm 1, \Delta \mathrm{K} = \pm 1$$

With these selection rules the Q branch transition is allowed. An analysis of more complicated molecular geometries such as asymmetric rotors can be found in Herzberg [3]. The spectrum of the ν_4 band of Methane, which is a spherical top polyatomic molecule is shown in Figure 2.2.3.

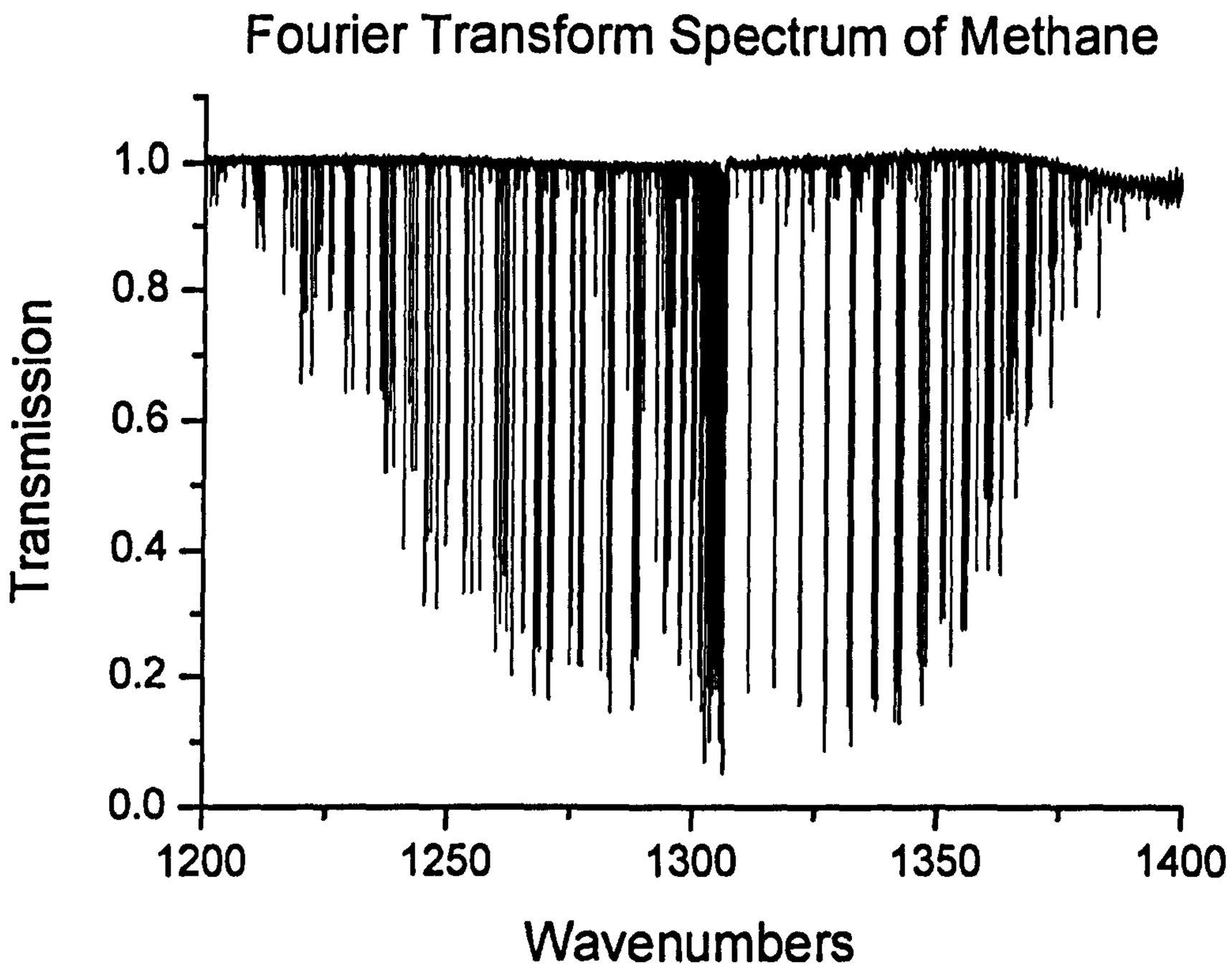

Figure 2.2.3 – *The Fourier Transform Spectrum of the v_4 band of Methane.*

2.2.12 Linear Absorption Spectroscopy

In linear absorption spectroscopy the radiation intensity used to probe a system is assumed to be not large enough to perturb the population distribution of the energy levels in the system. If we consider the change in light intensity, dI(ν), as a light beam passes through a medium of thickness dx:

$$dI(\nu) = -k(\nu) I(\nu) dx$$

where I(ν) is the initial light intensity and k(ν) is the absorption coefficient of the medium at the frequency ν. By integrating with respect to x for the above equation we obtain the following equation:

$$I(\nu) = I_0 \exp\left[-k(\nu)x\right]$$

where I_o is the initial light intensity and x is the thickness of the absorbing medium. The integrated absorption coefficient over an absorption line can be obtained by integrating over the absorption coefficient k(ν):

$$\int_{j\leftarrow i} k(\nu)d\nu = \frac{h\nu_{ji}}{c} B_{ji}\left(N_i - N_j\right)$$

where i and j are the lower and upper levels associated with the absorption and N_i and N_j are the populations of those levels. Bji is the Einstein B coefficient of stimulated absorption, such that:

$$\int_{j\rightarrow i} k(\nu)d\nu = \frac{8\pi^3}{3hc}\left(\frac{N_i}{g_i} - \frac{N_j}{g_j}\right)\nu_{ji}S_{ji} = S_{line}$$

$$k(\nu) = S_{line} f\left(\nu - \nu_0\right)$$

$$S_{line} = S^0 P$$

where g_i and g_j are the statistical weights of the levels i and j. S^0 has dimensions of linear absorption coefficient ($cm^{-1}atmosphere^{-1}$). P is the number density such that S_{line} has units of $cm^{-1}molecule^{-1}$.

The Beer-Lambert law is only valid if there is no appreciable saturation of absorption. At high gas pressure the law begins to go nonlinear. In some of the work done in this thesis noticeable power saturation has been observed. A description of power saturation can be found in Section 4.

2.2.13 Lineshape Function

In the measurements made in this thesis the natural lineshape of absorption lines has fallen into three different categories. These three categories are the Doppler broadened lineshape, the pressure broadened lineshape and the intermediate case. All states, except the ground state, decay with a characteristic lifetime, τ. By the uncertainty relation the energy of such a state cannot be exactly determined. The energy is uncertain by an amount of order $\hbar/\tau$. This leads to all radiative transitions having a characteristic linewidth. This linewidth can be altered when molecules undergo collisions. Collisions broaden the energy levels of the molecules and, in general, lead to larger linewidths.

At low gas pressures Doppler broadening, which is the broadening arising from the motion of the molecules relative to the detection system, dominates the lineshape of a transition. The shape of the line undergoing Doppler broadening is a Gaussian function of the form:

$$g(\nu-\nu_0)=\frac{1}{\delta\sqrt{\pi}}\exp\left[-\left(\frac{\nu-\nu_0}{\delta}\right)^2\right]$$

where $\delta=\frac{\nu_0}{c}\sqrt{\frac{2kT}{M}}$. The half width at half height is given by $\delta\sqrt{\ln 2}$.

At high pressures the pressure broadened lineshape is Lorentzian function of the form:

$$g(\nu-\nu_0)=\frac{1/\gamma_L}{\left[(\nu-\nu_0)^2+\gamma_L^2\right]}$$

where the half width at half maximum, γ, is given by:

$$\gamma_L = [\gamma_a P_a + \gamma_b P_b] \sqrt{\frac{T_0}{T}}$$

where γ_a and γ_b are the self and foreign gas broadening coefficients and P_a and P_b are the partial pressure of the gases.

When the gas pressure is at an intermediate level the lineshape function is a convolution of a Lorentzian and a Gaussian. This convolved lineshape is called a Voigt function, which takes the form:

$$g(\nu - \nu_0) = \frac{Bx}{\pi} \int_{-\infty}^{+\infty} \left(\frac{\exp[-y^2]}{\left(x^2 + (z-y)^2\right)} \right) dy$$

where:

$$B = \frac{1}{\gamma_D} \sqrt{\frac{\ln 2}{\pi}}$$

$$x = \frac{\gamma_L}{\gamma_D} \sqrt{\ln 2}$$

$$z = \frac{(\nu - \nu_0)}{\gamma_D} \sqrt{\ln 2}$$

The integral can be approximated in many different ways, such as the Humlicek [4] derivation. The width of the function can be empirically determined using the following expression:

$$\gamma_\nu = 0.536\gamma_L + \sqrt{\left(0.2166\gamma_L^2 + \gamma_D^2\right)}$$

2.2.14 References

1) Infrared Vibration-rotation Spectroscopy: From Free Radicals to the Infrared Sky, G. Duxbury, John Wiley, (2000)

2) Molecular Quantum Mechanics, P. W. Atkins and R. S. Friedman, Oxford, (1997)

3) Infrared and Raman spectra of Polyatomic molecules, G. Herzberg, Van Nostrand, (1945)

4) An efficient method for evaluation of the complex probability function: the Voigt function and its derivatives, J. Humlicek, J. Quant. Spec. Radiat. Trans., **21**, 309-314, (1979)

2.3 Astigmatic Herriott Cell

2.3.1 Introduction

The astigmatic Herriott cell is a multipass cell [1] based on the Herriott cell first proposed by D. R. Herriott [2] in 1965. The cell consists of two identical mirrors separated by a distance d. Unlike the standard Herriott mirrors, which are standard spherical mirrors, an astigmatic Herriott mirror has two radii of curvature. The laser beam enters and exits through a small hole located centrally on one of the mirrors. As the laser beam propagates around the cell bouncing between the mirrors the asymmetry of the astigmatic mirrors spreads the spots on the mirrors more evenly across the faces of each mirror. This allows for more passes to be made around the cell when the astigmatic mirrors are used compared to the standard spherical mirrors. An example of an astigmatic mirror is shown in Figure 2.3.1.

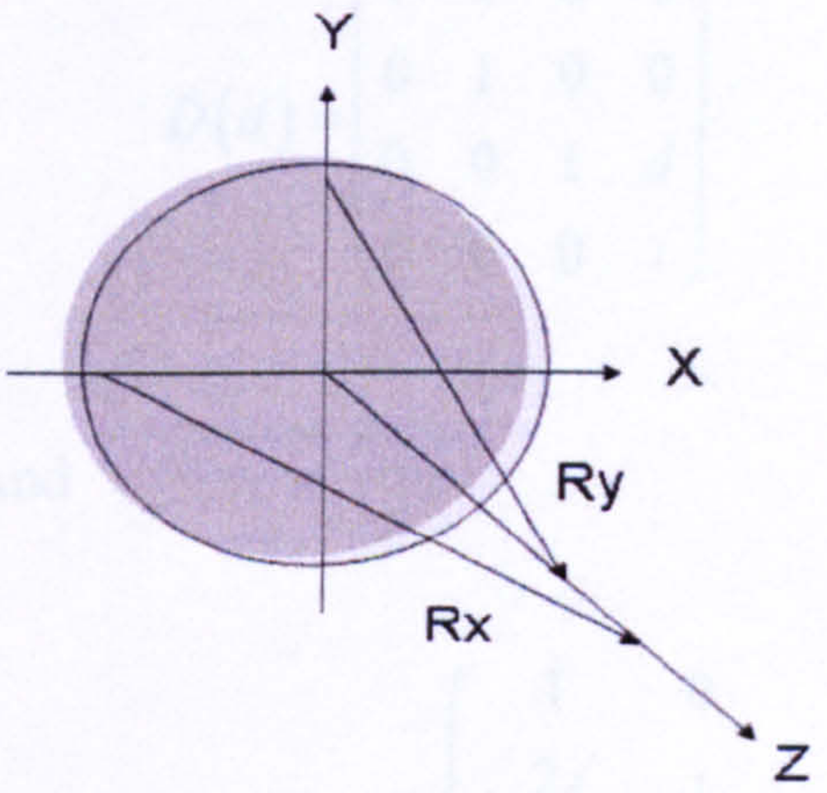

Figure 2.3.1 – *An astigmatic Herriott cell mirror schematic.*

The asymmetry of the mirrors focuses light by different amounts in the two optical axes. In order to achieve a re-entrant solution any manufacturing flaws in the mirrors must be compensated for. It has been shown by J. B. McManus et al [1] that by rotating one of the mirrors about its middle and by changing the separation of the mirrors the sufficient corrections can be made. This allows the manufacturing tolerances on the mirrors to be reduced.

2.3.2 Astigmatic Herriott Cell Model

The propagation of light in an astigmatic Herriott cell can be modelled using a set of ray tracing matrices. The matrix for one complete traversal of the cell, C(R,d), is the product of the free space propagation matrix, D(d), and the reflection matrix, $R(R_x,R_y)$, such that;

$$C(R,d) = R(R)\cdot D(d)\cdot R(R)\cdot D(d)$$

Where:

$$D(d) = \begin{pmatrix} 1 & d & 0 & 0 \\ 0 & 1 & 0 & 0 \\ 0 & 0 & 1 & d \\ 0 & 0 & 0 & 1 \end{pmatrix}$$

And

$$R(R_x,R_y) = \begin{pmatrix} 1 & 0 & 0 & 0 \\ -2/R_x & 1 & 0 & 0 \\ 0 & 0 & 1 & 0 \\ 0 & 0 & -2/R_y & 1 \end{pmatrix}$$

Such that d is the separation of the two astigmatic mirrors and R_x and R_y are the two radii of curvature of the astigmatic mirrors. In order to fully understand the propagation of light through the cell the rotation of one of the mirrors must be taken into account.

This is done by modifying the reflection matrix by adding the rotation matrix, $T(\theta_t)$, into the ray tracing equation.

$$T(\theta_t)=\begin{pmatrix} \cos\theta_t & 0 & \sin\theta_t & 0 \\ 0 & \cos\theta_t & 0 & \sin\theta_t \\ -\sin\theta_t & 0 & \cos\theta_t & 0 \\ 0 & -\sin\theta_t & 0 & \cos\theta_t \end{pmatrix}$$

Where the rotation angle of the mirror is θ_t.

The modified reflection matrix, $R'(R_x,R_y)$, becomes;

$$R'(R_x,R_y)=T(-\theta_t)\cdot R(R_x,R_y)\cdot T(\theta_t)$$

The coordinate of the beam spot after n passes, Z_n, is given by $C^n(R,D)\cdot Z_0$ where;

$$Z_0=\begin{vmatrix} x_0 \\ x_0' \\ y_0 \\ y_0' \end{vmatrix}$$

And

$$Z_n=\begin{vmatrix} x_n \\ x_n' \\ y_n \\ y_n' \end{vmatrix}$$

Where x_0, y_0, x_n and y_n are the spatial coordinates of the spot at zero passes and n passes and x_0', y_0', x_n' and y_n' are the slopes of the vectors after zero and n passes. These equations have been used to create a MATLAB [3] program which has been used to investigate the properties of the astigmatic Herriott cell.

2.3.3 Astigmatic Herriott Cell Solutions

The solutions to the model vary with the changing of the radii of curvature of the mirrors used. In this case the radii of curvature were fixed to the values present in the mirrors that were already owned by the research group. The radii of curvature of these mirrors were designed by a previous PhD student from the group [4]. For all of the solutions used;

$$R_x = 77.274cm$$
$$R_y = 67.425cm$$

During the course of my work different astigmatic Herriott cell solutions were used, however the mirror separation, d, for all of the solutions was approximately 50cm. The separation of the mirrors was limited by the size of the glass pipe used to house the cell. The first of the solutions used during the initial testing phase of the instrument development was an 18.1m, 36 pass, solution. This solution was created by setting the mirror separation to 50.35cm and rotating the back mirror by 28.1°. The back and front mirror solutions are shown in Figure 2.3.2.

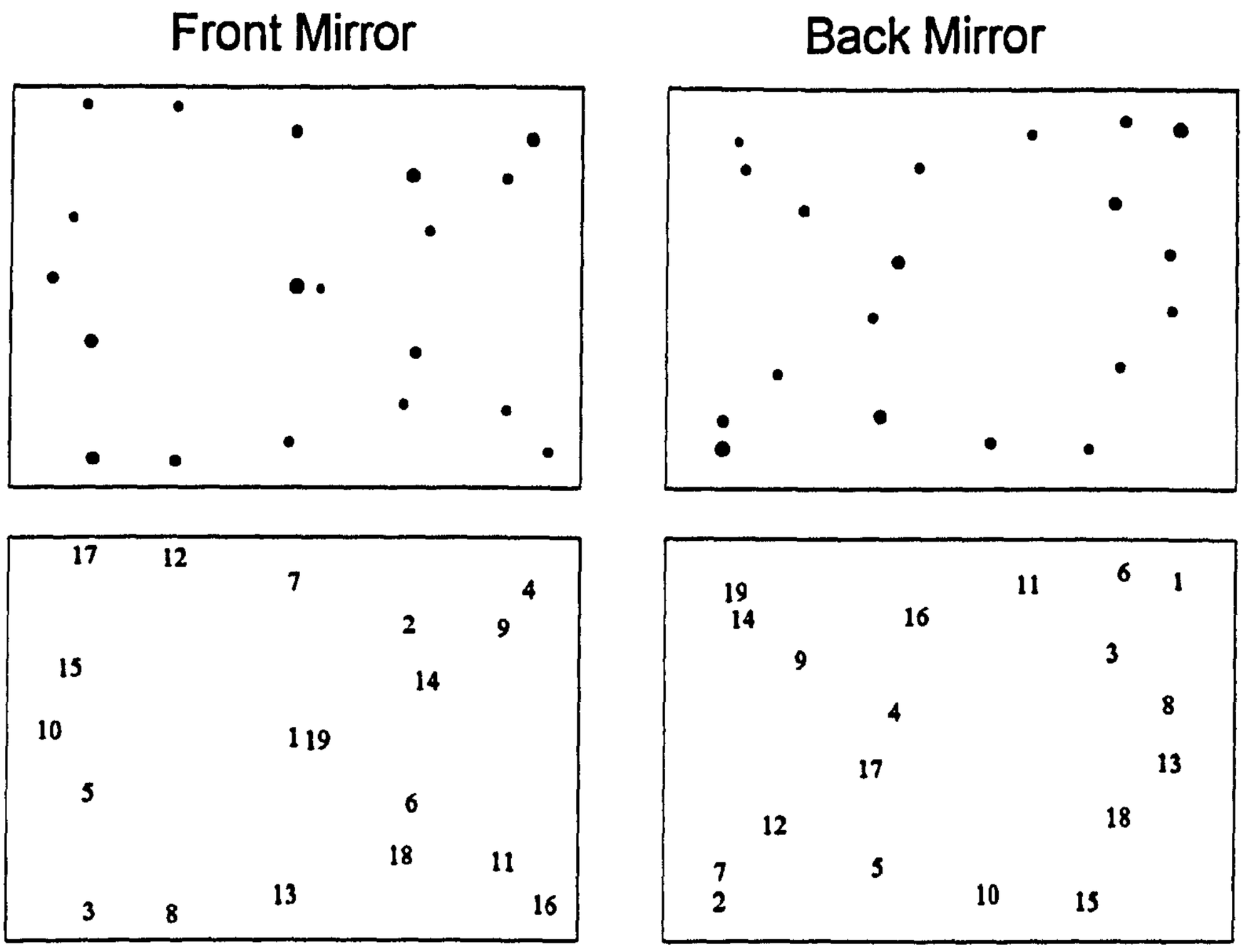

Figure 2.3.2 – *The left two graphs show the spot pattern for the front mirror and the right two graphs show the spot pattern for the back mirror.*

For the top two graphs the larger diameter spots come nearer the start of the solution and the smaller diameter spots occur at longer times into the solution. The bottom two graphs show the spot number on each of the mirrors. On the front mirror spot 1 is the entrance spot and spot 19 is the exit spot. This solution was used in the testing phase of the instrument because it was found to be very insensitive to tilt, rotation and separation changes, which is ideal when first testing the astigmatic Herriott cell. The other good point of this solution is that it is easily recognisable, which is a key part to aligning the cell. Due to the relatively short pathlength achieved with this solution no measurements made with this solution are reported in this work. The second solution to be used was a 202 pass solution. This solution involved setting the mirror separation to 49.967cm and the mirror rotation to 19.9°. This yields a pathlength of 100.9cm. The back and front mirror spot patterns for this solution are shown in Figure 2.3.3.

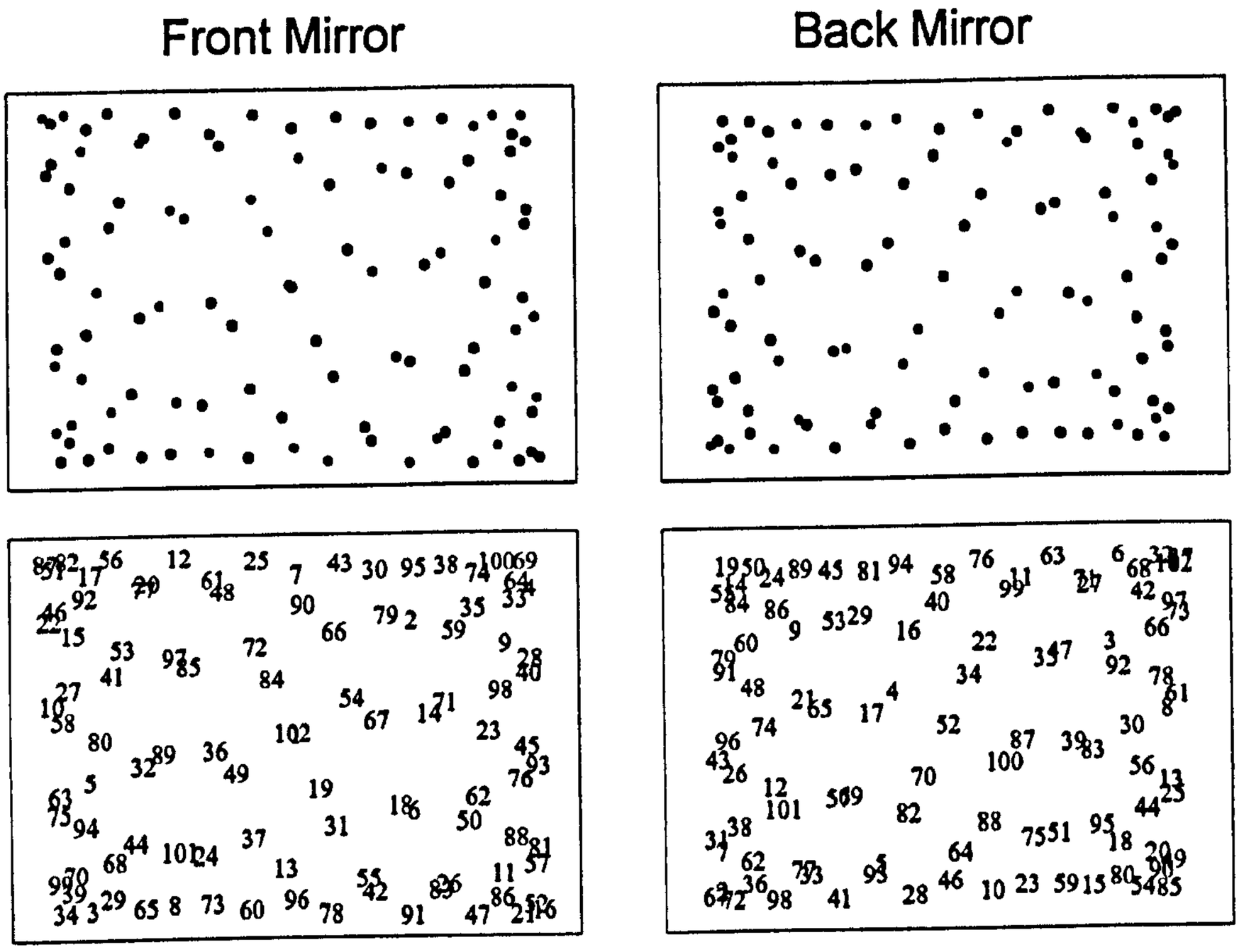

Figure 2.3.3 – *The left two graphs show the spot pattern for the front mirror and the right two graphs show the spot pattern for the back mirror.*

For the top two graphs the larger diameter spots come nearer the start of the solution and the smaller diameter spots occur at longer times into the solution. The bottom two graphs show the spot number on each of the mirrors. On the front mirror spot 1 is the entrance spot and spot 102 is the exit spot. Much of the work done in this thesis at 10μm was carried out using this solution. The rotation and separation sensitivities of this solution have been calculated before [4] to be 0.76mm and ±1.23°. A photo of the back mirror for this solution is compared to the simulated spot pattern in Figure 2.3.4.

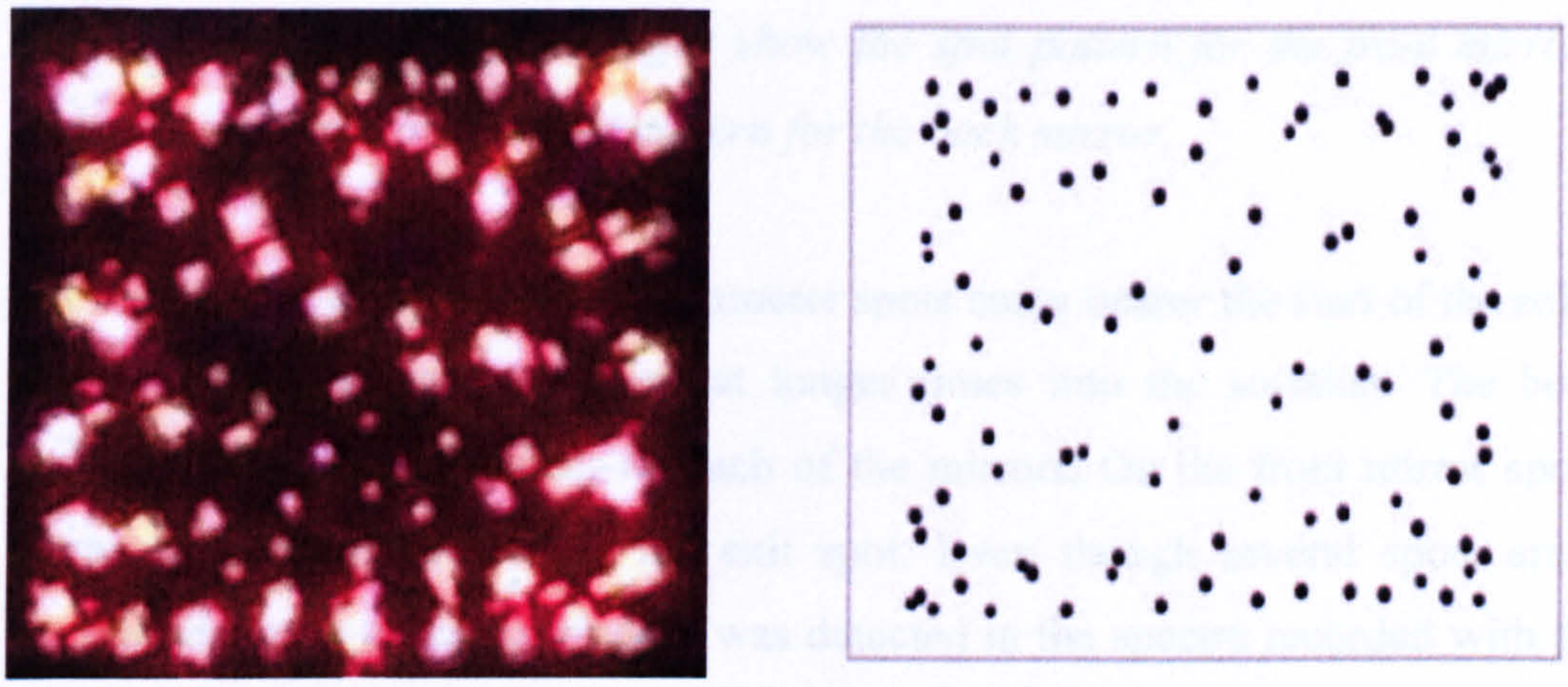

Figure 2.3.4 – *The back mirror of the 202 pass solution.*

For the rest of the work done at 10μm a 132 pass solution was used. This solution was produced by setting the mirror separation to 50.1cm and the mirror rotation to 16.8°. This yielded a pathlength of 66.1m. The back and front mirror spot patterns for this solution are shown in Figure 2.3.5.

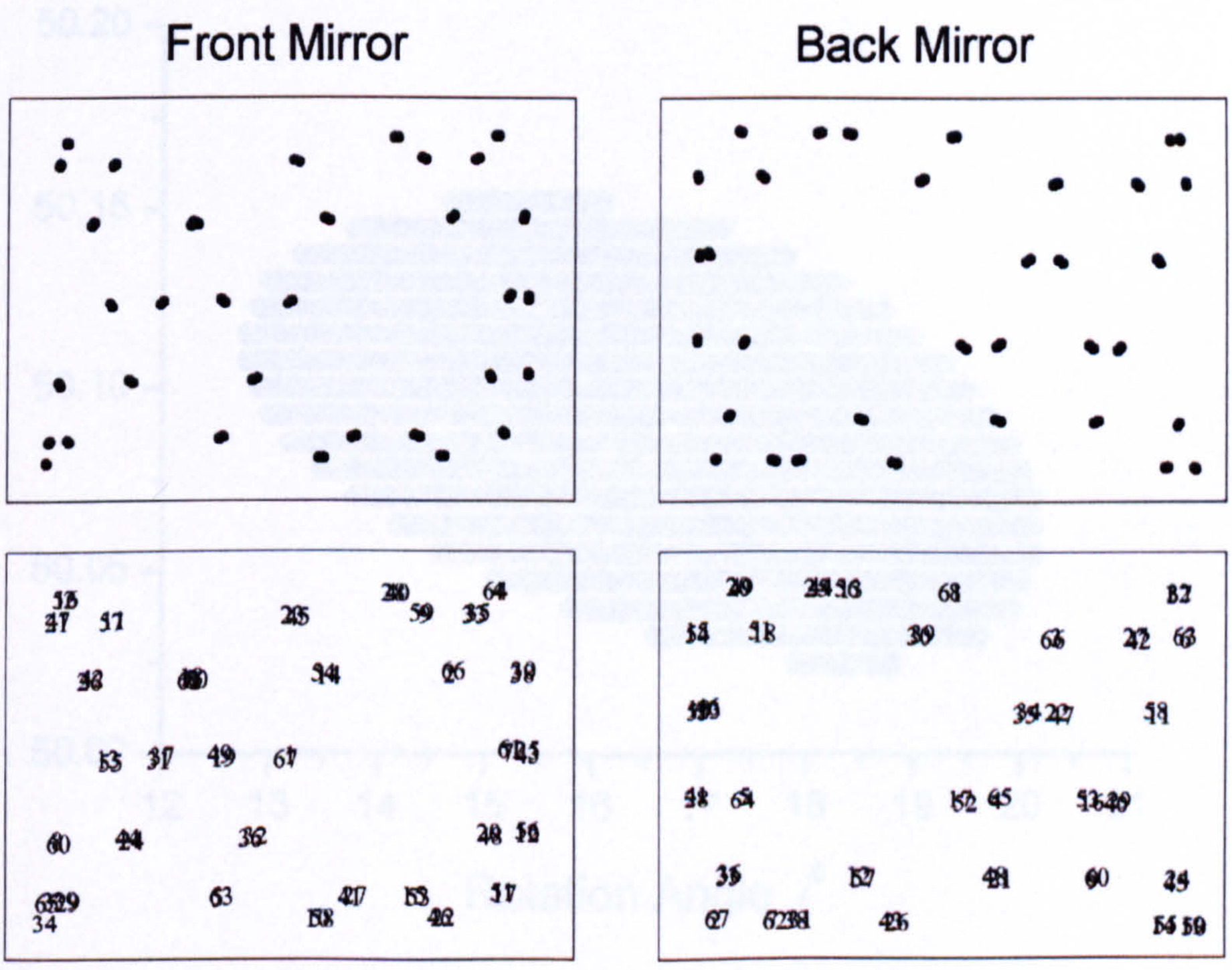

Figure 2.3.5 – *The left two graphs show the spot pattern for the front mirror and the right two graphs show the spot pattern for the back mirror.*

For the top two graphs the larger diameter spots come nearer the start of the solution and the smaller diameter spots occur at longer times into the solution. The bottom two graphs show the spot number on each of the mirrors. On the front mirror spot 1 is the entrance spot and spot 67 is the exit spot. Even though several spots are close to overlapping each other no fringing was detected in the spectra recorded with this setup. In order to test the stability of this pattern an iterative version of the astigmatic Herriott cell modeling program was written and used. This program calculated the number of passes in the Herriott cell over a range of angles and mirror separations, which gave a map of solutions. The stability of the 132 pass solution is shown in Figure 2.3.6 as a function of rotation angle and mirror separation.

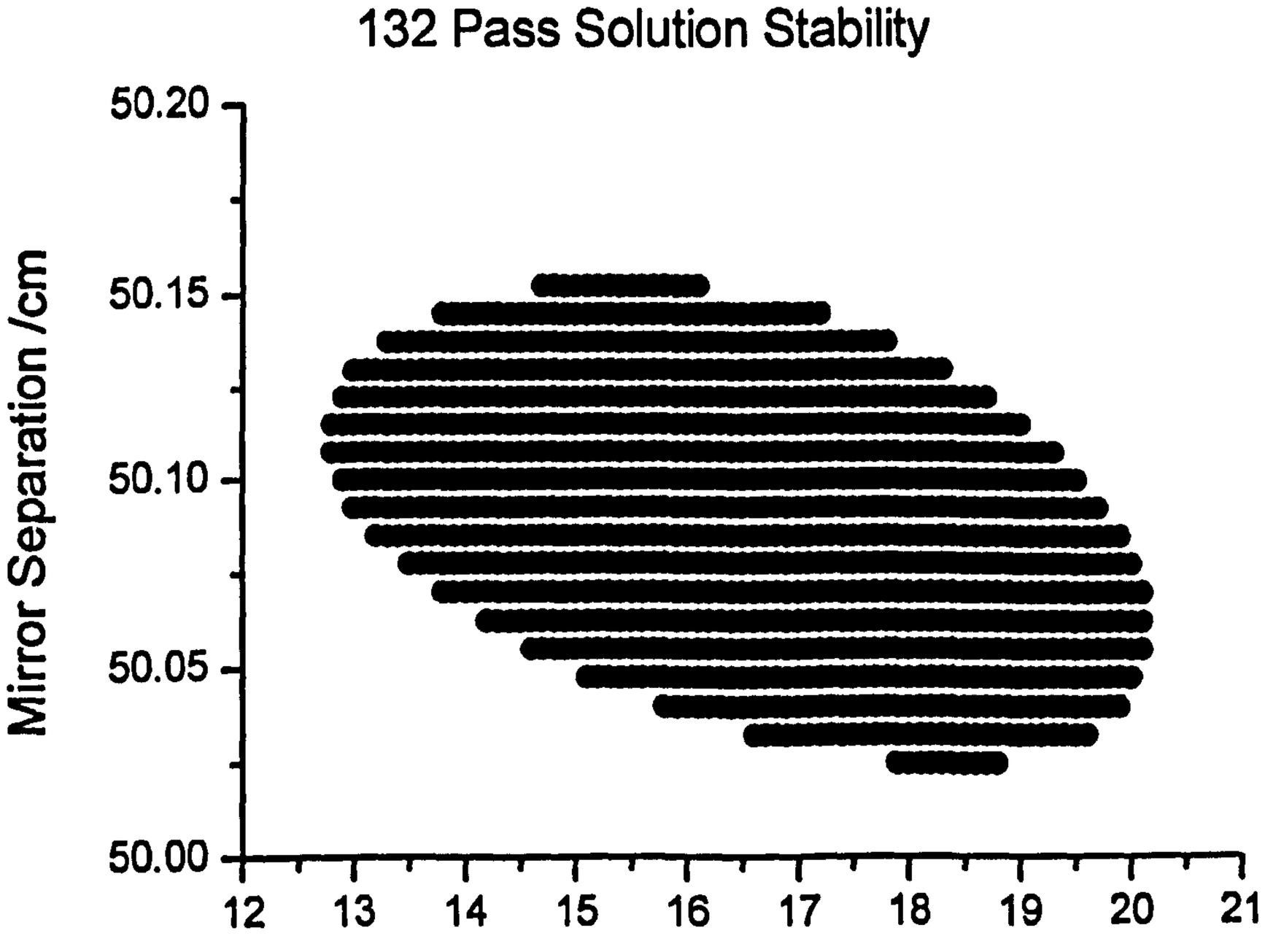

Figure 2.3.6 – *The stability of the 132 pass solution as a function of mirror separation and mirror rotation angle.*

Each of the dots represents a point on the iteration map. The resolution of the integration was 0.1° and 0.0075cm. The sensitivity of the astigmatic Herriott cell was found to be more tolerant to changes in mirror rotation than mirror separation, which is why the angle resolution used was coarser than the mirror separation resolution.

For the work done in this thesis at 8μm a longer pathlength solution was found to increase the sensitivity of the spectrometer. A 232 pass solution was settled upon. This solution can be created using a mirror separation of 49.49cm and a mirror rotation angle of 15.7°. This solution provides a pathlength of 114.8m. The back and front mirror spot patterns for this solution are shown in Figure 2.3.7.

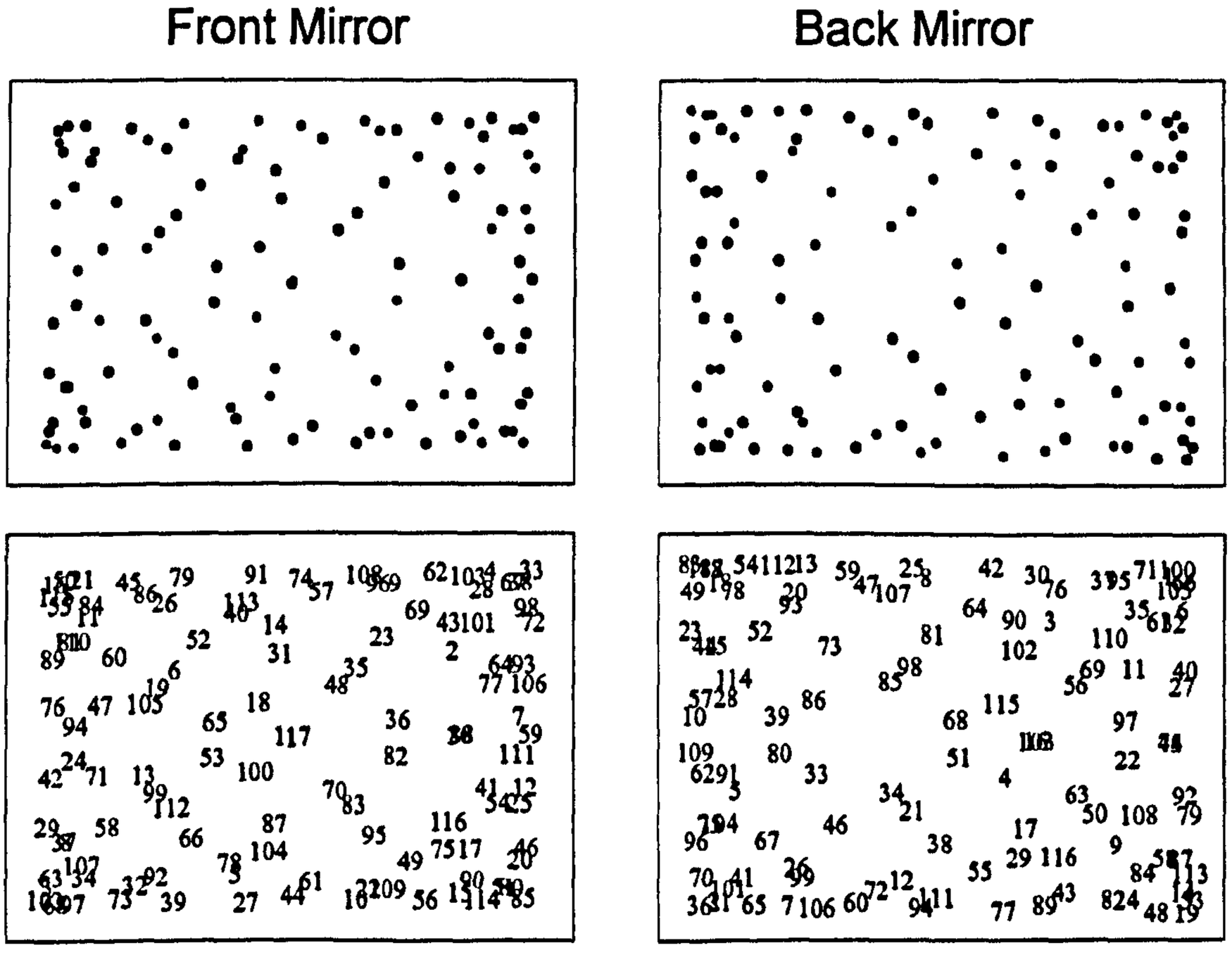

Figure 2.3.7 – *The left two graphs show the spot pattern for the front mirror and the right two graphs show the spot pattern for the back mirror.*

For the top two graphs the larger diameter spots come nearer the start of the solution and the thinner diameter spots occur at longer times into the solution. The bottom two graphs show the spot number on each of the mirrors. On the front mirror spot 1 is the entrance spot and spot 117 is the exit spot. This solution has an easily recognised spot pattern with well separated spots. Using the MATLAB iteration program the stability of this solution has been tested. The stability of the 232 pass solution is shown in Figure 2.3.8 as a function of rotation angle and mirror separation.

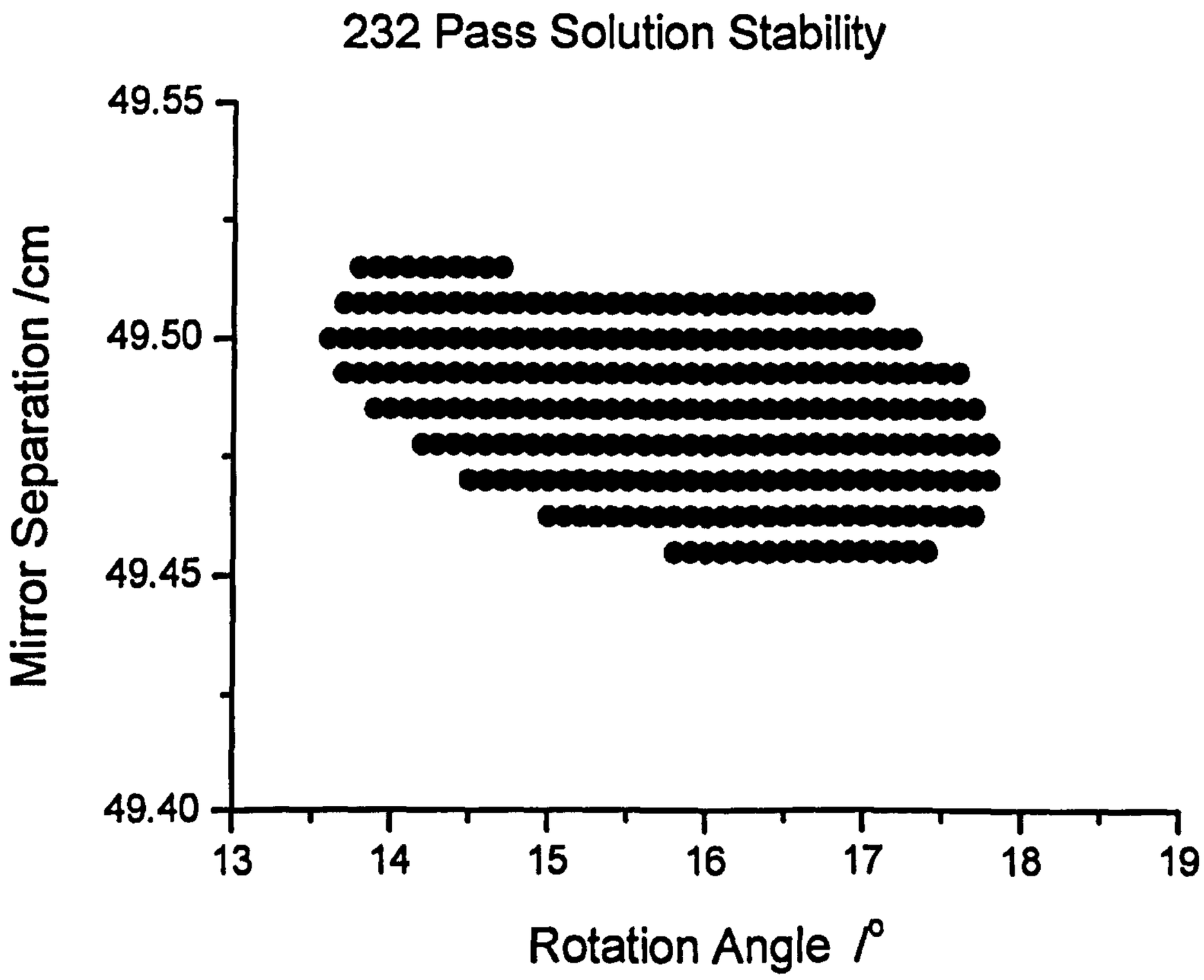

Figure 2.3.8 – *The stability of the 232 pass solution as a function of mirror separation and mirror rotation angle.*

This solution is less stable than the previous 132 pass solution. This is because the Herriott cell acts like a pair of irises separated by the pathlength created by the mirrors.

As the pathlength increases the allowed tolerances on the light getting through the cell decreases and thus the stability of the solutions decrease with increasing pass numbers.

2.3.4 Conclusions

A MATLAB program has been written to model the propagation of a laser beam through an astigmatic Herriott cell. This program has been used to find long pathlength solutions and to test the stability of these solutions. The spot patterns from these solutions have been tested against the actual spot patterns when the cell is setup and they have been found to be in good agreement. It was found that the stability of a solution decreased as the number of passes increased.

2.3.5 References

1) Astigmatic mirror multipass absorption cells for long-path-length spectroscopy, J. B. McManus, P. L. Kebabian and M. S. Zahniser, App. Opts., **34**, 18, 3336-3348, (1995)

2) Folded optical delay lines, D. R. Herriott and H. J. Schulte, App. Opts., **4**, 8, 883-889, (1965)

3) MATLAB v6.5, The Mathworks, http://www.mathworks.com/

4) Near infrared tunable diode laser absorption spectrometer for trace gas detection, I. F. Howieson, PhD Thesis, Department of Physics and Applied Physics, University of Strathclyde, (1997)

3.1 Spectrometer Design

3.1.1 Introduction

This chapter describes the development of a high resolution (~0.005cm^{-1}) Quantum Cascade laser based mid infrared absorption spectrometer (QCLAS). The need for accurate and precise measurements of trace atmospheric gases has been discussed in chapter 1. These gases, released from industrial and agricultural sources, have brought the publics attention to the subject of global warming and the consequences of air pollution. Several techniques have been developed to monitor gases in the atmosphere. Traditionally lead salt lasers have been used to probe trace gases in the mid infrared. These systems [1] are capable of high resolution and high sensitivity; however they require cryogenic cooling and suffer from temperature cycling. In recent years the development of Quantum Cascade lasers [2] has allowed the development of new mid infrared spectrometers. Two techniques have been pioneered for the use of these new lasers. Most of the present generation of QC based absorption spectrometers are based on the method developed by Namjou *et al* [3]. These systems use short current pulses (~ 3 to 10 ns) applied to the QC, which generates a pulse in the spectral domain. This spectral pulse is tuned through an absorption feature by applying a slowly varying sub threshold current ramp to the pulse train. This results in a quadratic tuning function. Using this technique tuning ranges of 0.23 cm^{-1} to 0.74 cm^{-1} have been reported [4]. Once the data has been recorded this quadratic tuning effect must be corrected. For systems utilising phase sensitive detection in order to achieve trace level sensitivity a modulation of several kilohertz is applied to the current ramp and as a result the rate at which data can be collected is limited. The second method for driving Distributed feedback Quantum Cascade lasers was developed as a result of work done within the group [5]. Our technique applies long current pulses (50ns – 1500ns) to our laser. This generates a pulse in the frequency domain, which frequency down chirps up to 5 cm^{-1}. We infer spectral information from the time domain pulse. This allows us to observe the spectral profiles of gases in real time at very high repetition rates. The signal to noise ratio of our system is maximised by sequentially averaging large numbers of scans rapidly, giving a $\sqrt{n}$ signal to noise improvement over n scans. The scan is linearised using a Germanium

etalon. Our technique has several advantages, such as we record an entire spectrum with each laser pulse as opposed to building up a spectrum one data point per laser pulse. Also the electronics used in our setup are less complicated as we do not require lockin amplifiers or Bias-T's.

During this work two lasers have been used for the majority of work. Both lasers were bought from Alpes Laser. The first diode operated at 10.2 μm, which covered Carbon Dioxide and Water in the atmosphere and Ethylene, Ammonia, Water and Carbon Dioxide in combustion processes. The second laser operated at 7.84 μm, which covered Methane, Water and Nitrous Oxide in the atmosphere and Methane, Water, Nitrous Oxide, Carbon Dioxide, Acetylene and Formaldehyde in combustion processes. The instrument is designed to make high sensitivity measurements with excellent selectivity of multiple gases in the atmosphere or in combustion exhausts.

3.1.2 Optical Setup

In this section the optical setup of the QCLAS will be discussed. Figure 3.1.1 shows a schematic of the optical layout of the QCLAS.

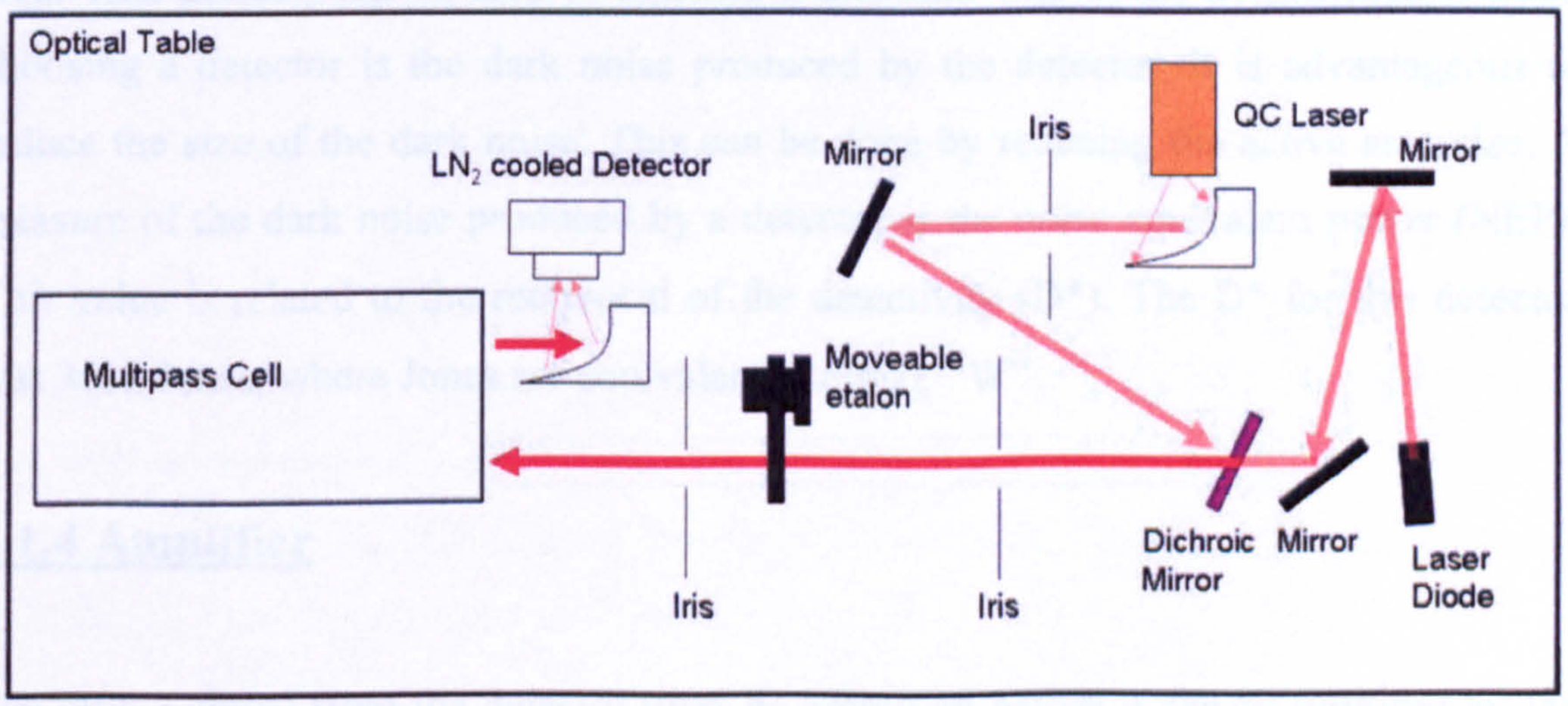

Figure 3.1.1 – *Optical Layout of QCLAS*

The thermoelectrically cooled Quantum Cascade laser is housed in a box. The 10.24μm laser uses an Alpes Laser box, whereas the 7.84μm laser uses an in house built box, described in section 3.2. The output from the laser is diverging, so in order to obtain a parallel beam an off axis parabaloid is used. The infrared laser beam is combined with a red diode laser beam at the dichroic mirror, which reflects in the infrared but transmits in the visible. The two beams are made collinear through the two irises, which are separated by about 30cm. Between the irises is a moveable etalon. This etalon is used for calibration purposes. The beams then enter the astigmatic Herriott cell. The output beam from the cell exits from the same window as the entrance beam. This output beam is focused onto the high speed Kolmar MCT [6] detector by an off axis paraboloid.

3.1.3 Detector

The main detector used in this work was a Kolmar KV104 MCT liquid nitrogen cooled detector, which had a wavelength cut off of 11.5μm. The detector was sold as having greater than 100MHz bandwidth. During this work the bandwidth was found to be closer to 450MHz. In order to achieve a large bandwidth a detector must have a small active area. This detector has an area of 0.25mm x 0.25mm. One of the considerations when choosing a detector is the dark noise produced by the detector. It is advantageous to reduce the size of the dark noise. This can be done by reducing the active area size. A measure of the dark noise produced by a detector is the noise equivalent power (NEP). This value is related to the reciprocal of the detectivity (D*). The D* for this detector was 3e10 Jones, where Jones are equivalent to $cmHz^{1/2}W^{-1}$.

3.1.4 Amplifier

The output signal from the detector must be amplified before it can be digitised by the computers on board digitiser. Two amplifiers have been used during this work. Both were fixed gain amplifiers manufactured by Femto GmbH. Both amplifiers were of the

same design except for the bandwidth, where one was a 1GHz bandwidth and the other was a 2GHz bandwidth. The gain of these amplifiers was 40dB, which is 5kV/A. The equivalent input current noise of the 2GHz amplifier was 13pA/√Hz. These amplifiers provided two identical output channels, one of which was 50Ω terminated if it was not required. In order to reduce noise the distance between the detector output and the amplifier input was kept to a minimum. The connection was made using a 3cm SMA connector.

3.1.5 Digitiser

Once the detector signal had been amplified it had to be digitised. This was done using an Acqiris AP200 Averager. The high repetition rate of the laser (up to 30kHz) required a digitiser with a short dead time. Other digitisation systems were tested during this work. An Agilent Infiniium oscilloscope and a LeCroy WavePro oscilloscope were tested. Both oscilloscopes had bandwidths of greater than 1GHz. The Agilent oscilloscope had a computer built in that ran windows, which allowed data to be stored and analysed through the windows interface. The LeCroy oscilloscope had a GPIB port, which allowed computer control. The Agilent oscilloscope did not allow sequential averaging of waveforms, which meant that pulses were being missed by the oscilloscope and the acquisition rate fell as a consequence. The LeCroy oscilloscope did allow sequential averaging of the waveforms, however it was limited to 8000 sequential pulses and the time to write the data from the oscilloscope to the PC was too long. These two digitisation systems were therefore not deemed satisfactory for this work. The AP200 used an onboard Field Programmable Gate Array (FPGA) to record sequentially all of the laser pulses detected by the detector and average them in real time. The AP200 allowed up to 65536 pulses to be averaged together. The bandwidth of this digitiser was 500MHz and the sample rate was 2GS/s.

3.1.6 Evacuatable Astigmatic Herriott Cell

Figure 3.1.2 shows a schematic of the cell. The body of the cell is a 4inch diameter section of QVF glass pipe. The glass pipe is closed off by two aluminium end plates, sealed with two rubber o-rings. One of the end plates contains a wedged salt window (KBr Graseby Specac, 40mm) on axis and the other plate is a blanking off plate. The wedged window reduces any fringing effects from the two surfaces of the window. The cell is attached to the optical table using two metal clamping frames. These frames use three screws each to locate the cell.

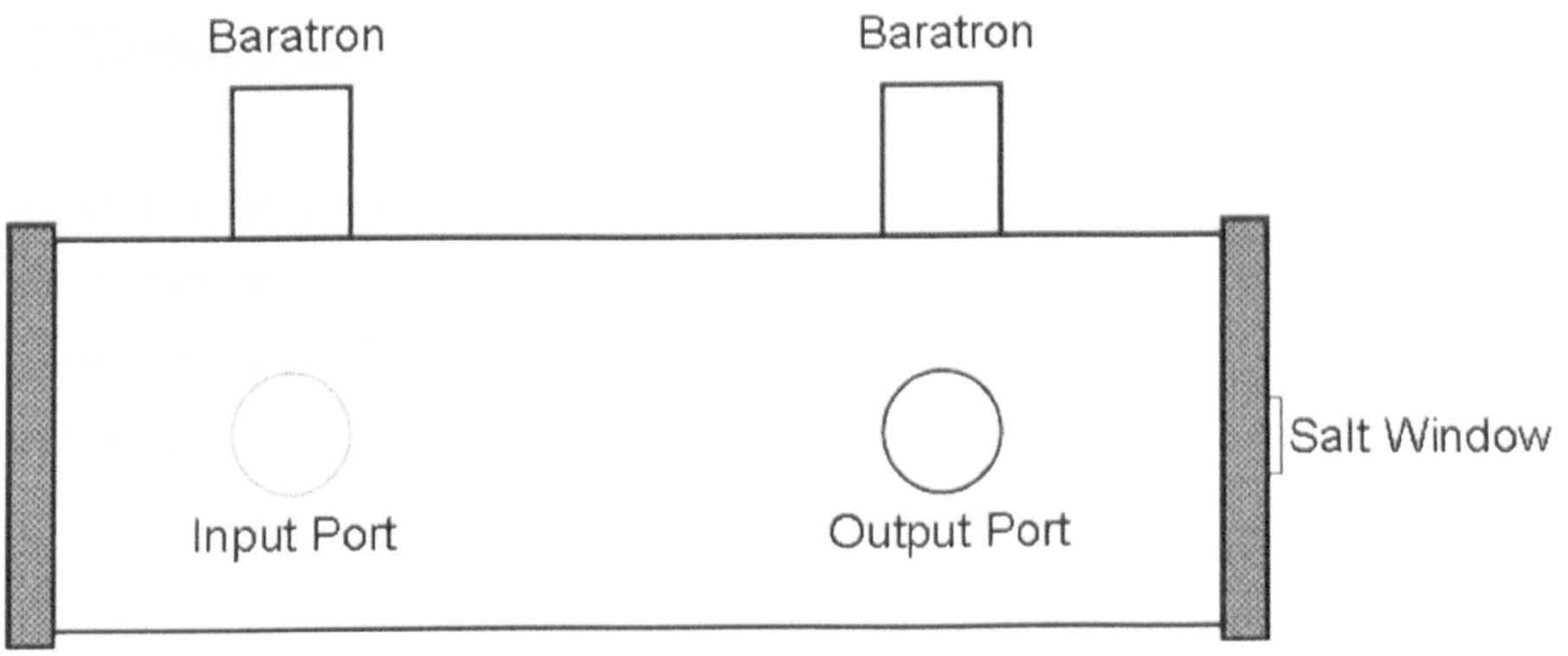

Figure 3.1.2 – *Schematic of the Astigmatic Herriott cell*

On the inside of the cell the astigmatic mirrors are located at either end of an aluminium frame. This frame was 50cm long. A micrometer travel was located at the back end of the cell. This allowed the hole less astigmatic mirror to be displaced up to 0.5cm along the axis of the cell. Both ends allowed tilt of the mirrors.

The cell has four 1.5inch ports on it. Two on top of the cell and one on either side of the cell. The two ports on top of the cell are used to monitor the pressure inside the cell by a low pressure (1Torr) baratron gauge and a high pressure (1000Torr) baratron gauge. The

ports on either side of the cell allow gas to be flowed through the cell. These ports are offset from each other. Unlike commercial astigmatic Herriott cells [7], which flow gas along the direction of the cell, our design allows the gas to flow perpendicular to the direction of the cell. This is done to minimise the contact of the gas and the astigmatic mirrors. When flow control was required an MKS instruments type 640 pressure controller (0Torr – 100Torr) was used at the input port of the cell. The cell was pumped at the output port of the cell, using a rotary pump, and the pressure in the cell was kept at a constant pressure by the pressure controller. For atmospheric measurements a 3m PTFE tube was used to sample atmosphere out the laboratory window. For car exhaust measurements a 50m garden hose was used to sample the car exhaust from outside the laboratory window and down the two storeys to the car park.

3.1.7 Electronics

The control electronics used in this work have been bought commercially with the exception of the laser power supply. This power supply was designed by a previous PhD student in the group [8]. A schematic diagram below, Figure 3.1.3, shows the setup of the electronics.

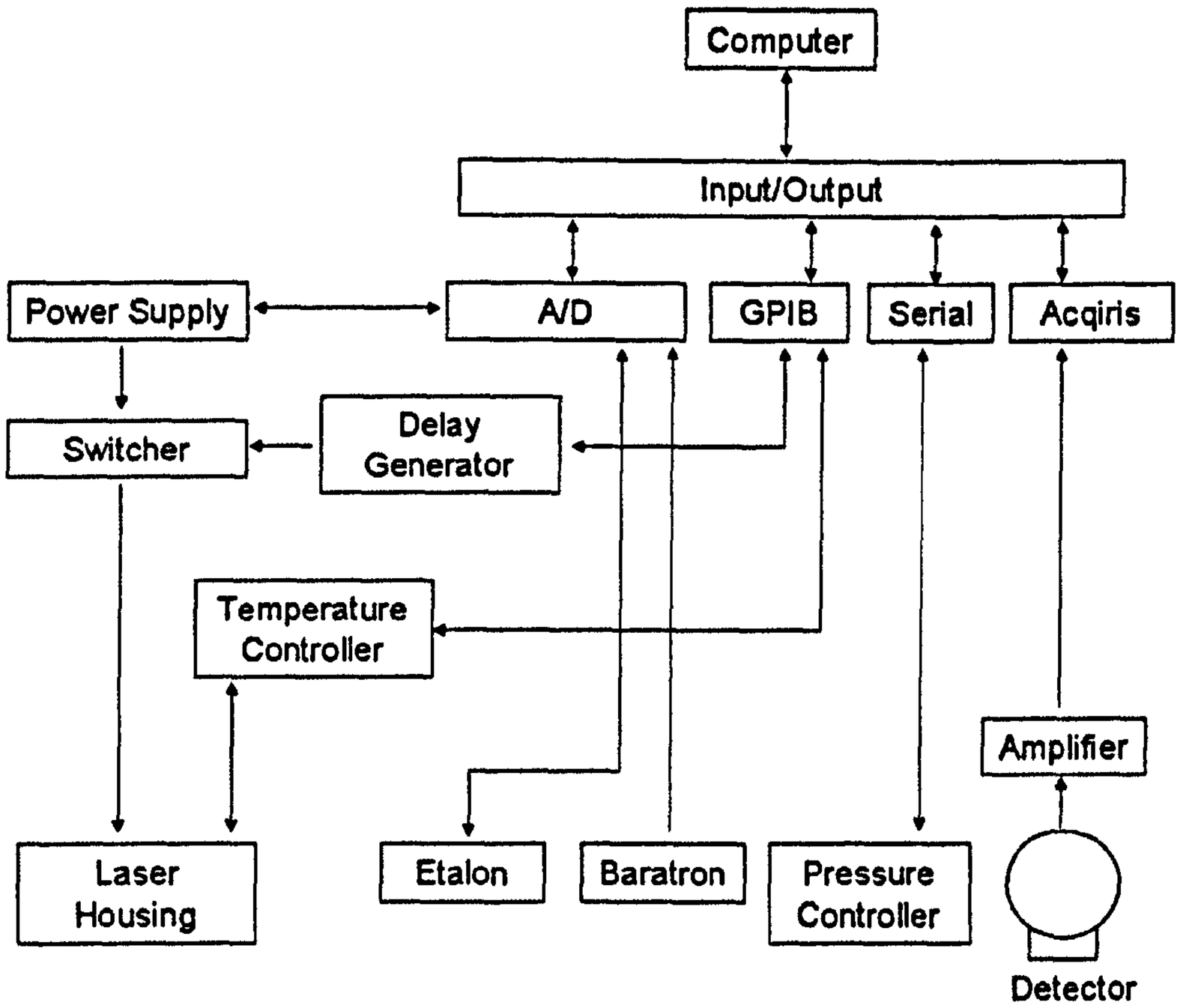

Figure 3.1.3 – *Schematic of the electronics*

All of the electronics used to control and drive the laser were computer controlled using a LabVIEW vi described in this chapter. In this section I will describe the electronics independently of the computer control. As the LabVIEW vi was designed after the system was up and running some of the work described in this thesis was pre computer control. The power supply designed by Erwan Normand was capable of providing a high voltage and a high current output. Typically the power demands were 250V and 5A at up too 2.5% duty cycle. Unlike other systems [3], which use low impedance lines to their devices, we 50Ω match as close to the laser as possible. This is done because we use long pulses which would produce large electrical ringing effects if we used long low impedance lines from the 50Ω switcher output. The other systems [3, 4] use short pulses, which are too short to worry about ringing processes. This means that they can use less high duty power supplies than we do. The switcher was a Directed Energy Inc. HV1000

pulser. This switcher could produce top hat shaped current pulses from 55ns to 10μs wide, with up to 17A of current. The shot to shot temporal jitter was less than 100ps. The temperature of the laser was controlled and monitored by a Newport 3040 temperature controller. This device was stable to within ±0.01°C. The 4A output was capable of cooling our lasers down to -10°C when air cooled and -40°C when liquid cooled. The trigger signal was produced by a Stanford DG535 delay generator. This 4 channel delay generator developed a variable trigger signal from ns to μs, with a resolution in the ps range.

3.1.8 Radio Frequency (RF) removal

During early experiments RF interference was picked up on the spectra being recorded. Sometimes the interference signal was larger than the absorption feature of interest. The main cause of this interference was found to be the switcher. The switcher was giving off RF when switching either on or off. There was also background RF given off from the other electronics and the cables connecting them. The switcher RF was not a problem in some cases because the optical delay of the astigmatic Herriott cell was longer than the pulse. This meant that the RF from the switcher was picked up before the laser pulse reached the detector. This is shown below in Figure 3.1.4.

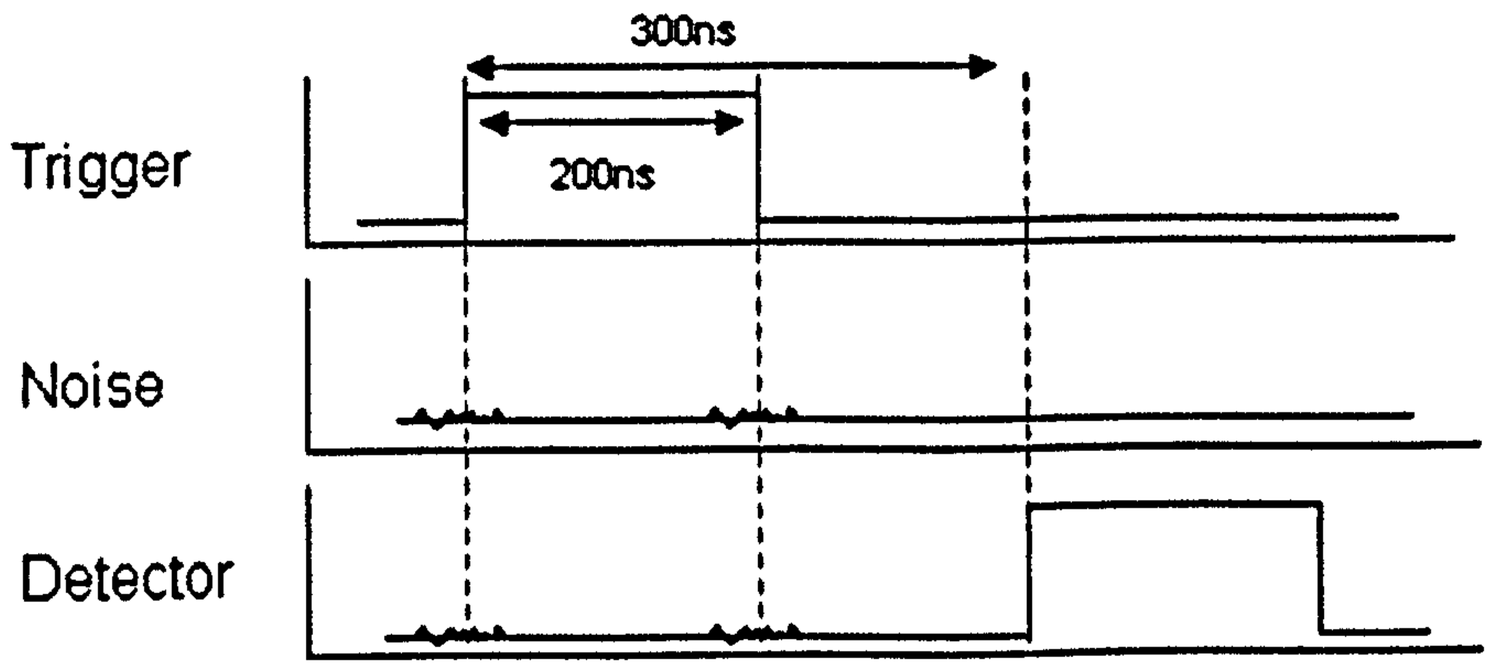

Figure 3.1.4 – *Switcher noise seen by the detector*

An optical delay of approximately 300ns is created by the astigmatic Herriott cell when it is setup for 100m of optical path. If a 200ns trigger pulse is used the RF from the switcher is not picked up by the detector at the same time as the laser pulse. The background RF interference was more of a problem as it acted like continuous white noise. In order to counter these problems the detector housing was covered in a copper mesh. This completely removed the background RF interference and significantly reduced the switcher RF interference. This means that as long as the optical delay is longer than the pulse width of the laser no RF interference should be picked up. However much of the work in this thesis has been done with pulse widths longer than the optical delay of the system. Figure 3.1.5 below shows this regime.

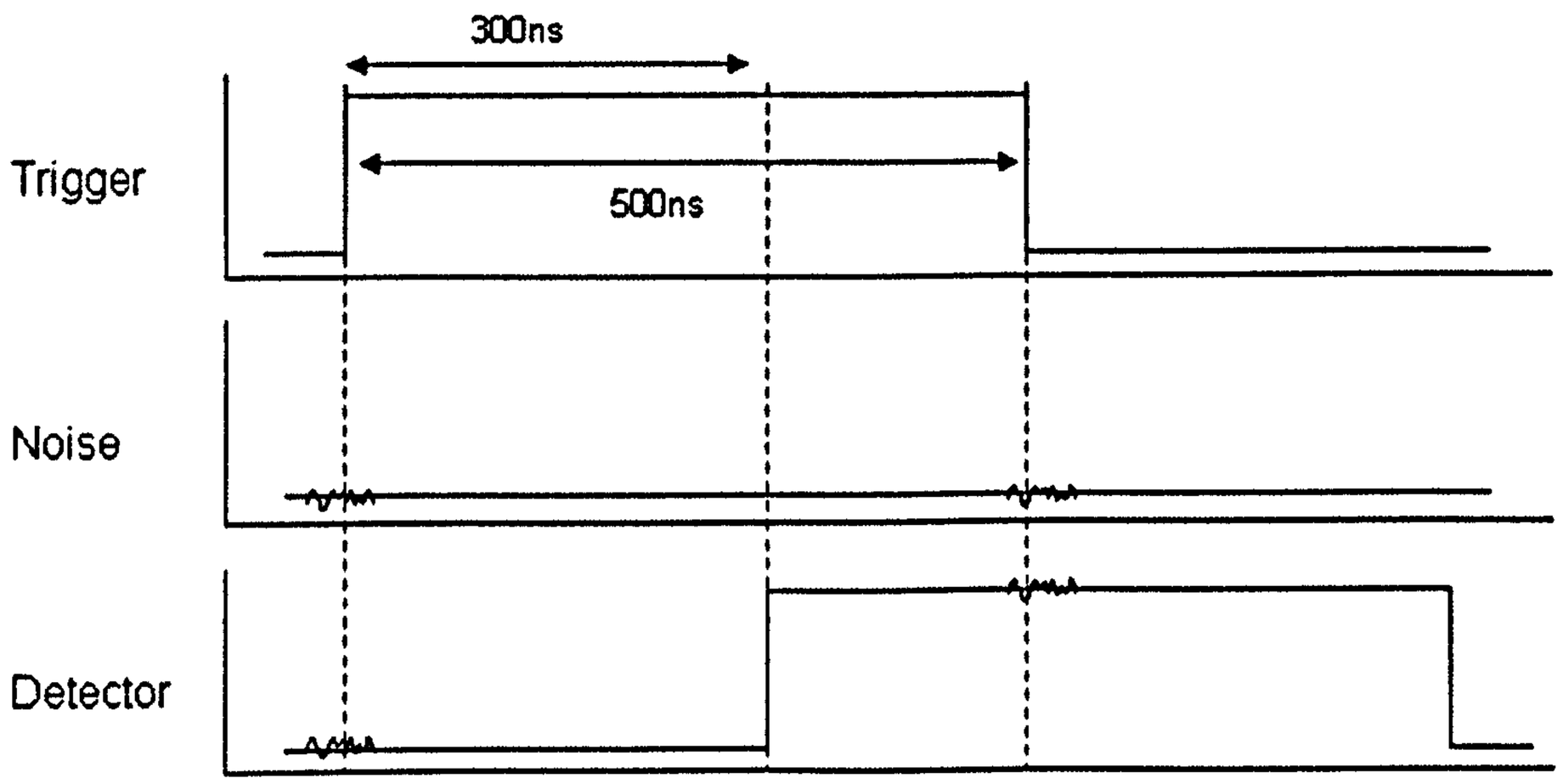

Figure 3.1.5 – *Switcher noise seen by the detector*

If the alignment is optimised the effect of this RF interference on the pulse is minimised.

3.1.9 Detection Scheme

The detection scheme used by a spectrometer has a great effect on the sensitivity of the instrument. The data collection rate and selectivity of the instrument are also affected by the detection scheme. For the purposes of our instrument we required to be able to

monitor more than one absorbing gas simultaneously with a high sensitivity and a good time resolution. In the mid infrared the absorption of molecules is much stronger than in the near infrared, which allows less complicated detection systems than frequency or amplitude modulation. The strength of the absorptions in the mid infrared allows for direct absorption to be used. This scheme looks for small changes to a large signal, which is limited by the noise of the laser. In order to improve the signal to noise sweep integration was used. This technique involves recording an absorption feature several times and averaging the scans to produce a single spectrum of the absorption feature. Theoretically the signal to noise should improve as the square root of the number of scans averaged. In our scheme we record an entire spectrum of many absorption features simultaneously and then average the whole spectrum. Shown below is the comparison of a two of lines of Nitrous Oxide recorded with three different numbers of scans.

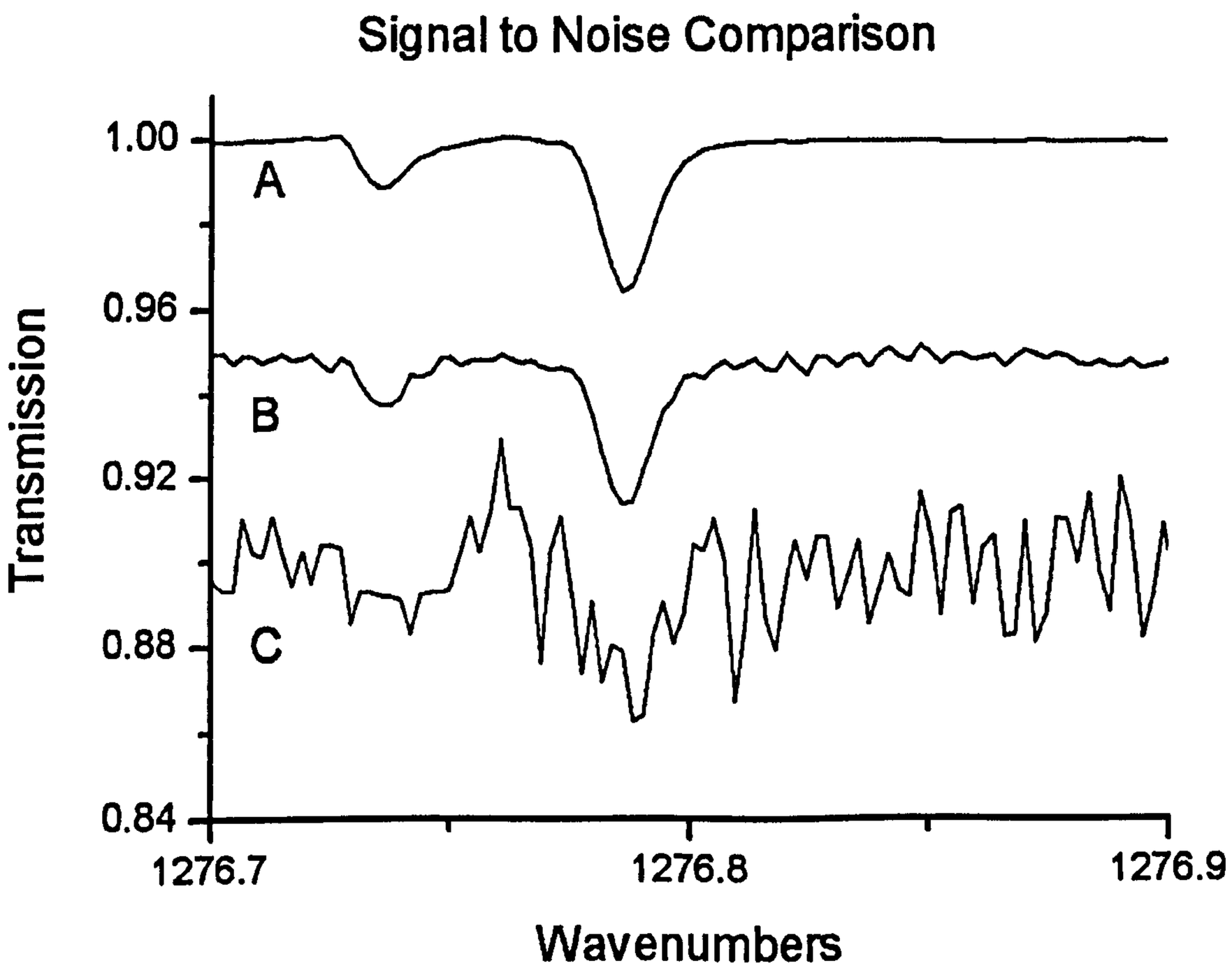

Figure 3.1.6 – *Trace A shows a Nitrous Oxide spectrum with an average of 20000 pulses. Trace B shows a Nitrous Oxide spectrum with an average of 250 pulses. Trace C*

shows a Nitrous Oxide spectrum with an average of 2 pulses. Traces B and C have been offset for clarity.

In order to produce the spectra shown above three averaged scans must be recorded. The first averaged scan is the background spectrum, which is recorded with the cell fully evacuated. The second averaged scan is a spectrum of the etalon, which is used to linearise the absorption the spectrum. The third averaged scan is a spectrum of the absorbing gas, which is recorded with the cell containing the gas or gases of interest. These three scans are shown in Figure 3.1.7 below. The third averaged scan is divided by the first averaged scan to give a transmission spectrum. The units of this spectrum are then converted from time into relative wavenumbers using the second averaged scan. The etalon fringes are equally spaced in the frequency domain, but in our case not in the time domain. To be able to correct this a polynomial fit is made to the fringe peaks. In order to convert to absolute wavenumbers the absorption lines must be identified from HITRAN [9], literature or from FTS spectra recorded during this work.

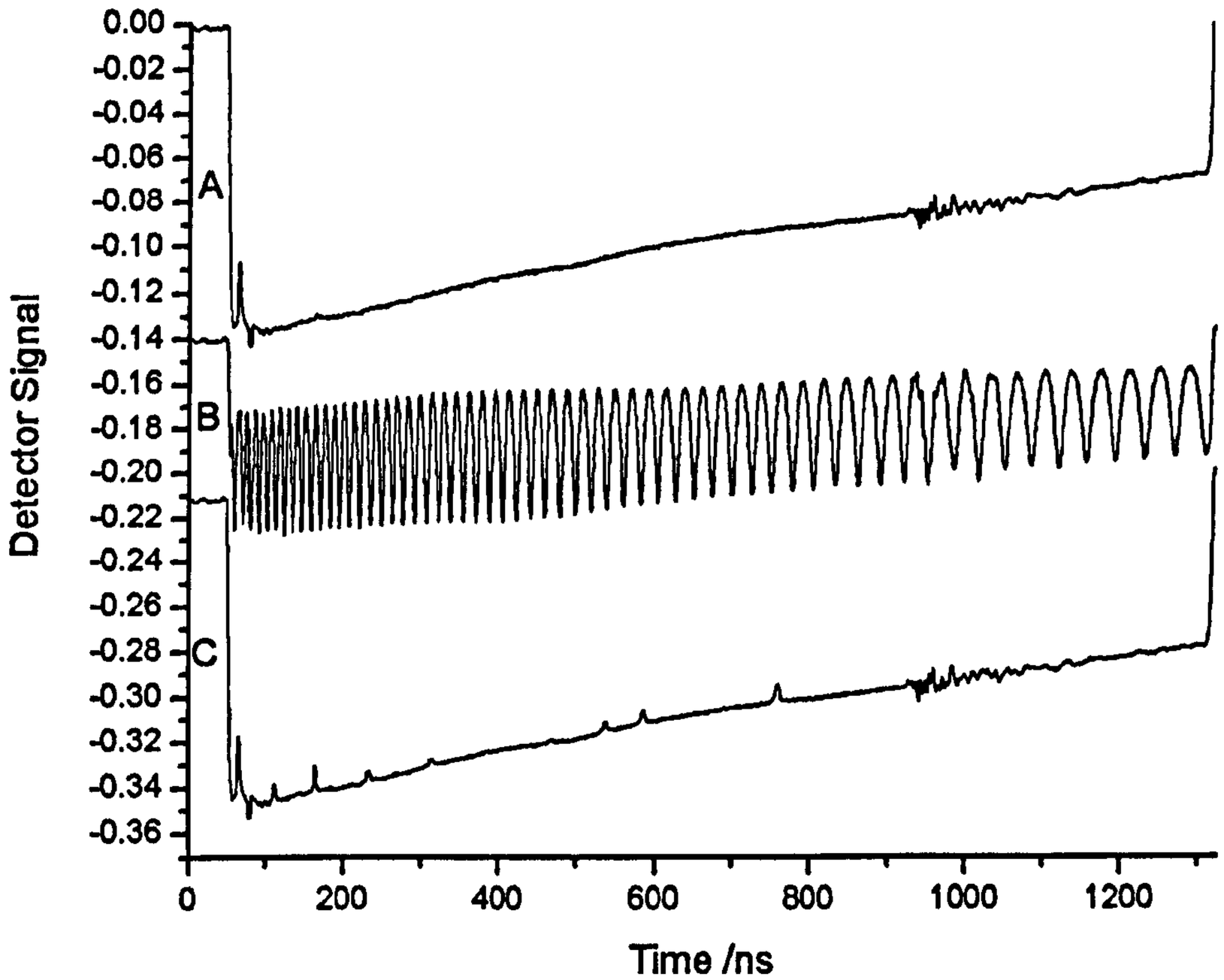

Figure 3.1.7 – *Trace A shows the background scan recorded by the digitiser. Trace B is the etalon scan and Trace C is the spectrum scan. Traces B and C have been offset for clarity*

The noise at about 1000ns which can be seen on traces A and C can be attributed to the RF generated by the switcher.

3.1.10 Resolution

The resolution of this system is determined by the chirp rate of the laser and the temporal response of the detection system rather than the effective line width of the laser. In both the inter pulse (short pulses) method and the intra pulse (long pulses) method the uncertainty relation gives us a minimum value of the bandwidth duration

product. This relationship has been described in detail by Bracewell [10], who showed that the equivalent duration, Δt, and the equivalent bandwidth, $\Delta\nu$, must be at least equal to C, which is a constant determined by the pulse shape. If using a rectangular time window $\Delta t \Delta \nu \geq C = 0.886$. For a Gaussian time window $\Delta t \Delta \nu \geq C = 0.441$. Kosterev *et al.* [11] have shown that their resolution of 290MHz cannot be significantly improved by changing the pulse duration. If they shortened the pulse a Fourier transform limitation would determine the resolution and if the pulse length was increased the frequency chirp would be too great. A similar analysis is outlined for the inter pulse system developed during this work. The laser frequency will chirp by $d\nu/dt \cdot \tau$ in a time window τ. If a smaller time window was used the Fourier limited frequency interval $\Delta\nu$ would increase, whereas the chirp limited frequency interval would decrease. The optimum time window, τ, is therefore set by $C/\tau = d\nu/d\tau \cdot \tau$. Rewriting this equation in terms of $\Delta\nu$ gives, $\Delta\nu = d\nu/d\tau \cdot C/\Delta\nu$, therefore $\Delta\nu = \sqrt{C d\nu/d\tau}$. If C=1, which is the limiting case, assuming a chirp rate of 200MHz/ns, the resolution limit would be 447MHz (0.015cm^{-1}). If a rectangular window was used (C=0.886) the resolution limit would be 421MHz (0.014cm^{-1}). If a Gaussian window was used the limit would be 297MHz (0.01cm^{-1}). A significant improvement in the resolution would require the use of lasers with improved thermal dissipation, which would slow the chirp rate of the laser. As described in section 3.2 one of the lasers used in this work has a strong non linear chirp rate during the current pulse applied to it. This laser, if a long current pulse of more than 1.2μs is applied to it, demonstrates a change in chirp rate over the pulse of an order of magnitude. At the start of the pulse the chirp rate is at its highest and is approximately 200MHz/ns. At the end of the pulse where the chirp rate has slowed down, chirp rates as low as 22MHz/ns have been seen during this work. This corresponds to a resolution limit of 140MHz (0.005cm^{-1}), assuming a rectangular window. Figure 3.1.8 below shows the effect on resolution for a changing chirp rate.

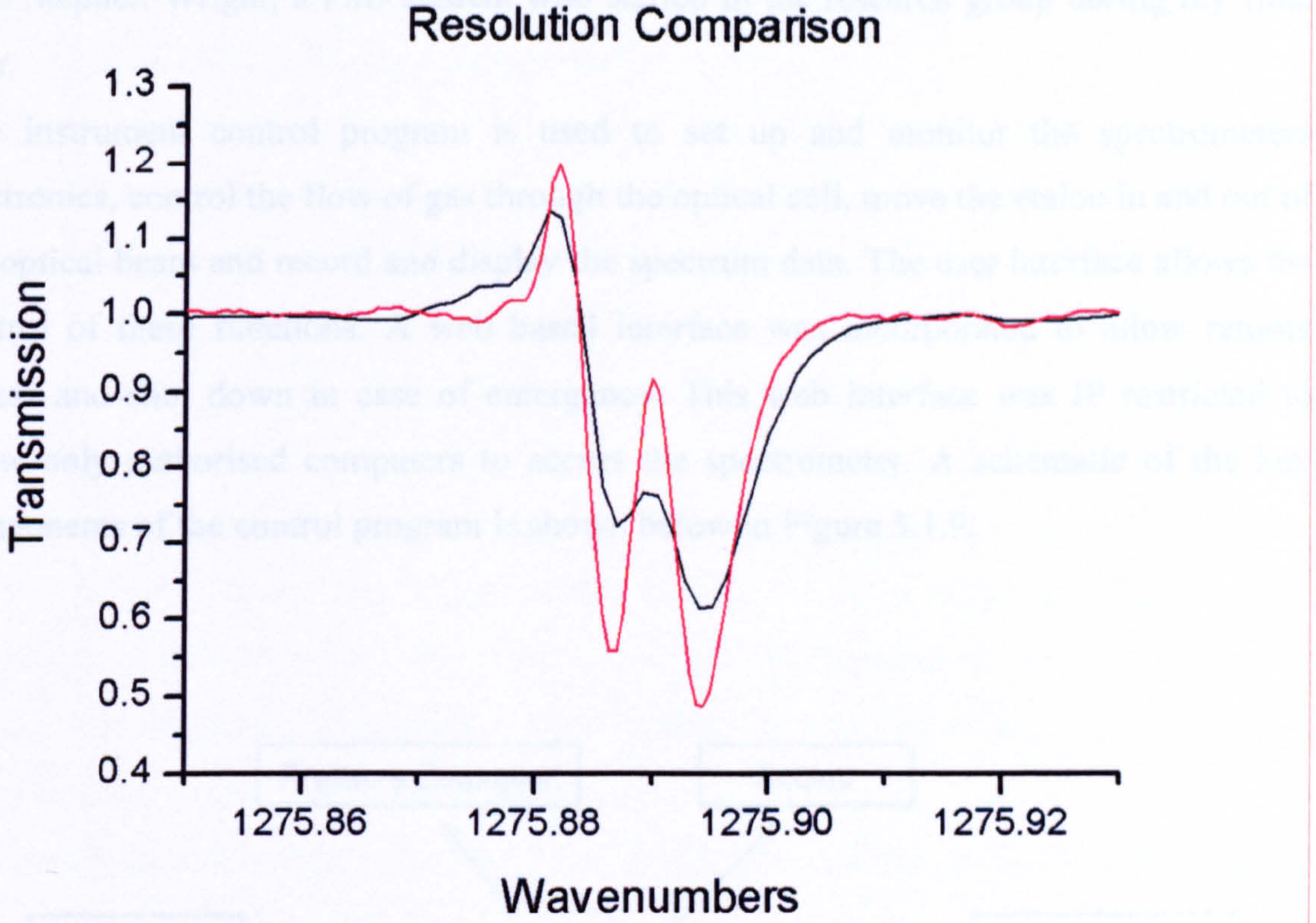

Figure 3.1.8 – *Both Traces show a doublet of NNO recorded using an Alpes 8μm Laser. The chirp rate of the Red Trace is 35.5MHz/ns and the chirp rate of the Black Trace is 70MHz/ns*

3.1.11 Software

Part of my work involved the development of control and analysis software for use with the inter pulse spectrometer. I will describe in this section the key components of this software suite. The spectrometer was not computer controlled when I started and analysis was done manually. The original set of analysis programs I wrote where written in the MATLAB programming language. These programs were rewritten in the LabVIEW programming language. The rewrite was required because the control software was written in LabVIEW and therefore it was easier to have everything working in the same language. I will discuss the outline of how these programs work, which is language independent. The instrument control program was written jointly

with Stephen Wright, a PhD student who started in the research group during my final year.

The instrument control program is used to set up and monitor the spectrometers electronics, control the flow of gas through the optical cell, move the etalon in and out of the optical beam and record and display the spectrum data. The user interface allows the control of these functions. A web based interface was incorporated to allow remote access and shut down in case of emergency. This web interface was IP restricted to allow only authorised computers to access the spectrometer. A schematic of the key components of the control program is shown below in Figure 3.1.9.

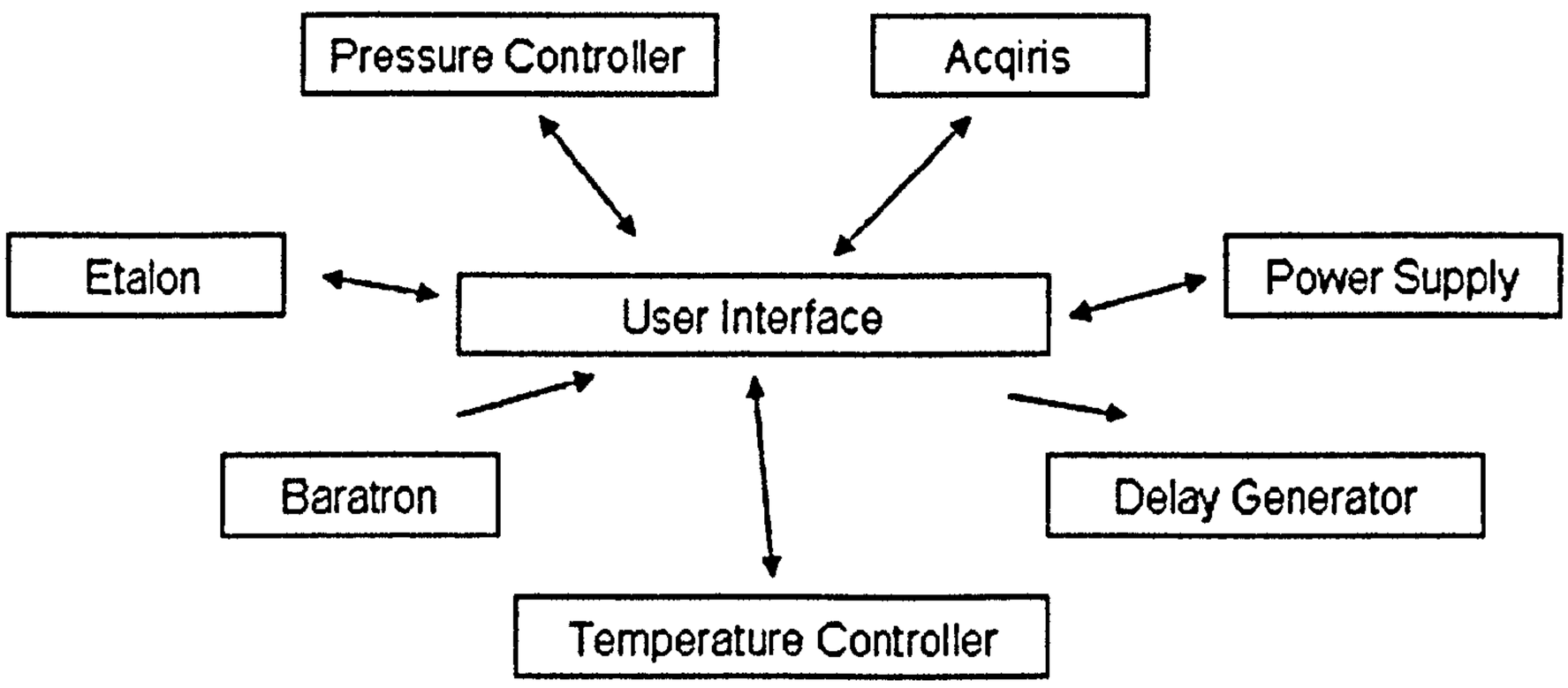

Figure 3.1.9 – *Schematic of the control program*

The program runs in a loop, which allows settings to be changed once per loop. The speed of the loop is determined by how many calculations need to be performed per loop. The program was capable of running at several kilohertz. During each loop the program checks the status of all the buttons on the front panel. If any of the buttons are pressed the action associated with that button is performed. The sequence of execution of pressed buttons is not necessarily the order in which they were pressed. The buttons are checked in a certain order, which could cause an unexpected execution order. If an

event structure had been used in the program instead of case structure then the buttons would execute in the order they were pressed.

The Baratron subvi, which reads the pressure in the cell, utilises a National Instruments A/D converter to read the signals from the 1000 Torr Baratron and the 1 Torr Baratron gauges. The pressure is only read once during each measurement.

The temperature control of the laser is made through the GPIB connection on the temperature control unit. This allows two way communications with the unit. The temperature is set and the control loop is run on the temperature control unit. This means that the computer is not using valuable processing time to control the temperature of the laser. The temperature can be monitored by the control program during spectrum acquisition. This reduced the scan rate because the communication with the temperature control unit was slow. The temperature was only checked before and after a series of measurements to improve data acquisition rates.

The delay generator was controlled from the programs front panel so that the pulse width of the laser pulses and the repetition rate of the pulses were set. A duty cycle limit of 3.5% was built in so that the laser was not damaged by a mistyped setting. There was not sufficient time to program a feedback from the delay generator to the main program. During the test phase no incorrect pulse widths or repetition frequencies were observed so a feedback loop was deemed unnecessary. The keys on the delay generator lock out when in remote mode so no changes could be made without going through the computer.

The power supply, described in detail in Erwan Normands Thesis [8], was originally not designed for computer control. No GPIB or Serial connections could be made. The power supply did have a 0-5V modulation input. This BNC input was designed to allow the user to add a sine or ramp function from a function generator to the output of the supply. It was determined that if a constant voltage was applied then the output from the supply would be constant. This BNC input was connected to an output channel from the National Instruments A/D converter. The voltage of the A/D channel was set in the control program and stepped up to that voltage, then latched until the voltage was changed by the user. If the computer rebooted the voltage of the A/D output channel

reset to a default value which had to be changed to 0V so as not to damage the power supply or the laser in the event of an unexpected reboot.

The moveable etalon was controlled using the other output channel from the A/D. The default setting was out of the beam and a 3V signal was required to move the etalon into the beam. This was done either manually or automatically if the spectrometer was set on autonomous mode.

The flow of gas through the cell was controlled by the MKS Pressure Controller. The connection to the computer was made via the serial port. Unlike GPIB, which allows thirty devices to be connected to a single port, a serial port allows only one device to be connected at any one time. The pressure control loop was performed by the pressure controllers readout unit. This freed up valuable computer processing power. The pressure controller was only used in autonomous mode, so the only user input to the device was the desired flow rate. Any feedback information was dealt with by the program.

The data collection part of the program was designed around the PCI based Acqiris digitiser card. This part of the program ran as a loop, which the other parts of the program fitted into. Figure 3.1.10 below shows a flow diagram of the execution order of the data acquisition loop.

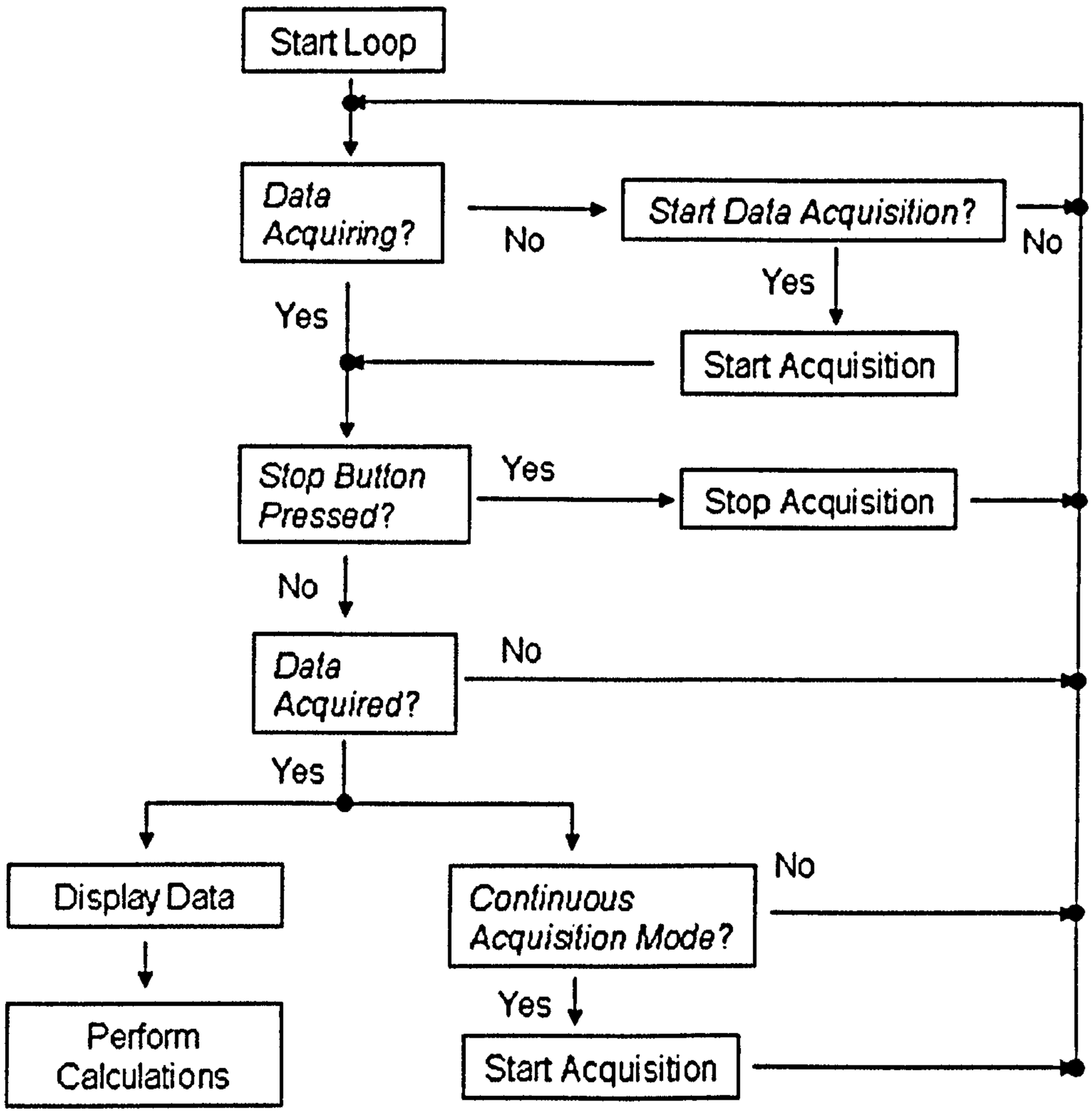

Figure 3.1.10 – *Outline of the acquisition part of the control program*

The acquisition settings were set before the start of the loop. This meant that the trigger settings were hard wired into the loop. This meant that the loop could execute faster because these settings did not have to be checked or reset. In order to change these settings the execution of the loop had to be stopped and any data being acquired during the stopped loop would be lost. The number of averages to be performed could be set during the loop; however the data acquisition would be restarted. This was like a quick reboot of the settings rather than setting everything back up if the loop execution was stopped. Communications with the Acqiris digitiser card were made using LabVIEW

subvi's. These vi's were small parts of code accessed by the larger program. They called the Acqiris C library, which did the communication with the digitiser. To start acquisition of the data the program told the digitiser to start averaging the number of trigger events preset by the user. The trigger and averaging settings were stored onboard the digitiser. Then during each loop the program queried the digitiser to check to see if the acquisition was complete. By not waiting on the completion of an average other processing could be done without slowing the data acquisition rate. Once the query came back positive the averaged spectrum was transferred to the program. If the user had set continuous acquisition the digitiser was told to start acquiring data again before anything else was done. This again maximised the data collection rate. Once the digitiser had been restarted the processing of the acquired data was performed. This included saving the data to disk, calculating the transmission spectrum using the previously recorded background and calculating the scan rate. Figure 3.1.11 below shows the time line for data collection and processing.

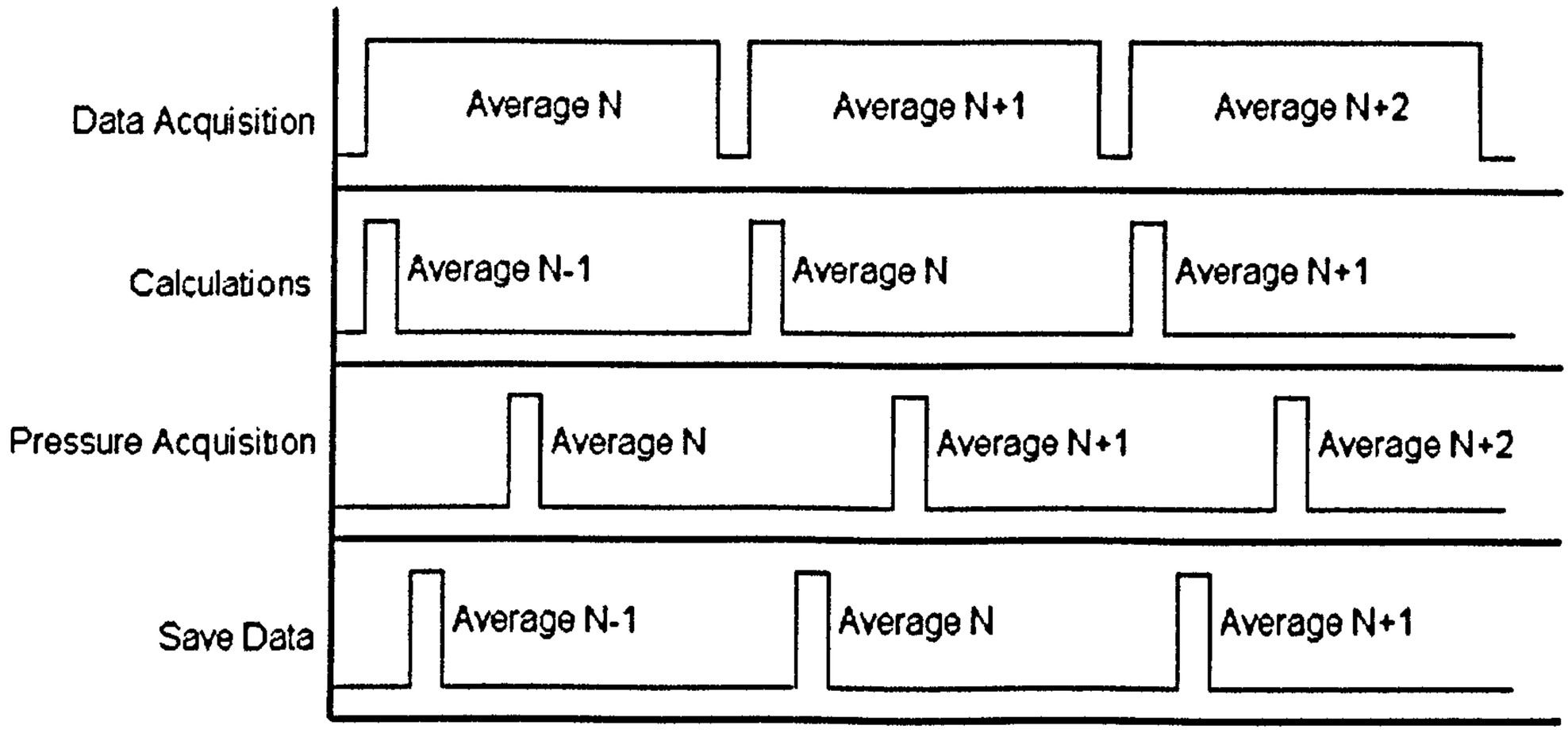

Figure 3.1.11 – *Data acquisition and processing time line*

From the program execution timeline it can be seen that the ultimate limitation of the acquisition rate is time taken to perform the other tasks such as saving data, recording

the pressure and calculating the transmission spectrum. If the time take to record an average is shortened, by either increasing the laser repetition rate or decreasing the number of trigger events to be averaged, then a point is reached where the "house keeping" processes take longer than the data acquisition. At this point the time between acquisitions, the so called dead time, increases. In order to reduce the time taken to perform the extra calculations several options are available. The data could be stored in RAM and written to hard disk later. Instead of recording the pressure every average it could be recorded every second. During this work the maximum scan rates were determined as follows in table 3.1.1 below.

Scans/s	Averages	Repetition Frequency (KHz)	Record Pressure?	Calculate Transmission?	Save Data to Disk?
8.25	2	20	Yes	Yes	No
8.22	250	20	Yes	Yes	No
225	2	20	No	Yes	No
50	250	20	No	Yes	No
226	2	20	No	No	No
50	250	20	No	No	No
0.939	20000	20	No	Yes	Yes
0.311	64000	20	No	Yes	Yes
0.92	20000	20	Yes	Yes	Yes
0.308	64000	20	Yes	Yes	Yes

The pressure acquisition was the main slow down of the data acquisition. This is not unexpected as the pressure signals of the two baratron gauges must be read in through a 1MHz A/D input channel as one waveform for each gauge. The noise on the input meant that several thousand data points were required for each waveform in order to achieve an accurate reading of the pressure in the cell. If the data acquisition rate is below a few hertz the calculations, pressure acquisition and data saving can be performed without significantly affecting the performance of the system. During this work acquisition rates were typically around the hertz to sub hertz level.

Once the data had been saved to disk work has to be done to extract useful information such as line positions and intensities, which lets us calculate the concentrations of the various constituents of the spectrum. The first stage is to calibrate the spectrum into

relative wavenumbers. This is performed automatically by a LabVIEW program. This program uses the etalon peaks, which are evenly spaced in frequency, to generate a relative wavenumber scale. This gives an unevenly spaced set of data points. Using the same program the spectrum is shifted from relative wavenumbers to absolute wavenumbers by identifying known absorption lines in the spectrum. The position and separation of these lines is used to check the calibration. As the background is recorded at a different time from the spectrum file errors in the background can occur. This is a problem that increases with time. This means that the baseline of the spectra recorded at the beginning of a run is better than the baseline of the spectra recorded at the end of a run. In order to correct for this a LabVIEW program was developed by me. This program, at this stage of development, requires user input to function correctly. Figure 3.1.12 below shows the typical baseline error experienced during this work.

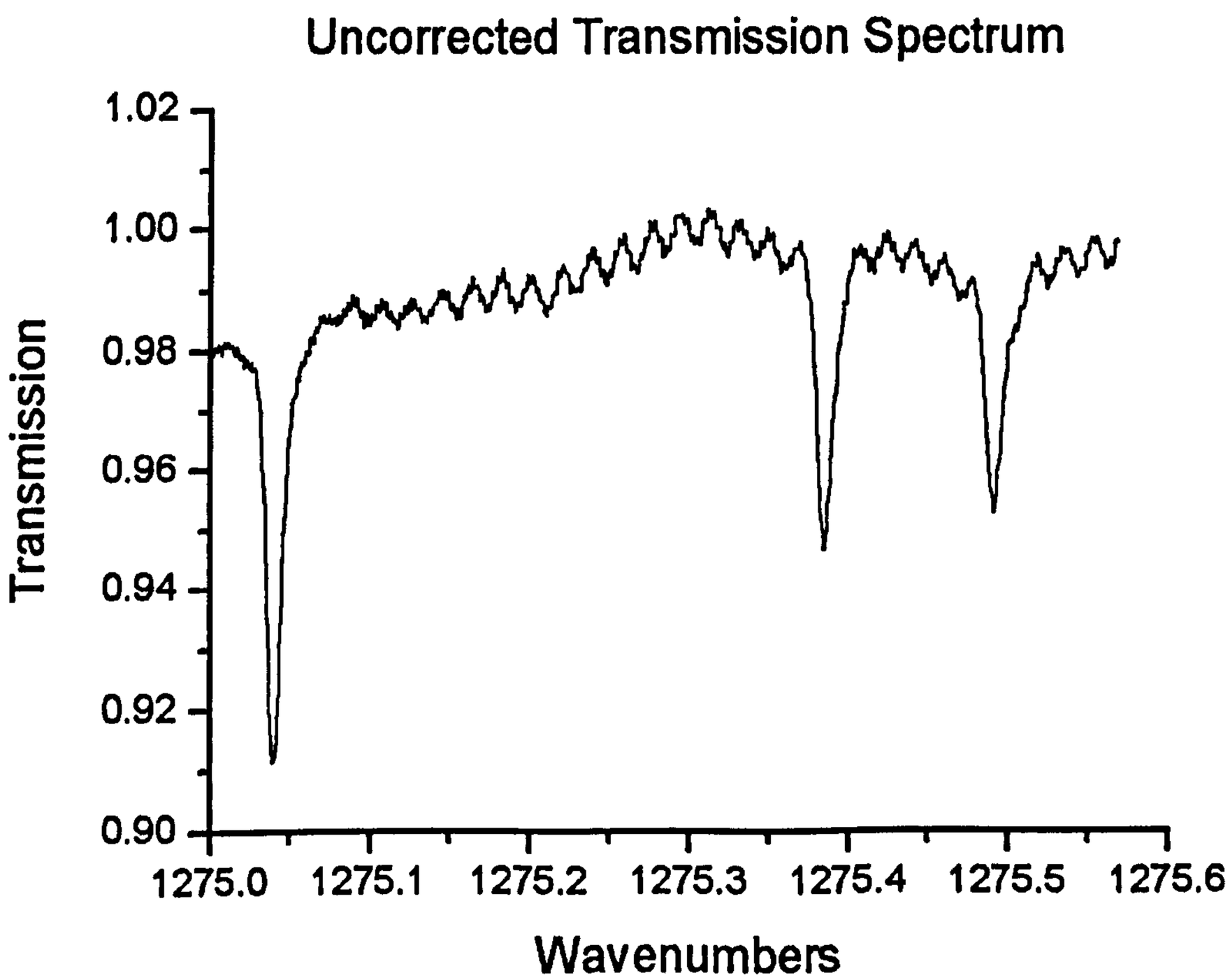

Figure 3.1.12 – *The uncorrected transmission spectrum of three absorption lines in the atmosphere*

It can be seen from the figure above that there are two components to the baseline error. The first is a slowly varying function and the second is a high frequency oscillation. The first stage of correction is to identify several points on the pulse that are background points. An interpolation is then made between these points on the background pulse and the spectrum pulse. This gives two curves like the ones shown in Figure 3.1.13 below.

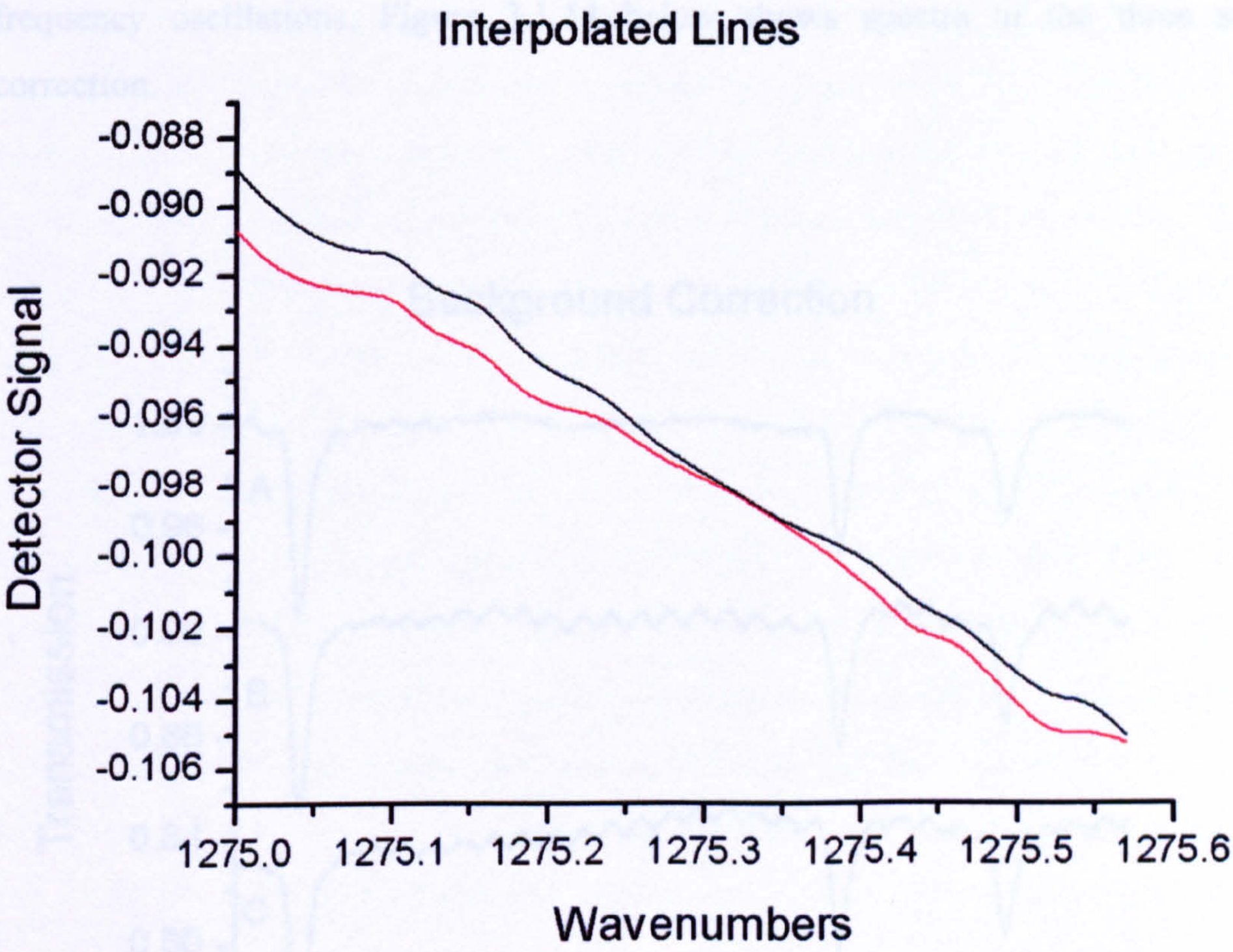

Figure 3.1.13 - *The red line shows the interpolation of the background and the black line shows the interpolation of the spectrum*

By using an interpolation this technique limits the useable amount of data to the data between the first and last interpolation points. Any data outside of these points will not be corrected because the interpolation function is not physical in this region. The interpolation of the spectrum is then divided by the interpolation of the background. This

is then multiplied by the original background to give a new background. The spectrum is then divided by the new background to give the transmission spectrum. This transmission spectrum has only been half corrected though. The high frequency oscillation must be removed as well. This is done by selecting on the transmission spectrum a range of points that cover at least three periods of the oscillation but no absorption features. A sine function is then fitted to this set of data points. From the sine fit an extrapolation is made to cover the whole region of the first interpolation. This set of points is then subtracted from the transmission spectrum to remove the high frequency oscillations. Figure 3.1.14 below shows spectra at the three stages of correction.

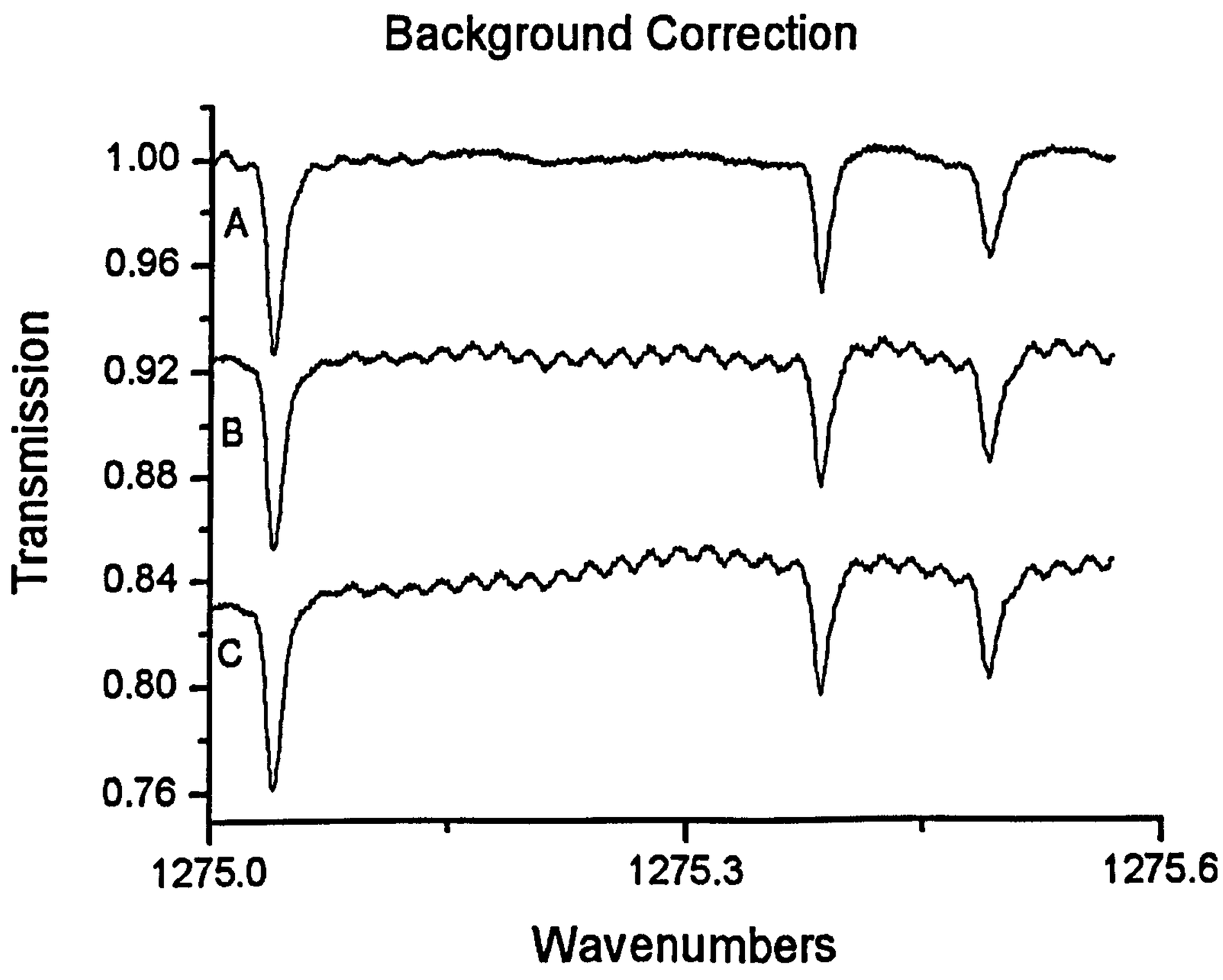

Figure 3.1.14 – *Trace C shows the uncorrected transmission spectrum. Trace B shows the transmission spectrum after the low frequency component of the baseline error has*

been removed. Trace A shows the fully corrected transmission spectrum. Traces B and C has been offset for clarity.

3.1.12 Concentration Retrieval

The final stage of data processing of a spectrum is the retrieval of concentrations for the known lines in the spectrum [12, 13]. For all of the work done in this thesis the concentration retrieval procedure has remained similar. A LabVIEW program has been written to perform the concentration retrieval. The first step is to identify the absorption line of interest. This can be done by matching the spectrum to lines from the HITRAN [9] database or a previously identified spectrum. Due to the speed of the chirp and power of the laser power saturation and other nonlinear effects must be thought about during the concentration retrieval process. The power saturation can be reduced by increasing the total cell pressure. Power saturation and other nonlinear effects can lead to asymmetric line shapes which make spectral fitting more difficult. An examination of these processes has been done in section 4.1. If the line of interest is well separated, which is generally the case in human breath measurements or nitrogen broadening of a single light molecular gas, from any nearby lines the concentration retrieval process is simplified. Assuming this is the case the absorption line is fitted to with a function. The function used depends on the pressure in the cell. For low cell pressures a Gaussian function is used as the Doppler broadening dominates the line at low pressures. At high cell pressures a Lorentzian function is used as the pressure broadening dominates the line at high pressures. For intermediate cell pressures a Voigt function is used. A comparison of these functions is made in Figure 3.1.15.

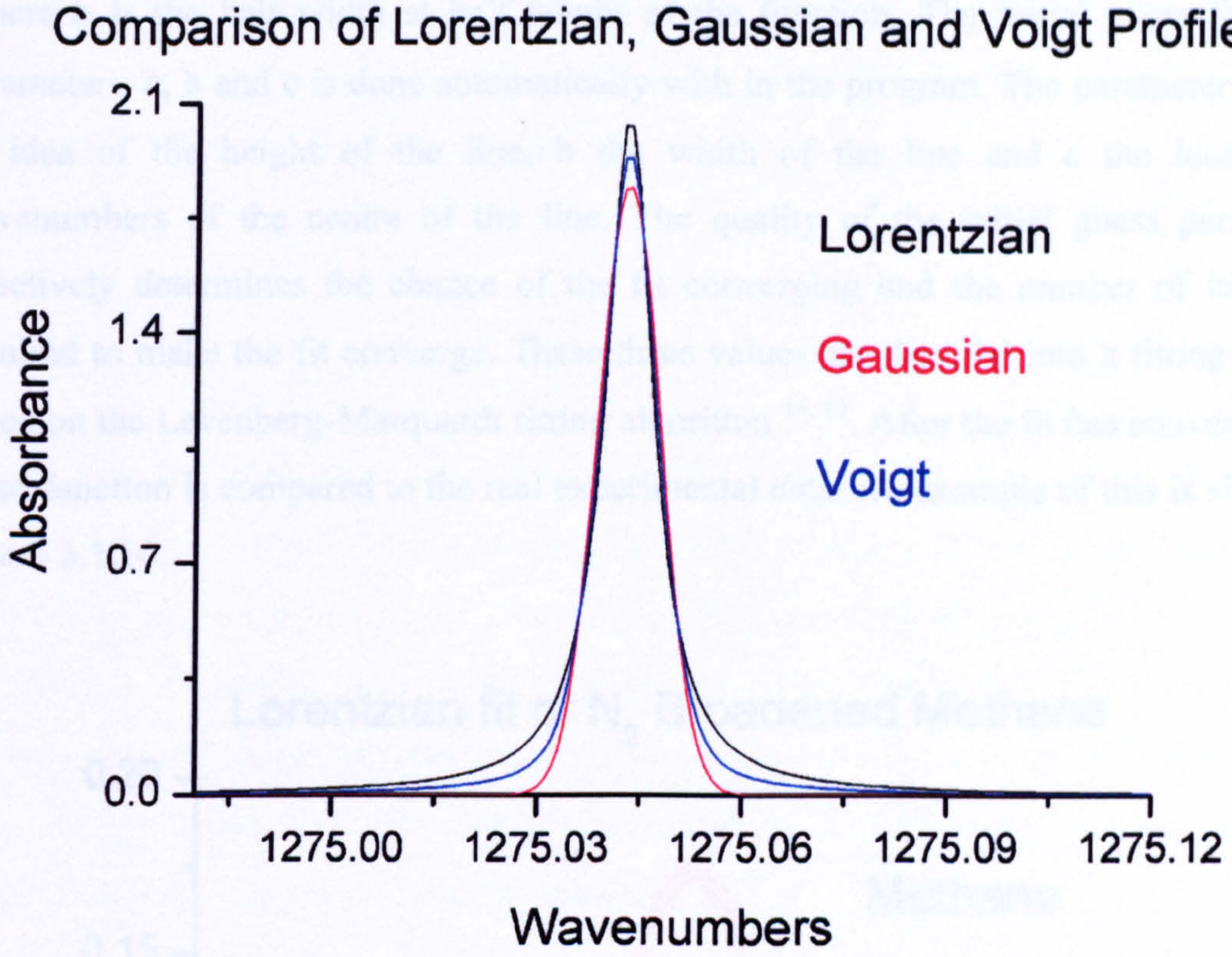

Figure 3.1.15 – *The Black trace shows the Lorentzian function. The Red trace shows the Gaussian function. The Blue trace shows the Voigt function.*

The Lorentzian function is spread more to the wings of the absorption line than the Gaussian function. The Voigt function used is a 50% Lorentzian, 50% Gaussian function. The Voigt, as expected, falls half way between the other two functions.

Once the absorption line has been identified and the total pressure in the cell work out so that the appropriate fitting function can be chosen the initial guess coefficients for the fit must be made. In the case of a Lorentzian function, of the form shown below, there are three variables that need to be calculated.

$$F(x) = a \cdot \frac{b}{(x-c)+b^2}$$

Where b is the half width at half height of the function. The initial guess for these parameters, a, b and c is done automatically with in the program. The parameter a gives an idea of the height of the line, b the width of the line and c the location in wavenumbers of the centre of the line. The quality of the initial guess parameters effectively determines the chance of the fit converging and the number of iterations required to make the fit converge. These three values are then fed into a fitting routine based on the Levenberg-Marquardt fitting algorithm [14, 15]. After the fit has converged the fitted function is compared to the real experimental data. An example of this is shown in Figure 3.1.16.

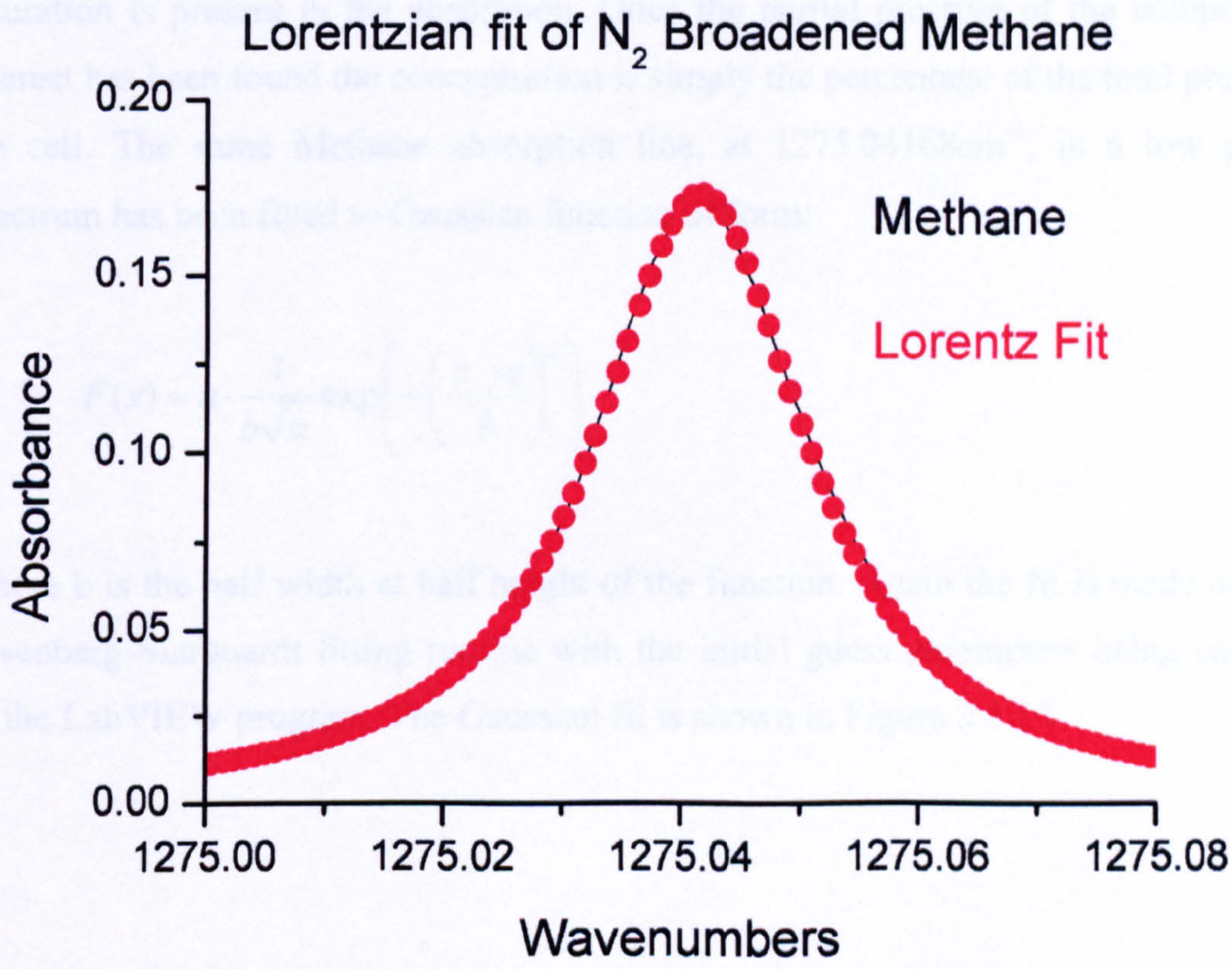

Figure 3.1.16 – *The Black trace shows the spectrum of Methane. The Red dots show the Lorentzian fit.*

The spectrum was fitted to a Nitrogen broadened Methane spectrum. Approximately 15milliTorr of Methane was added to the astigmatic Herriott cell and the total cell

pressure was made up to 150Torr with Nitrogen. The area under the fitted function is then worked out using an integration routine. The pressure of the absorption line is then calculated using the following equation:

$$P = \frac{A}{l \cdot S}$$

Where A is the area under the absorption line, l is the pathlength of the astigmatic Herriott cell in cm and S is the intensity of the absorption line in $cm^{-1}/(Atm \times cm^{-2})$. This equation assumes that the absorption follows the Lambert-Beer law and that no power saturation is present in the absorption. Once the partial pressure of the component of interest has been found the concentration is simply the percentage of the total pressure in the cell. The same Methane absorption line, at $1275.04168cm^{-1}$, in a low pressure spectrum has been fitted to Gaussian function of form:

$$F(x) = a \cdot \frac{1}{b\sqrt{\pi}} \exp\left(-\left(\frac{x-c}{b}\right)^2\right)$$

Where b is the half width at half height of the function. Again the fit is made using the Levenberg-Marquardt fitting routine with the initial guess parameters being calculated by the LabVIEW program. The Gaussian fit is shown in Figure 3.1.17.

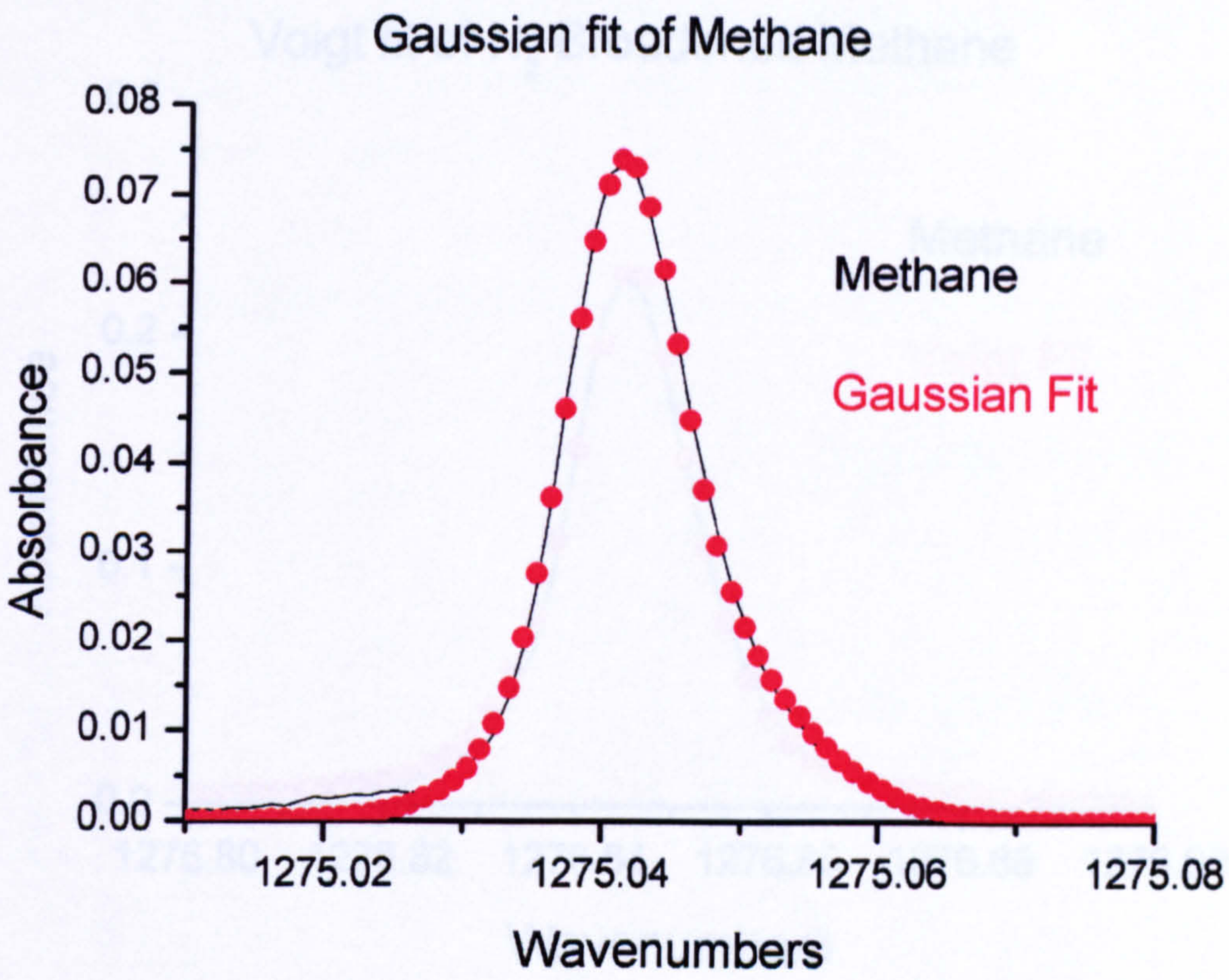

Figure 3.1.17 – *The Black trace shows the spectrum of Methane. The Red dots show the Gaussian fit.*

Approximately 9milliTorr of Methane was added to the astigmatic Herriott cell and the total cell pressure was made up to 12Torr with Nitrogen. The discrepancy of the real data and the fitted data at approximately 1275.02cm^{-1} is due to a slight change in the background of the spectrum. To look at the Voigt function fit a spectrum of Methane broadened with Nitrogen was recorded. The Methane pressure was 15milliTorr and the total cell pressure was made up to 35Torr with Nitrogen. This spectrum and the Voigt fit is shown in Figure 3.1.18.

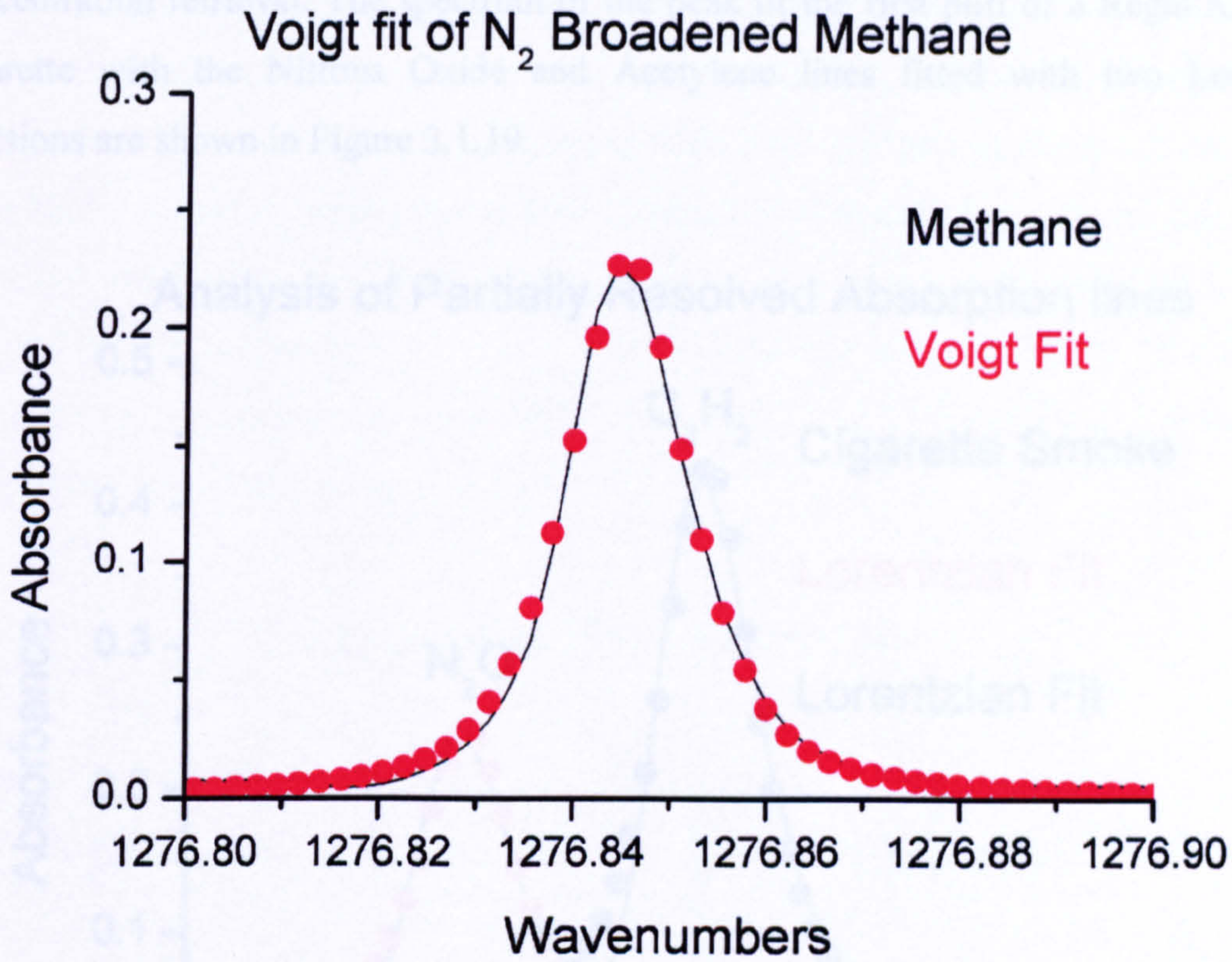

Figure 3.1.18 – *The Black trace shows the spectrum of Methane. The Red dots show the Voigt fit.*

So far only simple spectra of well isolated lines have been looked at. In some of the work done in this thesis the spectra of partially resolved and completely unresolved lines have been looked at. These types of spectra generally occur in heavy molecules or in mixtures of many gases, such as cigarette smoke. In this case a slightly more complicated approach is required. In the case of partially resolved lines a fit must be made to all of the lines that blend with the line of interest so that the contribution of these extra lines can be removed from the absorption of the line of interest. This means that instead of a single fit multiple fits must be made. Examples of two lines that are partially resolved are the Acetylene line at 1275.512169 cm^{-1} and the Nitrous Oxide line at 1275.49287 cm^{-1} in cigarette smoke. For a spectrum in which other similar strength absorption lines are present these lines could be used instead of the partially resolved lines, however there is only one strong Acetylene line in region so it must be used for

concentration retrieval. The spectrum of the peak of the first puff of a Regal King size cigarette with the Nitrous Oxide and Acetylene lines fitted with two Lorentzian functions are shown in Figure 3.1.19.

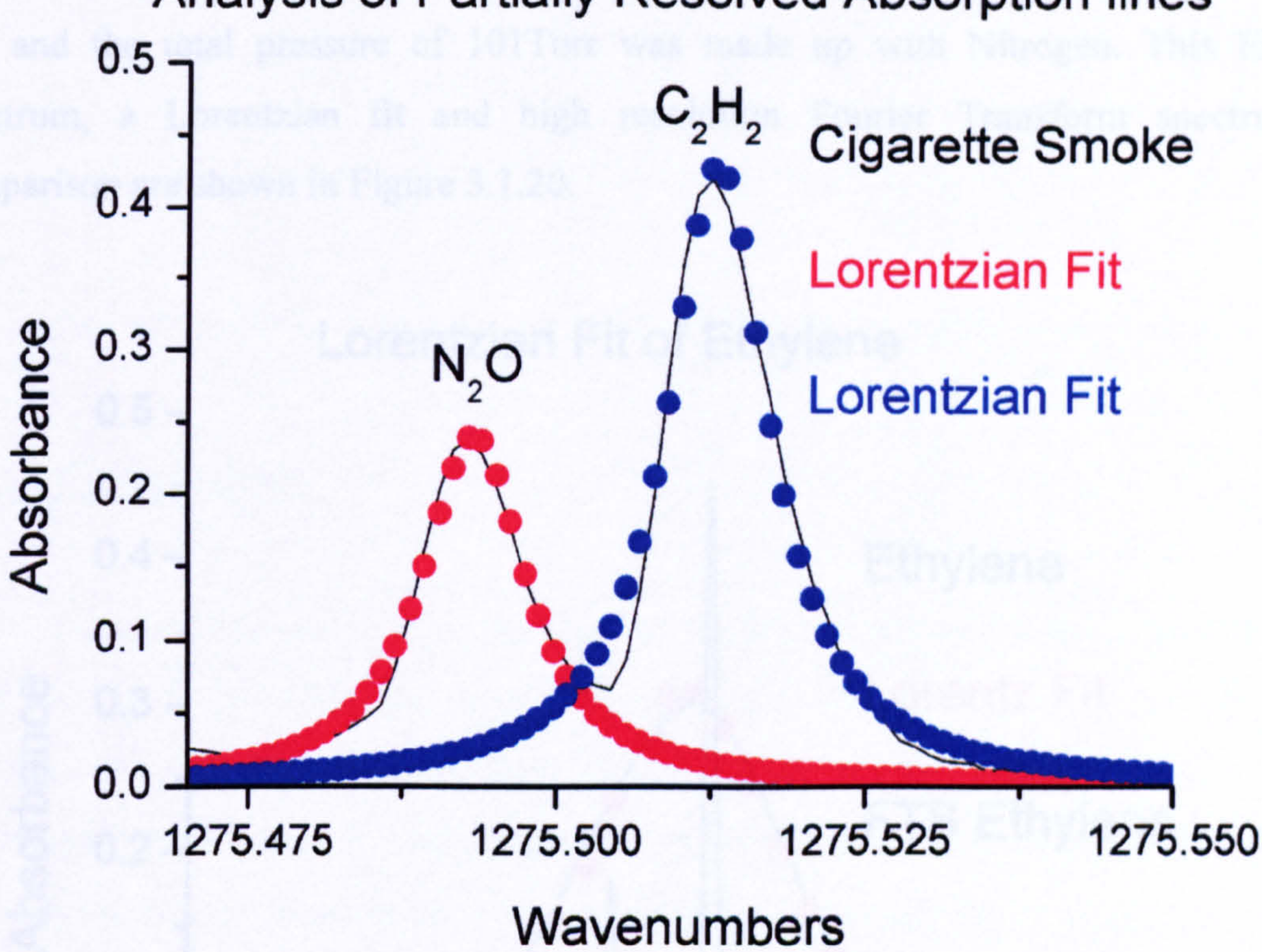

Figure 3.1.19 – T*he Black trace shows the spectrum of Cigarette smoke. The Red dots show the Nitrous Oxide Lorentzian fit. The Blue dots show the Acetylene Lorentzian fit.*

The LabVIEW program uses the fitted functions of the other absorption lines that are part of the unresolved feature to remove their absorption contribution from the absorption line of interest. This allows the concentration to be calculated as before. The other case, where there are completely unresolved lines, is a different proposition again. If the lines that are overlapping are from different molecules then the LabVIEW program will not work. The separation of the different absorptions would require analysing other unblended absorption lines from each of the interfering gases. This should be a relatively easy thing to do. This function was not required during this work,

as any gases of interest had strong absorption lines that meant any absorption features that fell into this category could be ignored. In the Ethylene spectrum near 10μm a triplet of lines provides the perfect example of the blended lines problem. The three lines are within 0.03cm^{-1} of each other and are completely unresolved at reduced atmospheric pressures. Approximately 20milliTorr of Ethylene was added to the astigmatic Herriott cell and the total pressure of 101Torr was made up with Nitrogen. This Ethylene spectrum, a Lorentzian fit and high resolution Fourier Transform spectrum for comparison are shown in Figure 3.1.20.

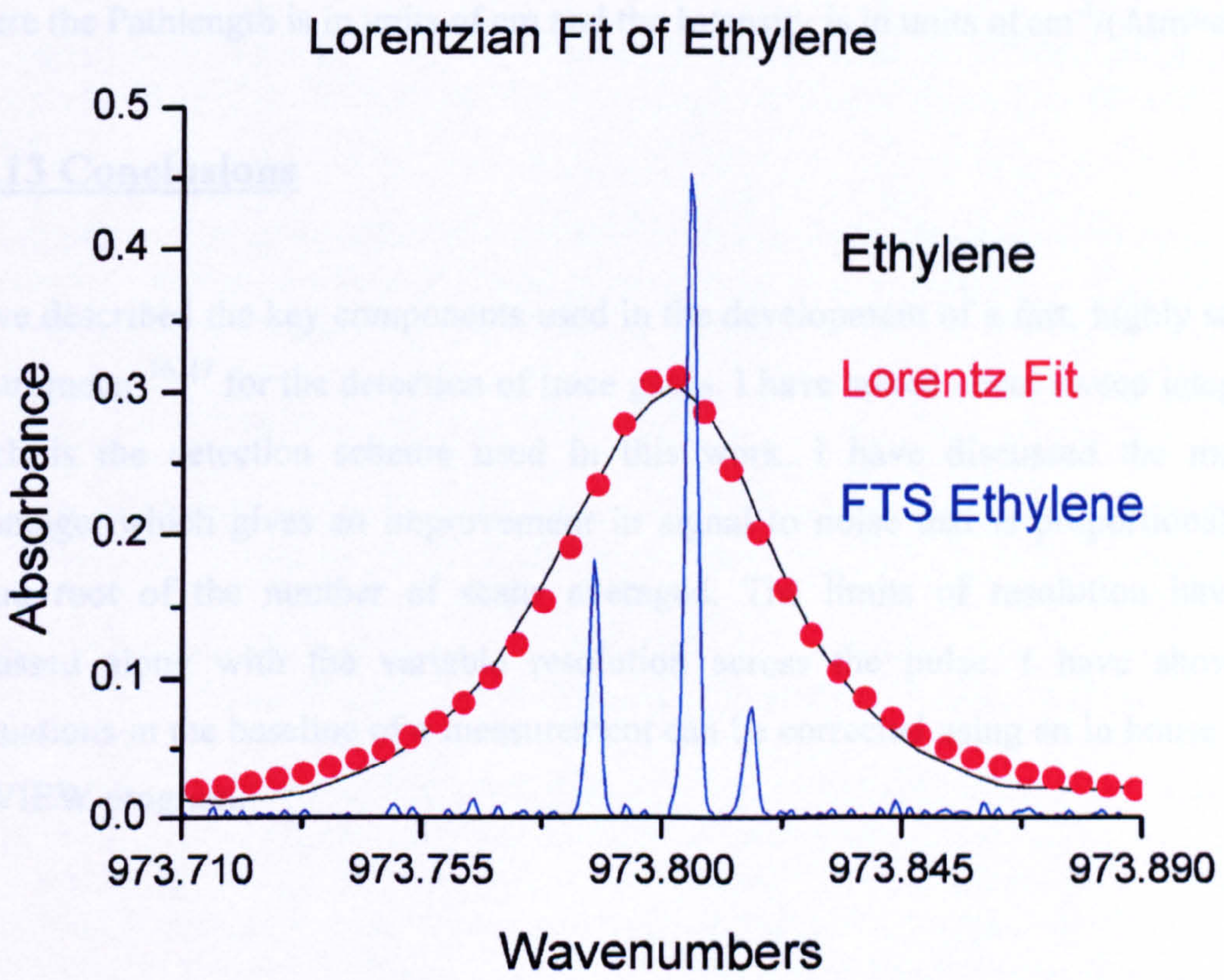

Figure 3.1.20 – T*he Black trace shows the spectrum of Ethylene. The Red dots show the Lorentzian fit. The Blue trace shows the comparison FT spectrum.*

The comparison Fourier Transform spectrum was recorded using 0.5Torr of Ethylene in a 15cm using the Bruker FTS at the Rutherford Appleton laboratory with a resolution of 0.0018cm^{-1} and a run of 25 co-averaged scans.

Instead of using the line intensity of a single absorption line the three intensities for the lines under the blended feature are added together to calculate the pressures and then the concentrations. To convert the integrated area into a pressure the intensity of the absorption line and the optical path length of the absorption cell must be known. The partial pressure of the gas of interest is retrieved by solving the equation below:

$$\text{Pressure} = \frac{\text{Area}}{\text{Pathlength} \bullet \text{Intensity}}$$

Where the Pathlength is in units of cm and the Intensity is in units of $cm^{-1}/(Atm \times cm^{-2})$.

3.1.13 Conclusions

I have described the key components used in the development of a fast, highly sensitive spectrometer [16, 17] for the detection of trace gases. I have talked about sweep integration, which is the detection scheme used in this work. I have discussed the multiplex advantage, which gives an improvement in signal to noise that is proportional to the square root of the number of scans averaged. The limits of resolution have been discussed along with the variable resolution across the pulse. I have shown that fluctuations in the baseline of a measurement can be corrected using an in house written LabVIEW program.

3.1.14 References

1) Stratospheric Monitoring Using a Balloon-borne Tunable Diode Laser Spectrometer, C.R. Webster and R.T. Menzies, Laser Analyt. Lett. **1**, 1 (1984)

2) Quantum Cascade Laser, J. Faist, F. Capasso, D. L. Sivco, C. Sirtori, A. L. Hutchinson and A. Y. Cho, Science, **264**, 553, (1994)

3) Sensitive absorption spectroscopy with a room temperature distributed-feedback quantum cascade laser, K. Namjou, S. Cai, E. A. Whittaker, J. Faist, C. Gmachl, F. Capasso, D. L. Sivco and A. Y. Cho, Optics Letters, **23**, 219, (1998)

4) Monitoring of ethylene by a pulsed quantum cascade laser, D. Weidmann, A. A. Kosterev, C. Roller, R. F. Curl, M. P. Fraser and F. K. Tittel, App Opts, **43**, 3329-3334 (2004).

5) Characterisation of the spectral behaviour of pulsed quantum cascade lasers using a high resolution Fourier transform infrared spectrometer, E. Normand, G. Duxbury and N. Langford, Opts. Comms., 197, **1**, 115-120, (2001)

6) Kolmar Technologies, www.kolmartech.com

7) Astigmatic mirror multipass absorption cells for long-path-length spectroscopy, J. B. McManus, P. L. Kebabian and M. S. Zahniser, App. Opts., 34, 18, 3336-3348, (1995)

8) Fast Ultra-Sensitive Real Time Quantum Cascade Laser Spectrometer, E. L. Normand, PhD Thesis, Department of Physics, University of Strathclyde, (2003)

9) The HITRAN Molecular Spectroscopic Database and Hawks (HITRAN Atmospheric Workstation): 1996 edition, L. S. Rothman, C. P. Rinsland, A. Goldman, S. T. Massie, D. P. Edwards, J.-M. Flaud, A. Perrin, C. Camy-Peyret, V. Dana, J.-Y. Mandin, J. Schroeder, A. McCann, R. R. Gamache, R. B. Wattson, K. Yoshino, K. V. Chance, K. W. Jucks, L. R. Brown, V. Nemtchinov and P. Varanasi, J. Quant. Spec. Rad. Trans., **60**, 5, 665-710, (1998)

10) The Fourier Transform and its applications, R. N. Bracewell, McGraw-Hill, (1998)

11) Effective utilization of quantum-cascade distributed-feedback lasers in absorption spectroscopy, A.A. Kosterev, R.F. Curl, F.K. Tittel, C.Gmachl, F.Capasso, D.L. Sivco, J.N. Baillargeon, A.L. Hutchinson and A.Y. Cho, Applied Optics, **39**, 4425-4430 (2000)

12) Infrared Line strengths and Pressure Broadening Coefficients in the ν_{12} Vibrational Band of Hydrazine Measured by Infrared Tunable Diode Laser Spectroscopy, S.E. Plunkett, M.S. Zahniser, M.E. Parrish, D.D. Nelson, J.H. Shorter, J. Wormhoudt and K.H. Shafer, J. Mol. Spec., **211**, 241-247 (2002)

13) Methane Concentration and Isotopic Composition Measurements with a Mid-Infrared Quantum Cascade laser, A. A. Kosterev, R. F. Curl, F. K. Tittel, C. Gmachl, F. Capasso, D. L. Sivco, J. N. Baillargeon, A. L. Hutchinson and A. Y. Cho, Optics Letters, **24**, 23, 1762-1764, (1999)

14) A Method for the Solution of Certain Problems in Least Squares, K. Levenberg,, Quart. Appl. Math, **2**, 164-168, (1944)

15) An Algorithm for Least Squares Estimation of Nonlinear Parameters, D. Marquardt, J. Appl. Math, **11**, 431-441, (1963)

16) Fast, Real time Spectrometer based on a Pulsed Quantum-Cascade Laser, E. Normand, M. T. McCulloch, G. Duxbury and N. Langford, Optics Letters, **28**, 1, 16-19, (2003)

17) Highly Sensitive Detection of Trace gases using the Time resolved Frequency Downchirp from pulsed Quantum Cascade Lasers, M. T. McCulloch, E. Normand, G. Duxbury and N. Langford, Opt. Soc. Am. B, **8**, 1761-1768, (2003)

3.2 Laser Characterisation

3.2.1 Introduction

In this chapter I will discuss the characterisation of the main two lasers used in this work. Both of these lasers were fabricated by Alpes Laser. They were both Distributed Feedback (DFB) Quantum Cascade lasers. These lasers have been characterised using measurements made with two Fourier Transform Spectrometers (FTS) and using data recorded using my spectrometer. The first FTS used was the BOMEM FTS, which is run within the research group. The second FTS was the Bruker FTS, which is operated by the Molecular Spectroscopy Facility at the Rutherford Appleton Laboratory.

The first section of this chapter will cover the characterisation of the 10.2μm laser. The second section of this chapter will cover the characterisation of the 7.8μm laser. I will also discuss the spectroscopy of Methyl Fluoride using a Fabry Perot Quantum Cascade laser, which was fabricated by Thales to lase at 9.46μm.

3.2.2 Alpes Laser 10.24μm DFB Quantum Cascade Laser

The first laser used in this work was manufactured by Alpes Laser [1]. The device was packaged in an Alpes Laser box. This box contained a dry nitrogen atmosphere. The light was coupled out of the anti reflection coated ZnSe window. The substrate of the laser was mounted on a Peltier Cooler, which varied the temperature of the substrate from -30°C to +30°C. The laser was excited by top hat shaped current pulses of up to 5A with pulse widths of up to 300ns and a maximum repetition rate of 50KHz. At a substrate temperature of 0°C the threshold of the laser was 3.2A. When using a pulse width of 200ns the frequency down chirp rate of the laser is linear to within 1%. With pulse widths of more than 200ns the chirp rate becomes non linear. An example of the output from the laser is shown in Figure 3.2.1.

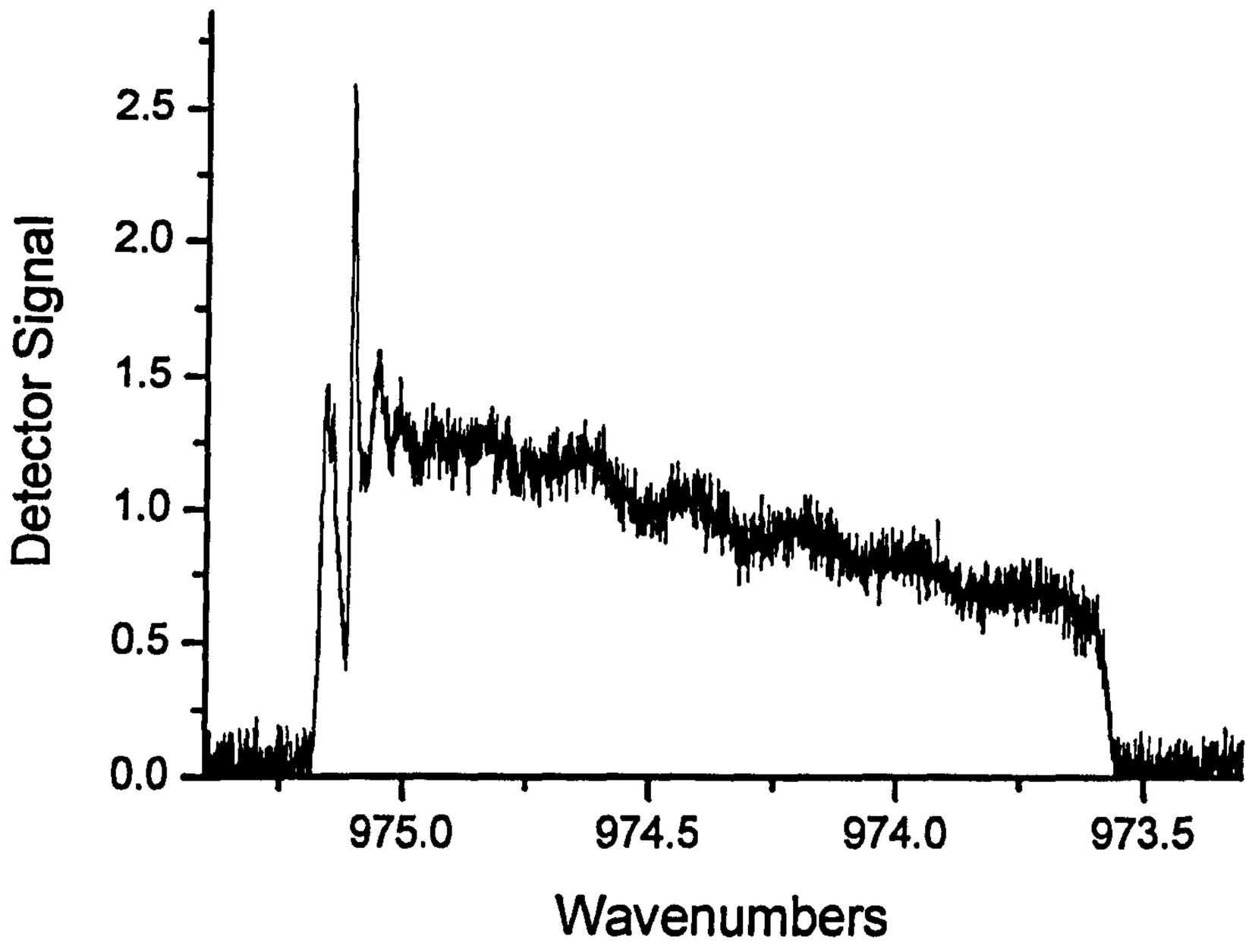

Figure 3.2.1 – *The output spectrum from the 10.24μm Alpes Laser.*

The laser was driven by a 4.6A current with a pulse width of 250ns and a pulse repetition rate of 15KHz. The laser substrate temperature was maintained at -9.52°C. This spectrum was recorded using the Bruker FTS at the Rutherford Appleton Laboratory. The resolution was 0.0015cm^{-1} for the 4 scans that were averaged together to give the spectrum. The output of the laser was passed straight into the Bruker FTS. The high frequency ringing at the start of the pulse is the switch on transient of the laser. The low frequency ringing on the rest of the spectrum is an unwanted etalon signal that was present in the optics of the Fourier Transform Spectrometer. By varying the drive current applied to the laser the chirp rate of the laser can be varied. Figure 3.2.2 shows the effect of varying the drive current from 4.2A to 5.2A in 0.2A steps with a constant pulse width of 200ns and a constant substrate temperature of -9.52°C and a pulse repetition rate of 40KHz.

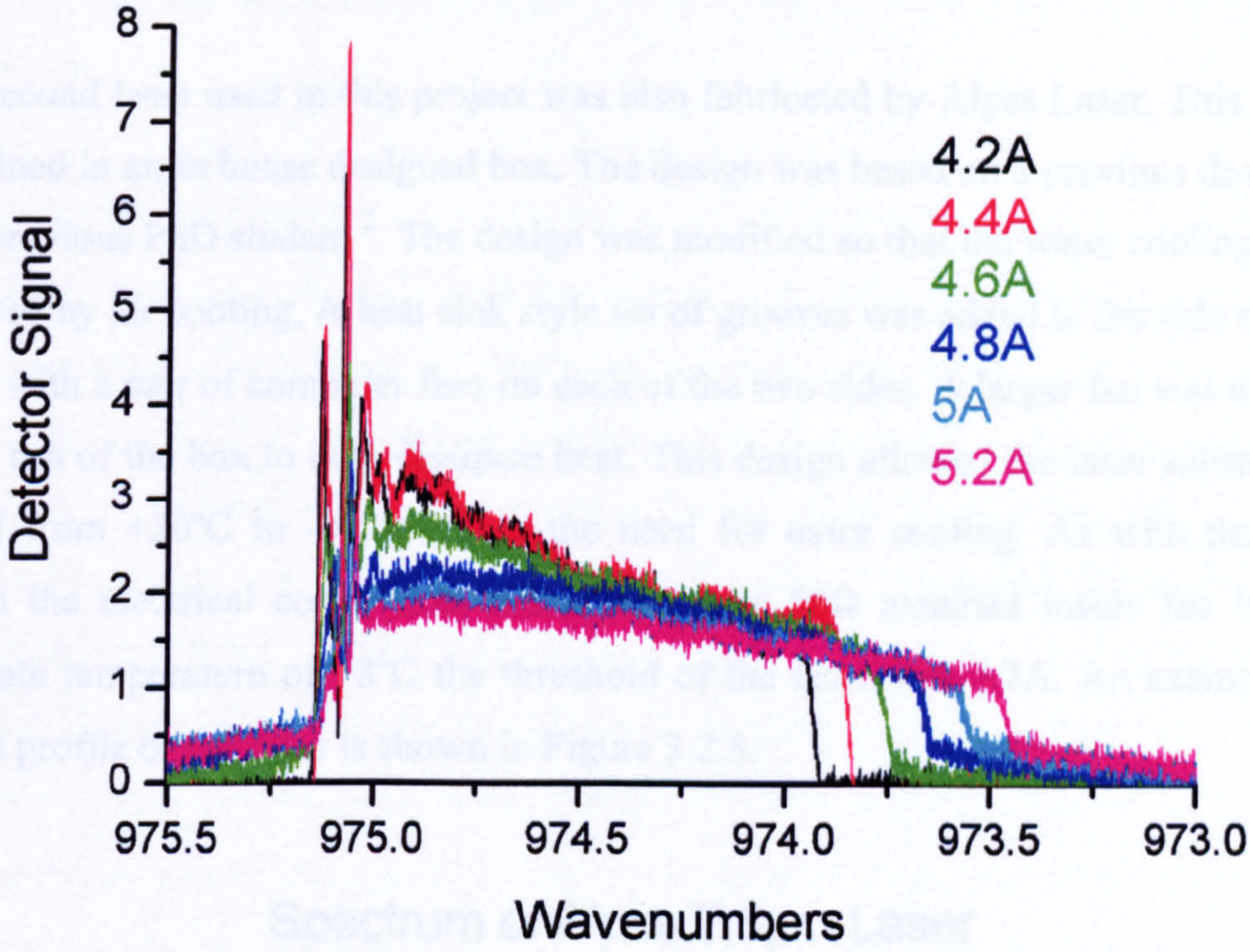

Figure 3.2.2 – *The Black trace shows the output with a 4.2A drive current. The Red trace shows the output with a 4.4A drive current. The Green trace shows the output with a 4.6A drive current. The Blue trace shows the output with a 4.8A drive current. The Cyan trace shows the output with a 5A drive current. The Magenta trace shows the output with a 5.2A drive current.*

These spectra were recorded using the Bruker FTS at the Rutherford Appleton Laboratory. The resolution was 0.0015cm^{-1} for the 2 scans that were averaged together to give each of the spectra.

The maximum spectral micro window of 2.5cm^{-1} could be achieved by driving the laser with a 5A current with a pulse width of 300ns. By using this micro window and temperature tuning from +10ºC to -10ºC a range of about 5cm^{-1} could be achieved. A typical chirp rate for this laser, when driving with a 4.3A current and 150ns pulses, is 200MHz/ns. The full characterisation of this laser has been discussed previously [2, 3].

3.2.3 Alpes Laser 7.8μm DFB Quantum Cascade Laser

The second laser used in this project was also fabricated by Alpes Laser. This laser was contained in an in house designed box. The design was based on a previous design made by a previous PhD student [2]. The design was modified so that the water cooling could be replaced by air cooling. A heat sink style set of grooves was added to the side of the box along with a pair of computer fans on each of the two sides. A larger fan was also added to the top of the box to help dissipate heat. This design allowed the laser substrate to be varied from +30°C to -8°C without the need for extra cooling. As with the original design the electrical connection to the laser was 50Ω matched inside the box. At a substrate temperature of +3°C the threshold of the laser was 2.2A. An example of the output profile of the laser is shown in Figure 3.2.3.

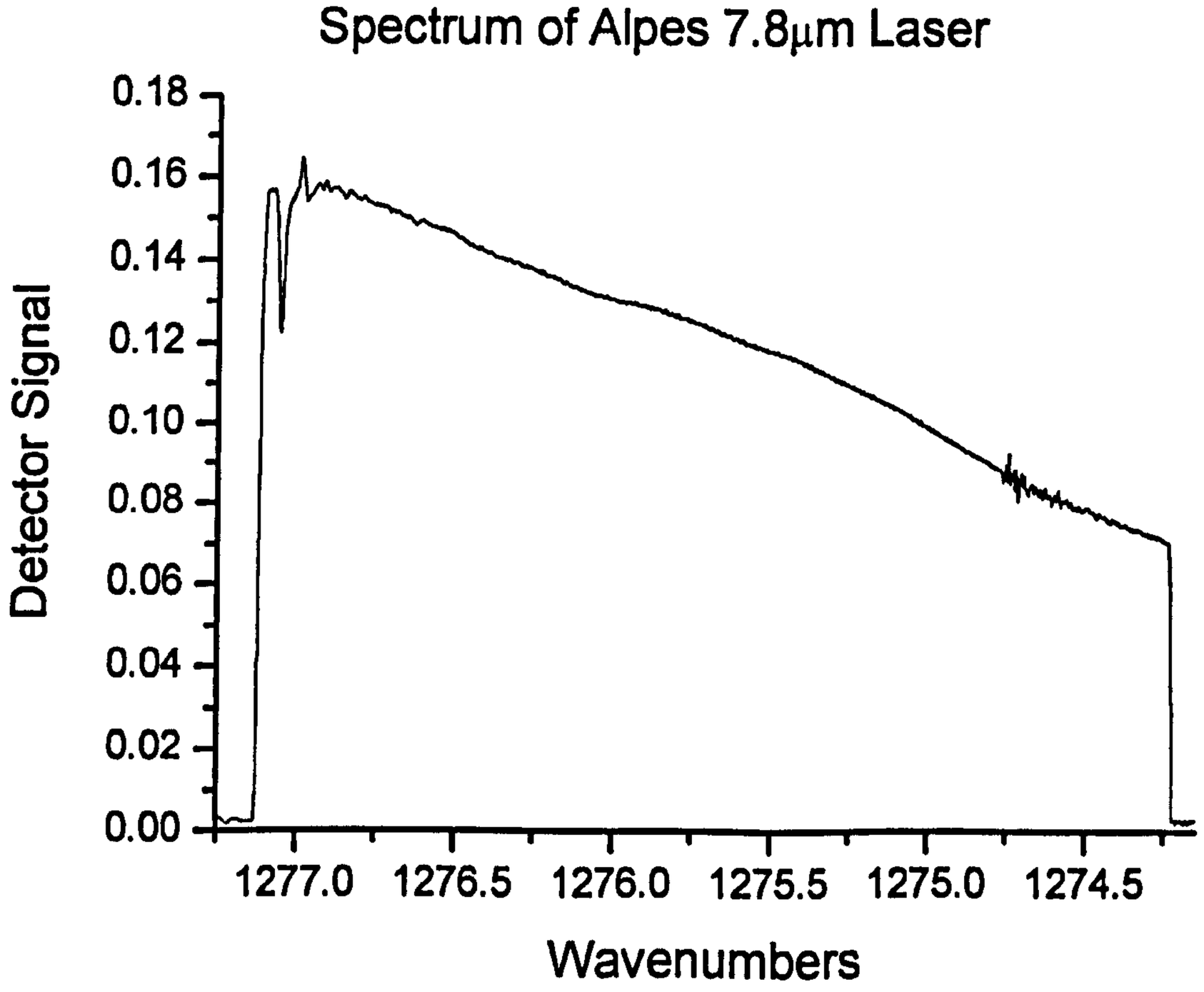

Figure 3.2.3 – *Spectrum of Alpes 7.8μm laser driven with a 3.5A drive current of pulse width 1270ns. The substrate temperature was set to +3°C and the pulse repetition rate was 20KHz.*

The wavenumbers scale has been reversed to show the temporal start of the pulse on the left hand side of the trace and the temporal end of the pulse on the right hand side of the trace. Compared to the Alpes 10.24μm laser the switch on transient for the Alpes 7.8μm laser is much less. This is due to the better electrical matching of the box used to house the 7.8μm laser compared to the Alpes box used to house the 10.24μm laser. This better electrical matching is achieved by moving the 50Ω matching resistor inside the box from outside the box, which reduces the length of the low impedance line and therefore the electrical ringing created at the impedance mismatch point [2]. This laser was driven over a range of temperatures, pulse widths, repetition rates and drive currents. Some of the parameters have been changed to highlight the different size micro windows available to the user. At a constant temperature of +3°C and constant pulse repetition rate of 20KHz the pulse width of the laser as well as the drive current used to pulse the laser were varied, which is shown in Figure 3.2.4.

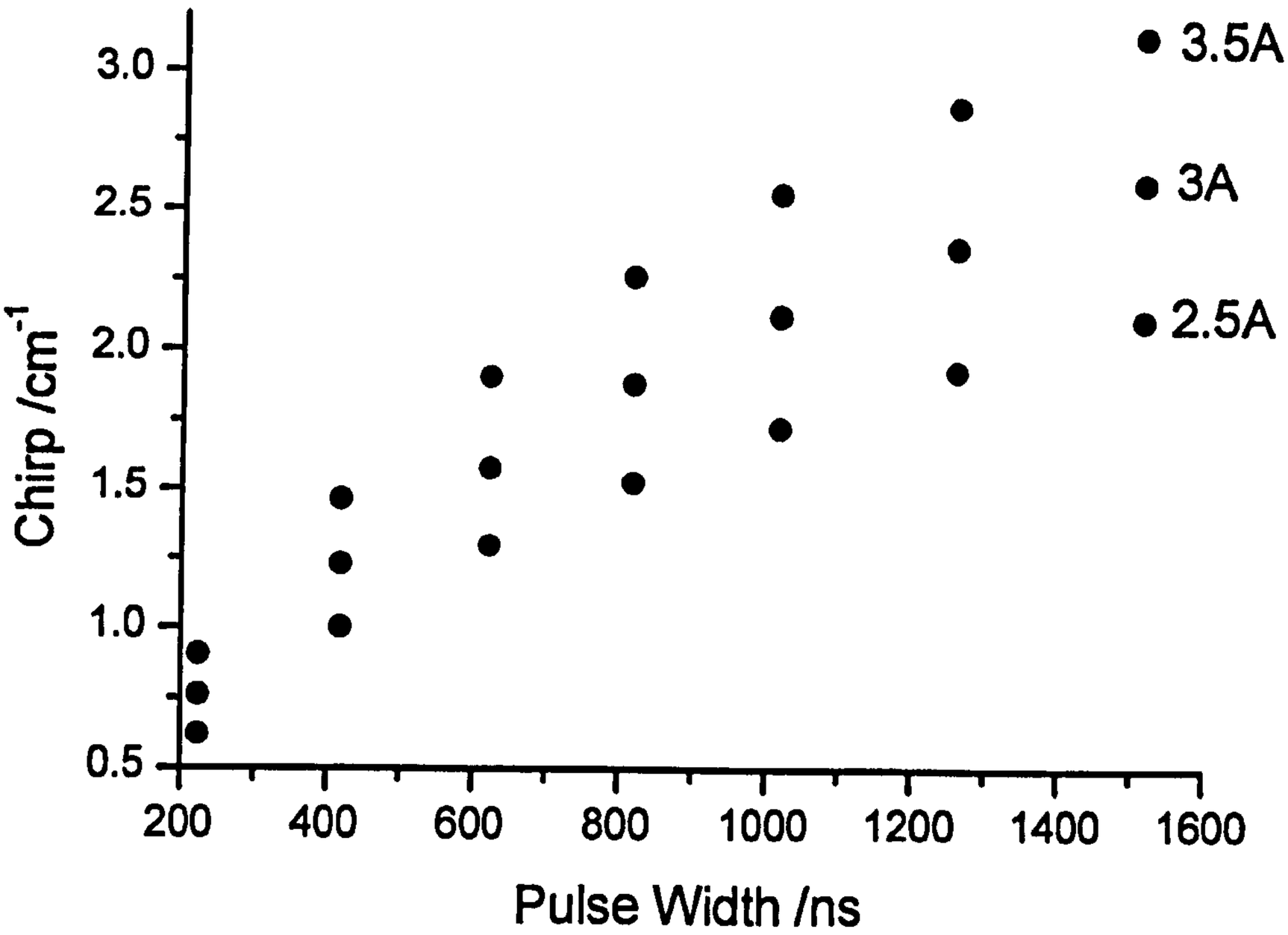

Figure 3.2.4 – *The top set of Black dots show the total chirp of the laser when driven by a 3.5A drive current as a function of pulse width. The middle set of Black dots show the total chirp of the laser when driven by a 3A drive current as a function of pulse width. The bottom set of Black dots show the total chirp of the laser when driven by a 2.5A drive current as a function of pulse width.*

The total chirp of the laser over the entire laser pulse increases at a slower rate than a linear increase for an increasing pulse width. As the frequency down chirp in the laser is caused by the thermal loading of the laser the larger the drive the current the larger the thermal loading and therefore the faster the chirp. The temperature of the laser substrate was reduced to -1.5°C and the experiment was repeated. The total laser chirp as a function of the pulse width and drive current for a fixed temperature of -1.5°C and a constant pulse repetition rate of 20KHz is shown in Figure 3.2.5.

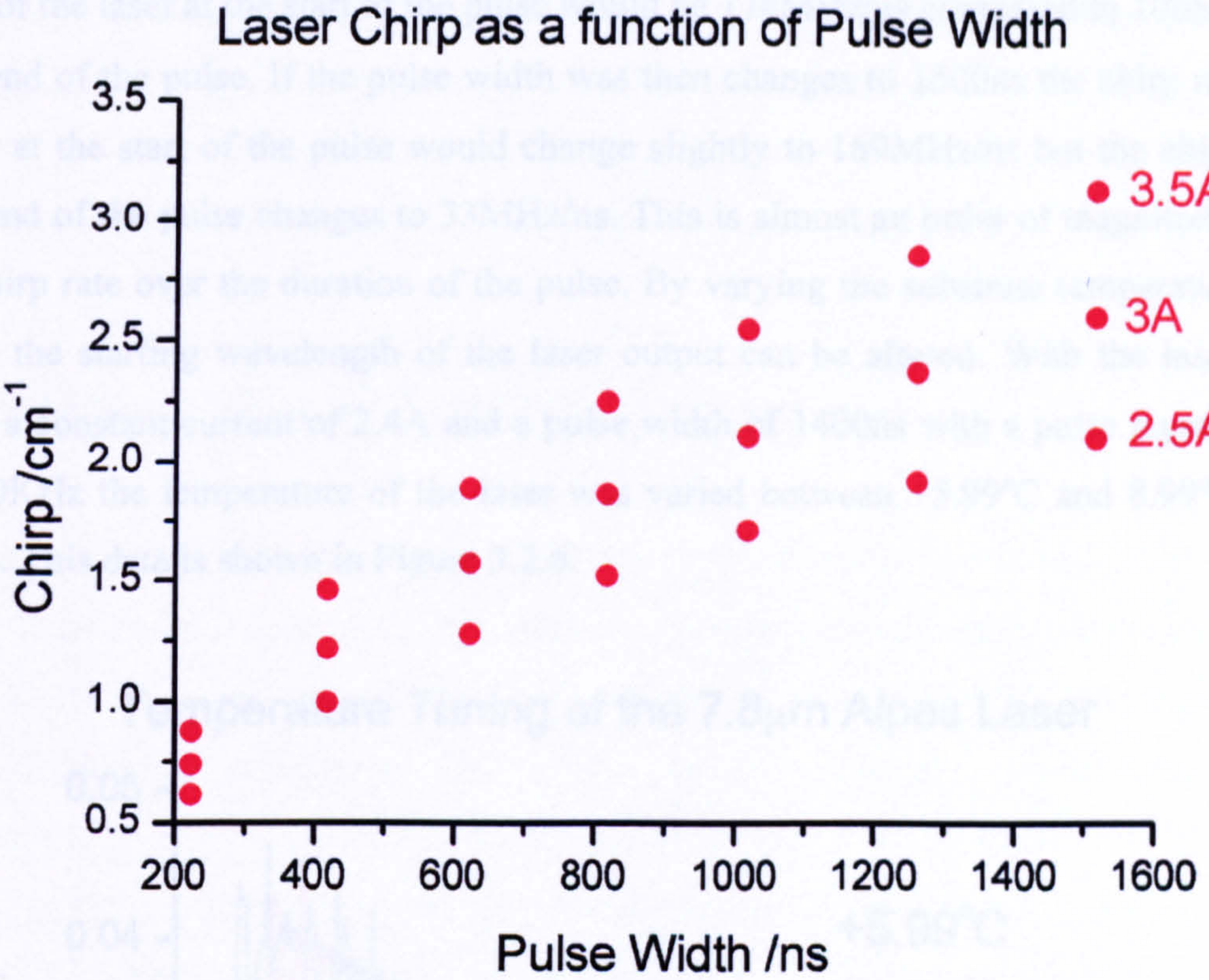

Figure 3.2.5 – *The top set of Red dots show the total chirp of the laser when driven by a 3.5A drive current as a function of pulse width. The middle set of Red dots show the total chirp of the laser when driven by a 3A drive current as a function of pulse width. The bottom set of Red dots show the total chirp of the laser when driven by a 2.5A drive current as a function of pulse width.*

When compared to the previous +3°C measurements the total chirp for the laser for equivalent laser settings for the -1.5°C measurements is very similar. For all of the data the differences in total chirp is within 3%. The total chirp of the laser is slightly larger for the colder temperature setting except in 2 settings out of 21 settings. The standard deviation in the percentage difference in total chirp between the two sets of data is 0.72%. As the tuning is nonlinear the chirp rate of the laser decreases across the pulse. This effect is magnified when the pulse width used is increased. For example if the laser was driven with a drive current of 3.5A and a pulse width of 224ns with a stabilised substrate temperature of +3°C and a pulse repetition frequency of 20KHz then the chirp

rate of the laser at the start of the pulse would be 174MHz/ns compared to 100MHz/ns at the end of the pulse. If the pulse width was then changes to 1500ns the chirp rate of the laser at the start of the pulse would change slightly to 169MHz/ns but the chirp rate at the end of the pulse changes to 33MHz/ns. This is almost an order of magnitude change in chirp rate over the duration of the pulse. By varying the substrate temperature of the laser the starting wavelength of the laser output can be altered. With the laser driven with a constant current of 2.4A and a pulse width of 1400ns with a pulse repetition rate of 10KHz the temperature of the laser was varied between +5.99ºC and 8.99ºC in 1ºC steps. This data is shown in Figure 3.2.6.

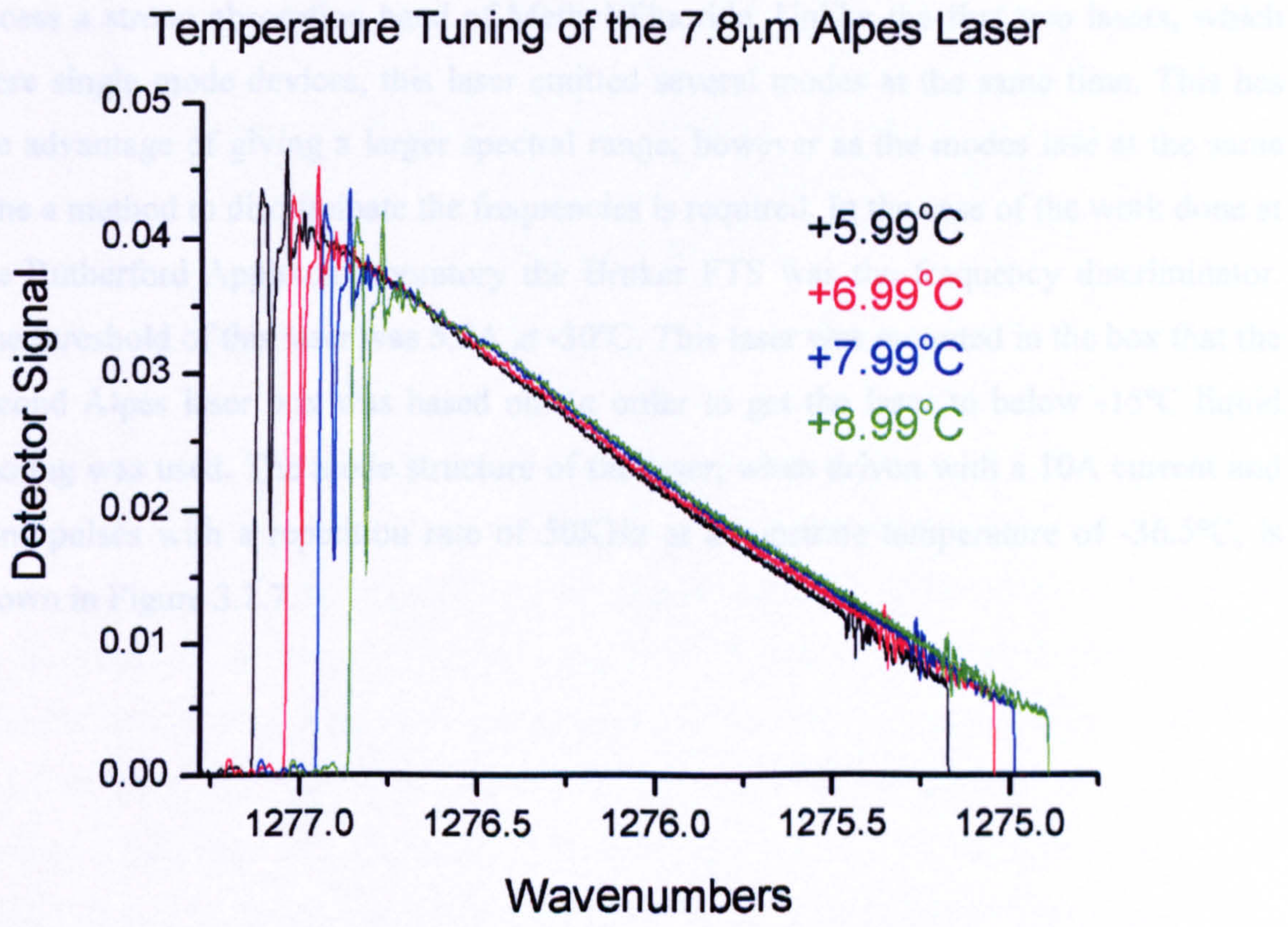

Figure 3.2.6 – *The Black trace shows the laser substrate temperature of +5.99ºC. The Red trace shows the laser substrate temperature of +6.99ºC. The Blue trace shows the laser substrate temperature of +7.99ºC. The Green trace shows the laser substrate temperature of +8.99ºC.*

The wavenumbers scale has been reversed to show the temporal start of the pulse on the left hand side of the trace and the temporal end of the pulse on the right hand side of the trace. The spectra were recorded using the fast MCT detector. As the temperature of the substrate is increased the starting wavelength of the laser increases as well.

3.2.4 Thales 9.46µm FP Quantum Cascade Laser

As part of the work I carried out at the Rutherford Appleton laboratory a Thales [4] Fabry Perot Quantum Cascade laser was studied. Operating at 9.46µm this laser was able to access a strong absorption band of Methyl Fluoride. Unlike the first two lasers, which were single mode devices, this laser emitted several modes at the same time. This has the advantage of giving a larger spectral range; however as the modes lase at the same time a method to discriminate the frequencies is required. In the case of the work done at the Rutherford Appleton laboratory the Bruker FTS was the frequency discriminator. The threshold of this laser was 5.5A at -30°C. This laser was mounted in the box that the second Alpes laser box was based on. In order to get the laser to below -15°C liquid cooling was used. The mode structure of the laser, when driven with a 10A current and 10ns pulses with a repetition rate of 50KHz at a substrate temperature of -36.5°C, is shown in Figure 3.2.7.

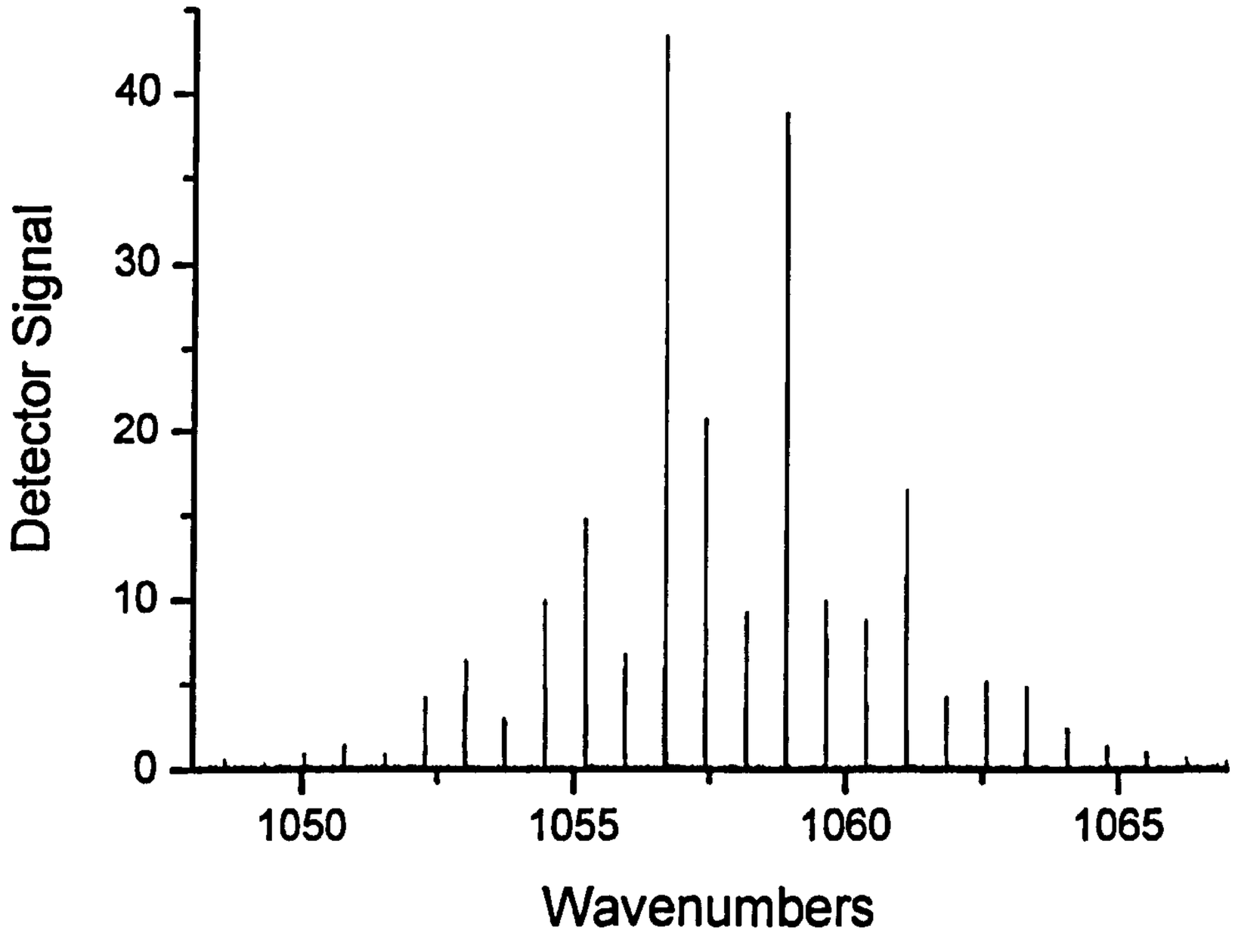

Figure 3.2.7 – *The mode structure of the Thales 9.46μm FP QCL.*

The spectrum was recorded using the Bruker FTS with a resolution of 0.0015cm^{-1} and an average of 15 scans. A full description of Fabry Perot lasers can be found in section 2.1.2. A 26cm single pass optical cell was placed inside the Bruker FTS in the path of the beam. Three different pressures of Methyl Fluoride were added to the cell and a spectrum was recorded for each gas pressure. The pressures were 0.79 Torr, 0.16 Torr and 0.08 Torr. The laser was driven with a 9.8A current of pulse width 55ns and a repetition frequency of 10KHz. The substrate temperature from the first measurement was -37°C and the temperature was -38.5°C for the other two measurements. These three spectra were recorded with the Bruker FTS using a resolution of 0.005cm^{-1} and an average of 5 scans. A comparison spectrum recorded using a Globar as the light source was recorded using the BOMEM FTS within the group. The comparison spectrum was recorded at a resolution of 0.03cm^{-1} with an average of 400 scans. The sample used was

1 Torr of Methyl Fluoride in White Cell [5] with a 7.2m optical path. These spectra are shown below in Figure 3.2.8.

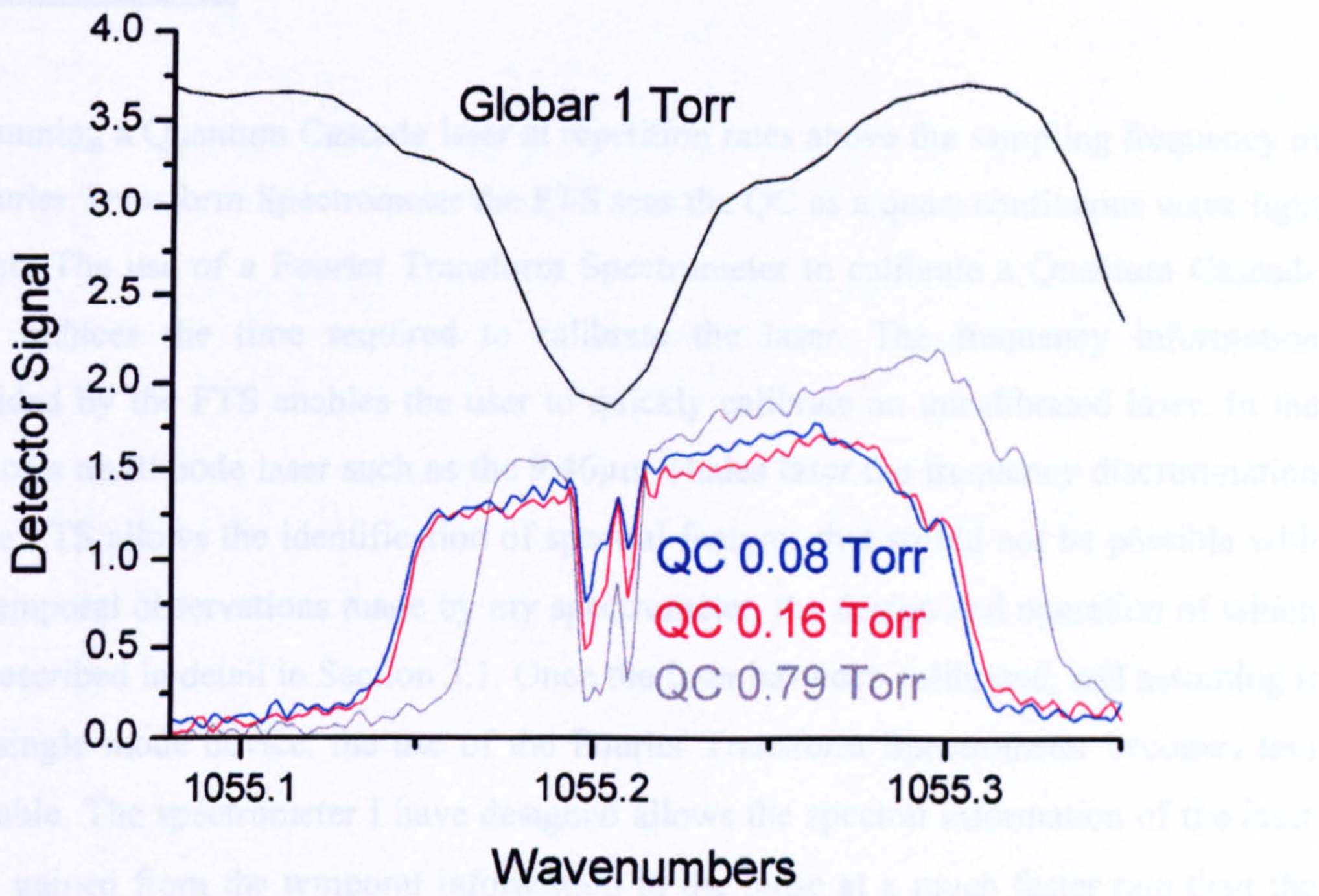

Figure 3.2.8 – *The Black trace shows the 1 Torr Methyl Fluoride Globar spectrum. The Grey trace shows the 0.79 Torr Methyl Fluoride QC spectrum. The Red trace shows the 0.16 Torr Methyl Fluoride QC spectrum. The Blue trace shows the 0.08 Torr Methyl Fluoride QC spectrum.*

The spectrum has been zoomed in onto show the QC mode which shows the strongest absorption. The resolution difference between the Globar spectrum and the QC spectra is apparent such that the absorption in the QC spectra is more than one line, but in the Globar spectrum the doublet is not resolved. As the first QC spectrum was recorded with a different substrate temperature to the subsequent two there is a frequency shift between them. This frequency shift helps to confirm that the absorption is real and not an artifact of the laser. Although the strong Methyl Fluoride lines are sparsely separated the multi

mode Fabry Perot output from the laser allows a coincidence of laser emission and Methyl Fluoride absorption.

3.2.5 Discussion

By running a Quantum Cascade laser at repetition rates above the sampling frequency of a Fourier Transform Spectrometer the FTS sees the QC as a quasi continuous wave light source. The use of a Fourier Transform Spectrometer to calibrate a Quantum Cascade laser reduces the time required to calibrate the laser. The frequency information provided by the FTS enables the user to quickly calibrate an uncalibrated laser. In the case of a multimode laser such as the 9.46μm Thales laser the frequency discrimination of the FTS allows the identification of spectral features that would not be possible with the temporal observations made by my spectrometer, the design and operation of which are described in detail in Section 3.1. Once the laser has been calibrated, and assuming it is a single mode device, the use of the Fourier Transform Spectrometer becomes less desirable. The spectrometer I have designed allows the spectral information of the laser to be gained from the temporal information in the pulse at a much faster rate than the Fourier Transform Spectrometer. The signal to noise of my spectrometer is also vastly better than the FTS and the size of my spectrometer is smaller.

3.2.6 References

1) Demonstration of High-Performance 10.16μm Quantum Cascade Distributed Feedback lasers Fabricated without Epitaxial Regrowth, D. Hofstetter, J. Faist, M. Beck, A. Műller and U. Oesterie, App. Phys. Lett., **75**, 5, 665-667

2) Fast ultra-sensitive real time quantum cascade laser spectrometer, E. L. Normand, PhD Thesis, Department of Physics, University of Strathclyde, (2004)

3) Characterisation of the spectral behaviour of pulsed quantum cascade lasers using a high resolution Fourier transform infrared spectrometer, E. Normand, G. Duxbury and N. Langford, Opts. Comms., **197**, 115-120, (2001)

4) Quantum Cascade Laser: The Quantum Technology for Semiconductor lasers in the mid-far-infrared, C. Sirtori and J. Nagle, C. R. Physique, **4**, (2003) 639-648

5) Long optical paths of large aperture, J. U. White, J. Opt. Soc. Am., **32**, 285-288, (1942)

4 Nonlinear Optics

4.1 Introduction

At the start of this work the spectrometer was assumed to monitor the molecular gases without affecting them. This was soon found to be a bad assumption. The speed of chirp of the laser combined with the relatively high peak powers means that the system cannot be treated as a linear absorption spectrometer in all circumstances. When the laser frequency is swept rapidly through an absorption line an asymmetric line shape is observed followed by wiggles. This effect was commonly observed in swept frequency nuclear magnetic resonance spectroscopy (NMR) and is due to rapid passage (or passage) when the sweep rate is faster than the longitudinal relaxation time of the nuclear spin system [1]. The behaviour of magnetic dipole transitions of this type has been described in detail by Ernst [1]. Similar time dependent effects have also been seen in electric dipole transitions in the infrared region [2]. In this chapter I will cover the basic theory for the non linear effects seen in electric dipole vibration-rotation transitions studied in this work, and will provide examples of each of the effects.

4.2 Rabi Frequency

In a weak field the probability of finding a molecule in the ground state is not to all intents and purposes unchanged by the interaction with the field. This leads to a time independent transition probability. When a molecule interacts with a strong field a time dependent transition probability occurs. The strong signal theory developed by Rabi [3] leads to a time dependent probability of finding a molecule in the ground state. Figure 4.1 below shows the energy levels of a 2 level system.

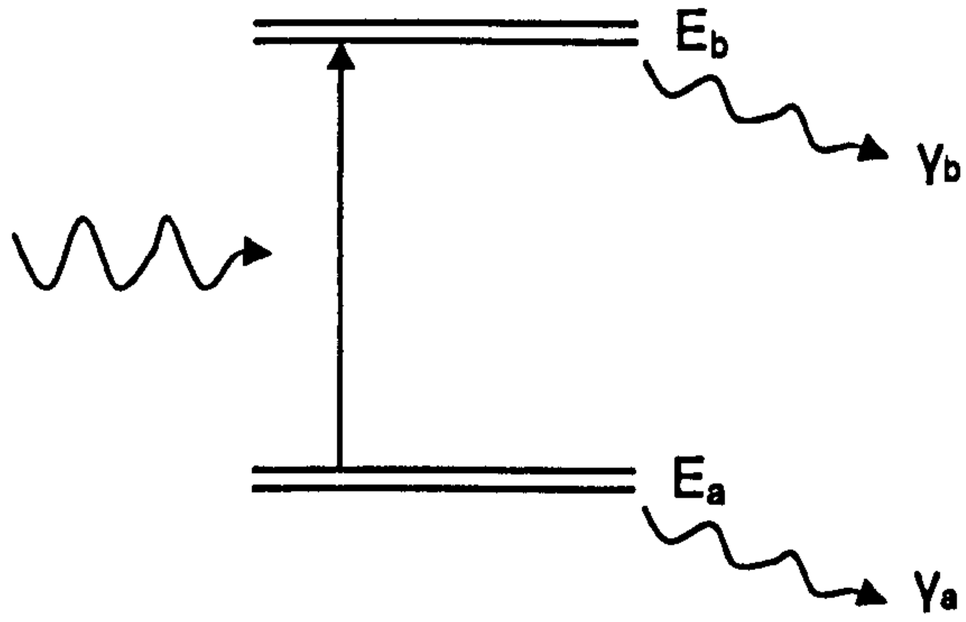

Figure 4.1 – *A two level system*

E_a and E_b are the lower and upper levels in a molecule absorbing a photon of radiation of wavelength λ. γ_a and γ_b are the relaxation processes. In the strong field case the population of the two levels oscillates as shown in Figure 4.2.

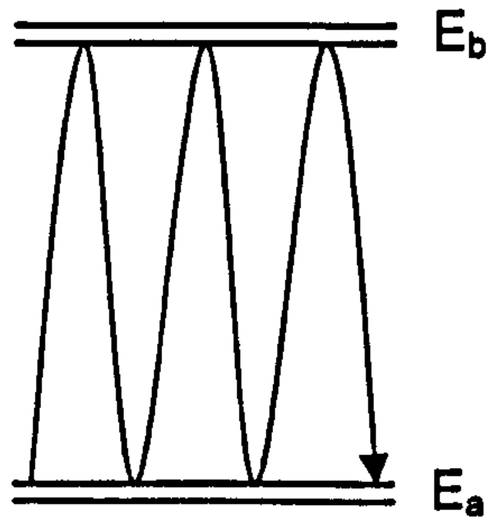

Figure 4.2 – *The Rabi Flopping of a two level system*

The frequency of the oscillation is known as the "Rabi Flopping frequency" [3], Ω, and is given by:

$$\Omega = \frac{\mu E}{h}$$

where μ is the dipole moment and E is the field strength.

4.3 Rapid Passage

In NMR spectroscopy, the time dependent behaviour of transitions between the lower and upper levels of a two level system may be analysed using the Bloch equations [1]. In laser spectroscopy of electric dipole transitions the optical analogue of the NMR Bloch equations, the optical Bloch Equations [2], may be used to treat the time dependent behaviour of a two level system [2,3].

The Bloch components of the Bloch vector, u, v and w, are given by:

$$\frac{du}{dt} = -\Delta(t)v - \gamma_2 u$$

$$\frac{dv}{dt} = -\Delta(t)u - \gamma_2 v + \kappa E w$$

$$\frac{dw}{dt} = -\kappa E w - \gamma_1 \left(w - w_{eq}\right)$$

$$\Delta(t) = w_a - \left(w_i + \alpha t\right),\ \kappa = \frac{\mu}{\hbar}$$

where $\gamma_1 = 1/T_1$, $\gamma_2 = 1/T_2$, κ is the molecule field coupling constant and $\Delta(t)$ is the detuning from resonance.

A numerical calculation of the u (real refractive index), v (imaginary refractive index) and w (population difference) components of the Bloch equations has been done by Nigel Langford for a range of laser frequency sweep rates, power densities and collisional relation times. By using a Rabi Frequency of 50MHz the u, v and w components have been calculated for chirp rates of -200MHz/ns and -20MHz/ns. Due to the nonlinear tuning of the 8μm laser the -200MHz/ns chirp rate approximates the start

of the laser pulse and the -20MHz/ns chirp rate approximates the end of the laser pulse. This data is displayed in Figure 4.3.

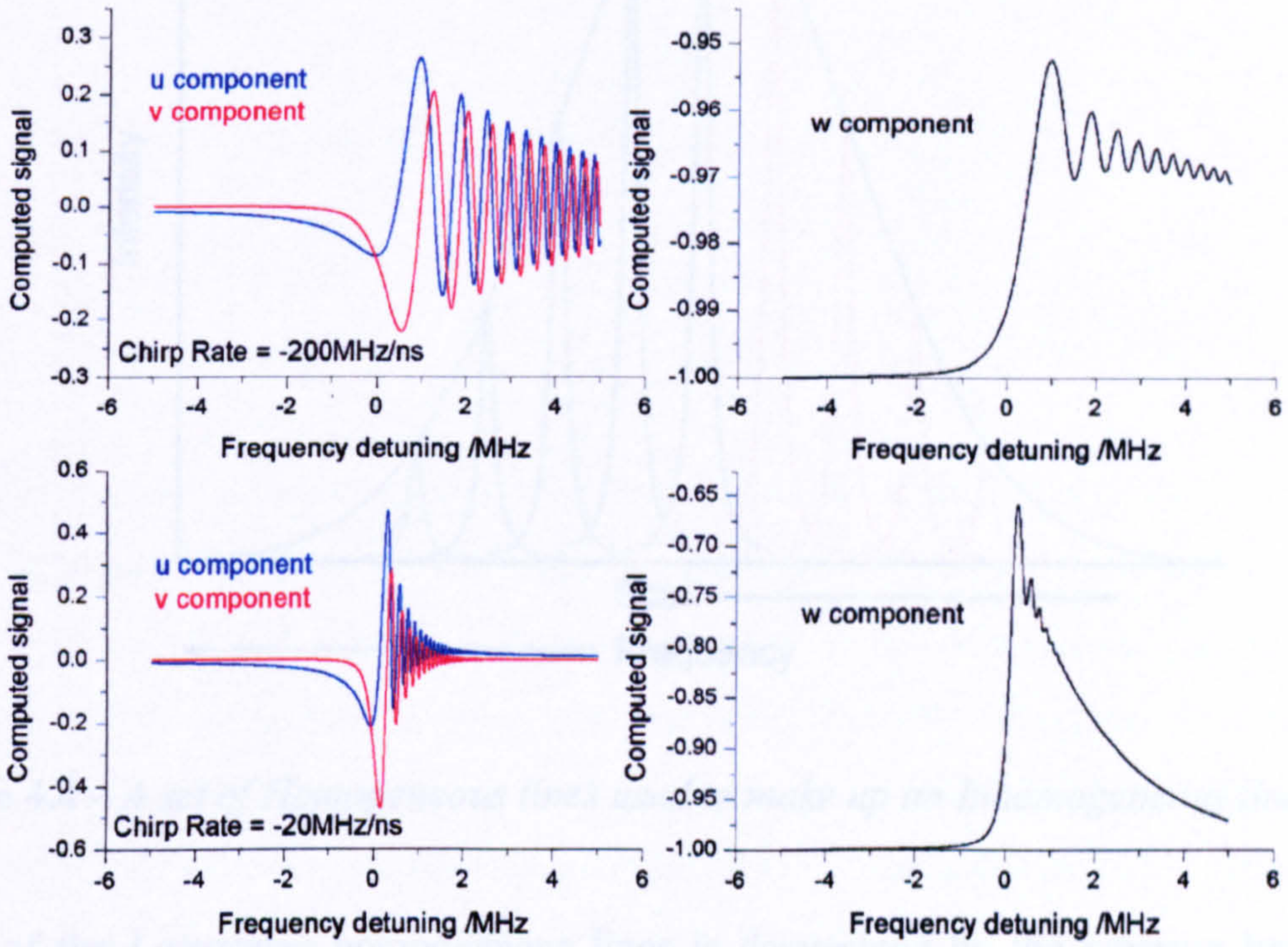

Figure 4.3 – *The Black traces show the w component of the Bloch equation as a function of frequency detuning. The Red traces show the v component of the Bloch equation as a function of frequency detuning. The Blue traces show the u component of the Bloch equation as a function of frequency detuning.*

The wiggles on the w component of the Bloch equations should be seen in the overshoot signal in the experimental results. By varying the chirp rate that an absorption line experiences the effect on the overshoot signal can be seen. As this simulation only covers one inhomogeneous component of an absorption line the results in practice should be different due to the interaction of the field with many inhomogeneous components.

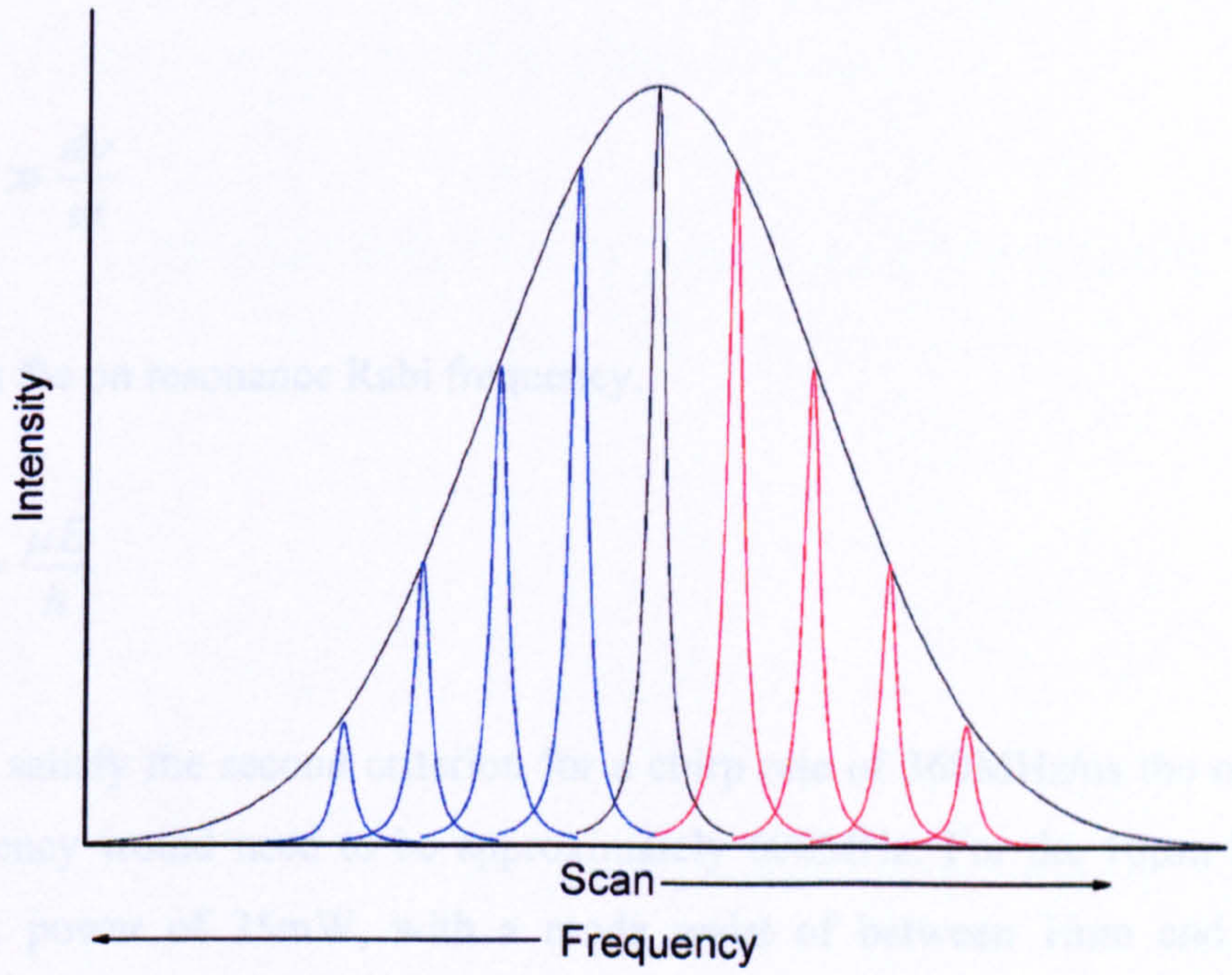

Figure 4.4 – *A set of Homogeneous lines used to make up an Inhomogeneous line.*

Each of the Lorentzian homogeneous lines is determined by the pressure broadening present in the system, which is at low pressure, and the envelope is the Gaussian Doppler profile. Each of these homogenous lines represents a different velocity group of molecules. The result of having many velocity components is a superposition of u, v and w components and leads to a damping of the wiggles in the w component of the Bloch equations and is seen in the experimental results later.

The limiting case of rapid passage is adiabatic rapid passage (ARP), in which complete population inversion is produced by the rapidly swept laser. The two criteria that need to be met in order to observe ARP have been highlighted by Loy et al [4] and Shoemaker et al [2]. The first criterion is that the frequency of the laser must be swept through the linewidth of the absorbing feature of interest in a time which is shorter than T_1. This is the condition which has been met in the rapid passage conditions discussed previously.

The second criterion is that the laser field must be strong enough to satisfy the adiabatic condition:

$$\Omega^2 \gg \frac{d\nu}{dt}$$

Where Ω is the on resonance Rabi frequency.

$$\Omega = \frac{\mu E}{h}$$

In order to satisfy the second criterion for a chirp rate of 360MHz/ns the on resonance Rabi frequency would need to be approximately 600MHz. For the 10μm laser, which has a peak power of 25mW, with a mode waist of between 1mm and 1.3mm the calculated Rabi frequency for the strong Ammonia transition observed is about 1MHz. This Rabi frequency is far too low to generate ARP. An analysis by Shoemaker [2] showed that for a transition near 10μm irradiated by a 2mm Gaussian laser beam of 20W power a typical Rabi frequency would be 125MHz. If the laser were to chirp at a rate of 4000MHz/μs the second criteria would be satisfied.

Even for the observation of rapid passage signals the laser field seen by the molecules appears to be too low. However, there are other processes at work such as self focussing which may enhance the power density of the laser within the gas cell. Simulations have been done in the group by Nigel Langford in order to better understand the self focusing of the system. The model for the self focusing follows the work by Grischowski [5, 6]. This model is based on rapid passage, in which the self focusing occurs on the blue side of the line undergoing rapid passage and self defocusing on the red side of the line centre. Experimental results below show that the switch from absorption to emission occurs close to line centre. The lasers used in this work chirp from blue to red. It would be expected that the switch from absorption to emission should occur once the driving field

is reduced as one switches from focussing to defocusing. However, at higher gas pressures of the strongly absorbing Ammonia, the switch from absorption to emission may be delayed by up to 5ns. This effect is shown in Figure 4.5.

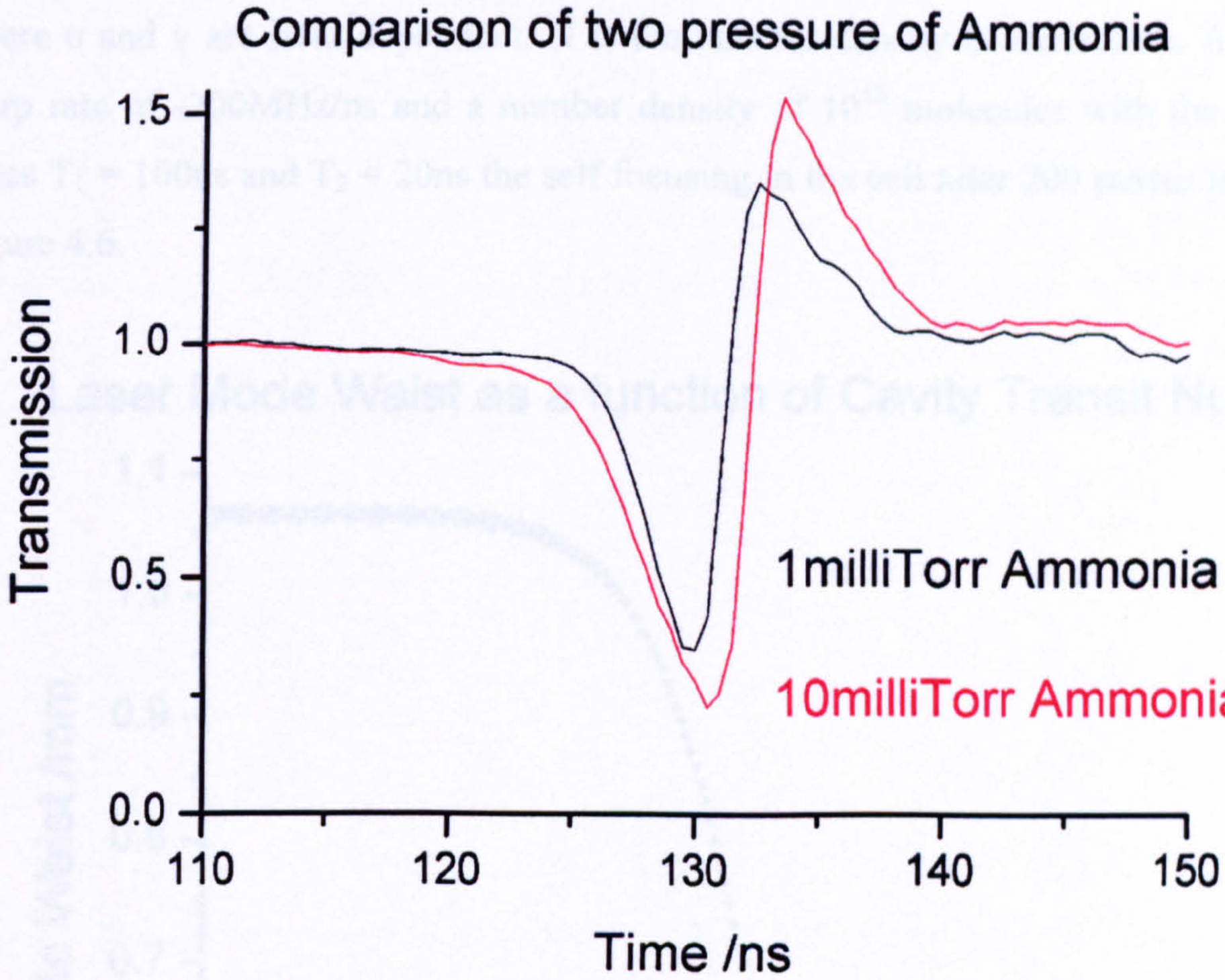

Figure 4.5 – *The Red trace shows the absorption and overshoot signals from 10milliTorr of Ammonia. The Black trace shows the absorption and overshoot signals from 1milliTorr of Ammonia.*

This indicates that another type of nonlinear process is occurring. One possibility is the occurrence of another type of self focusing such as transient orientational self focusing described by Wong and Shen [7] and by Reintjes, Carman and Shimizu [8]. The propagation of the light through the cell was considered using the nonlinear propagation equation:

$$\nabla_T^2 E(x,y,z,w) - 2ik\frac{dE}{dZ}(x,y,z,w) + k^2 P(x,y,z,w) = 0$$

$$P(x,y,z,w) = -\frac{N\mu}{\varepsilon_0}(u - iv)$$

where u and v are field dependent. N is the number density of molecules. Assuming a chirp rate of -200MHz/ns and a number density of 10^{13} molecules with the relaxation times T_1 = 100ns and T_2 = 20ns the self focusing in the cell after 200 passes is shown in Figure 4.6.

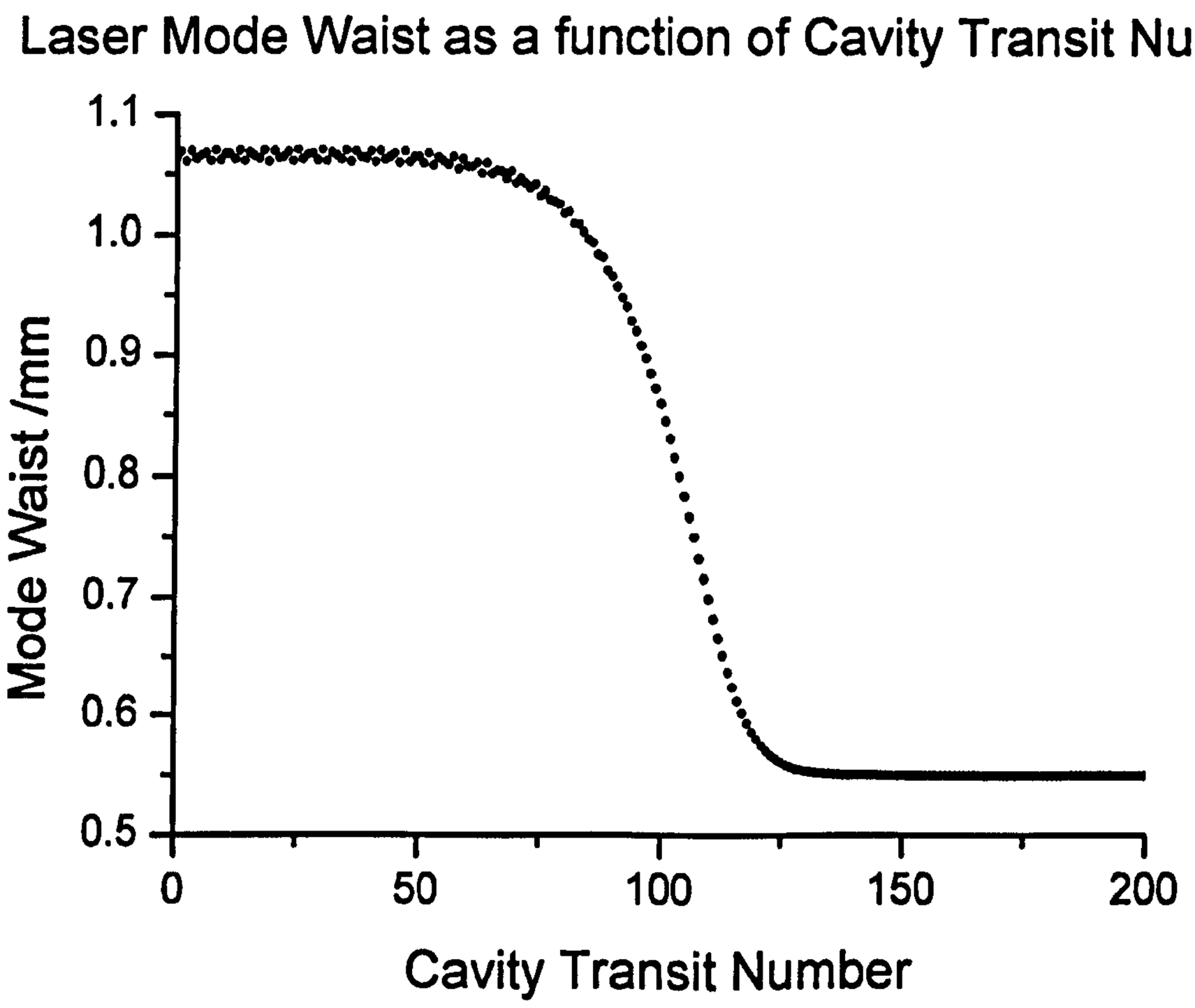

Figure 4.6 – *The self focusing in the astigmatic Herriott cell as a function of cavity transit number. Figure courtesy of Nigel Langford.*

It can be seen that the mode waist of the laser when on resonance decreases significantly. Even with these effects the power density of the laser does not seem to be large enough to cause adiabatic rapid passage to be observed in our spectrometer.

However the fact that these effects are seen as strongly as they are indicates that rapid passage is occurring.

One method which we have used in order to try to estimate the power densities of the laser during self focussing is that due originally to Horwitz [9], and in the form used below by Shoemaker [2]. Howitz derived an analytical expression for the asymptotic final state which is a result of a "non-adiabatic frequency chirp", this is synonymous with our definition of chirp which induces rapid passage. Although his method yields complicated solutions for the motion during the pulse, the expression for the final population of the upper state is a simple analytic expression. The ratio of the final population, w(final), after the rapid passage to the initial population, w(initial), is given by:

$$w(final)/w(initial) = 2\exp\left(-\frac{\pi^2\Omega^2}{2\,dv/dt}\right) - 1$$

We have verified that the ratios of w(final) and w(initial) calculated in this way agree with those obtained by solving the optical Bloch equations as described earlier.

In our analysis of the rapid passage signals we have assumed that the magnitude of the effect may be approximated by using the ratio of the area under the overshoot and absorption of the transition line of interest. Initially it was thought that this ratio was a direct measurement of the ratio of w(final) to w(initial), however our later calculations have demonstrated that it is only indirectly related to the total population transfer. The interpretation of the labelling of w(final) / w(initial) on subsequent figures should therefore be that of an approximate figure of merit for the magnitude of the rapid passage signal.

One of the simplest examples of this phenomenon occurs in Ammonia. The line selected was the R(1,1) transition in the ν_2 band of Ammonia at 971.88cm^{-1}. The transition dipole of this transition is 0.175D [10]. The sparseness of the Ammonia spectrum means that there are no transitions close to this transition to cause interference. The absorption and overshoot signals of this transition can be seen in Figure 4.7

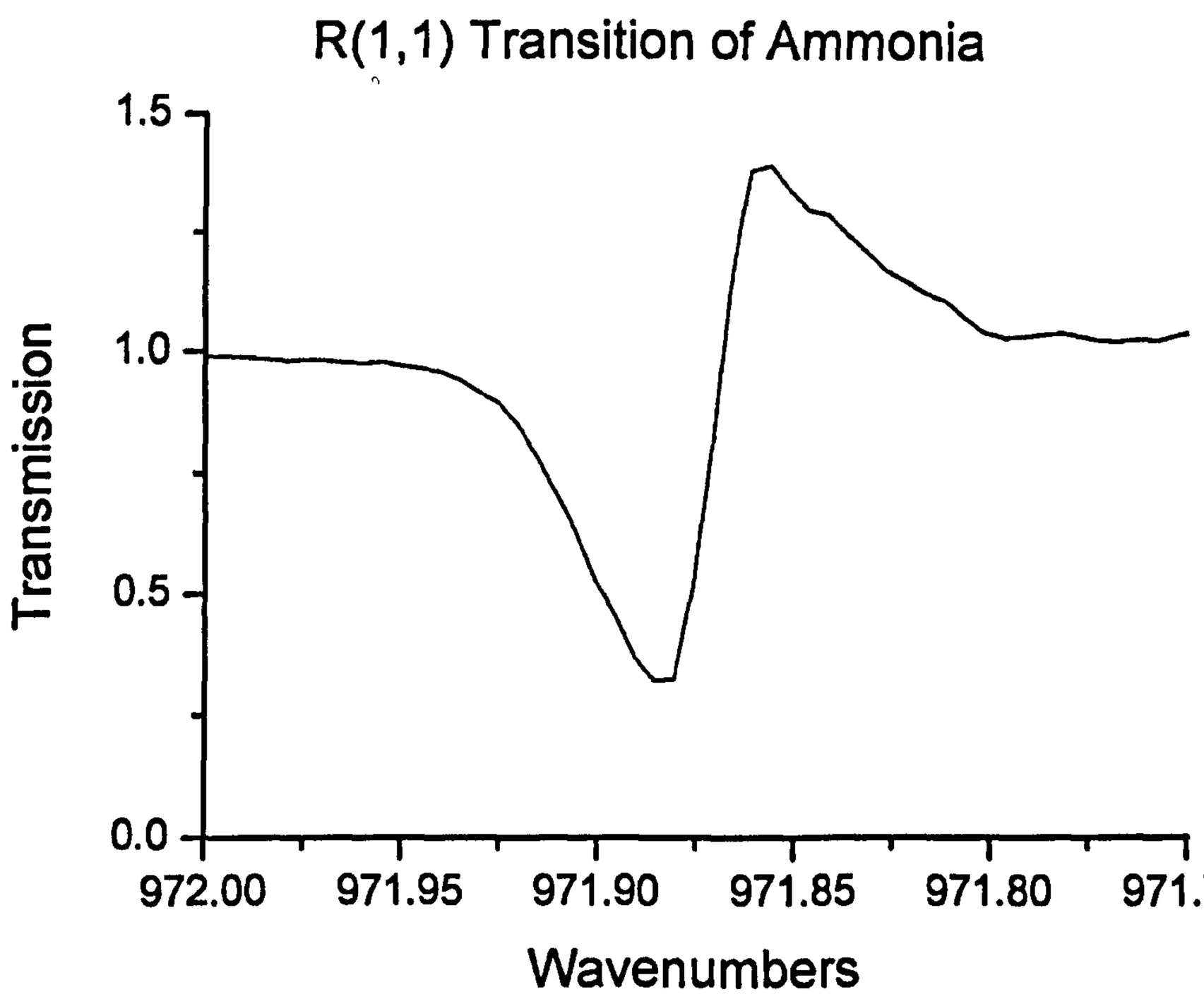

Figure 4.7 – *The absorption and overshoot signals of the R(1,1) Ammonia transition.*

The spectrum was recorded with a pressure of approximately 1milliTorr of Ammonia using a laser drive current of 5A. The pulse width of the laser was set to 140ns and the repetition rate was 20KHz. The laser substrate temperature was maintained at +11°C. The chirp rate of the laser was approximately -290MHz/ns. The approximate peak power of the 10μm laser is 25mW. The wavenumbers scale has been reversed to show the absorption on the left and the overshoot on the right of the trace. The pathlength used was 66m. By flowing a steady amount of gas into the astigmatic Herriott cell the

evolution of the overshoot and absorption signals can be found. By using the same laser settings as above the evolution of absorption and overshoot is shown in Figure 4.8.

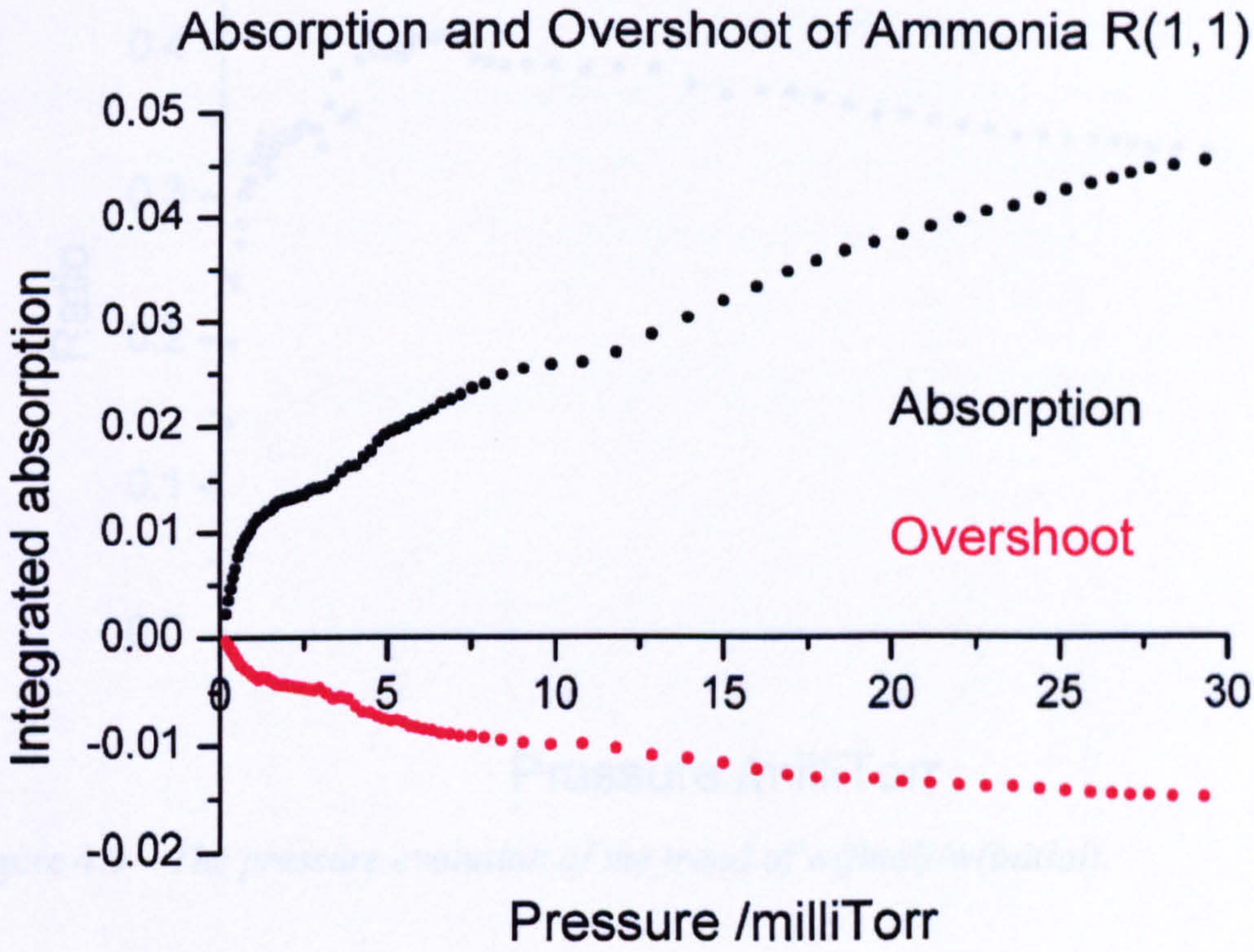

Figure 4.8 – *The Black dots show the integrated intensity of the absorption signal. The Red dots show the integrated intensity of the overshoot signal.*

The flow of gas was kept as constant as possible by varying the inlet valve. The ratio of Overshoot/Absorption has been calculated and is shown in Figure 4.9.

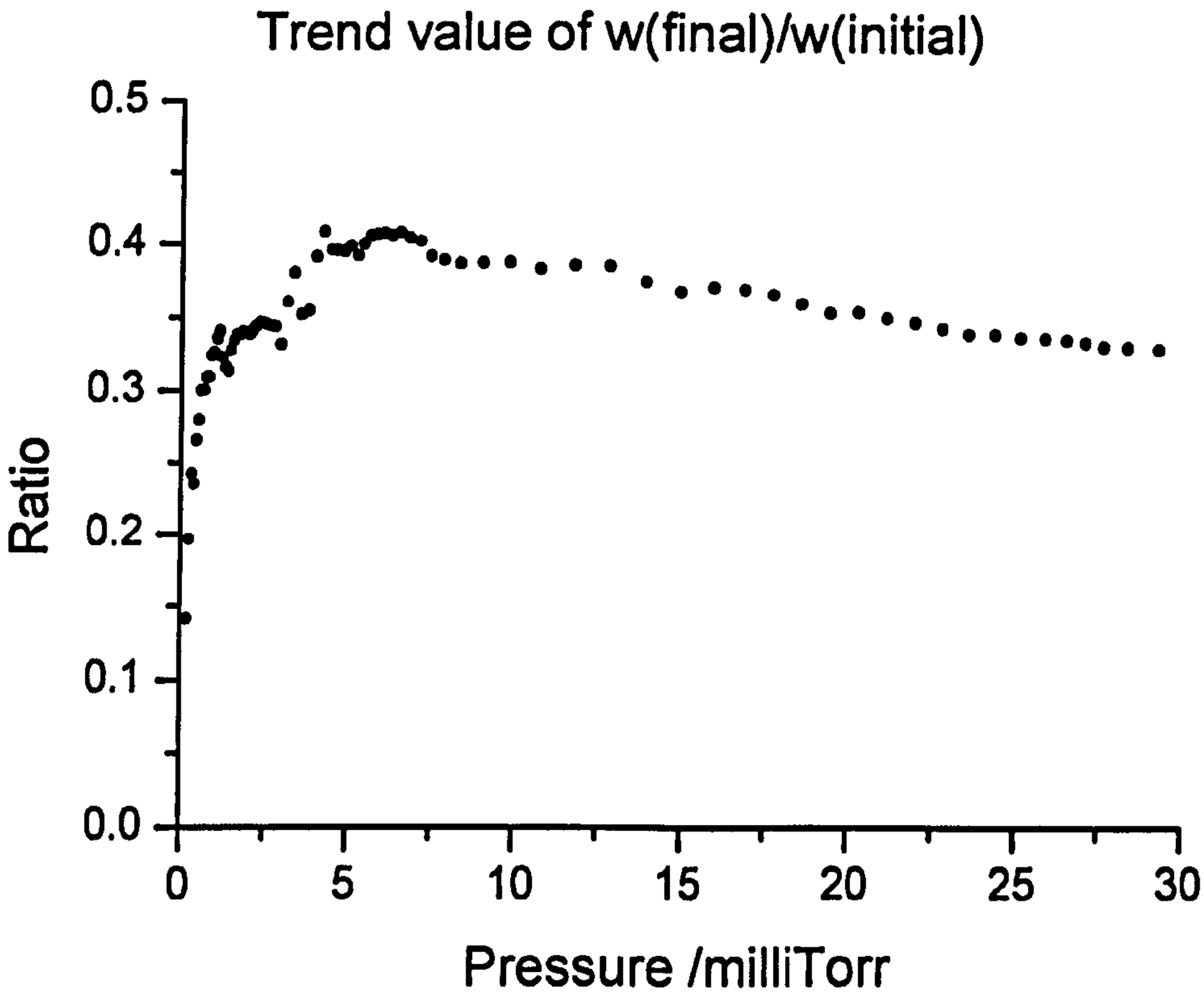

Figure 4.9 – *The pressure evolution of the trend of w(final)/w(initial).*

The ratio climbs rapidly initially before peaking at around 6milliTorr and then begins to decrease slowly. The ratio is approximately 0.4 at 6milliTorr. This leads to a value of $\Omega/\frac{dv}{dt}$ of about 0.24. The Rabi frequency of the system is 128MHz at 1milliTorr and 144MHz at 6milliTorr. The R(1,1) Ammonia transition is one of the strongest transitions known. This phenomenon has also been seen in much weaker transitions.

4.4 Power Saturation and Rapid Passage

So far we have only considered the rapid passage and self focussing phenomena. According to the Beer-Lambert law the absorption of light is a linear function of the number of molecules absorbing the light. This only applies when the light probing the sample does not change the state of the molecules. This is not the case in Rapid Passage

when a large percentage of the ground state population is moved to the upper state. As shown previously in this work this percentage can be as high as 40%. In this situation we see power saturation effects. Power saturation means that the absorbing signal is less than one would expect given the number of absorbing molecules and the path length of the system. One of the best examples of power saturation seen in this work occurs in Ethylene. Figure 4.10 shows three spectra recorded of Ethylene at the pressures 17.8milliTorr, 22.9milliTorr and 28.5millTorr using the 10μm laser.

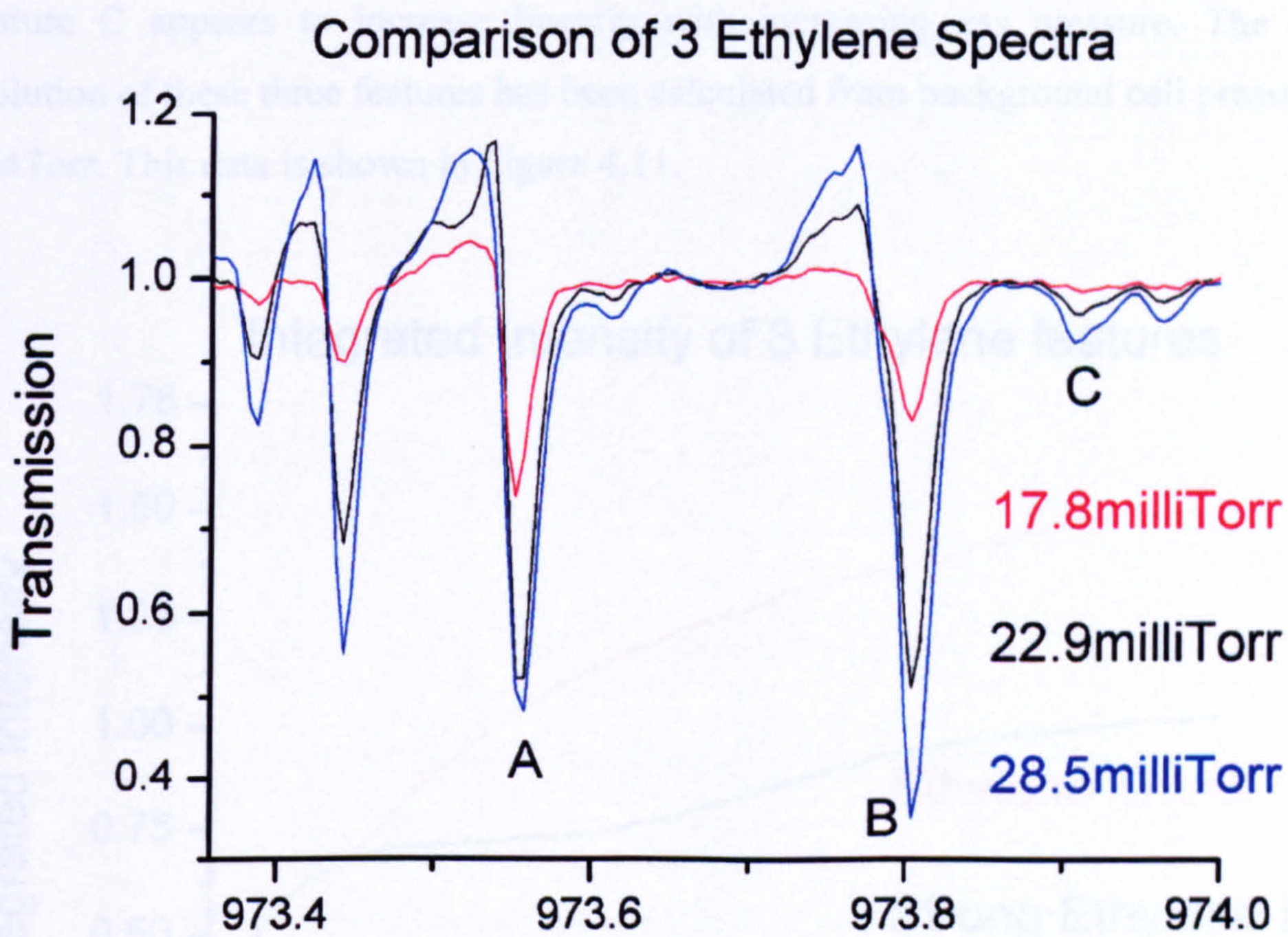

Figure 4.10 – *The Black trace shows the 22.9milliTorr Ethylene spectrum. The Red trace shows the 17.8milliTorr Ethylene spectrum. The Blue trace shows the 28.5milliTorr Ethylene spectrum.*

The three spectra were recorded using the 66m astigmatic Herriott cell. The 10μm laser was driven with a 5A drive current. The pulse width was set to 140ns and the pulse repetition rate was 5KHz. The substrate temperature of the laser was maintained at -

1.52°C. The three features A, B and C show different behaviour as the gas pressure increases. Feature A is a triplet of lines 973.81618cm^{-1}, 973.80516cm^{-1} and 973.78698cm^{-1}. The transition dipole moment of the three lines is 0.111D, 0.128D and 0.127D. Feature B is a single strong line at 973.55204cm^{-1} with a transition dipole moment of 0.14D. Feature C is a single weak line at 973.9101cm^{-1}. It can be seen that feature B starts weaker than feature A but overtakes feature A as the gas pressure increases. This is evidence for power saturation. The single strong line of feature A power saturates at a quicker rate than the three slightly weaker lines of feature B. Feature C appears to increase linearly with increasing gas pressure. The pressure evolution of these three features has been calculated from background cell pressure up to 0.04Torr. This data is shown in Figure 4.11.

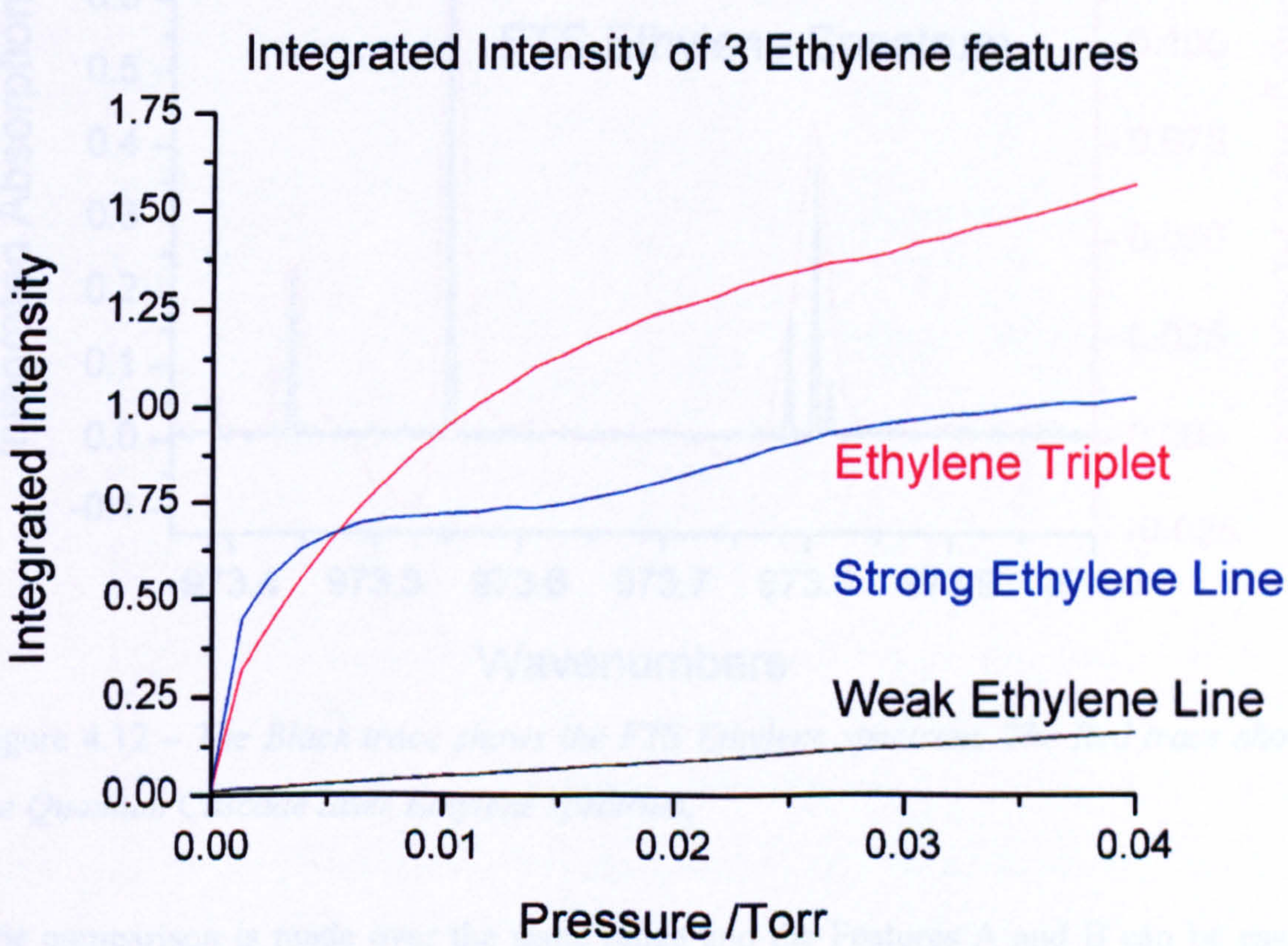

Figure 4.11 – *The Black trace shows the integrated intensity of Feature C. The Red trace shows the integrated intensity of Feature B. The Blue trace shows the integrated intensity of Feature A.*

The different rates of saturation for the features A and B can be easily seen. The evolution of feature C is linear with pressure to within 0.2% over the range of pressures shown. An FTS Ethylene spectrum provided by Blake et al [11] is compared to the 17.8milliTorr Quantum Cascade laser spectrum. The resolution of the FTS was set to $0.002cm^{-1}$. The pressure of Ethylene used was 4.98Torr in a 15cm single pass optical cell. The comparison is shown in Figure 4.12.

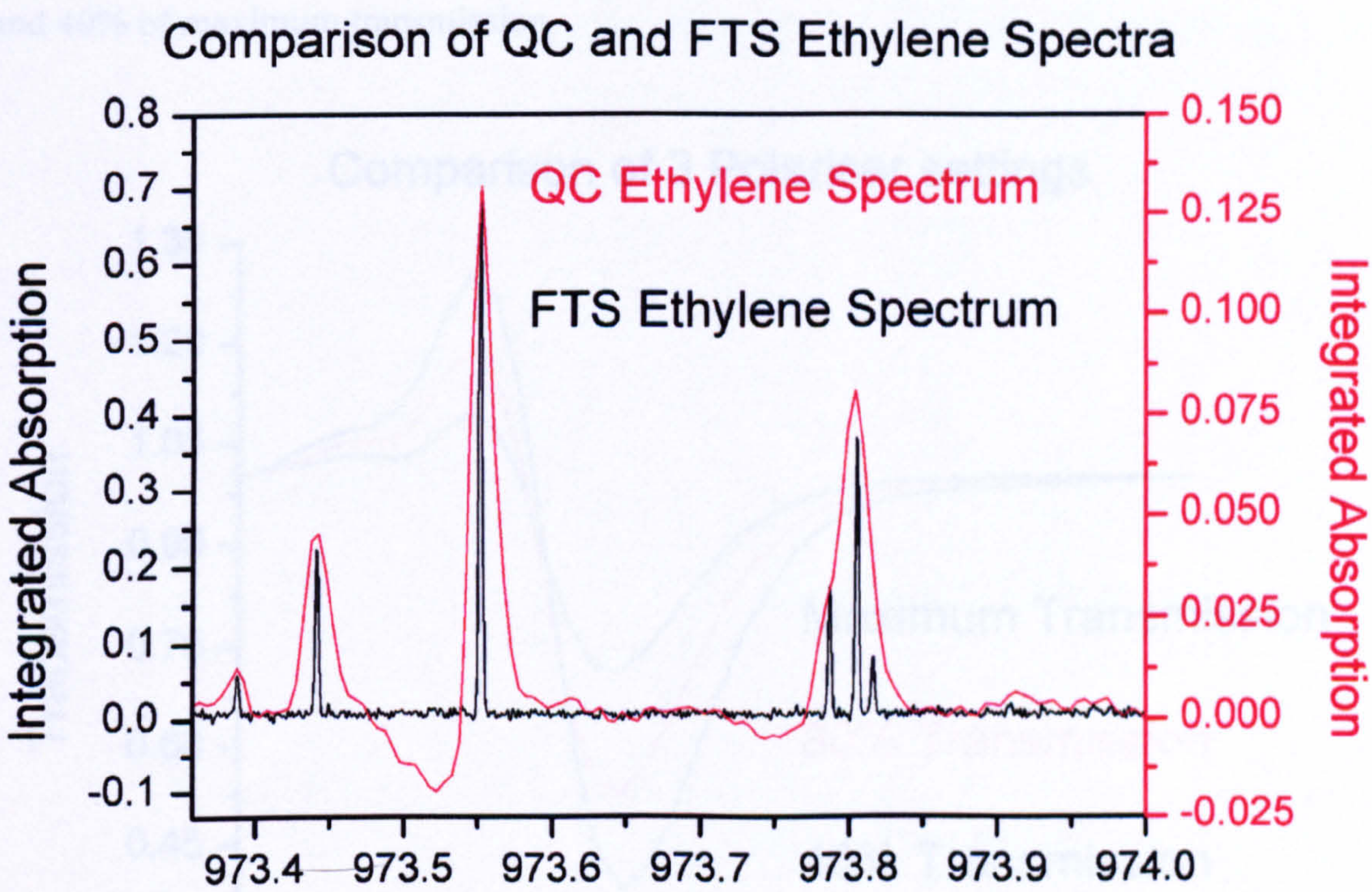

Figure 4.12 – *The Black trace shows the FTS Ethylene spectrum. The Red trace shows the Quantum Cascade laser Ethylene spectrum.*

The comparison is made over the same range and the Features A and B can be easily seen. Feature C can also be seen. Both spectra have been converted into absorbance spectra from transmission spectra.

In order to control the effects of power saturation a polariser was introduced into the beam to cut the power of the laser before it entered the optical cell. An experiment was carried out at 8μm on Nitrous Oxide to see the effect of cutting the power on the signals seen. The laser was driven with a current of 3.5A. The pulse width of the laser was 1270ns and the repetition rate of the laser was 20KHz. The substrate temperature of the laser was maintained at +3°C. The spectrum of Nitrous Oxide was recorded with several different polariser settings. Figure 4.13 shows the three spectra recorded of Nitrous Oxide that correspond to the maximum transmission, 80% of maximum transmission and 40% of maximum transmission.

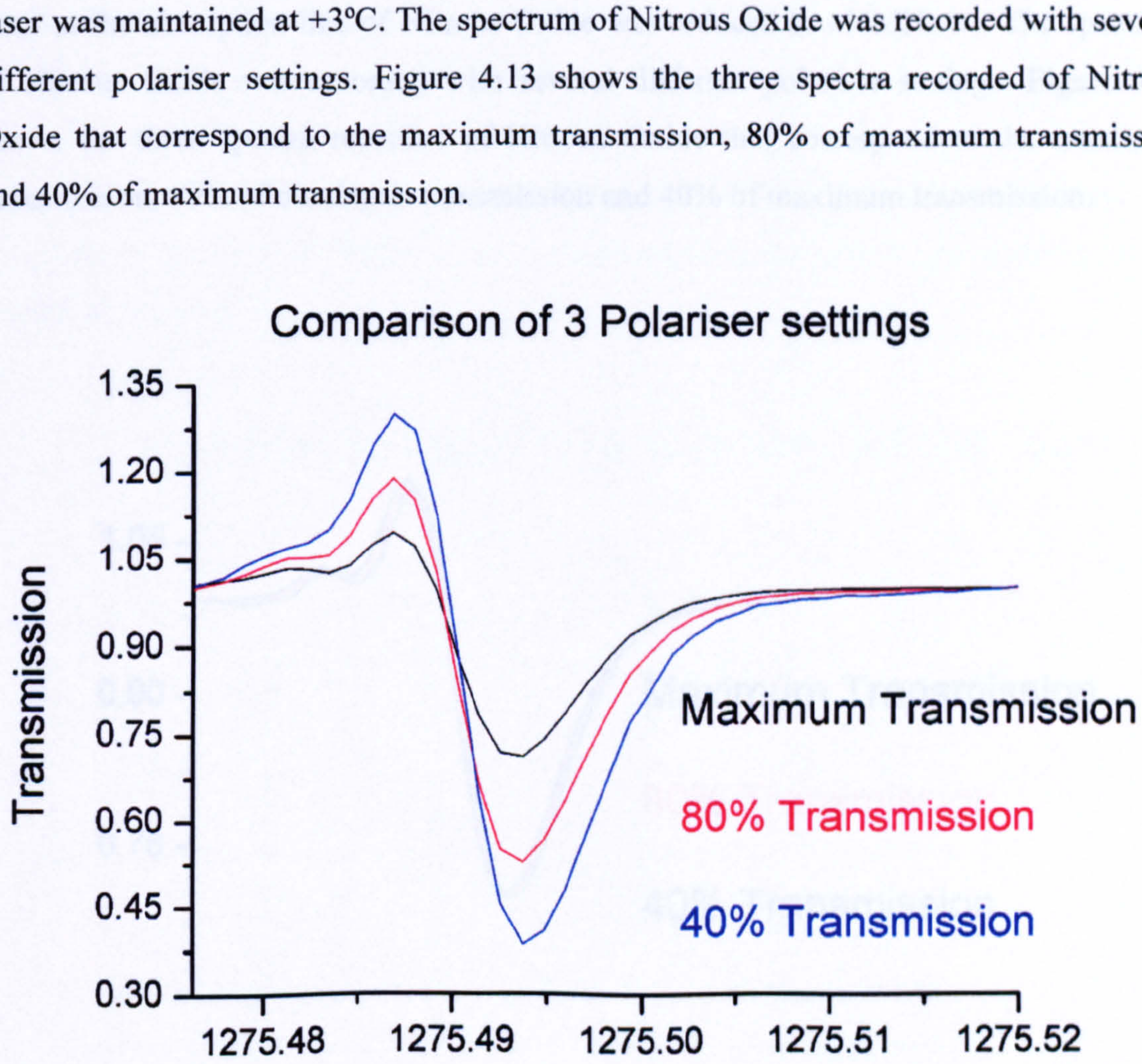

Figure 4.13 – *The Black trace shows the spectrum of Nitrous Oxide with maximum transmission. The Red trace shows the spectrum of Nitrous Oxide with 80% transmission. The Blue trace shows the spectrum of Nitrous Oxide with 40% transmission.*

It can be seen that as the power of the laser is decreased the absorption and overshoot signals increase. The chirp rate of the laser for these experiments at the absorption line shown is -68MHz/ns. The output power of the laser is approximately 250mW. The experiment was repeated with a reduced drive current of 3A. This reduced the initial laser power to approximately 70% of the previous laser power. The chirp rate of the laser at the absorption line of Nitrous Oxide was reduced to -44MHz/ns. The spectrum of Nitrous Oxide was recorded with several different polariser settings. Figure 4.14 shows the three spectra recorded of Nitrous Oxide that correspond to the maximum transmission, 80% of maximum transmission and 40% of maximum transmission.

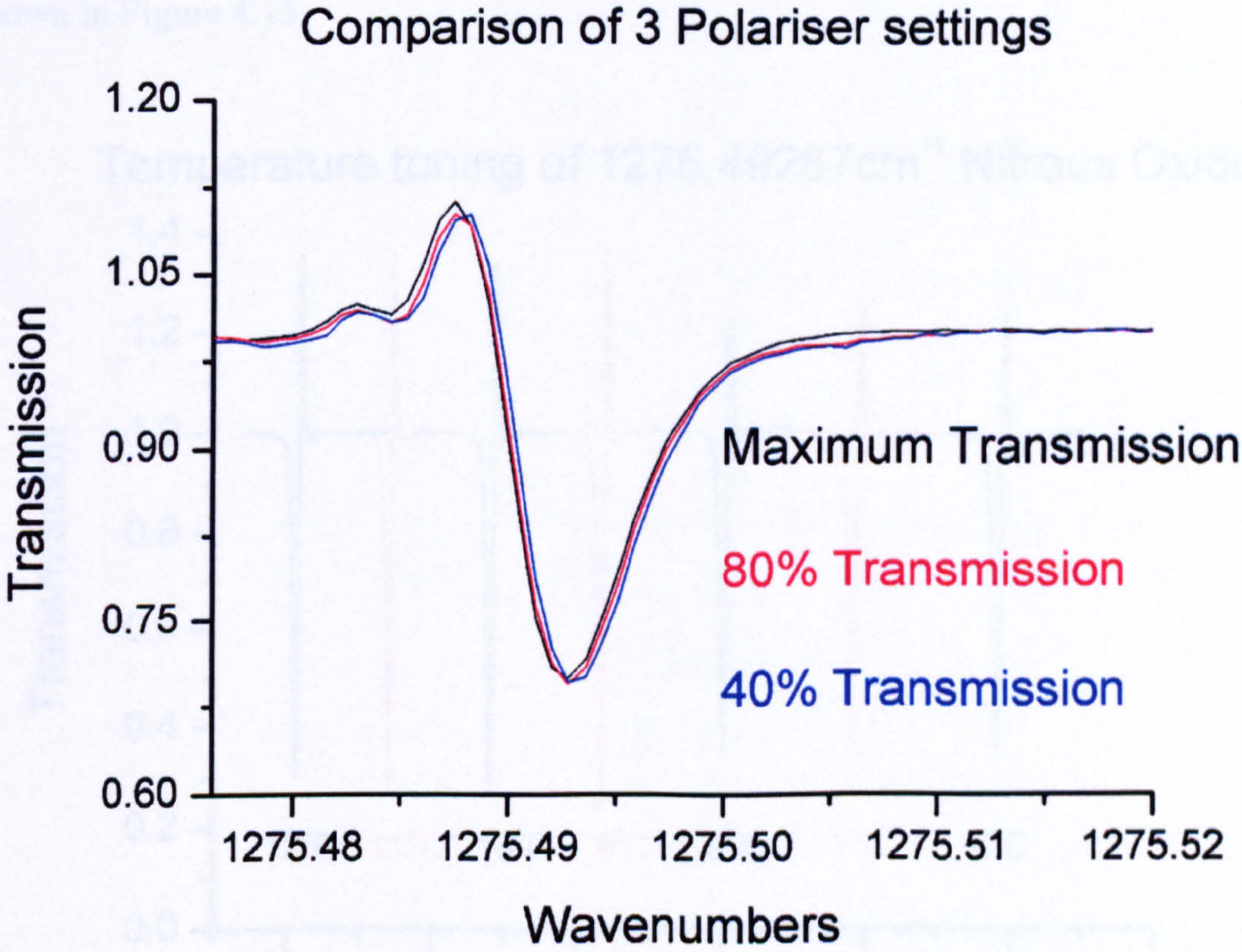

Figure 4.14 – *The Black trace shows the spectrum of Nitrous Oxide with maximum transmission. The Red trace shows the spectrum of Nitrous Oxide with 80% transmission. The Blue trace shows the spectrum of Nitrous Oxide with 40% transmission.*

By reducing the initial laser power and the chirp rate the power of the saturation of the absorption line is not changing over the power change shown. In the 115m astigmatic Herriott cell the 1275.49287cm^{-1} line of Nitrous Oxide, which has a line intensity of 1.41E^{-19}cm^{-1}molecule^{-1}, has been studied. By driving the laser with a current of 2.4A the temperature of the substrate was varied from +6°C to +12°C in 1°C steps. The pulse width of the laser was 1400ns and the pulse repetition rate was 10KHz. For each of the temperatures the spectrum of Nitrous Oxide was recorded at the same pressure of approximately 7.5milliTorr. The power of the laser was the same at the point on the pulse of the Nitrous Oxide line to within 5% over the temperature range tuned. The spectrum of the 1275.49287cm^{-1} line of Nitrous Oxide for each of the temperatures is shown in Figure 4.15.

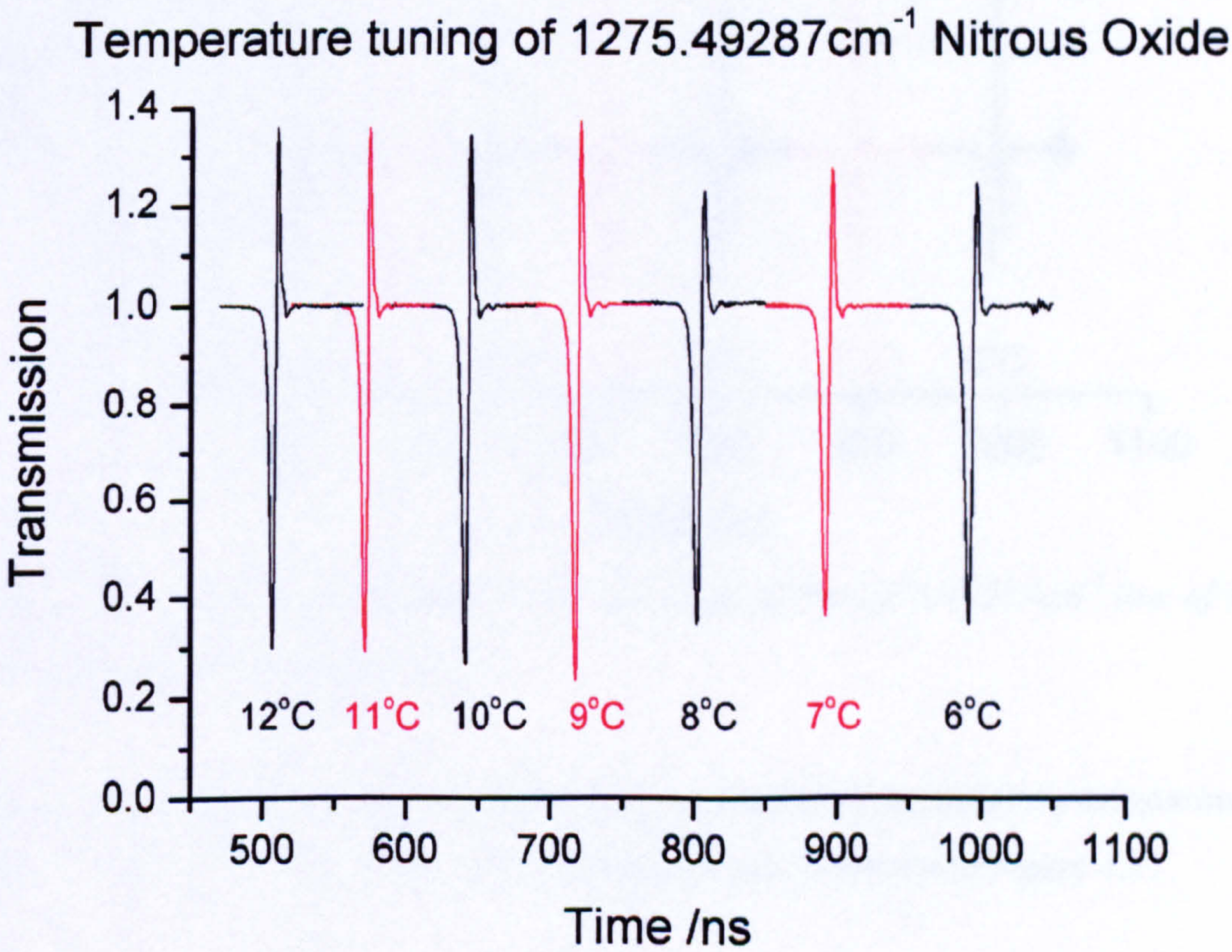

Figure 4.15 – *The spectrum of the 1275.49287cm^{-1} line of Nitrous Oxide for each of the temperatures.*

The spectra were recorded at different times and the difference in the size of the signal is a combination of the non linear processes and errors in pressure monitoring. In the raw transmission data the wiggles are difficult to observe. By differentiating the traces the wiggles can be made more apparent. Figure 4.16 shows the differential signal of the 1275.49287cm^{-1} line of Nitrous Oxide for each of the laser temperatures.

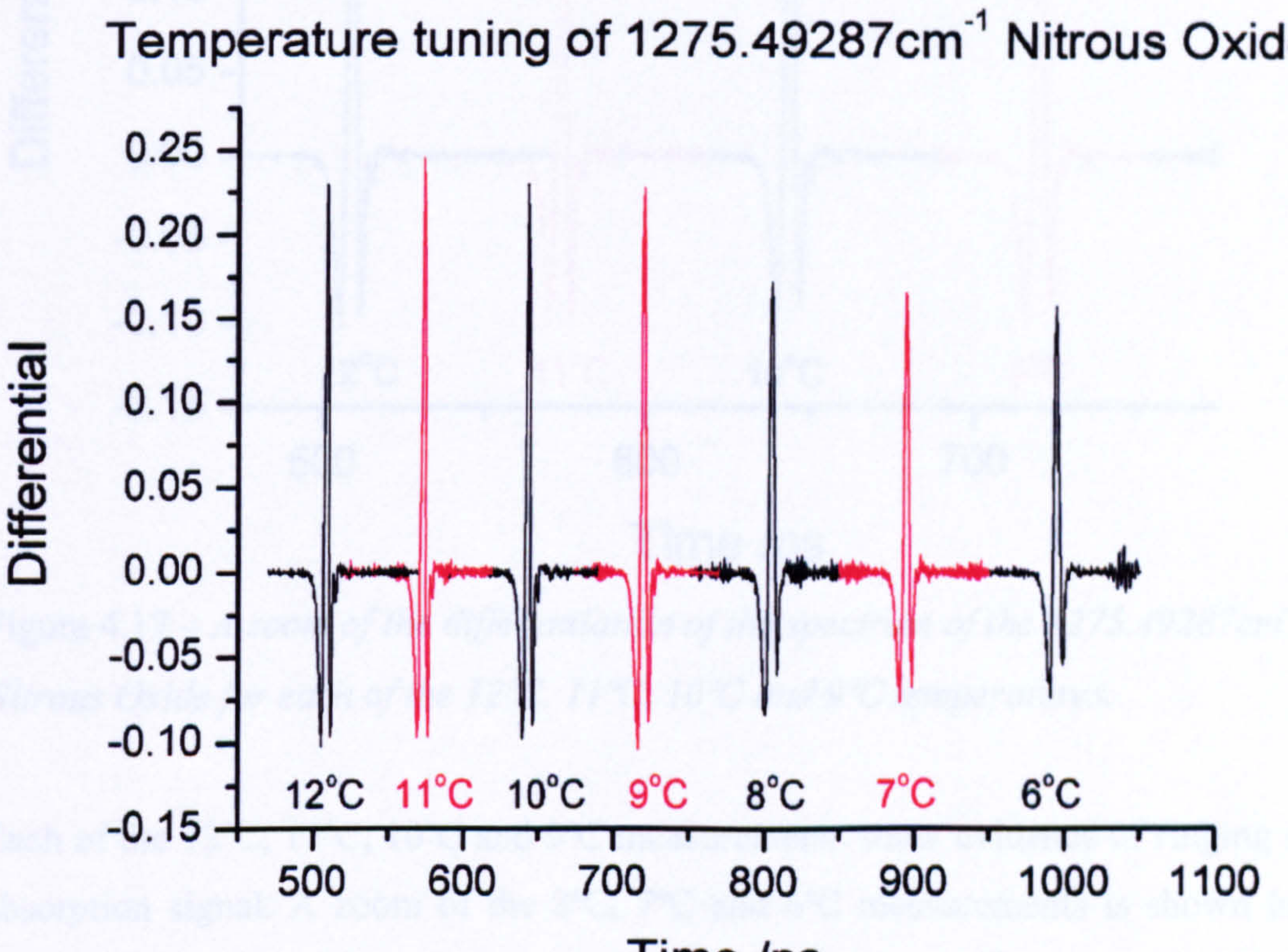

Figure 4.16 – *The differentiation of the spectrum of the 1275.49287cm^{-1} line of Nitrous Oxide for each of the temperatures.*

The wiggles after the absorption can be seen on the higher temperature measurements. A zoom of the 12°C, 11°C, 10°C and 9°C measurements is shown in Figure 4.17.

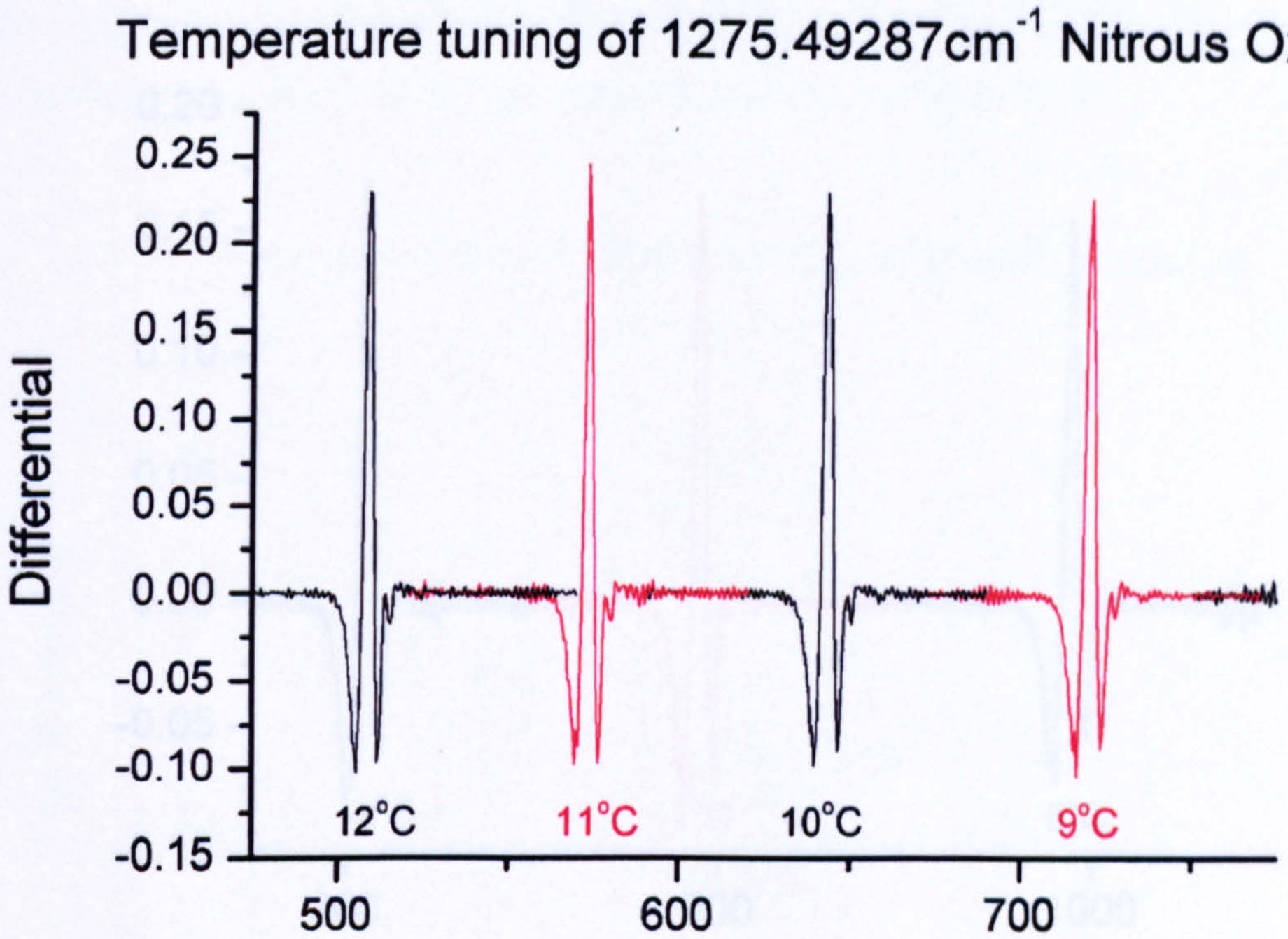

Figure 4.17 – *A zoom of the differentiation of the spectrum of the 1275.49287cm^{-1} line of Nitrous Oxide for each of the 12°C, 11°C, 10°C and 9°C temperatures.*

Each of the 12°C, 11°C, 10°C and 9°C measurements show evidence of ringing after the absorption signal. A zoom of the 8°C, 7°C and 6°C measurements is shown in Figure 4.18.

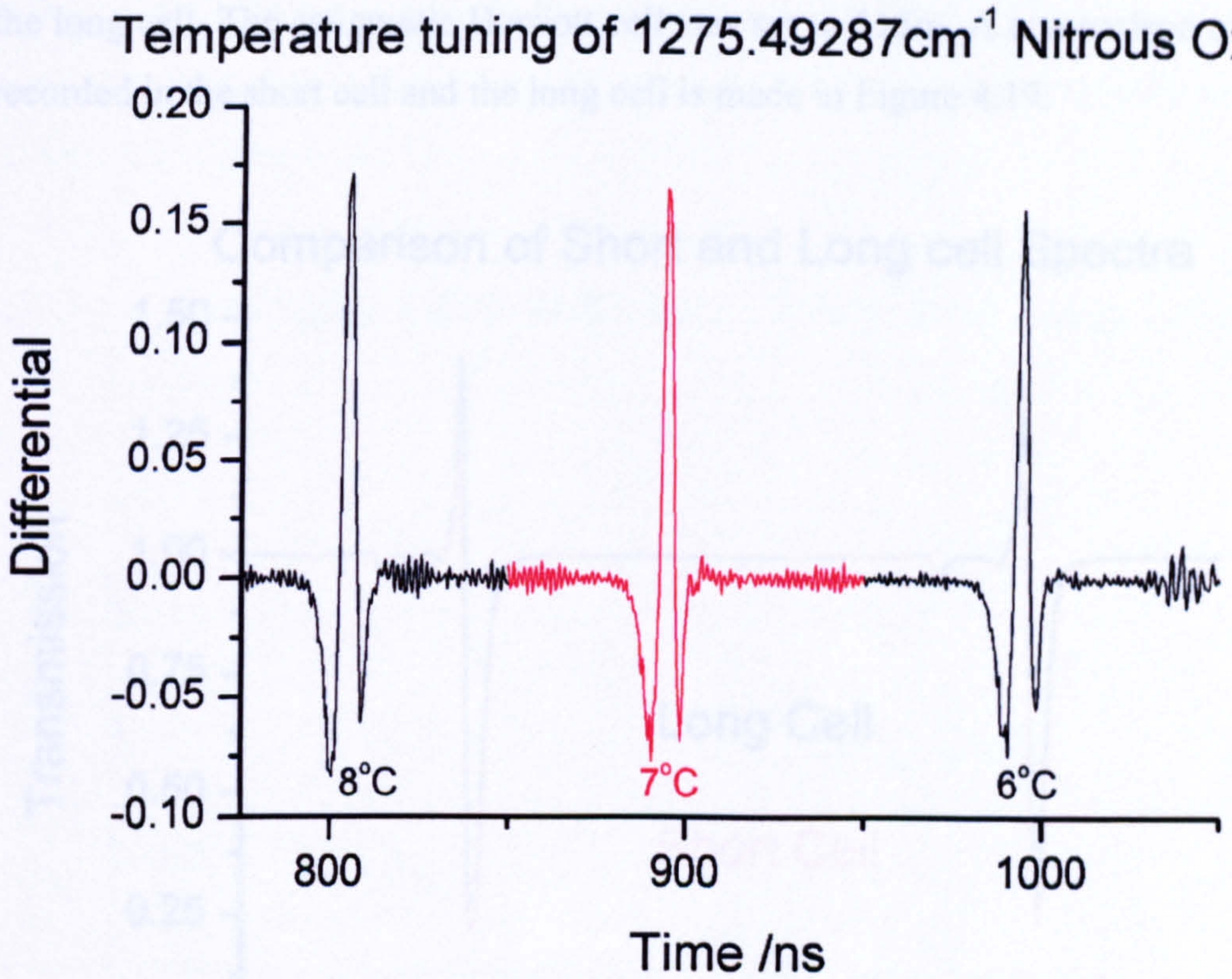

Figure 4.18 – *A zoom of the differentiation of the spectrum of the 1275.49287cm^{-1} line of Nitrous Oxide for each of the 8°C, 7°C, and 6°C temperatures.*

The 6°C measurement shows no sign of ringing and is close to the -20MHz/ns simulation by Langford. This measurement shows the conditions in the system are approaching those of the adiabatic limit[4]. So far the power of the laser and the chirp rate of the laser have been altered to see the effects on the overshoot signals seen. The effect of altering the pathlength used has been studied. To compare the results of the long pathlength astigmatic Herriott cell a single pass 10cm cell was introduced into the optical path. The astigmatic Herriott cell was left in place and used as an optical delay line, as its original design. By using the 8μm laser with a drive current 3.5A and pulse width 1500ns the spectrum of Methane has been studied in the Long and Short cells. The repetition rate was 20KHz and the substrate temperature of the laser was maintained at 3°C. The short pathlength cell measurements pressures were scaled up to the pressures of

the long cell. The astigmatic Herriott cell was set to 115m. A comparison of the spectra recorded in the short cell and the long cell is made in Figure 4.19.

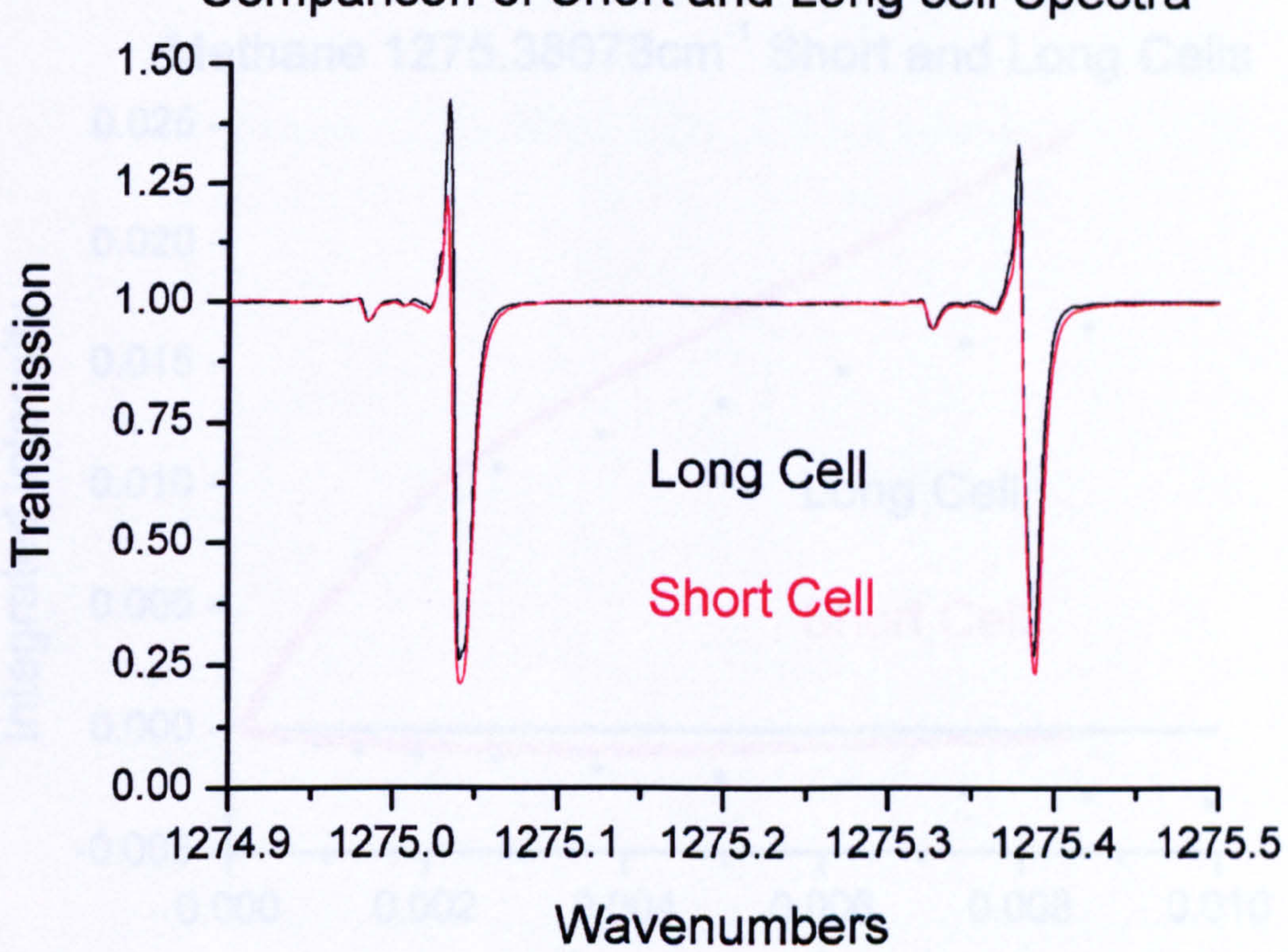

Figure 4.19 – *The Black trace shows the spectrum of Methane recorded in the astigmatic Herriott cell. The Red trace shows the spectrum of Methane recorded in the short cell.*

The astigmatic Herriott cell spectrum was recorded with a pressure of 3.75milliTorr of Methane and the short cell spectrum was recorded with a pressure of 4.34Torr of Methane. When scaled, using the 115m to 10cm pathlength conversion, the 4.34Torr in the short cell becomes the equivalent in the astigmatic Herriott cell of 3.78milliTorr. The amount of absorption for the equivalent pressures in the two cells is greater in the short cell for the two strong lines shown. The size of the overshoot is less for the short cell than the astigmatic cell. However the amount of absorption for the weaker lines to the left of each of the main lines appears to be the same to within the error of the pressure readings. The pressure evolution of the 1275.38678cm^{-1} line of Methane has been

looked at for both the astigmatic Herriott cell and the short cell. The short cell pressures have been scaled up to the equivalent pressures in the astigmatic Herriott cell. This data is shown in Figure 4.20.

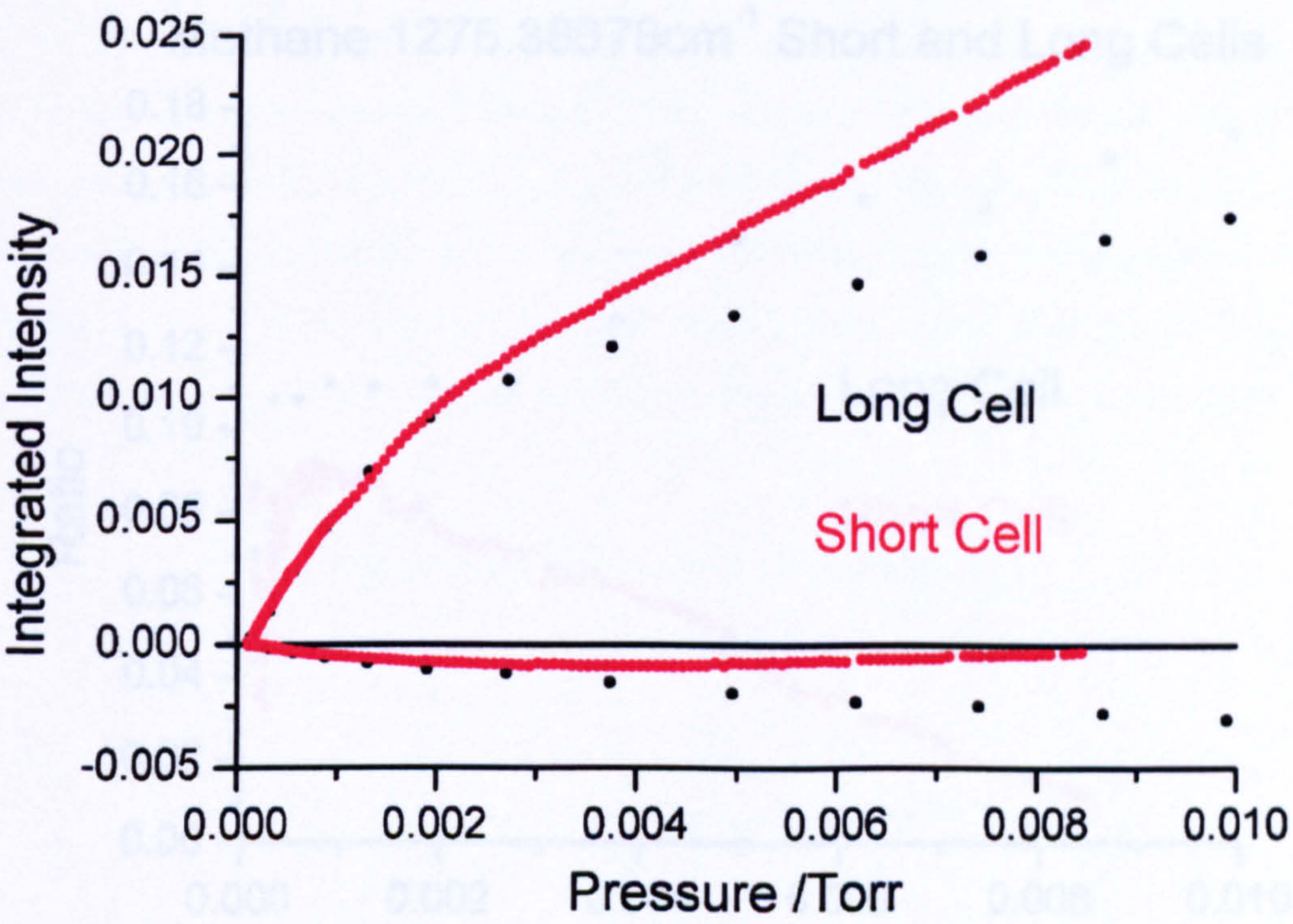

Figure 4.20 – *The Black traces show the absorption and overshoot integrated intensities for the astigmatic Herriott cell. The Red traces show the absorption and overshoot integrated intensities for the short cell.*

Over the first 2milliTorr the signals overlap quite well, however after 2milliTorr the increased power saturation in the astigmatic Herriott cell means that the amount of absorption in the two cells is no longer the same at the same equivalent pressure. This is good evidence for the presence of self focusing. In the short cell there is not the pathlength to focus the beam down to get the very high power densities that cause large power saturation in the astigmatic Herriott cell. This also confirms the theory that the self focusing requires there to be a threshold amount of gas to start the self focussing

because both absorption traces are near linear over the first 2milliTorr. The increased collisional dephasing in the short cell will also reduce the power saturation observed. The ratio of Overshoot/Absorption for the astigmatic Herriott cell data and the short cell data has been calculated and is shown in Figure 4.21.

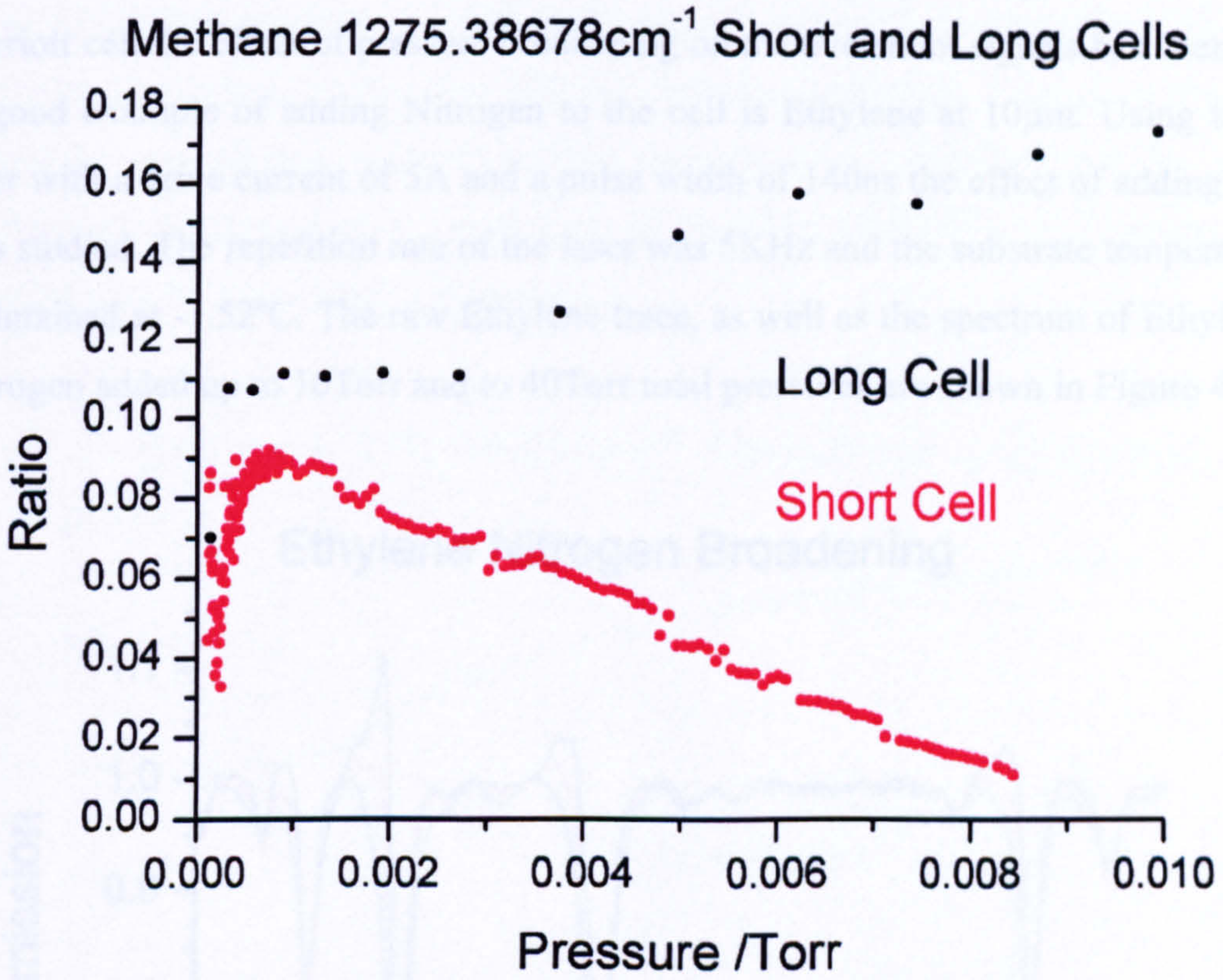

Figure 4.21 – *The Black trace shows the ratio of Observed/Absorption for the astigmatic Herriott cell. The Red trace shows the ratio of Observed/Absorption for the short cell.*

Both the astigmatic Herriott cell and short cell ratios rise initially and the long cell ratio then levels off before slowly climbing again. The short cell ratio quickly reaches a peak and then begins to fall. The peak population transfer for the short cell is approximately 9% whereas in the long cell the population transfer reaches almost double that.

4.5 Nitrogen Broadening and Concentration Retrieval

As well as varying the pathlength of the cell used to make the measurements the gas matrix in which the measurements have been made has been altered to see the effect on the overshoot signals and power saturation. By adding dry nitrogen to the astigmatic Herriott cell the effect of pressure broadening on the overshoot signals has been studied. A good example of adding Nitrogen to the cell is Ethylene at 10μm. Using the 10μm laser with a drive current of 5A and a pulse width of 140ns the effect of adding nitrogen was studied. The repetition rate of the laser was 5KHz and the substrate temperature was maintained at -1.52°C. The raw Ethylene trace, as well as the spectrum of Ethylene with Nitrogen added up to 10Torr and to 40Torr total pressures are shown in Figure 4.22.

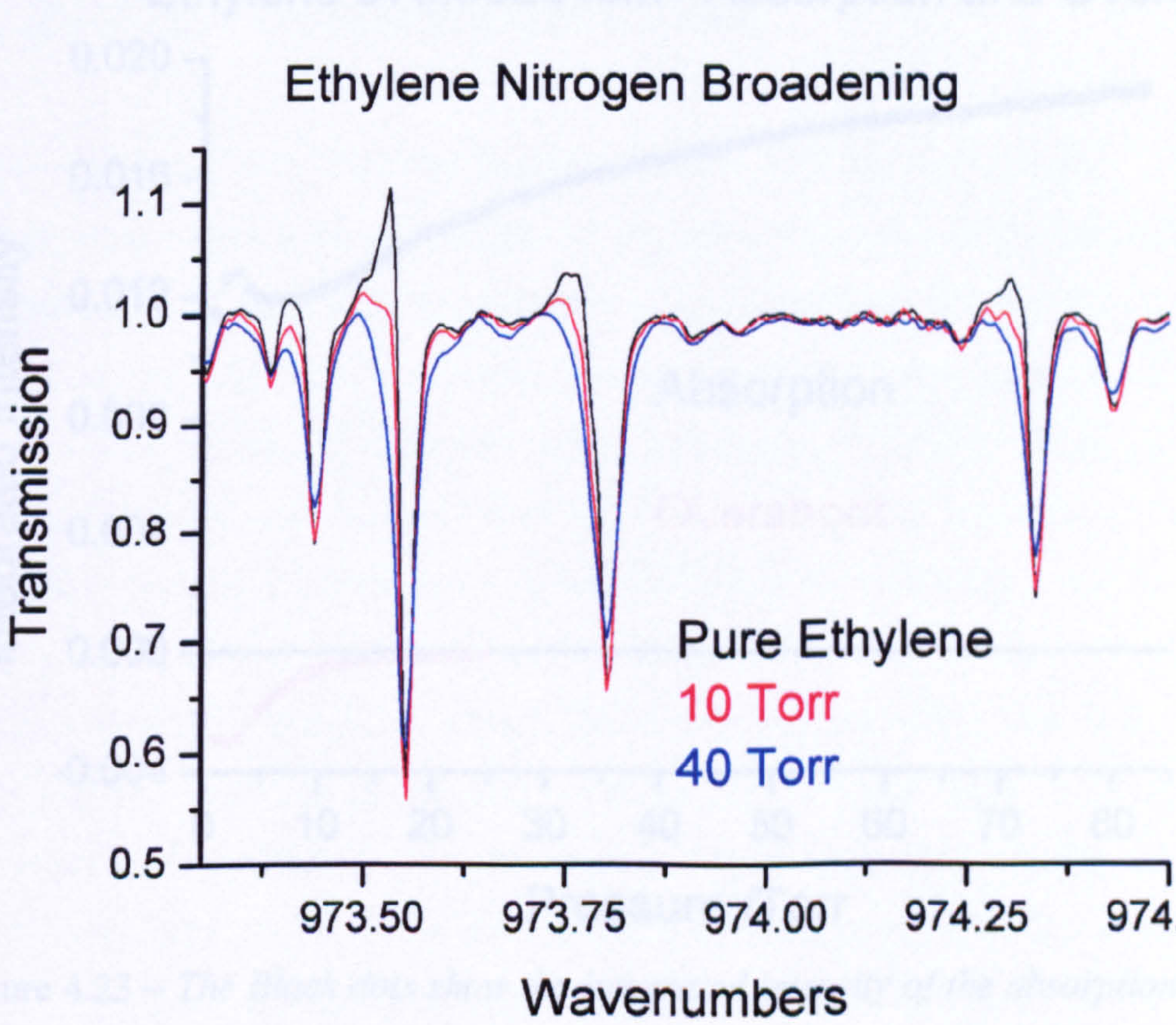

Figure 4.22 – *The Black trace shows the spectrum of pure Ethylene. The Red trace shows the spectrum of Ethylene and Nitrogen up to a total pressure of 10Torr. The Blue trace shows the spectrum of Ethylene and Nitrogen up to a total pressure of 40Torr.*

The overshoot signal can be easily seen on the stronger lines in the pure Ethylene trace of approximately 10milliTorr. At 10Torr the overshoot signals have been suppressed but the line shape is still asymmetric. At 40Torr the line shape is tending towards symmetric. The line does not get symmetrical until almost 100Torr total pressure. As the pressure of Nitrogen increases the upper state lifetime of the transitions of Ethylene decrease. This is because the time between collisions decreases. This gives the system a chance to recover and come back into thermodynamic equilibrium. The integrated intensity of the absorption and overshoot of the 973.55204cm^{-1} with a transition dipole moment of 0.14D is plotted in Figure 4.23.

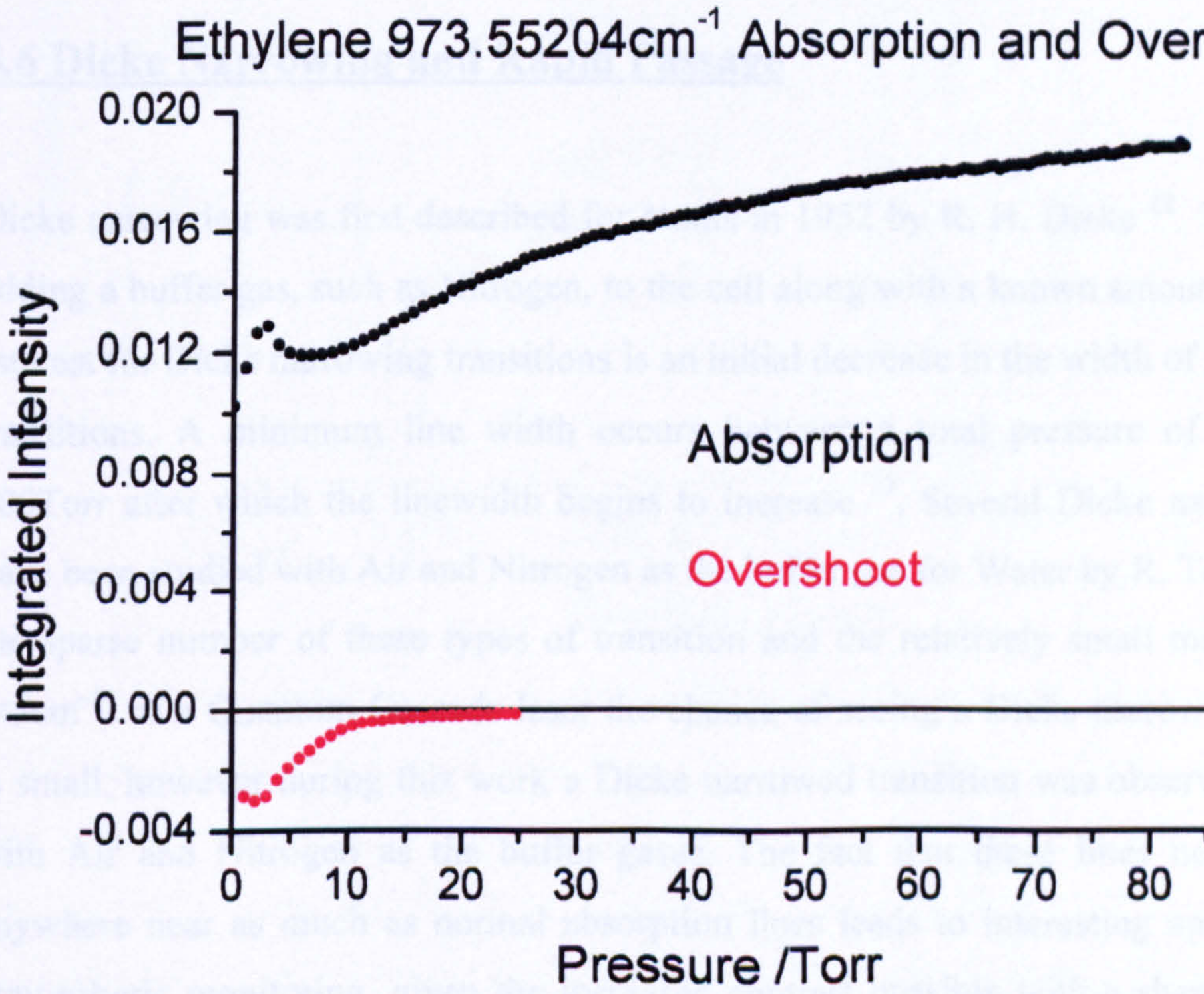

Figure 4.23 – *The Black dots show the integrated intensity of the absorption signal. The Red dots show the integrated intensity of the overshoot signal.*

The overshoot signal is completely removed before 30Torr and the absorption signal tends towards the asymptotic limit corresponding to the actual pressure of Ethylene in the cell. This has consequences when retrieving concentrations in the atmosphere. In order to achieve an accurate retrieval a high background pressure must be used. In the case shown with Ethylene the concentration would be retrieved using a weaker line, which will power saturate less but is still easily visible. In a situation where there are only the stronger lines of the gas are detectable then they must be used. As the power saturation is dependent on the amount of self focusing if the pressure of the gas of interest is lower than the self focusing threshold (<10milliTorr) and the background pressure is high (>40Torr) then the effects of power saturation can be ignored.

4.6 Dicke Narrowing and Rapid Passage

Dicke narrowing was first described for atoms in 1952 by R. H. Dicke [12]. The effect of adding a buffer gas, such as Nitrogen, to the cell along with a known amount of a gas of interest for Dicke narrowing transitions is an initial decrease in the width of the observed transitions. A minimum line width occurs between a total pressure of 50Torr and 200Torr after which the linewidth begins to increase [13]. Several Dicke narrowed lines have been studied with Air and Nitrogen as the buffer gas for Water by R. Toth [14]. Given the sparse number of these types of transition and the relatively small micro window ($<5cm^{-1}$) of a Quantum Cascade laser the chance of seeing a Dicke narrowed transition is small, however during this work a Dicke narrowed transition was observed in Water with Air and Nitrogen as the buffer gases. The fact that these lines never broaden anywhere near as much as normal absorption lines leads to interesting applications in atmospheric monitoring, given the increased contrast possible with a sharp absorption line. The narrowed transition observed occurs at $1276.62619cm^{-1}$ and is a transition from $J=16$, $K_a=1$ and $K_c=16$ in the lower state to $J=15$, $K_a=0$ and $K_c=15$ in the upper state. The other narrowing transitions observed in Water by R. Toth [14] also were transitions from high J, high K_c and low K_a values. The sample of Water used was

contaminated with Nitrous Oxide, which provides a good comparison for the pressure broadening. Water was added to the astigmatic Herriott cell up to a pressure 0.8Torr. Nitrogen was then flowed into the cell at a constant rate up to a total pressure of 600Torr. The spectra of total pressure 10Torr, 50Torr, 100Torr and 200Torr are shown in Figure 4.24.

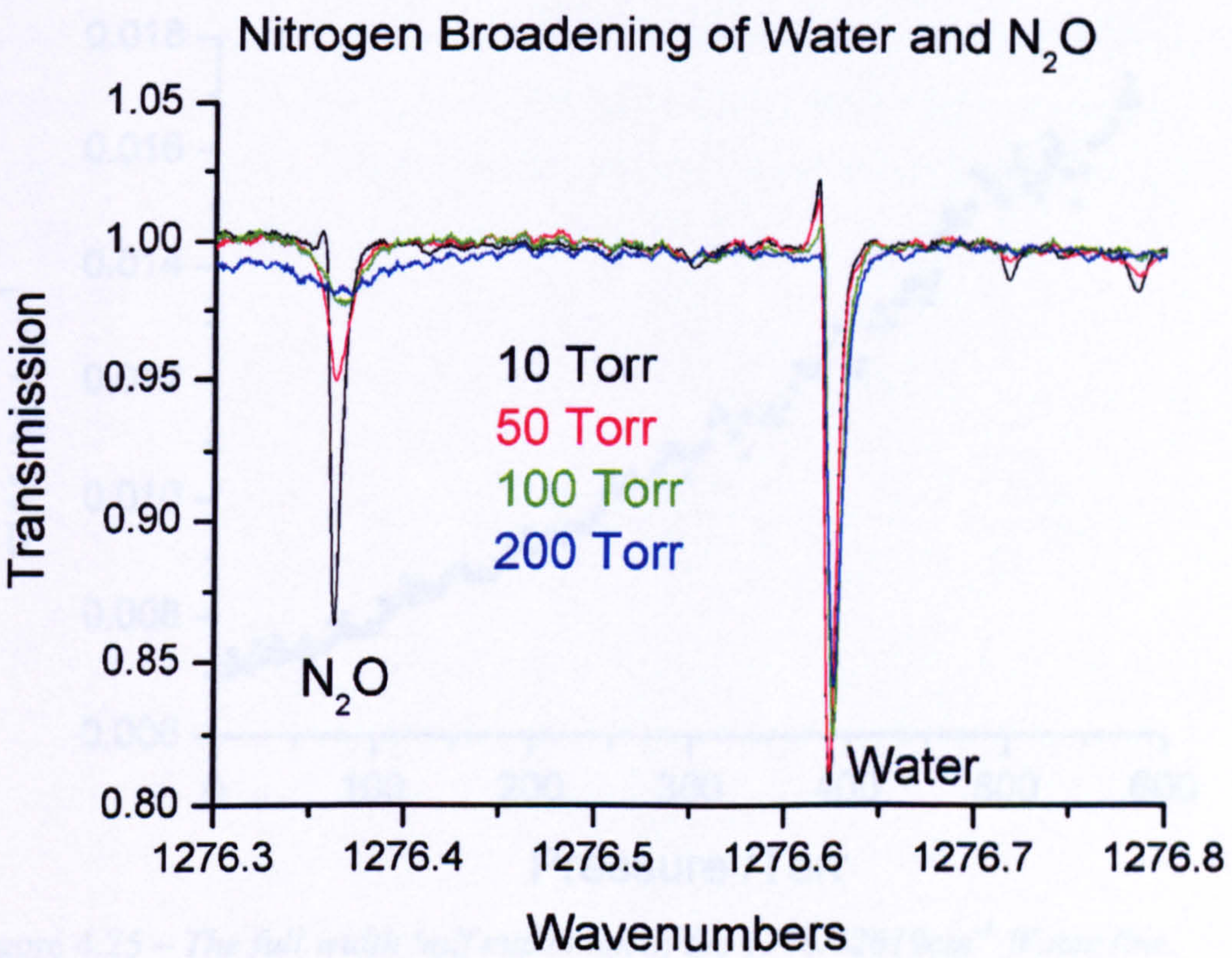

Figure 4.24- *The Black trace shows the spectrum of Nitrous Oxide, Water and Nitrogen at a total pressure of 10Torr. The Red trace shows the spectrum of Nitrous Oxide, Water and Nitrogen at a total pressure of 50Torr. The Green trace shows the spectrum of Nitrous Oxide, Water and Nitrogen at a total pressure of 100Torr. The Blue trace shows the spectrum of Nitrous Oxide, Water and Nitrogen at a total pressure of 200Torr.*

The difference in the pressure broadening is apparent between the Nitrous Oxide and Water. It can also be seen that the overshoot from the Water line is not suppressed until the total pressure is above 100Torr. This is about a factor of 5 to 10 greater pressure than

is required to suppress the overshoot from standard absorption lines. The Water line does not become symmetrical until the total pressure in the cell is above 200Torr. The full width half maximum of the Water line has been calculated for each of the total pressures. This data is shown in Figure 4.25.

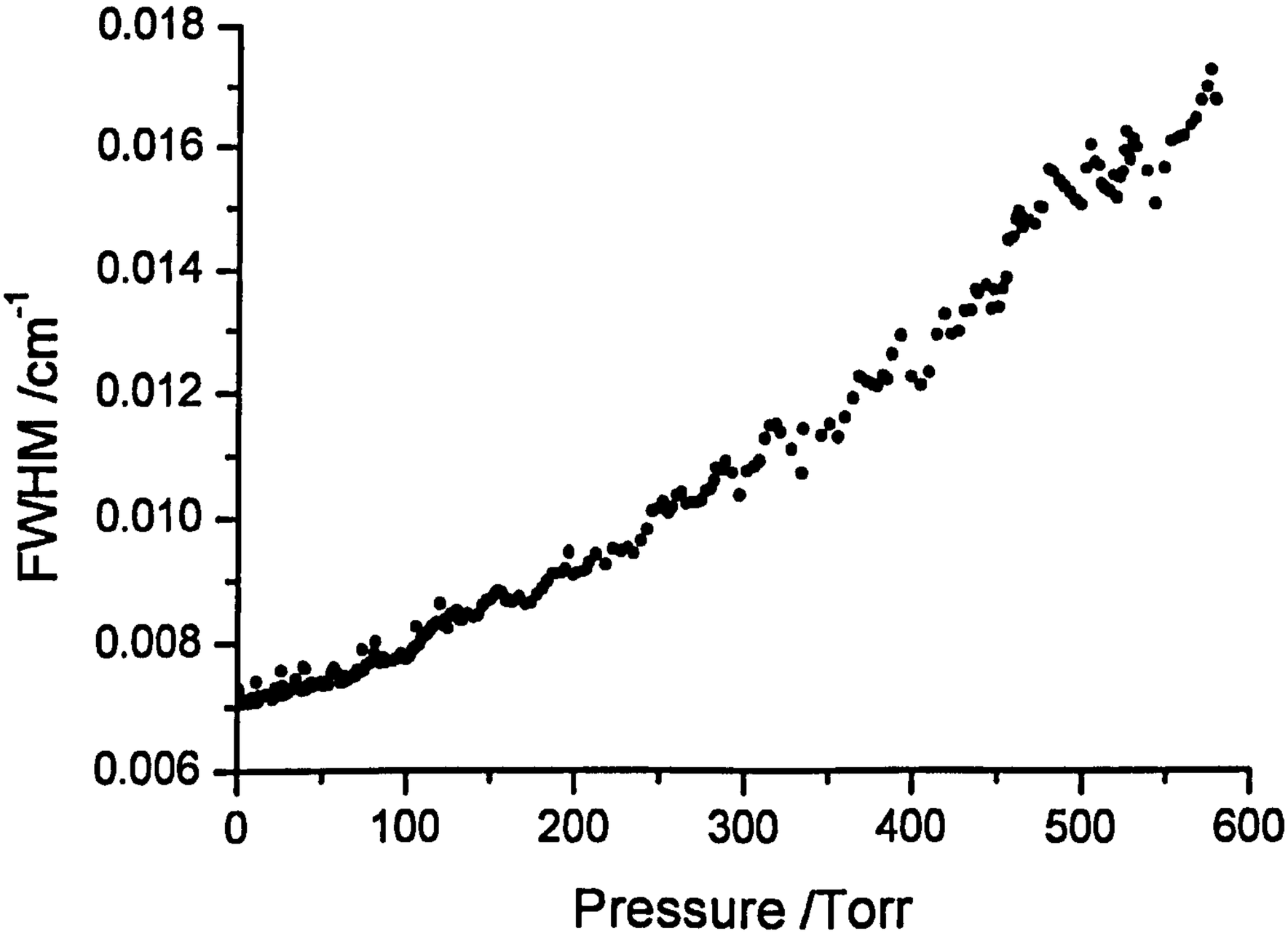

Figure 4.25 – *The full width half maximum of the 1276.62619cm^{-1} Water line.*

From the work by R. S. Eng [13] it is expected that the FWHM of the absorption line will narrow initially before bottoming out and increasing again. From my work the line appears to always increase in width. Due to the resolution of the instrument (~0.007cm^{-1}) the initial decrease in width would not be resolvable.

4.7 Conclusions

Evidence of rapid passage at 8μm and 10μm in polar and non polar molecules has been demonstrated. I have demonstrated evidence of rapid passage in strong and weak absorption lines. By varying the power of the laser using a polariser the effects on the rapid passage signals observed has been studied. The chirp rate of the laser has been varied by temperature tuning the substrate of the laser to observe the change in rapid passage signal. It has been shown that by increasing the background pressure of the cell the effects of power saturation can be removed. I have demonstrated an example of rapid passage of a Dicke narrowed line in Water.

4.8 References

1) Sensitivity Enhancement in Magnetic Resonance, R. R. Ernst, Adv. Mag. Reson., **2**, 1-135, (1936)

2) Coherent Transient Infrared Spectroscopy, R. L. Shoemaker in Laser and Coherence Spectroscopy, ed. J. I. Steinfeld, 197-371, Plenum Press, (1978)

3) Laser Spectroscopy: Basic Concepts and Instrumentation, 3rd ed., W. Demtröder, Springer, (2003)

4) Observation of Population Inversion by Adiabatic Rapid Passage, M. M. T. Loy, Phys. Rev. Letts., **32**, 814-817, (1974)

5) Self-Focussing of Light by Potassium Vapour, D. Grischkowsky, Phys. Rev. Letts., **24**, 16, 866-869, (1970)

6) Self-Defocusing of Light by Adiabatic Following in Rubidium Vapour, D. Grischkowsky and J. A. Armstrong, Phys. Rev. A, **6**, 4, 1566-1570, (1972)

7) Transient Self-Focusing in a Nematic Liquid Crystal in the Isotropic Phase, G. K. L. Wong and Y. R. Shen, Phys. Rev. Letts., **32**, 10, 527-530, (1974)

8) Study of Self-Focusing and Self-Phase-Modulation in the Picosecond-Time Regime, J. Reintjes, R. L. Carman and F. Shimizu, Phys. Rev. A, **8**, 10, 1486-1503, (1973)

9) Population Inversion by Nonadiabatic Frequency Chirping, P. Horwitz, app. Phys. Letts., **26**, 6, 306-308, (1975)

10) Absolute Intensity of the NH_3 ν_2 Band, M. Fabian and K. M. T. Yamada, J. Mol. Spec., **198**, 102, (1999)

11) T. A. Blake, R. L. Sams and S. W. Sharpe, Pacific Northwest National Laboratory, Richland, USA

12) The Effect of Collisions upon the Doppler Width of Spectral Lines, R. H. Dicke, Phys. Rev., **89**, 2, 472-473, (1953)

13) Tunable diode laser spectroscopy of CO_2 in the 10- to 15-μm spectral region—Lineshape and *Q*-branch head absorption profile, R. S. Eng and A. W. Mantz, J. Mol. Spec., 74, 3, 331-344, (1979)

14) Air- and N_2- Broadening Parameters of Water Vapor: 604 to 2271 cm^{-1}, R. A. Toth, J. Mol. Spec., **201**, 218-243, (2000)

5.1 Atmospheric Experiments

5.1.1 Introduction

The Earth's atmosphere has been studied for decades. The interest in studying the planets atmosphere comes from the concern of the effect of man on the environment. With an increase in industrialisation, chemicals have been pumped into our atmosphere at an increasing rate. By probing the atmosphere the impact of these chemicals on the natural levels of the atmospheric gases can be found. Many different techniques have been used to probe the atmosphere, including tunable diode lasers carried in balloons and satellite based instruments looking down through the atmosphere [1,2,3]. As part of this project was funded by the Natural Environmental Research Council (NERC) work has been done to study gases in the atmosphere. I have studied the atmosphere at ground level at 8μm and 10μm. At 8μm I was able to look at ambient Methane, Water and Nitrous Oxide levels and at 10μm I was able to detect the ambient levels of Water and Carbon Dioxide. The ultimate aim of the NERC funded project is to fly a version of my spectrometer on a plane to make measurements of the atmosphere at altitude. This work will be useful as a test for the future development of an airplane based instrument.

5.1.2 Experimental Setup

For a full description of my spectrometer see section 3.1. During the experiments only one laser was used at a time. For the work carried out at 8μm the astigmatic Herriott cell was setup to provide 115m of optical path. At 10μm the astigmatic Herriott cell was configured for 101m of optical path. A full description of the astigmatic Herriott cell can be found in section 2.3. At 10μm the atmosphere of the laboratory was studied. The sample of laboratory atmosphere was drawn into the empty cell directly up to a total pressure of 50Torr. For the first experiment at 8μm the laboratory atmosphere was studied in the same way as in the 10μm experiment. The second 8μm experiment involved sampling the outside atmosphere. This was done using a 2m long hose connected to the cell and dangled out the laboratory window. The laboratory window is

two floors above a car park so any cars entering or leaving the car park may cause fluctuations in the concentrations of the observed gases. The pressure controller was used to regulate the pressure in the cell and the rotary pump was used to draw the atmosphere through the cell. A semi autonomous version of the LabVIEW control program was written to control this experiment. This new control program allowed the instrument to be left on its own to record data for long periods of time. The program controlled the pressure controller so that new background and etalon files could be recorded every ten minutes to improve the signal to noise level. If the experiment was allowed to run for longer than ten minutes without a new background then the change in background shape became to large to correct for in the post processing of data. The time taken to record the new background and etalon was about one minute, which was due to the time taken to pump out the cell, record the data and then allow the cell to go back up to the 50Torr running level and stabilise. The time of each spectrum was logged to allow the data to be displayed as a function absolute time rather than relative time. With this new control program the only human interaction required was the filling of the detector with liquid nitrogen every six hours. A switch to a thermo electrically cooled detector would have allowed the system to run indefinitely without user interaction.

5.1.3 Results – 10μm

The 10μm QC laser was driven with a 5A drive current. The pulse width of the laser was 232ns with a pulse repetition rate of 5KHz. The substrate temperature of the laser was maintained at -1.52°C. Each of the spectra recorded was an average of 64000 pulses. The spectrum of the laboratory atmosphere at 50Torr is shown in Figure 5.1.1.

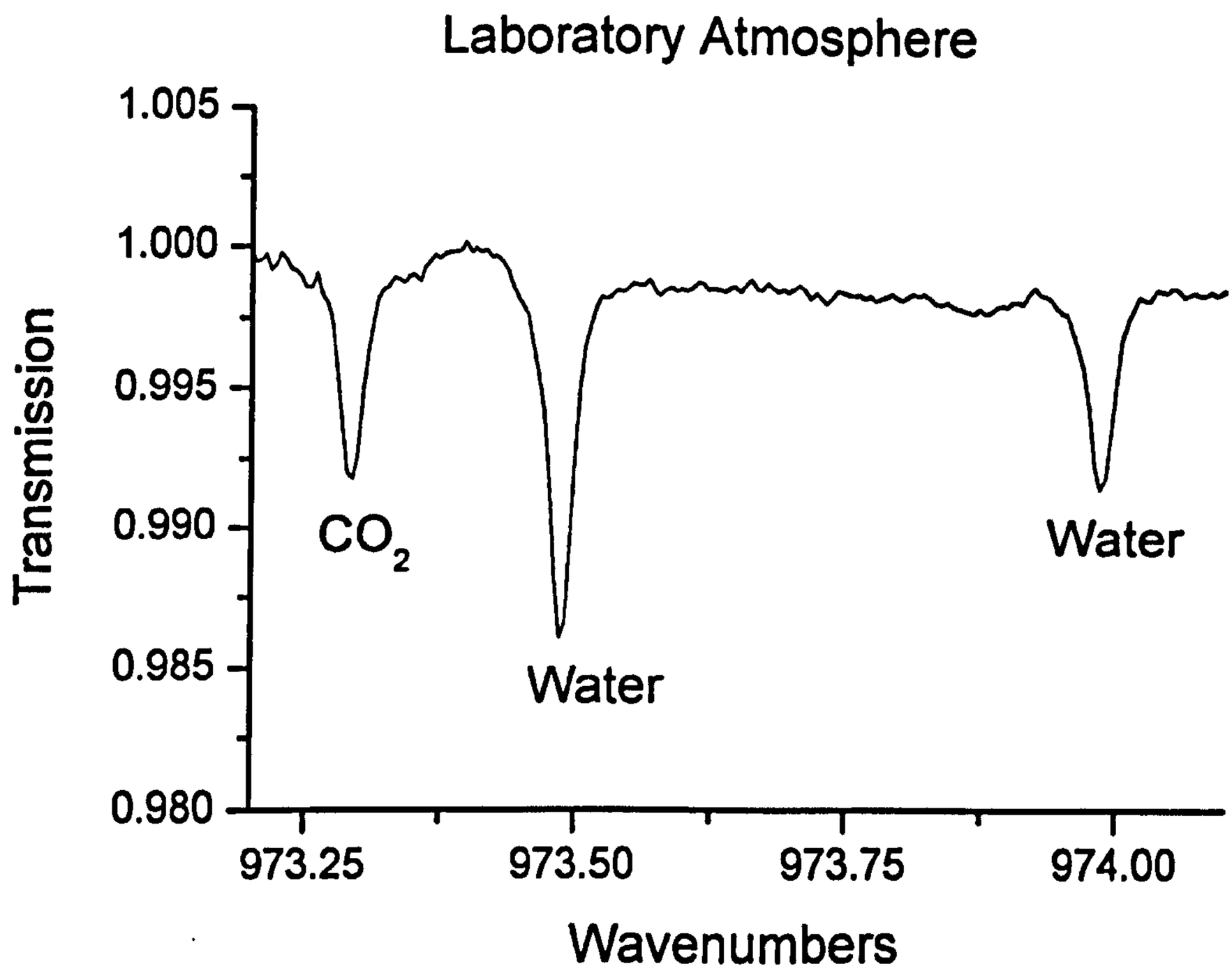

Figure 5.1.1 – *The spectrum of the laboratory atmosphere.*

The spectrum extends from 972.5cm^{-1} to 974.5cm^{-1} however only the three absorption lines shown are present in the spectrum. By using the concentration retrieval technique described in section 3.1 the concentrations of the Water and Carbon Dioxide gases has been calculated. The concentration of Carbon Dioxide was found to be 553ppmv, which compares to the year 2000 global Carbon Dioxide concentration of 369.4ppmv [4]. The elevated Carbon Dioxide levels in the laboratory can be explained by the poor ventilation and the presence of two humans producing Carbon Dioxide. The concentration of Water was found to 0.8% compared to the global Water concentrations of between 0-4% [4]. The water concentration was a calculated average of the two lines in the spectrum.

5.1.4 Results – 8μm

For the first experiment, involving sampling of the laboratory atmosphere, the 8μm QC laser was driven with a 3.5A drive current. The pulse width of the laser was set to 1500ns with a pulse repetition rate of 20KHz. The substrate temperature of the laser was maintained at a constant +3°C. Each of the spectra recorded is an average of 20000 pulses. The laboratory atmosphere was added up to a pressure of 50Torr. The spectrum of the laboratory is shown in Figure 5.1.2.

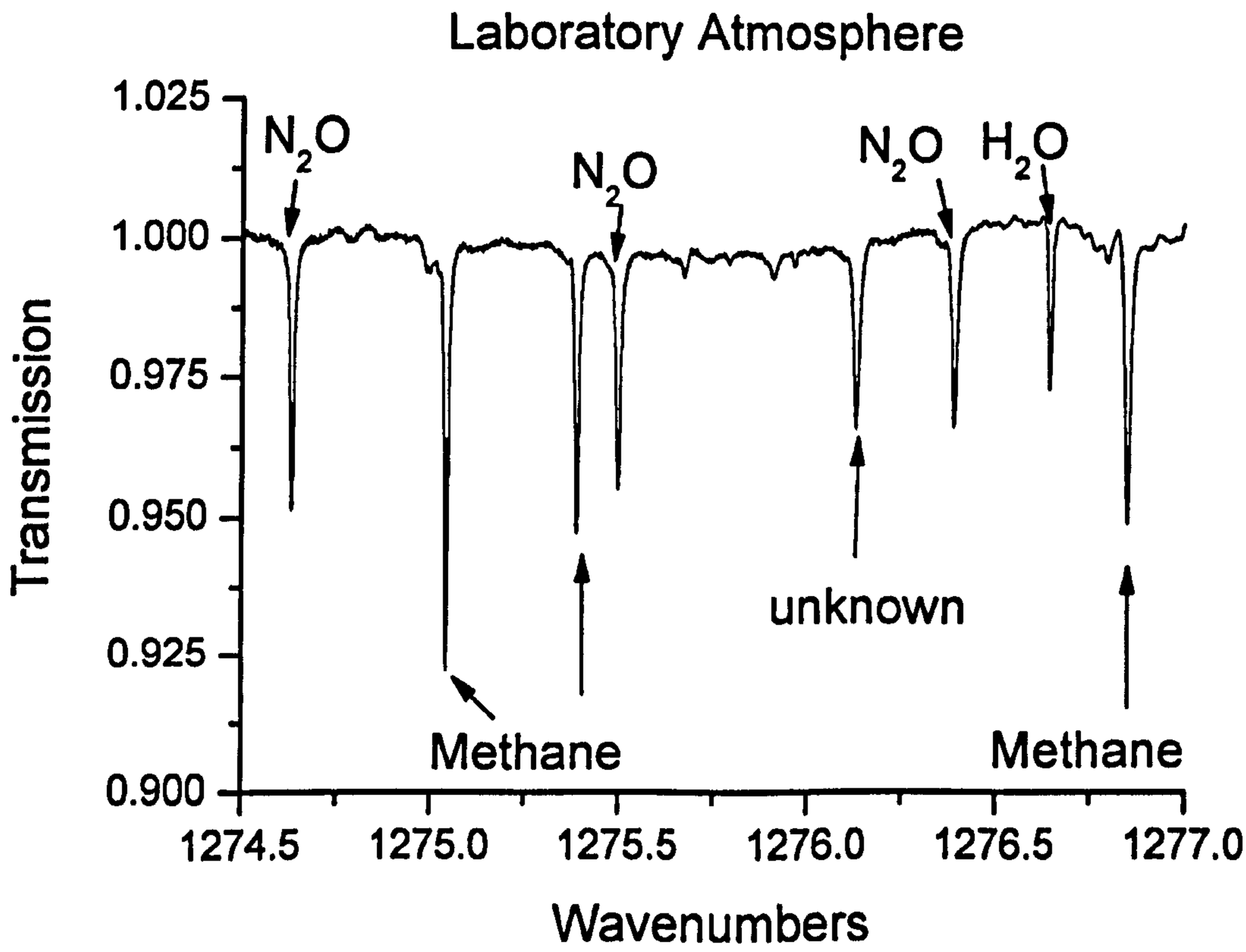

Figure 5.1.2 – *The spectrum of the laboratory atmosphere.*

The strong absorption lines of Methane, Nitrous Oxide and Water have been marked on the spectrum for comparison. Using the same concentration retrieval technique as I used with the 10μm laboratory atmosphere experiment the concentrations of the three identified gases have been calculated. The concentration of Methane was found to be

1.68ppmv, which compares to the 2001 global Methane concentration of 1.714ppmv [4]. The Nitrous Oxide concentration was calculated to be 308ppbv compared to the 2001 global Nitrous Oxide concentration of 315.4ppbv [4]. The water concentration in the laboratory was found to be 0.32% compared to the global atmospheric Water concentration of 0-4% [4]. Only Water was detected at both 8μm and 10μm. The two experiments were carried out on different days so a comparison between the two values is not valid due to the highly variable atmospheric Water concentration.

For the second experiment carried out at 8μm the laser was driven with a 3.5A current and a pulse width of 1270ns. The pulse repetition rate was 20KHz and the substrate temperature of the laser was maintained at +3°C. Each of the spectra recorded is an average of 64000 laser pulses. A comparison of the outside atmosphere 30s into the experiment with the spectra of Methane and Nitrous Oxide is made in Figure 5.1.3.

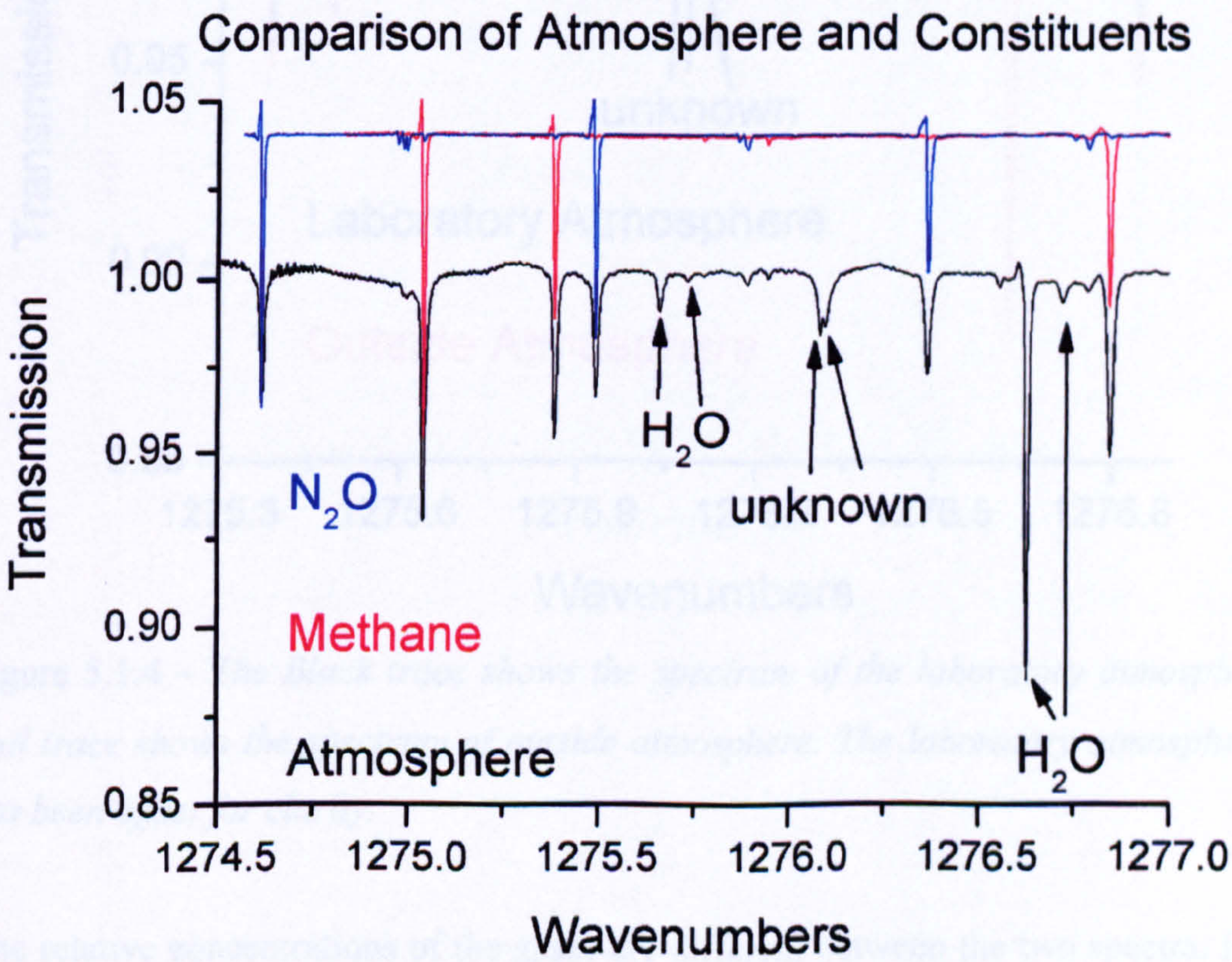

Figure 5.1.3 – *The Black trace shows the spectrum of the atmosphere. The Red trace shows the spectrum of Methane. The Blue trace shows the spectrum of Nitrous Oxide. The Nitrous Oxide and Methane traces have been offset for clarity.*

All of the major lines in the atmosphere spectrum can be identified except two unidentified lines between 1276cm^{-1} and 1276.5cm^{-1}. The laboratory atmosphere and the outside atmosphere spectra are compared in Figure 5.1.4.

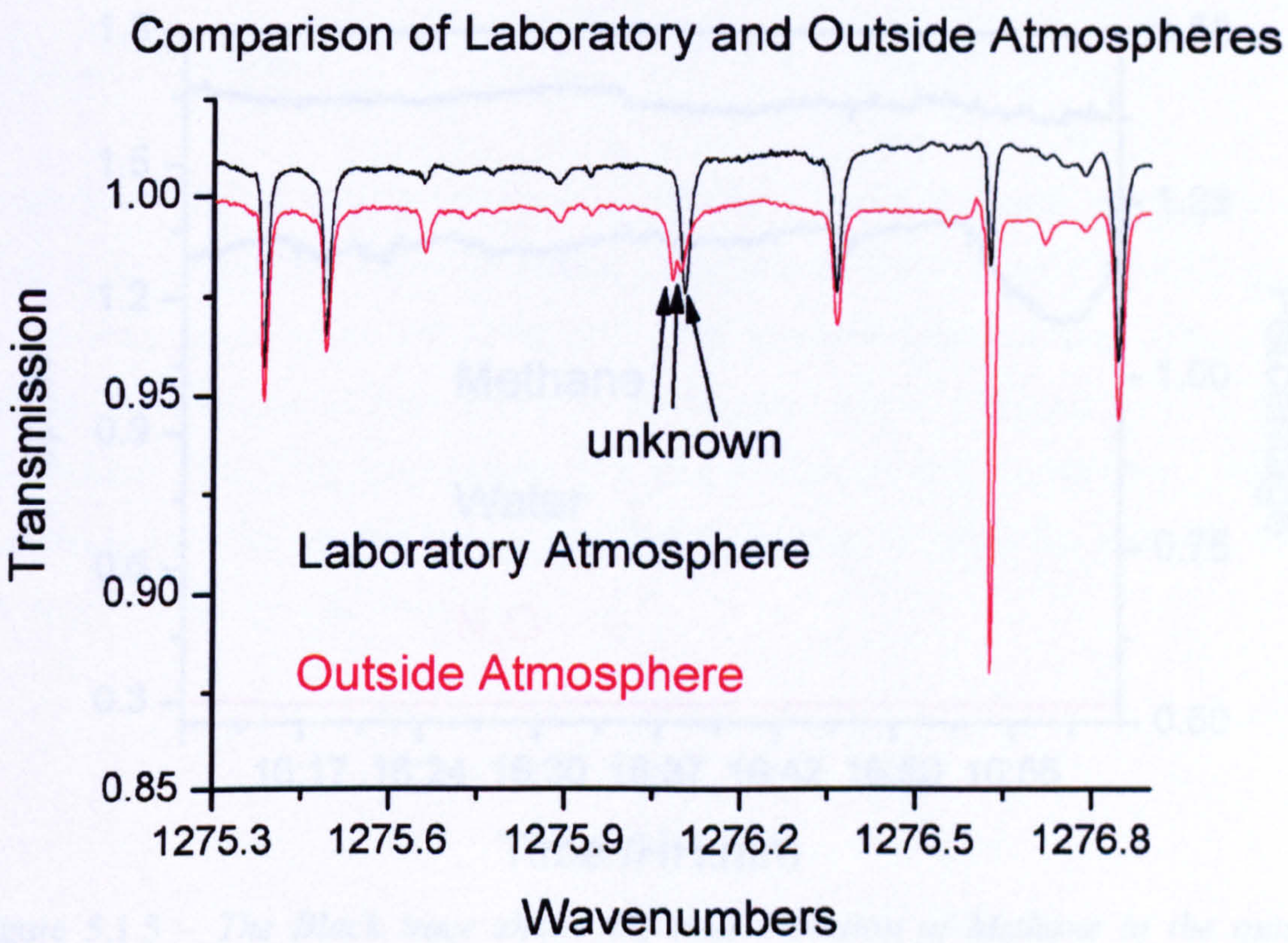

Figure 5.1.4 – *The Black trace shows the spectrum of the laboratory atmosphere. The Red trace shows the spectrum of outside atmosphere. The laboratory atmosphere trace has been offset for clarity.*

The relative concentrations of the gases are different between the two spectra. However the unknown lines in the two spectra are different. In the outside atmosphere there are two lines of similar intensity but in the laboratory atmosphere there is only one

unidentified line that does not correspond to either of the two lines in the outside atmosphere spectrum. The two unidentified lines in the outside atmosphere occur at 1276.0843 cm^{-1} and 1276.098cm^{-1}. The unidentified line in the laboratory atmosphere occurs at 1276.105 cm^{-1}. As the spectra of the outside atmosphere were continually recorded a time evolution of the three identifiable constituents can be made. This has been done in Figure 5.1.5.

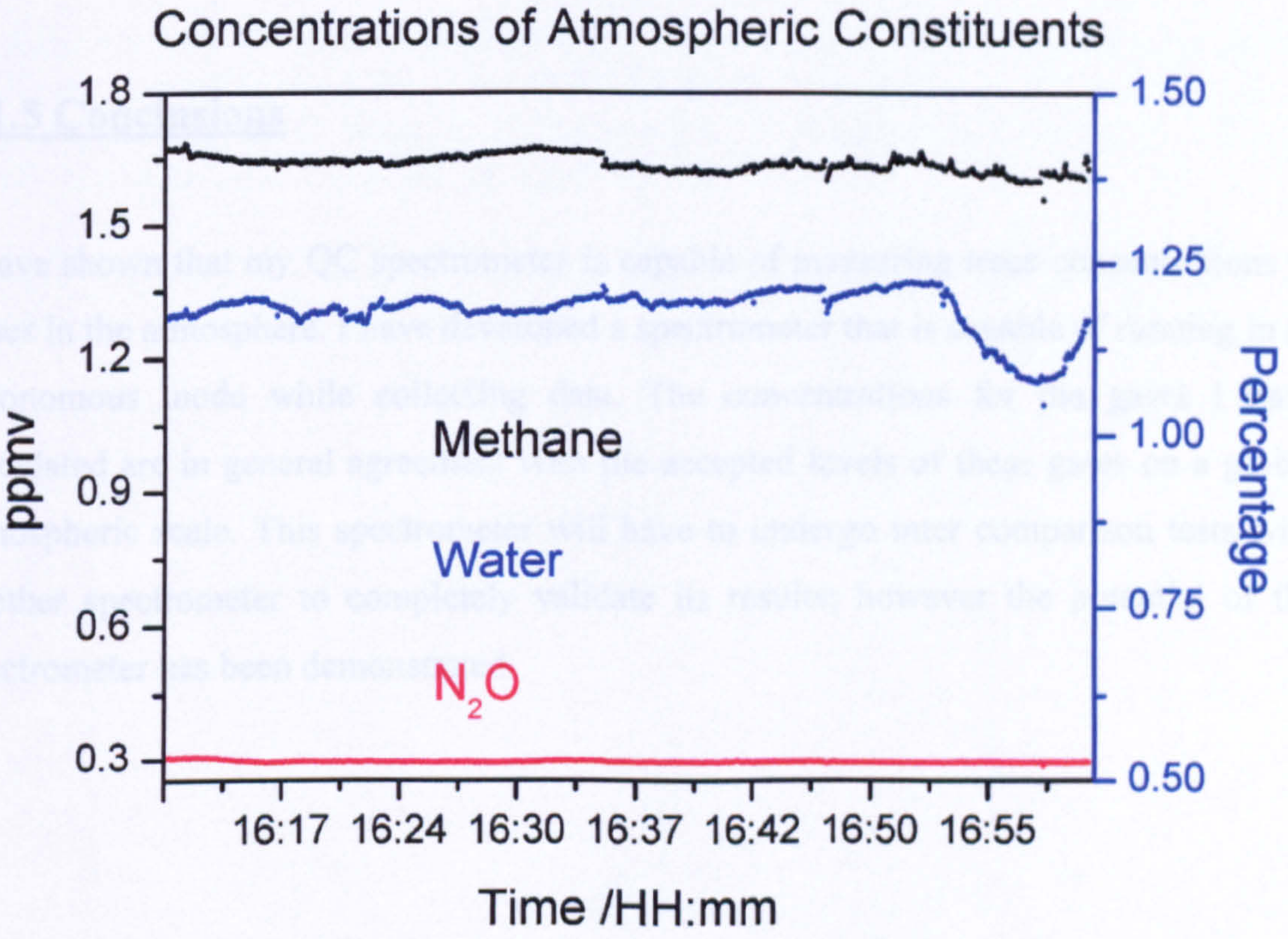

Figure 5.1.5 – *The Black trace shows the time evolution of Methane in the outside atmosphere. The time evolution of Nitrous Oxide in the outside atmosphere is shown by the Red trace. The Blue trace shows the time evolution of Water in the outside atmosphere.*

The Nitrous Oxide and Methane concentrations are plotted on the ppmv scale and the water concentration is plotted on the percentage scale. The average concentration of Methane over the entire measurement window was 1.64ppmv compared to the year 2001

global Methane atmospheric concentration of 1.714ppmv [4]. Over the measurement window the average Nitrous Oxide concentration was 293ppbv compared to the 2001 global Nitrous Oxide concentration of 315.4ppbv [4]. The average concentration of Water was found to be 1.2% compared to the global atmospheric Water concentration of 0-4% [4]. The Methane fluctuations around 16:40 onwards may be explained by cars leaving the car park at the end of the working day. The change in Water concentration is difficult to explain.

5.1.5 Conclusions

I have shown that my QC spectrometer is capable of measuring trace concentrations of gases in the atmosphere. I have developed a spectrometer that is capable of running in an autonomous mode while collecting data. The concentrations for the gases I have calculated are in general agreement with the accepted levels of these gases on a global atmospheric scale. This spectrometer will have to undergo inter comparison tests with another spectrometer to completely validate its results; however the potential of the spectrometer has been demonstrated.

5.1.6 References

1) Balloon-borne diode-laser absorption spectrometer for measurements of stratospheric trace species, R. T. Menzies, C. R. Webster and E. D. Hinkley, App. Opts., **22**, 17, 2655-3664, (1983)

2) ENVISAT, http://envisat.esa.int/

3) Airborne laser infrared absorption spectrometer (ALIAS-II) for in situ atmospheric measurements of N2O, CH4, CO, HCl and NO2, from balloon or remotely piloted aircraft platforms, D. C. Scott, R. L. Hermand, C. R. Webster, R. D. May, G. J. Flesch and E. J. Moyer, App. Opts., **38**, 21, 4609-4621, (1999)

4) Earthtrends portal, http://earthtrends.wri.org/searchable_db/index.cfm?theme=3

5.2 Breath Experiments

5.2.1 Introduction

In this chapter I will discuss the work that I have conducted looking at human breath. The most common breath analysis is made by the alcohol breathalyser, which was first introduced to Britain in 1983 to test the levels of alcohol in a person's body at the road side. The ability to detect compounds in breath that are present in a person's blood stream should allow for non invasive diagnosis. As well as the common gases, such as Nitrogen and Carbon Dioxide, there are many other gases found in exhaled breath. By looking at the variation in these gases the health of a person can be examined. For example elevated levels of Methane in a person's breath can indicate a bowel problem [1]. Compounds, such as Methane, are passed into exhaled breath from the blood stream in the lungs of a patient. The breath of four volunteers has been analysed using the 8μm laser to look for variations in the detectable exhaled gases in the lasers micro window.

5.2.2 Exhaled Breath Components

The typical exhaled breath from a human being is a complex mixture of gases. Water, Nitrogen, Oxygen and Carbon Dioxide are all found in exhaled breath at the percentage level. Several traces gases have been detected as well in exhaled breath such as Nitrous Oxide [2] and Methane [3]. It is these trace elements as well as the main constituents that allow the health of the whole human body, as well as its sub systems, to be monitored. The gases looked at in this work are Methane, Carbon Dioxide, Water and Nitrous Oxide.

5.2.3 Patients Studied

The exhaled breath of four volunteers was studied during this work. Of the four patients studied one patient, patient C, has a minor gastrointestinal problem. Two of the patients, patients A and D, suffer from asthma. Both of these patients require inhalers to control

their conditions. The other patient, patient B, did not knowingly suffer from any health conditions at the time of the experiment. All of the patients are male and the ages of the patients are as follows: Patient A was 40, Patient B was 24, Patient C was 60 and Patient D was 21. All of the patients are non smokers.

5.2.4 Experimental Setup

A full description of the spectrometer can be found in section 3.1. The pulses used to drive the 8μm laser varied from 1000ns to 1500ns. The chirp rate of the 8μm laser is extremely nonlinear when pulsed at 1270ns with a 3.5A drive current. An order of magnitude change in chirp rate from the start to the end of the pulse is possible. The astigmatic Herriott cell was configured for 115m of optical path. A full description of the astigmatic Herriott cell as well as the 115m pathlength mirror configuration can be found in section 2.3. The first set of measurements involved measuring samples from patients in normal breathing conditions. The breath samples were collected one at a time. The exhaled breath from a patient was used to inflate a balloon. The sample from this balloon was then transferred to the astigmatic Herriott cell by hooking the balloon up to a valve, which allowed the gas flow to be controlled. The astigmatic Herriott cell was filled up to a pressure of about 50Torr of breath. The balloons were unused and completely uninflated before use. The time taken between sampling the patient's breath and passing it in to the astigmatic Herriott cell was kept to below 15s. The second set of measurements, which were carried out several weeks after the first set of measurements, involved sampling the patient's breath under different conditions. The breath samples were taken after the patient had held their breath. A normal breathing sample was taken first as a point of reference and then the patient was asked to hold their breath for increasing lengths of time. Each of the samples was transferred to the astigmatic Herriott cell and probed by the spectrometer before the next sample was taken. The time between each sample being taken was at least five minutes, which gave the patient time to recover before the next sample. For all of the experiments the patients had not eaten in the hour before testing, nor had they partaken in any exercise in that hour.

5.2.5 Results

For all of the measurements made the laser was operated under the same conditions. The drive current was 3.5A with a pulse width of 1270ns. The pulse repetition frequency was 20KHz. The substrate of the laser was maintained at a temperature of +3°C. Each of the spectra recorded was an average of 20000 pulses, giving a 1s recording time. Figure 5.2.1 shows the background trace and the breath spectrum trace from patient A.

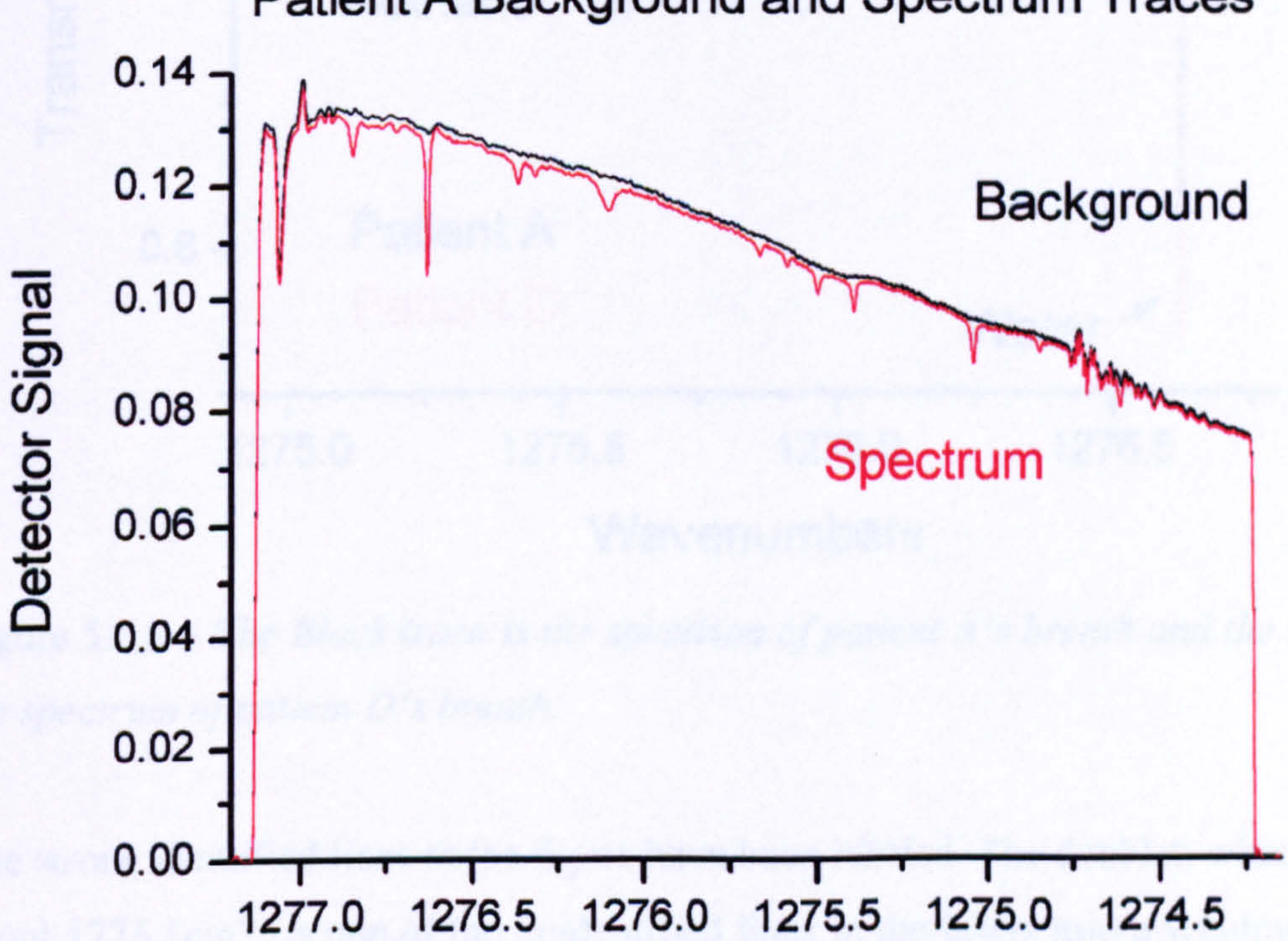

Figure 5.2.1 – *The Black trace shows the background pulse. The Red trace shows the spectrum pulse.*

The signal that appears on both traces at approximately 1274.5cm^{-1} is associated with the switcher RF, which is discussed in section 3.1. As well as the gases of interest at least four unidentified lines are present in the spectrum. A comparison of a part of the

spectrum of patient A's breath and a part of the spectrum of patient D's breath is shown in Figure 5.2.2.

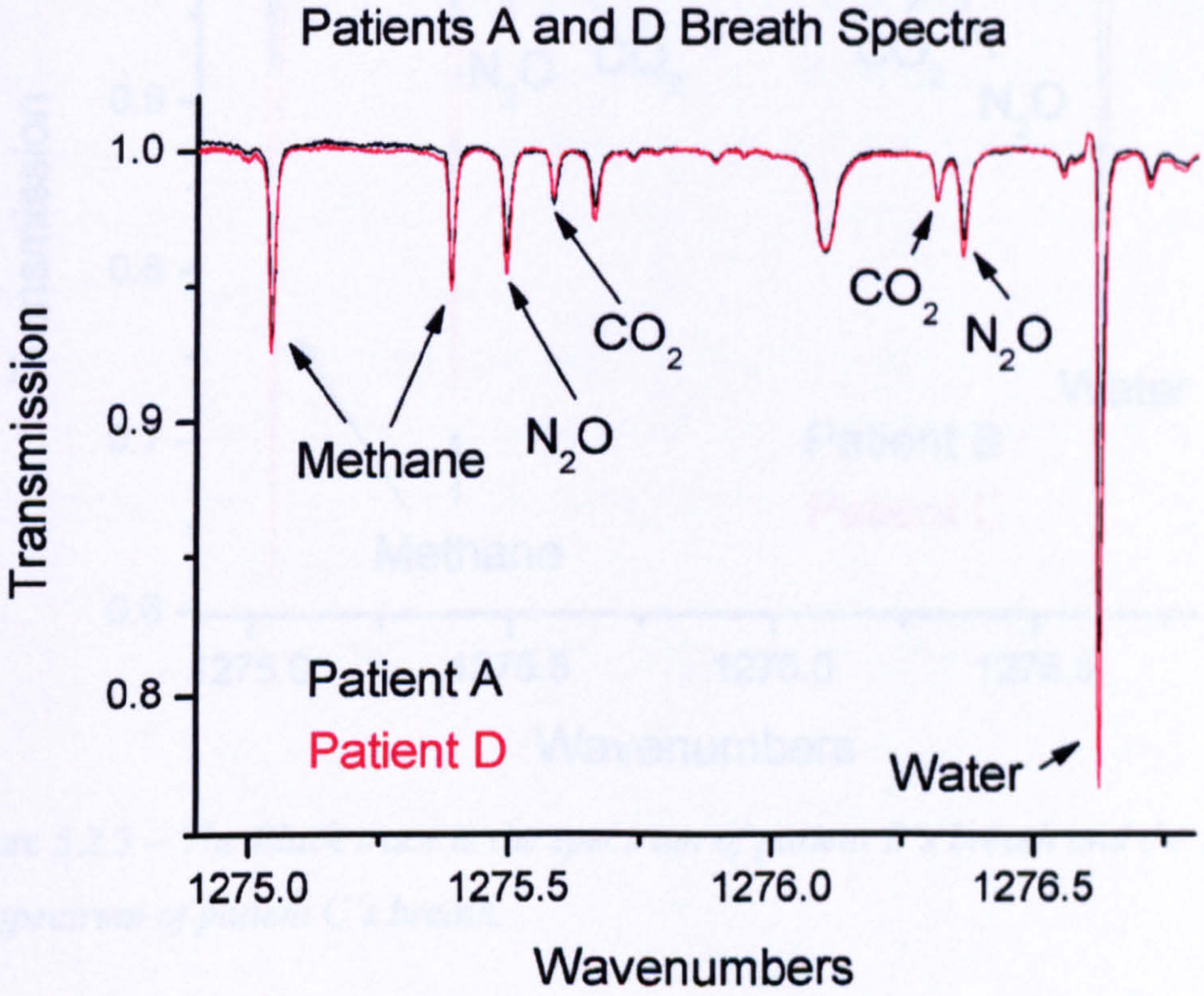

Figure 5.2.2 – *The Black trace is the spectrum of patient A's breath and the Red trace is the spectrum of patient D's breath.*

The strong identified lines in the figure have been labeled. The doublet, which appears at about 1276.1cm^{-1}, is one of the unidentified lines in the lasers micro window. All of the labeled lines overlap each other quite well. A comparison of a part of the spectrum of patient B's breath and a part of the spectrum of patient C's breath is shown in Figure 5.2.3.

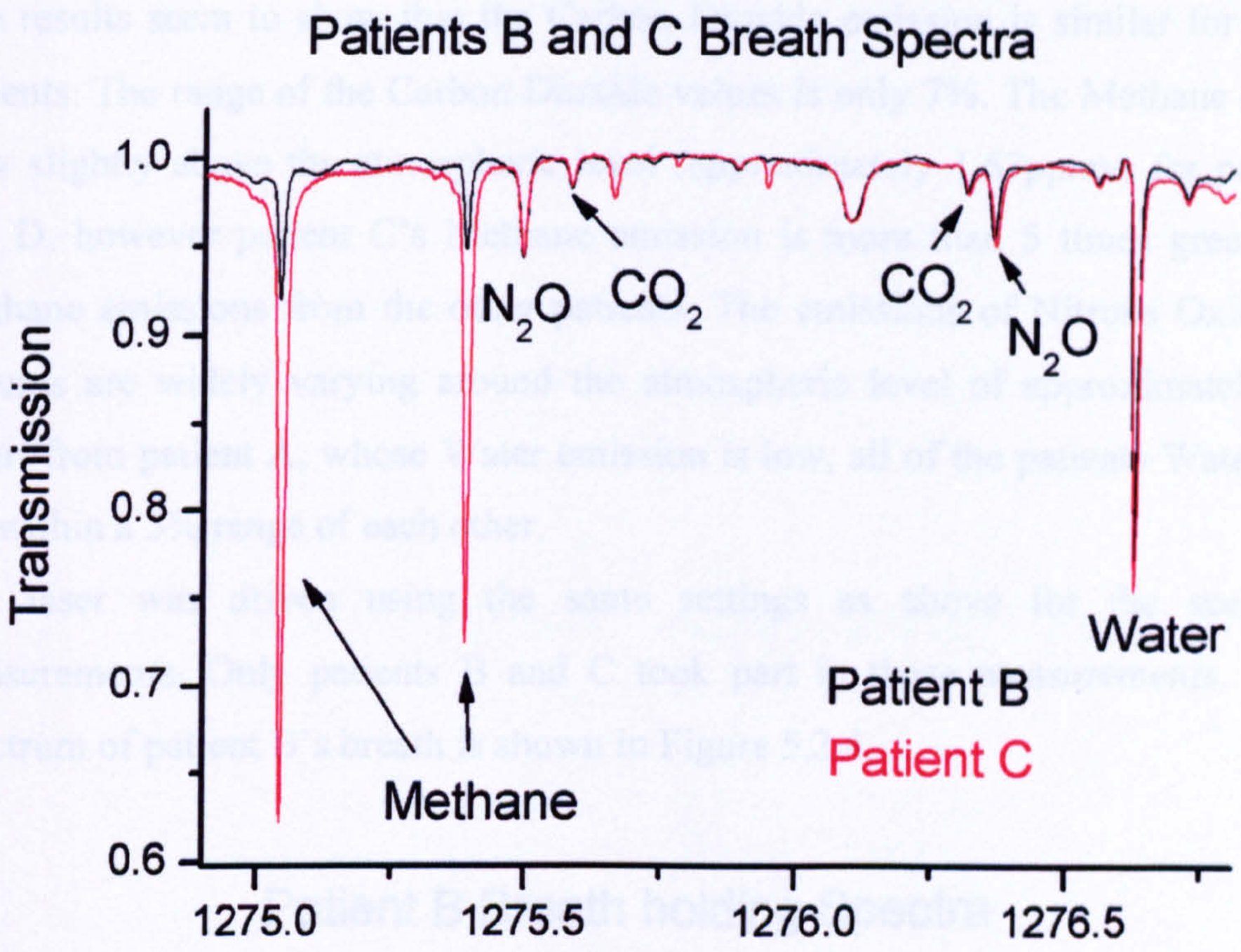

Figure 5.2.3 – *The Black trace is the spectrum of patient B's breath and the Red trace is the spectrum of patient C's breath.*

The Nitrous Oxide, Carbon Dioxide and Water lines over lap well, however the Methane lines in patient C's breath spectrum are much stronger than the Methane lines in patient B's breath spectrum.

The concentrations of the target gases were calculated using a LabVIEW program, which is described in section 3.1. The concentrations of each of the gases in each of the patients breath is shown in Table 5.2.1.

Patient	Carbon Dioxide (Percentage)	Methane (ppmv)	Nitrous Oxide (ppbv)	Water (Percentage)
A	2.54	2.17	231	1.84
B	2.47	2.35	361	2.33
C	2.38	12.2	326	2.43
D	2.56	2.04	280	2.31

The results seem to show that the Carbon Dioxide emission is similar for each of the patients. The range of the Carbon Dioxide values is only 7%. The Methane emissions is only slightly above the atmospheric level (approximately 1.67ppmv) for patients A, B and D, however patient C's Methane emission is more than 5 times greater than the Methane emissions from the other patients. The emissions of Nitrous Oxide from the patients are widely varying around the atmospheric level of approximately 300ppbv. Apart from patient A, whose Water emission is low, all of the patients Water emissions are within a 5% range of each other.

The laser was driven using the same settings as above for the second set of measurements. Only patients B and C took part in these measurements. Part of the spectrum of patient B's breath is shown in Figure 5.2.4.

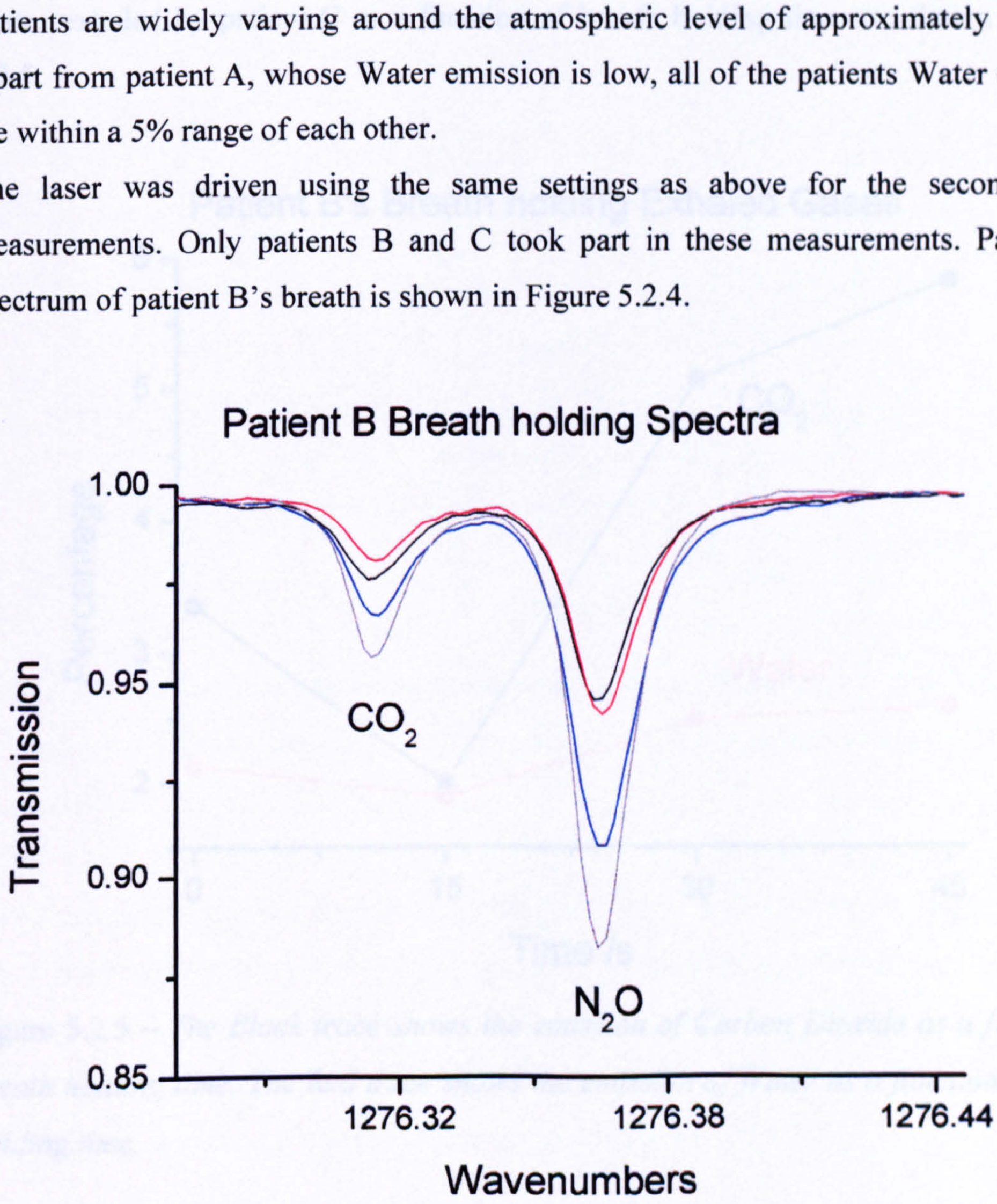

Figure 5.2.4 – *The Black trace shows patient B's normal breath spectrum. The Red trace shows patient B's breath spectrum after 15s of holding his breath. The Blue trace shows*

patient B's breath spectrum after 30s of holding his breath. The Grey trace shows patient B's breath spectrum after 45s of holding his breath.

The concentration of Nitrous Oxide increases in each of the spectra, whereas the Carbon Dioxide increases after an initial decrease. The concentrations of Carbon Dioxide and Water exhaled by patient C as a function of breath holding time are shown in Figure 5.2.5.

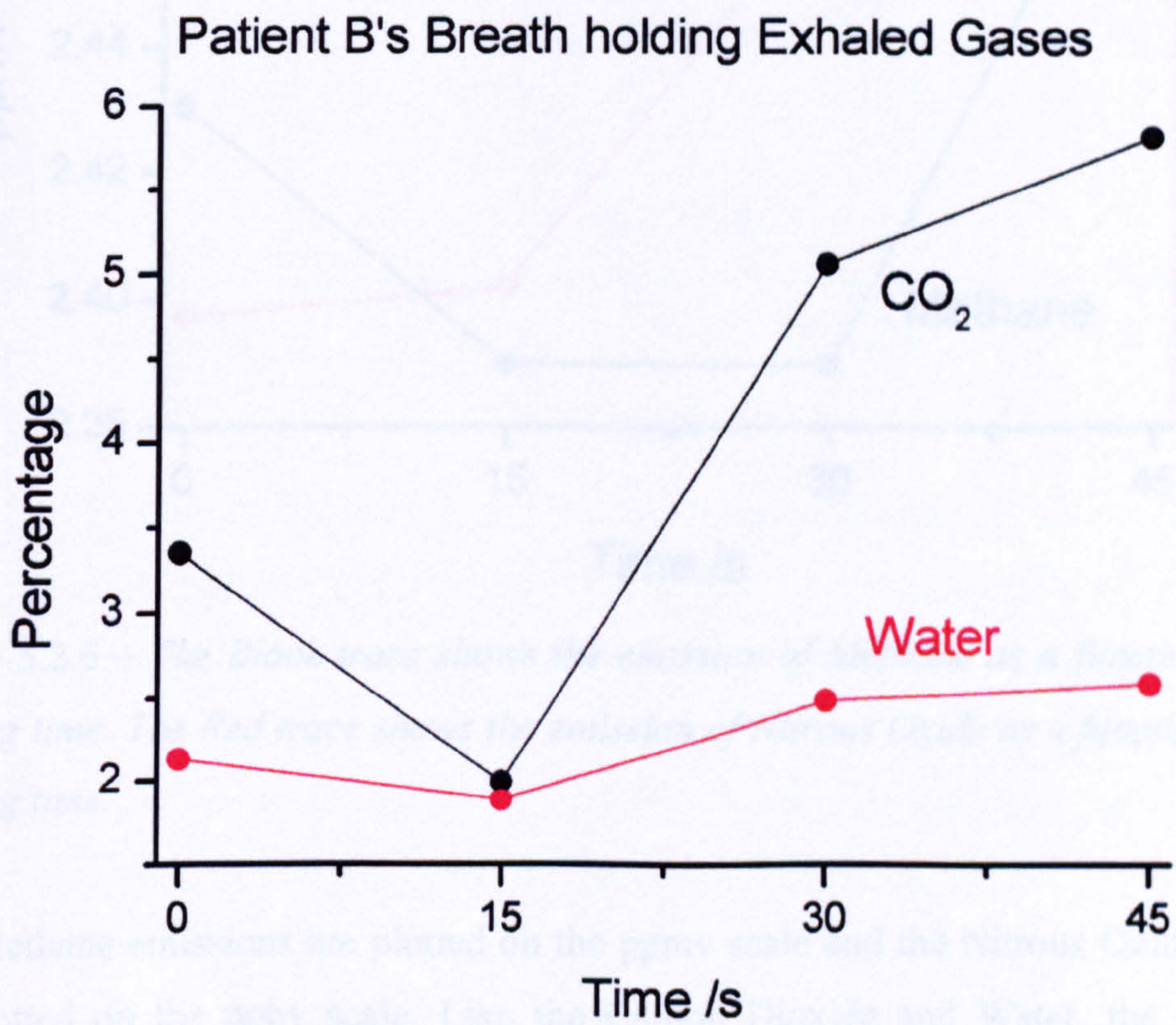

Figure 5.2.5 – *The Black trace shows the emission of Carbon Dioxide as a function of breath holding time. The Red trace shows the emission of Water as a function of breath holding time.*

The Water and Carbon Dioxide emissions are plotted as a percentage of the total exhaled breath. Both of these gases show an initial decrease before increasing as the length of time the patients breath is held increases. The concentrations of Nitrous Oxide and

Methane exhaled by patient B as a function of breath holding time are shown in Figure 5.2.6.

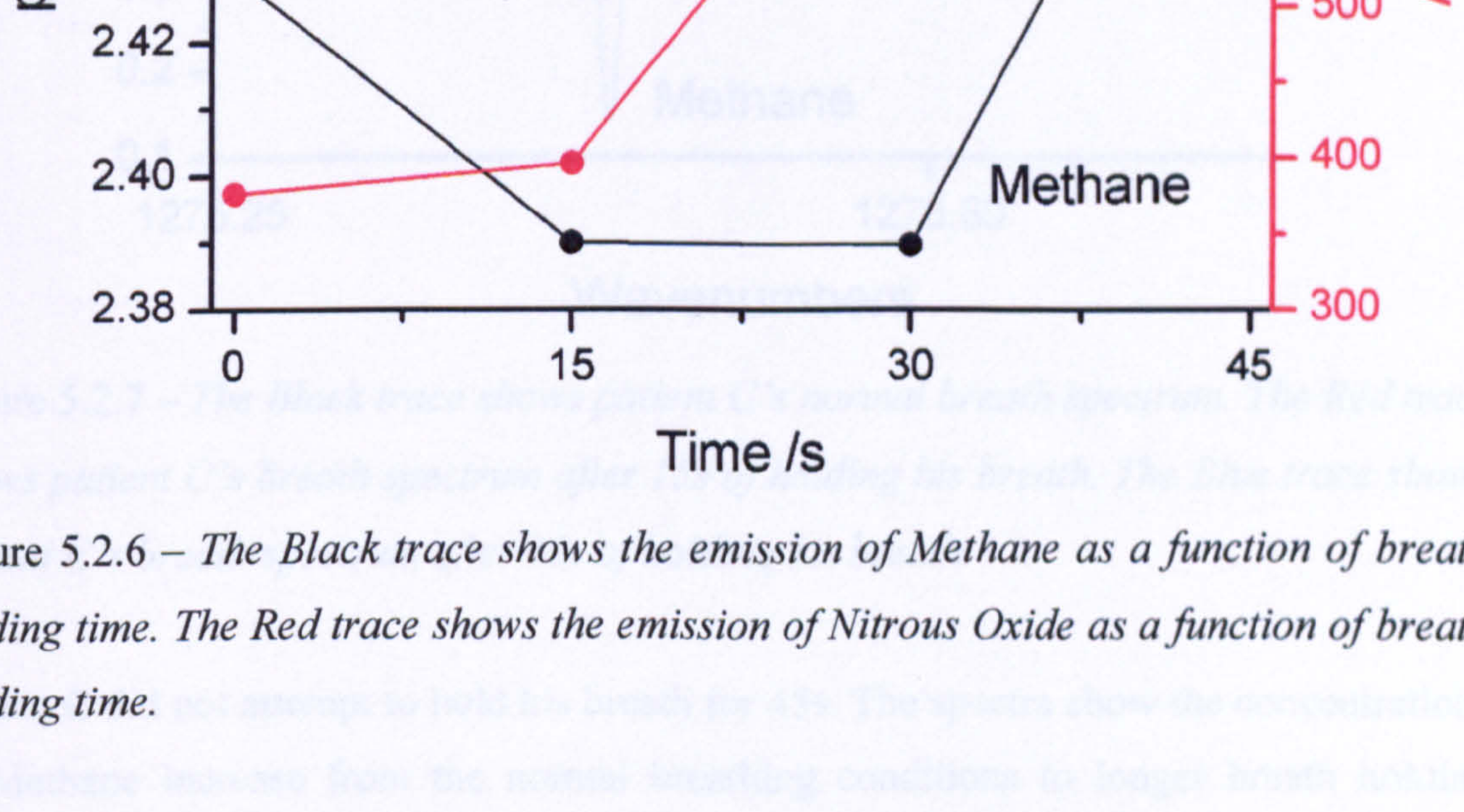

Figure 5.2.6 – *The Black trace shows the emission of Methane as a function of breath holding time. The Red trace shows the emission of Nitrous Oxide as a function of breath holding time.*

The Methane emissions are plotted on the ppmv scale and the Nitrous Oxide emissions are plotted on the ppbv scale. Like the Carbon Dioxide and Water, the emission of Methane initially decreases before finally increasing. The Nitrous Oxide steadily increases with increasing hold time.

Part of the spectrum of patient C's breath is shown in Figure 5.2.7.

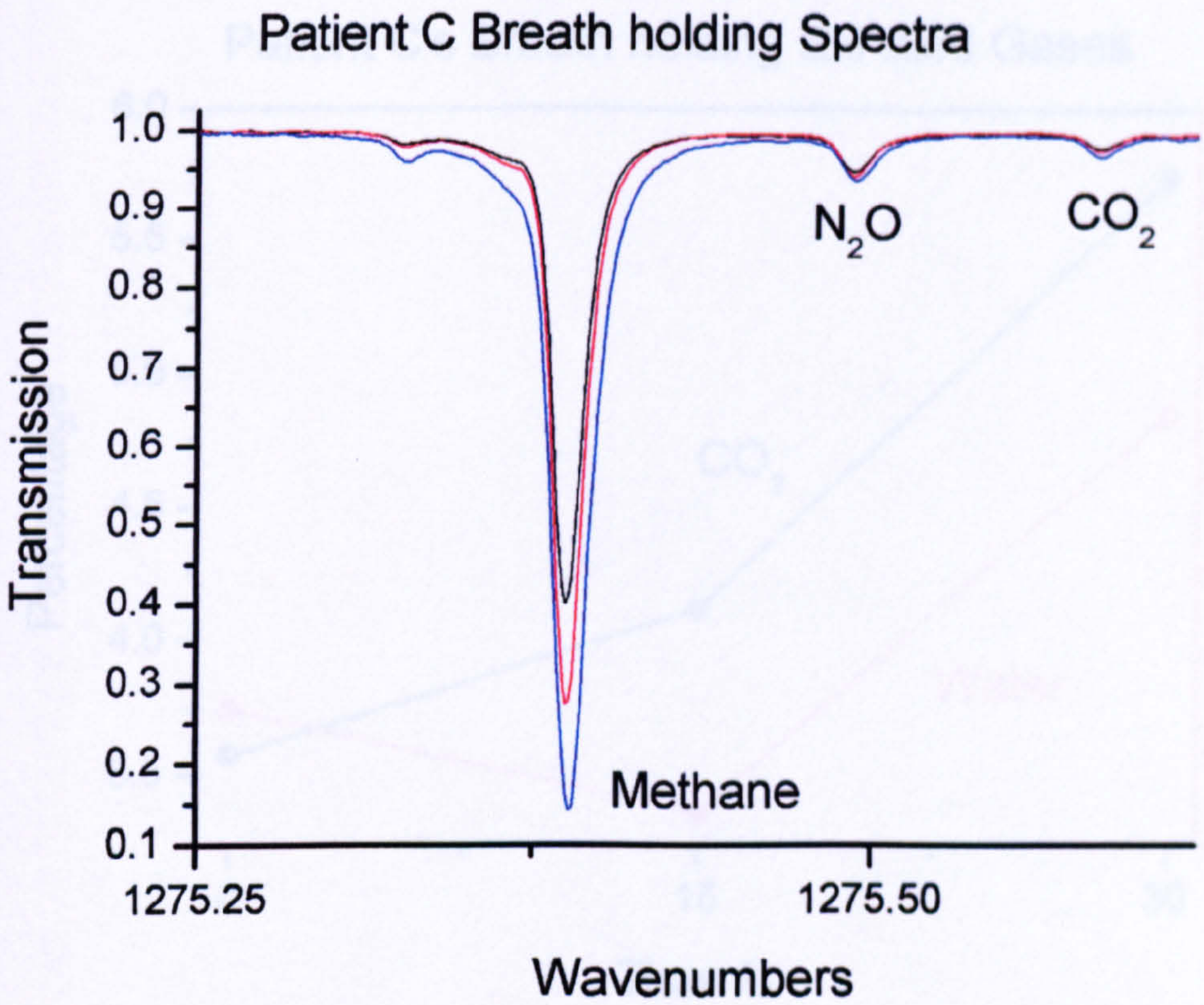

Figure 5.2.7 – *The Black trace shows patient C's normal breath spectrum. The Red trace shows patient C's breath spectrum after 15s of holding his breath. The Blue trace shows patient C's breath spectrum after 30s of holding his breath.*

Patient C did not attempt to hold his breath for 45s. The spectra show the concentrations of Methane increase from the normal breathing conditions to longer breath holding times.

The concentrations of Carbon Dioxide and Water emitted from patient C as a function of breath holding time are shown in Figure 5.2.8.

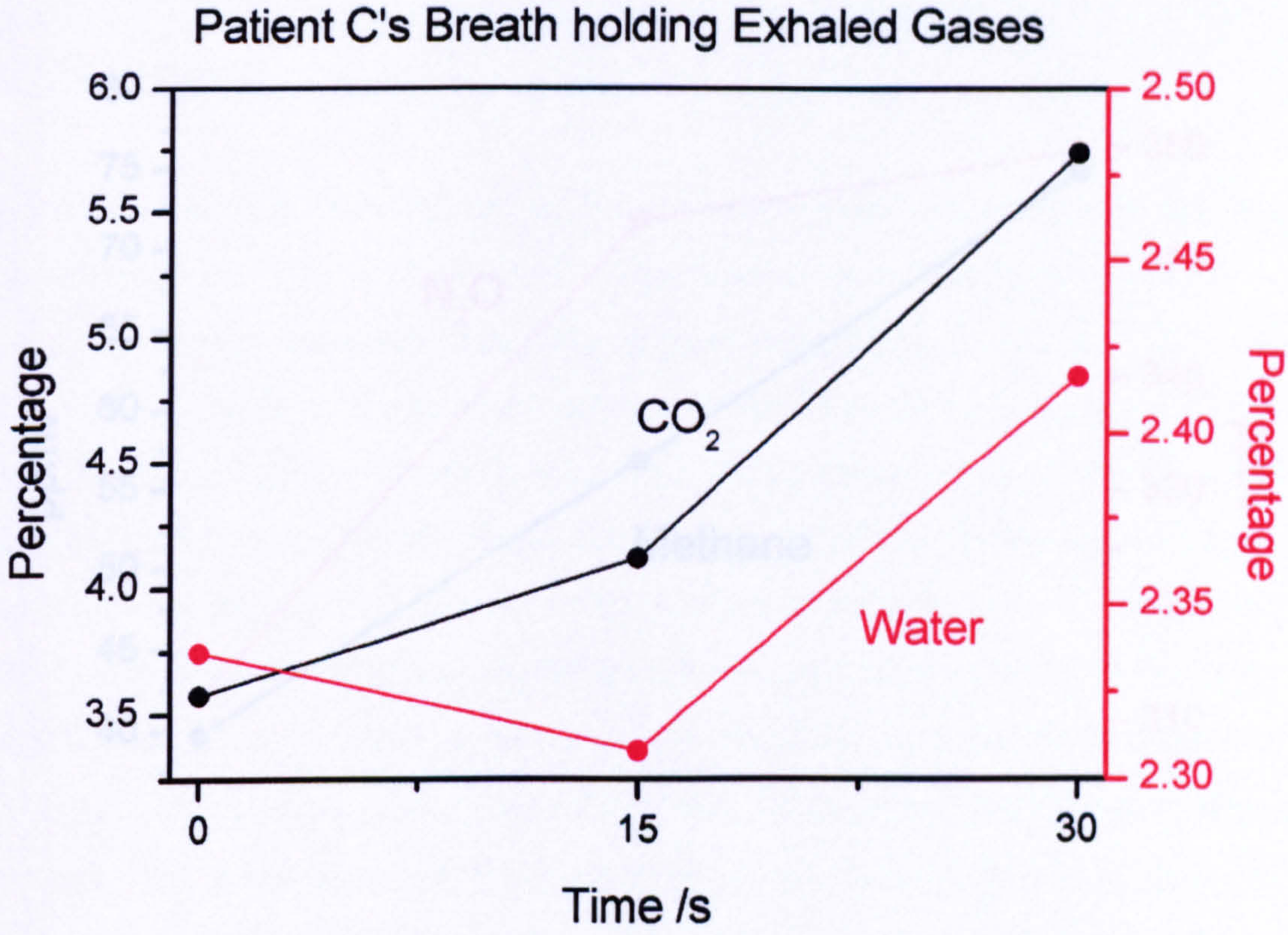

Figure 5.2.8 – *The Black trace shows the emission of Carbon Dioxide as a function of breath holding time. The Red trace shows the emission of Water as a function of breath holding time.*

The Water and Carbon Dioxide emissions are plotted as a percentage of the total exhaled breath with the red scale corresponding to the percentage of Water and the black scale corresponding to the Carbon Dioxide. Just like patient B, patient C's water emission initially decreases before increasing at longer breath hold times. Unlike patient B, patient C's Carbon Dioxide emissions steadily increase as a function of increasing breath hold time.

The concentrations of Nitrous Oxide and Methane emitted by patient C as a function of breath holding time are shown in Figure 5.2.9.

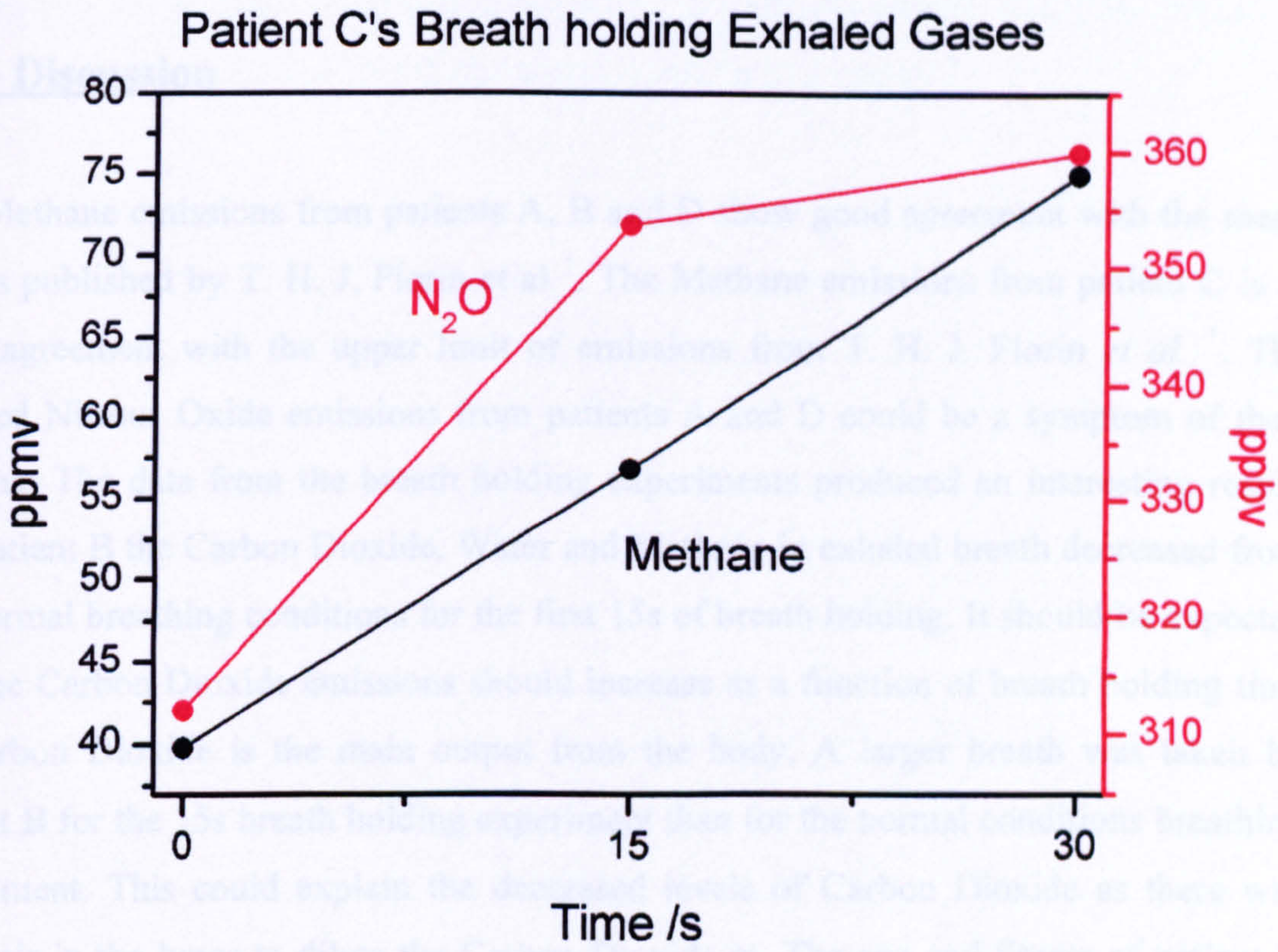

Figure 5.2.9 – *The Black trace shows the emission of Methane as a function of breath holding time. The Red trace shows the emission of Nitrous Oxide as a function of breath holding time.*

The Methane emissions are plotted on the black ppmv scale and the Nitrous Oxide emissions are plotted on the red ppbv scale. The exhaled concentration of Methane from patient C increases rapidly as a function of breath hold time. The Nitrous Oxide emissions from patient C also increase with increasing breath hold time, however at a much slower rate than in patient B. Table 5.2.2 shows the concentrations of the exhaled gases from patients B and C as a function of breath hold time.

	Patient B				Patient C			
Time	CO_2 percentage	Methane ppmv	N_2O ppbv	Water percentage	CO_2 percentage	Methane ppmv	N_2O ppbv	Water percentage
0s	3.34743	2.43027	375	2.1296	3.57167	39.71299	312	2.336032
15s	1.99535	2.39000	396	1.8814	4.11628	56.76866	353	2.307784
30s	5.05895	2.38978	675	2.4843	5.74153	74.97134	359	2.416311
45s	5.82244	2.48628	784	2.5796				

5.2.6 Discussion

The Methane emissions from patients A, B and D show good agreement with the mean results published by T. H. J. Florin et al [1]. The Methane emissions from patient C is in good agreement with the upper limit of emissions from T. H. J. Florin *et al.* [1]. The reduced Nitrous Oxide emissions from patients A and D could be a symptom of their Asthma. The data from the breath holding experiments produced an interesting result. For patient B the Carbon Dioxide, Water and Methane in exhaled breath decreased from the normal breathing conditions for the first 15s of breath holding. It should be expected that the Carbon Dioxide emissions should increase as a function of breath holding time as Carbon Dioxide is the main output from the body. A larger breath was taken by patient B for the 15s breath holding experiment than for the normal conditions breathing experiment. This could explain the decreased levels of Carbon Dioxide as there was more air in the lungs to dilute the Carbon Dioxide in. The age and fitness of patient B could also have been a factor. This decrease is not seen in the exhaled breath of patient C. The Methane emission from patient C increase in a similar fashion to the Nitrous Oxide levels in patient B as a function of breath holding time.

5.2.7 Conclusions

This work has highlighted a potential application of our spectrometer as a medical diagnostic tool. I have shown that the instrument is capable of detecting changes in exhaled gases concentrations between patients. The increased levels of emissions could be used to make an early diagnosis of a disease. This would have several advantages over current techniques used to look for chemical levels in the body such as blood and urine sampling. As a non invasive technique my spectrometer would be popular with patients that have a needle phobia. The ability for the results to be available almost immediately would also remove some of the stress patients suffer waiting on blood or urine test results to return from a laboratory. Other exhaled gases, and therefore other

disease indicators, could be looked at if a different laser wavelength was used. Increased levels of Ethane in exhaled breath can indicate cancer in a patient [4].

5.2.8 References

1) Shared and unique environmental factors determine the ecology of methanogens in humans and rates, T. H. J. Florin, G. Zhu, K. M. Kirk and N. G. Martin, The American Journal of Gastroenterology, **95**, 10, 2872-2879, (2000)

2) Increased breath Nitrous Oxide after ingesting nitrate in patients with atrophic gastritis and partial gastrectomy, T. Mitsui, T. Kondo, Clinica Chimica Acta, Article in Press, 2004

3) Human breath trace gas content study by tunable diode laser spectroscopy technique, K. L. Moskalenko, A. I. Nadezhdinskii and I. A. Adamovskaya, Infrared Physics and Technology, **37**, 181-192, (1996)

4) Oil industry tool sniffs out cancer, C. Fry, http://news.bbc.co.uk/1/hi/sci/tech/3059559.stm, (2003)

5.3 Cigarette Smoke Experiments

5.3.1 Introduction

As a result of the increased public interest over the past decades the contents of cigarette smoke have been increasingly studied. In this chapter I will discuss the work that I have carried out to investigate the contents of the cigarette smoke stream. I will discuss the contents of cigarette smoke. In the first section I will discuss work carried out at 10μm. I will then discuss work carried out at 8μm. Cigarette manufacturers have developed technology to try to reduce the harmful chemicals in the smoke stream. These technologies include filters and different papers to wrap the tobacco in. For each new technological development scientific research must be carried out into the cigarette smoke stream contents.

5.3.2 Cigarette Smoke

Several studies have looked at the constituents of cigarette smoke [1, 2], which have shown that there are many thousands of chemicals present in the smoke stream of cigarettes. Of these chemicals many are potential carcinogens such as Formaldehyde, Benzene, Arsenic, Vinyl Chloride and several others. As well as cancer, cigarette smoke is known to cause other diseases such as asthma [3] and other respiratory conditions. The first set of measurements made in this work were made at 10μm. The identifiable gases detected at 10μm were Ethylene, Ammonia, Carbon Dioxide and Water. The second set of measurements were carried out at 8μm. The identifiable gases from the second set of measurements were Formaldehyde, Methane, Acetylene, Water and Carbon Dioxide. At both wavelengths several unidentified absorption lines were observed.

5.3.3 Prior Art Cigarette Smoke work

Since the public first became concerned about the health implications of smoking thousands of studies and experiments have been done to look at the smoke produced by cigarettes and the effect it has on the smoker and those around them. I will highlight some of the work done in this field. Work has been done by Milton E. Parrish *et al* into the measurement of Formaldehyde using a tunable diode laser infrared spectrometer in the main smoke stream and the side stream [4]. Main stream smoke Formaldehyde was studied using a Fourier Transform Spectrometer by S. Li *et al* [5]. Two Quantum Cascade laser based absorption spectrometers were used by Quan Shi *et al* to study the main stream and side stream smoke at 10μm and 5μm [6], which allowed the detection of Ammonia and Ethylene at 10μm and Nitric Oxide at 5μm. In the cigarette spectra I have recorded there are several unidentified gases. One of the possible gases is Hydrazine, which Susan Plunkett *et al* looked at in cigarette smoke using a tunable diode laser based infrared spectrometer [7]. Susan Plunkett *et al* also studied other gases such as Ethylene, Formaldehyde and Ammonia using a dual channel tunable diode laser based absorption spectrometer [8].

5.3.4 Cigarettes Studied

Two different types of cigarette were used in this work. The first cigarettes were Marlboro Lights, which were purchased in Portugal duty free as a packet of 20. The description of these cigarettes from the packet is Class A filtered. The Tar content per cigarette was 8mg and the Nicotine content was 0.6mg. The second type of cigarettes were from a 10 packet of Regal King Size, which were purchased in a local shop near the University. According to the packaging the Tar content of each cigarette was 10mg. The Nicotine content was 0.9mg and the Carbon Monoxide produced was 10mg.

5.3.5 Experimental Setup

For a full description of my spectrometer see section 3.1. During the experiments only one laser was used at a time. These lasers were mounted in temperature controlled housings. The temperature of the laser in use was maintained at a constant level of around 0°C. The 10μm laser was driven with top hat shaped current pulses of up to 5A with a maximum pulse width of 300ns and a repetition rate of 15KHz for these experiments. The 8μm laser was driven with top hat shaped current pulses of up to 4.5A with a maximum pulse width of 1500ns and a repetition rate of up to 40KHz for these experiments. The light from the laser in use was directed into the astigmatic Herriott cell [9] using steering mirrors. For the 10μm experiments the astigmatic Herriott cell was setup for 66m of optical path. For the 8μm experiments the astigmatic Herriott cell was configured for 115m of optical path. The astigmatic Herriott cell and both of these solutions are described in detail in section 2.3. The first 10μm experiment involved evacuating a glass flask and using the vacuum in the flask to smoke the cigarette. This experiment provided no intra puff information. As the time taken to collect the smoke and then transfer the smoke from the flask to the cell was non-negligible any short lived species would have reacted away. The coupling of the cigarette to the flask was poor which meant that excessive air was allowed to enter the flask. It was therefore deemed that this method was not acceptable and another method had to be found. The second, and the utilised, method involved coupling the cigarette directly to the entrance of the cell. The valve used to connect to the cell was a Nupro valve with a connector that was the exact fit for the butt of a cigarette. The cigarette was pushed into this connector as shown in Figure 5.3.1.

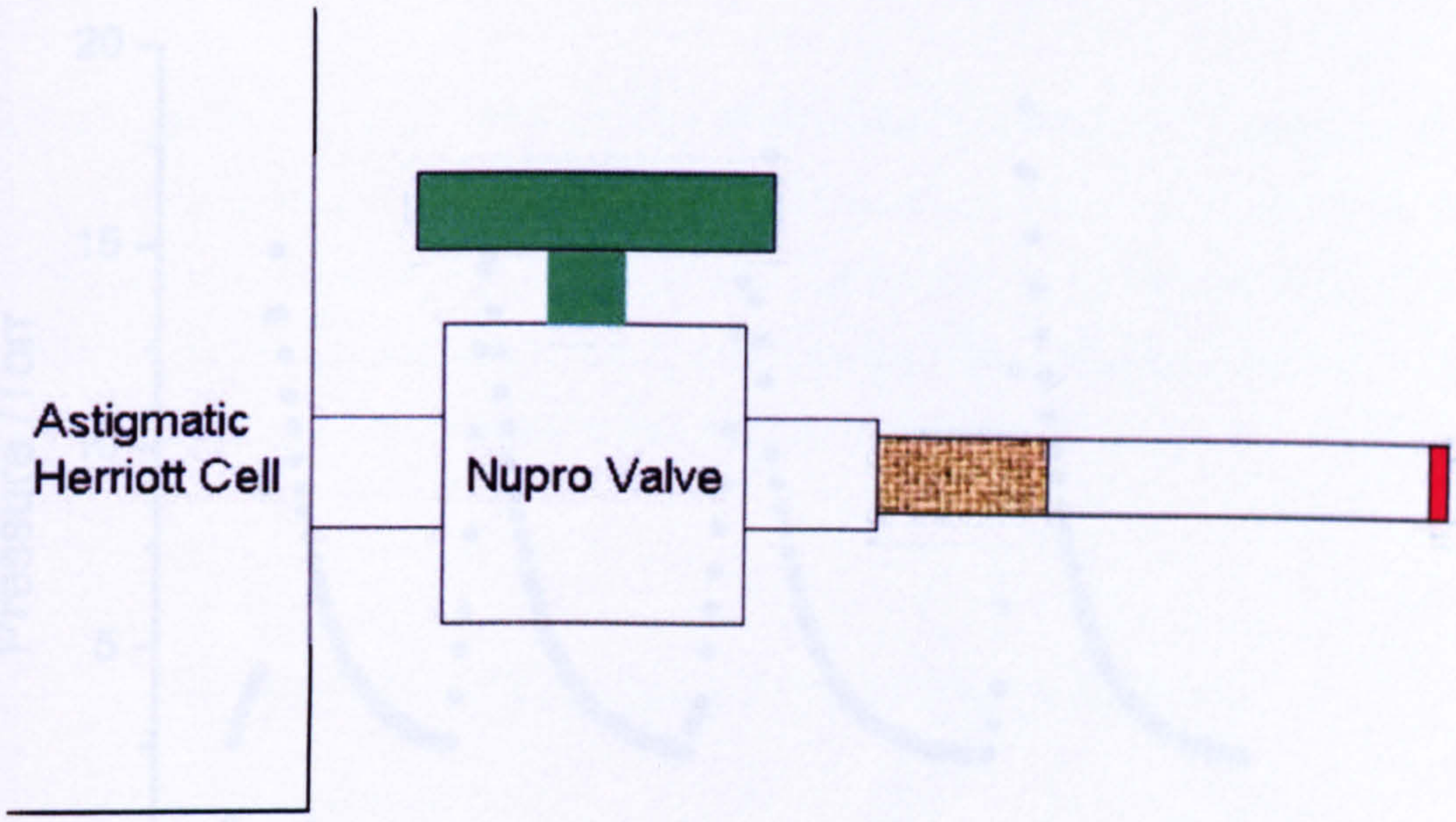

Figure 5.3.1 – *The cigarette sampling setup.*

The sampling of cigarette smoke was done by opening and closing of the Nupro valve while the rotary pump connected to the exit port of the cell was operating. This gives a sharp rise in pressure in the cell as the valve is opened followed by a slow decay of pressure after the valve is closed. For each puff of the cigarette the valve was opened for approximately the same time, which took the total pressure in the cell up to a similar pressure for each of the puffs. A new puff was added when the pressure in the cell had decayed to approximately 2 Torr. This method of smoking a cigarette differs from the accepted smoking technique described by the Canadian health board [10]. The pressure in the cell was logged for the 8μm experiments. An example of the logged pressure in the cell during one of the experiments is shown in Figure 5.3.2.

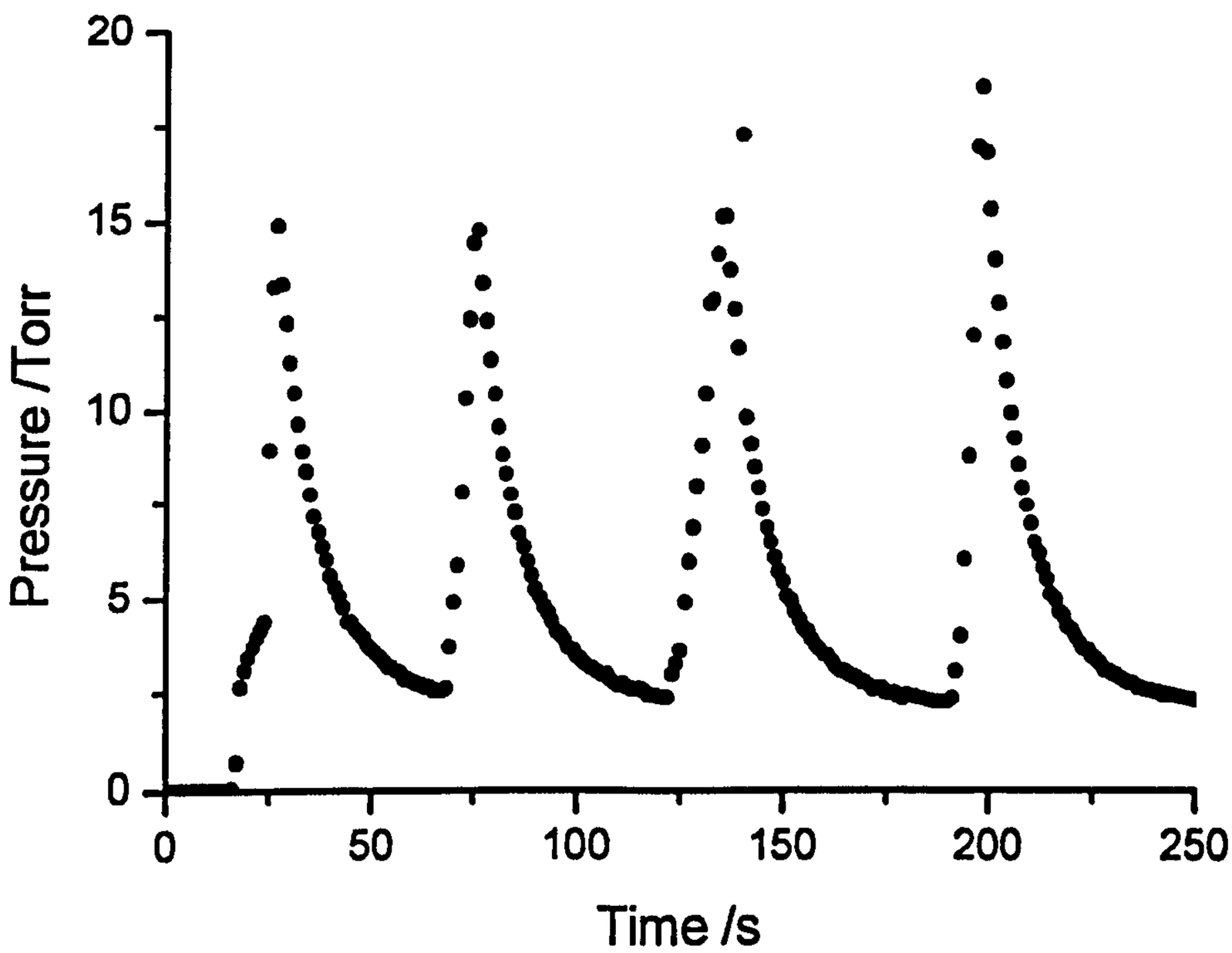

Figure 5.3.2 – The *puff by puff pressure in the astigmatic Herriott cell.*

In the experiment used as an example for Figure 5.3.2, four puffs were recorded in the space of 250s. In the 10μm experiments the pressure was not logged for each of the spectra recorded, however the peak pressure for each puff was noted. Due to the scattering of the laser beam by large molecules in the smoke stream the background pulse was scaled to fit the spectrum pulse to correct for the scattering, which gives information about the particulate concentration in the smoke stream. This procedure was done using a LabVIEW vi that looked for parts of the spectrum pulse that exhibited zero absorption and used these points to work out the scale factor to divide the background by. In general the closer to the peak of the puff the larger the scale factor and just before a puff is made, when there is little smoke contents in the cell, the scale factor is close to 1. The peak concentration for each of the gases studied was calculated for each puff using the concentration retrieval technique described in section 3.1.

5.3.6 Results – 10μm

The laser was driven with a 5A drive current of pulse width 140ns and a repetition rate of 15KHz. The base temperature of the laser was maintained at -1.52°C. Each of the spectra recorded was an average of 5000 scans giving a temporal resolution of ⅓s. Only the Marlboro Lights were used in the 10μm experiments. The spectrum recorded at the peak pressure of puff one compared to a broadened Ethylene FTS spectrum [11] is shown in Figure 5.3.3.

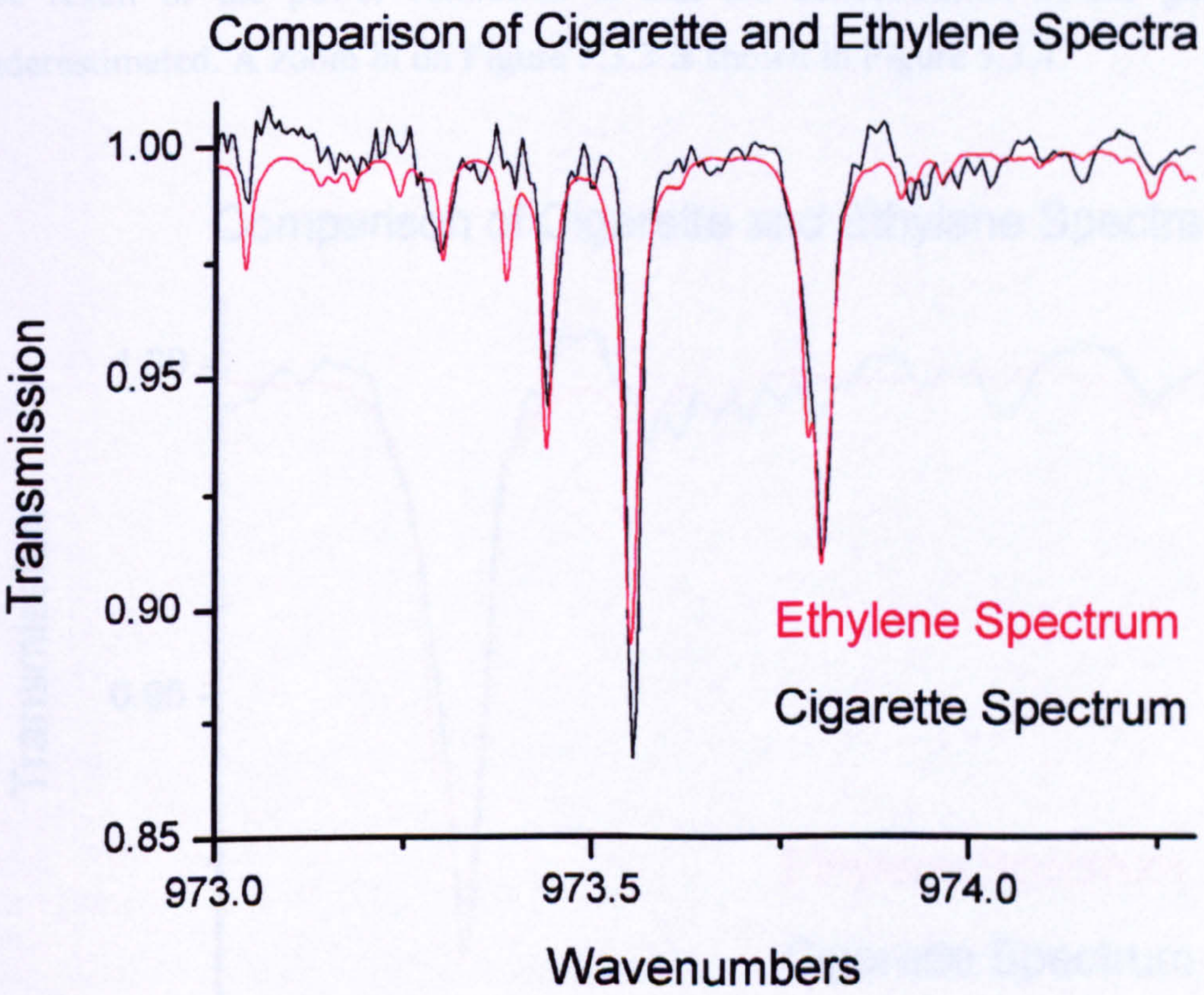

Figure 5.3.3 – *The Black trace shows the spectrum of the first puff of cigarette smoke. The Red trace shows a high resolution spectrum of Ethylene numerically broadened to a resolution of 0.12cm^{-1} recorded by the PNNL FTS.*

The Quantum Cascade spectrometer cigarette trace appears very noisy compared to the FTS Ethylene spectrum, however many of the features in the cigarette trace are real

absorption features. When compared to neat gas spectra using the same laser settings the signal to noise of my spectrometer is sufficient to see features as small as those in the cigarette trace above the genuine noise level. It can be seen that the relative intensities of the three strongest features do not match for the two traces. This can be explained by two different phenomena. The first is the that the absorption from the unknown gases is very different where the three strong Ethylene features are present, however the absorption over the rest of the spectrum from the unknown gases is fairly small compared to the strong Ethylene features. The more likely explanation is power saturation. This phenomena is explained, using Ethylene as an example, in section 4.1. The result of the power saturation is that the concentration of the gases may be underestimated. A zoom in on Figure 5.3.3 is shown in Figure 5.3.4.

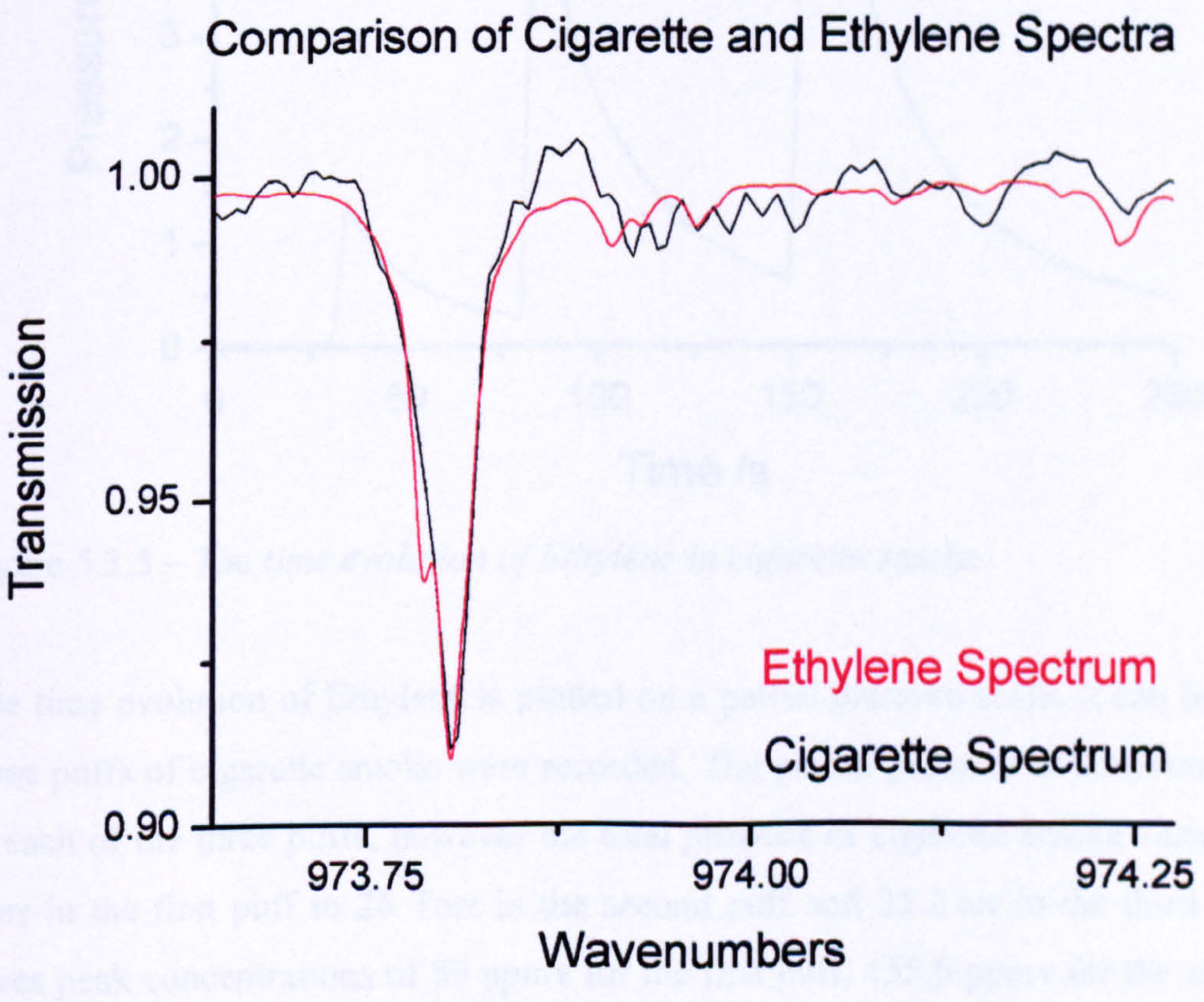

Figure 5.3.4 – *A zoom of Figure 5.3.3.*

The absorption of unknown gases can be seen across the entire zoomed spectrum. The FTS spectrum [11] used to compare with the cigarette spectrum was recorded at a resolution of 0.002cm^{-1} and numerically broadened to a resolution of 0.01cm^{-1}. The time evolution of the Ethylene in cigarette smoke is shown in Figure 5.3.5.

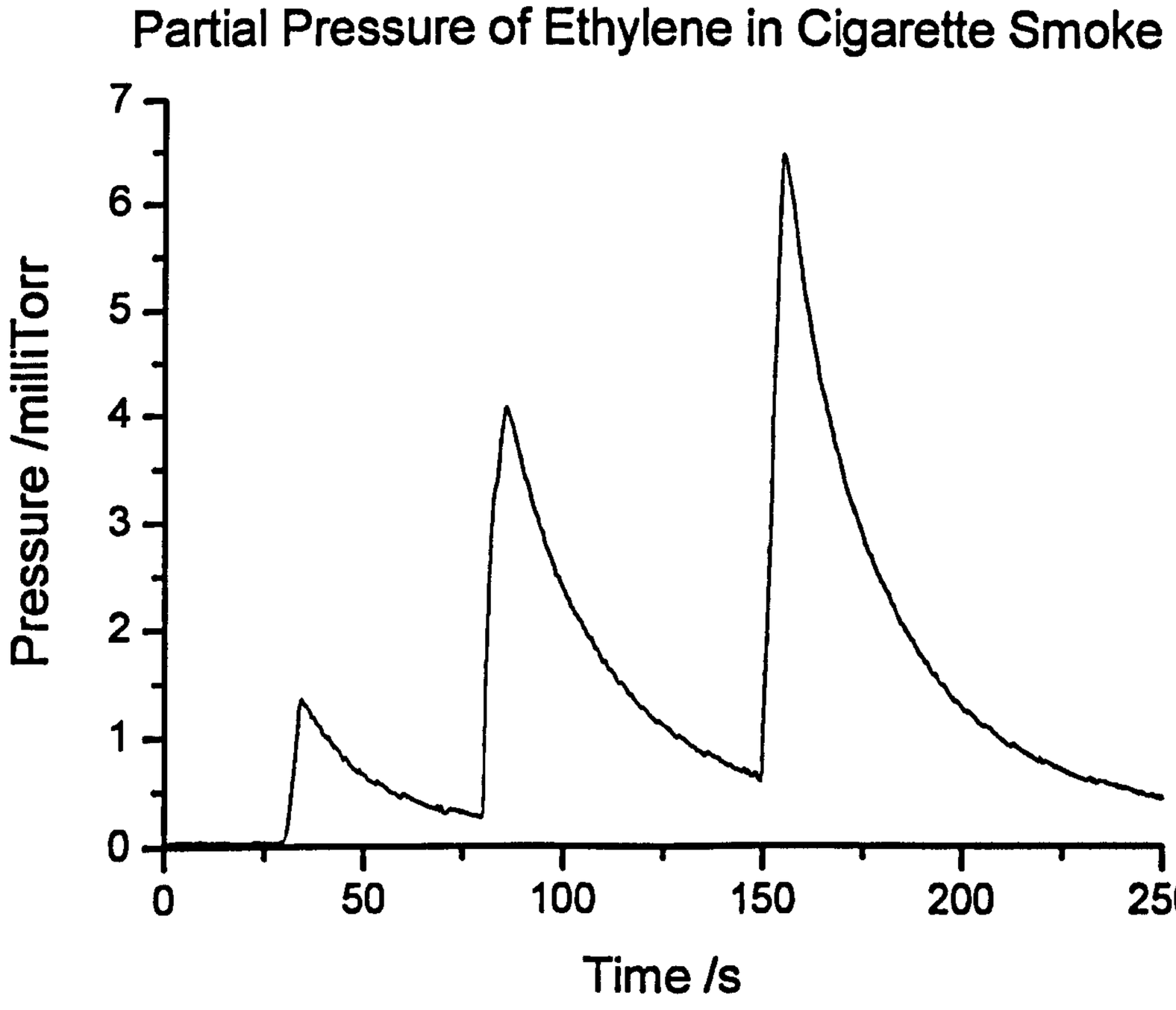

Figure 5.3.5 – *The time evolution of Ethylene in cigarette smoke.*

The time evolution of Ethylene is plotted on a partial pressure scale. It can be seen that three puffs of cigarette smoke were recorded. The partial pressure of Ethylene increases in each of the three puffs, however the total pressure of cigarette smoke varies from 23 Torr in the first puff to 26 Torr in the second puff and 25 Torr in the third puff. This gives peak concentrations of 59 ppmv for the first puff, 155.6 ppmv for the second puff and 259.3 ppmv for the third puff.

The base temperature of the laser was changed to +11°C and the repetition rate was increased to 20KHz. Each of the spectra recorded was an average of 10000 scans giving

a temporal resolution of 0.5s. By increasing the base temperature of the laser and the repetition rate the starting wavelength of the laser was increased, which allowed the laser to access a strong Ammonia line. A new cigarette from the same packet was used to repeat the measurements. The cigarette smoke spectrum recorded at the peak of puff one compared to a broadened Ethylene FTS spectrum [11] is shown in Figure 5.3.6.

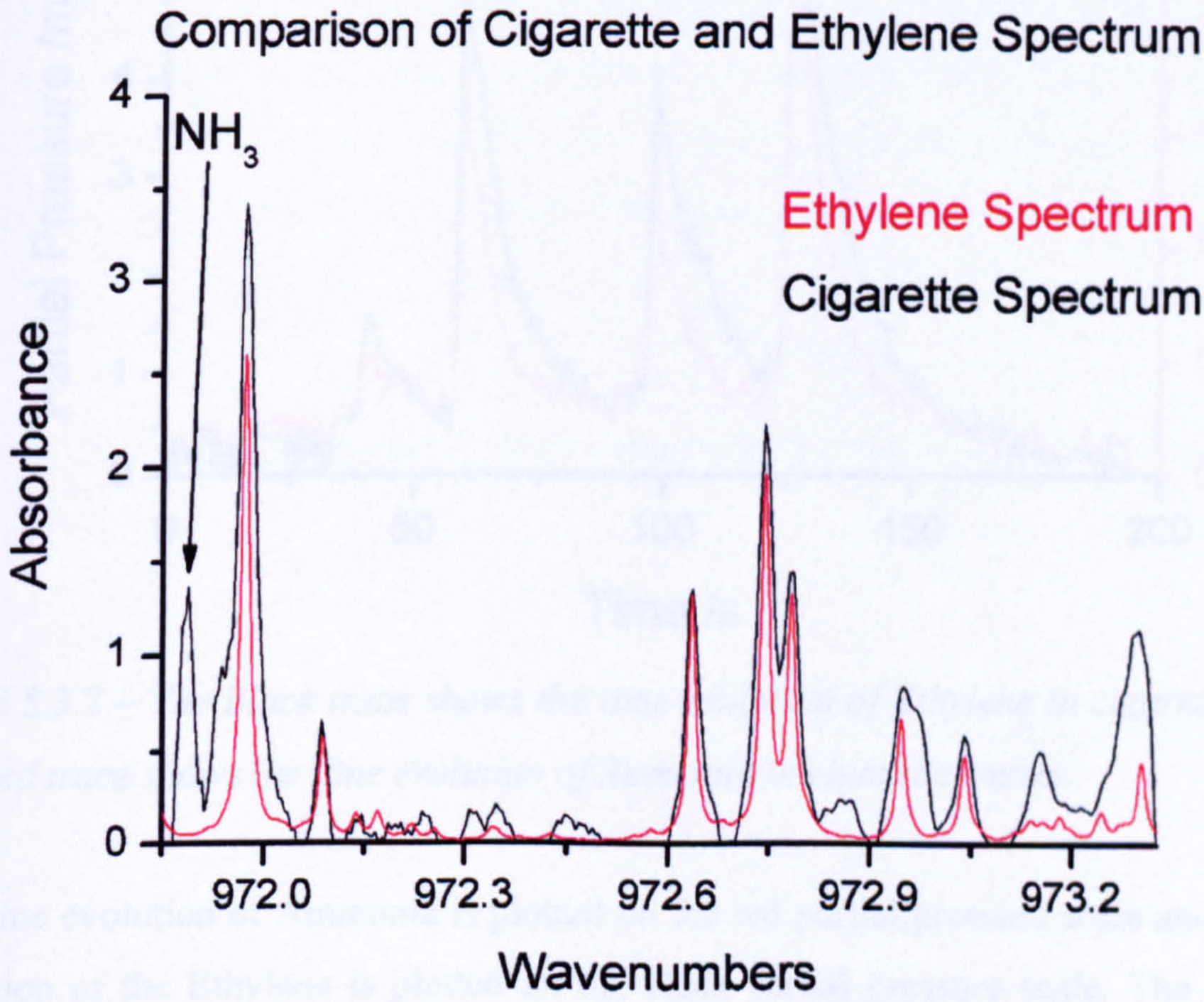

Figure 5.3.6 – *The Black trace shows the spectrum of the first puff of cigarette smoke. The Red trace shows a high resolution spectrum of Ethylene numerically broadened to a resolution of 0.12cm^{-1} recorded by the PNNL FTS.*

Both spectra are plotted on an absorbance scale, which is the negative natural logarithm of the transmission scale. Even though the laser has been tuned in wavelength there are still several unidentified lines. The Ammonia line highlighted at 971.85cm-1 is the only strong Ammonia absorption line in the operating range of the 10μm laser. The time evolution of the Ethylene and Ammonia in cigarette smoke is shown in Figure 5.3.7.

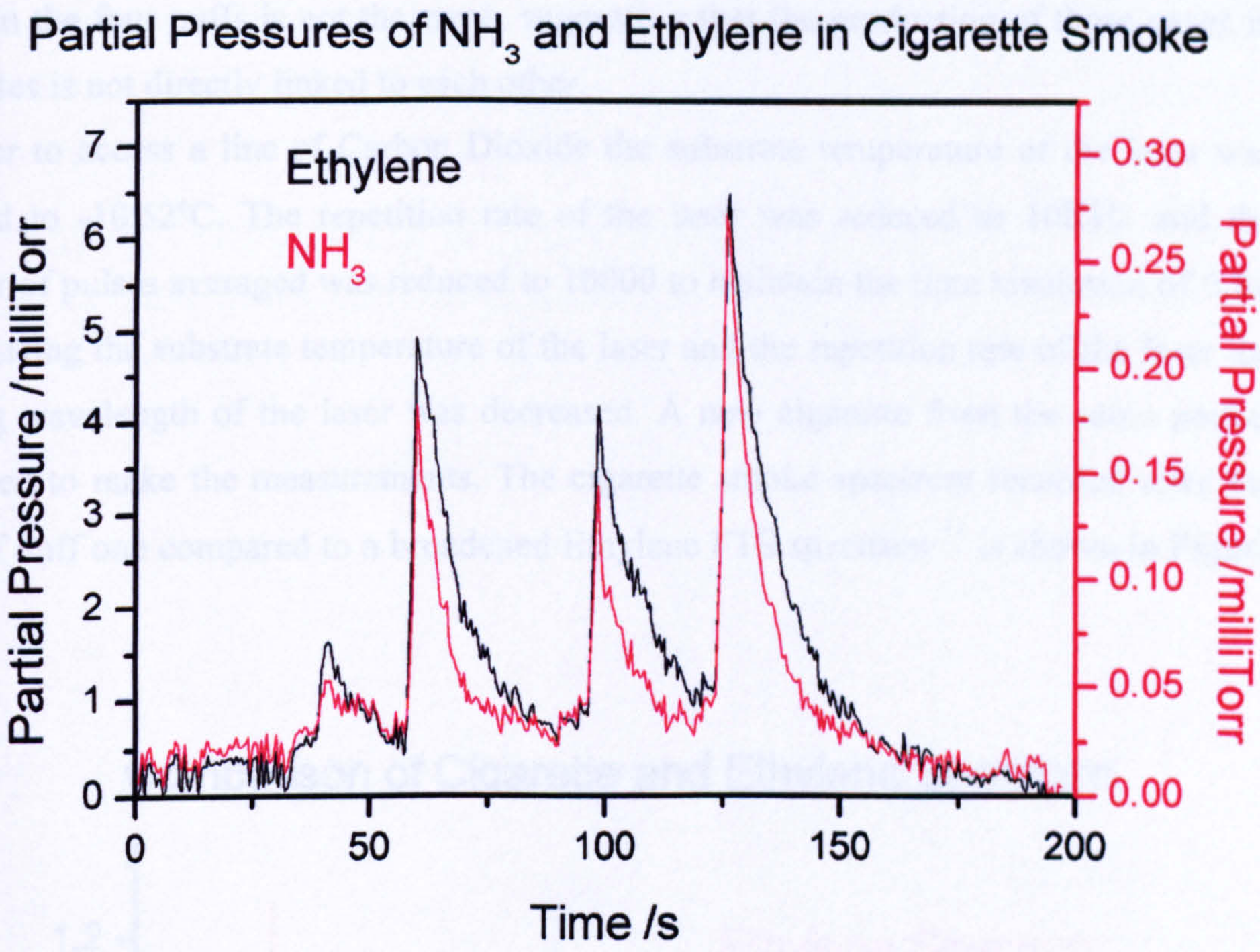

Figure 5.3.7 – *The Black trace shows the time evolution of Ethylene in cigarette smoke. The Red trace shows the time evolution of Ammonia in cigarette smoke.*

The time evolution of Ammonia is plotted on the red partial pressure scale and the time evolution of the Ethylene is plotted on the black partial pressure scale. The increased noise on the traces compared to the previous experiment can be explained by two things. The first is that the lines used to calculate the concentrations of Ethylene and Ammonia absorbed less light than the Ethylene line used in the first measurement. The second factor is the power of the laser; the higher temperature of the second experiment compared to the first experiment means that the total power emitted from the laser was less for the second experiment. The peak pressures for the four puffs in order of first puff to last puff were 11Torr, 20Torr, 16Torr and 26Torr. This gives peak concentrations for each of the four puffs for Ammonia of 4.79ppmv, 9.05ppmv, 8.93ppmv and 10.45ppmv. The peak concentrations of Ethylene for the four puffs were 148ppmv,

246.5ppmv, 261ppmv and 250ppmv. The relative concentration of the two gases between the four puffs is not the same, suggesting that the production of these gases in cigarettes is not directly linked to each other.

In order to access a line of Carbon Dioxide the substrate temperature of the laser was reduced to -10.52°C. The repetition rate of the laser was reduced to 10KHz and the number of pulses averaged was reduced to 10000 to maintain the time resolution of 0.5s.

By reducing the substrate temperature of the laser and the repetition rate of the laser the starting wavelength of the laser was decreased. A new cigarette from the same packet was used to make the measurements. The cigarette smoke spectrum recorded after the peak of puff one compared to a broadened Ethylene FTS spectrum [11] is shown in Figure 5.3.8.

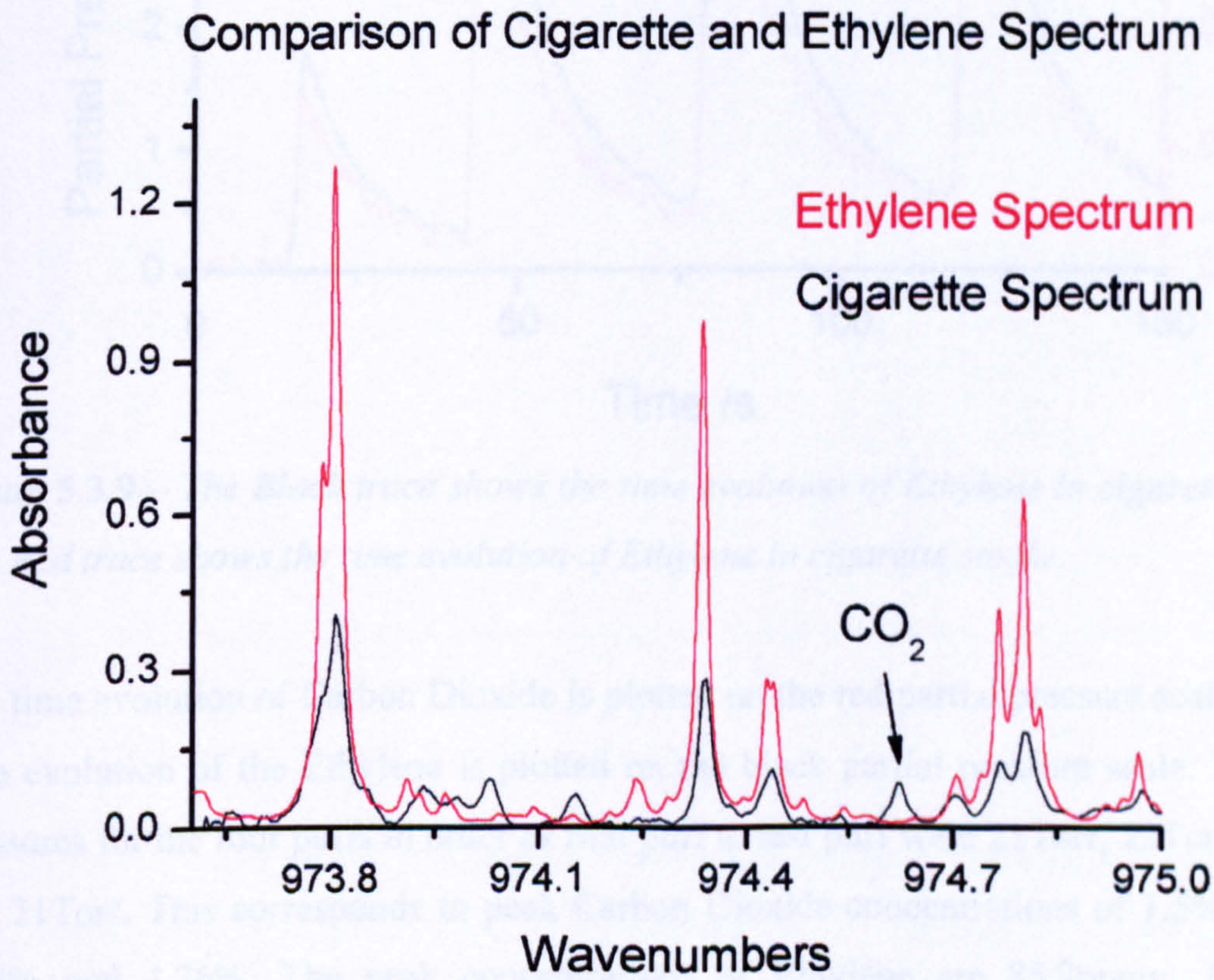

Figure 5.3.8 – *The Black trace shows the spectrum of the first puff of cigarette smoke. The Red trace shows a high resolution spectrum of Ethylene numerically broadened to a resolution of 0.12cm^{-1} recorded by the PNNL FTS.*

The time evolution of the Ethylene and Carbon Dioxide in cigarette smoke is shown in Figure 5.3.9.

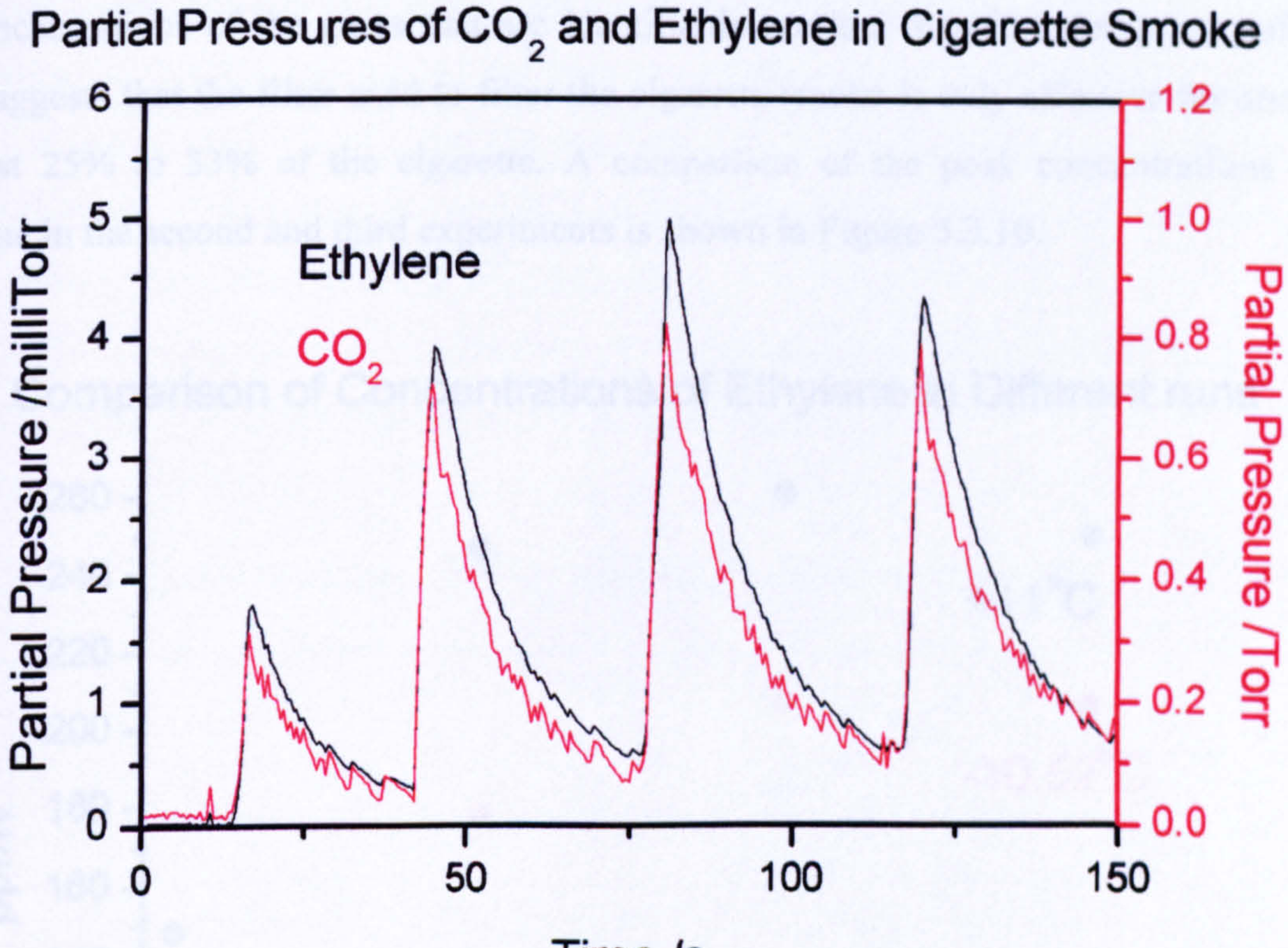

Figure 5.3.9 – *The Black trace shows the time evolution of Ethylene in cigarette smoke. The Red trace shows the time evolution of Ethylene in cigarette smoke.*

The time evolution of Carbon Dioxide is plotted on the red partial pressure scale and the time evolution of the Ethylene is plotted on the black partial pressure scale. The peak pressures for the four puffs in order of first puff to last puff were 21Torr, 22Torr, 24Torr and 21Torr. This corresponds to peak Carbon Dioxide concentrations of 1.5%, 3.27%, 3.42% and 3.76%. The peak concentrations of Ethylene are 85.2ppmv, 178ppmv, 207ppmv and 206ppmv.

5.3.7 Discussion – 10μm

From the work that I have carried out at 10μm there appears to be a pattern in the emission of gases from cigarettes. That pattern is that in the first of three or four puffs the concentrations of the gases that are identifiable are less than in subsequent puffs. This suggests that the filter used to filter the cigarette smoke is only effective for about the first 25% to 33% of the cigarette. A comparison of the peak concentrations of Ethylene in the second and third experiments is shown in Figure 5.3.10.

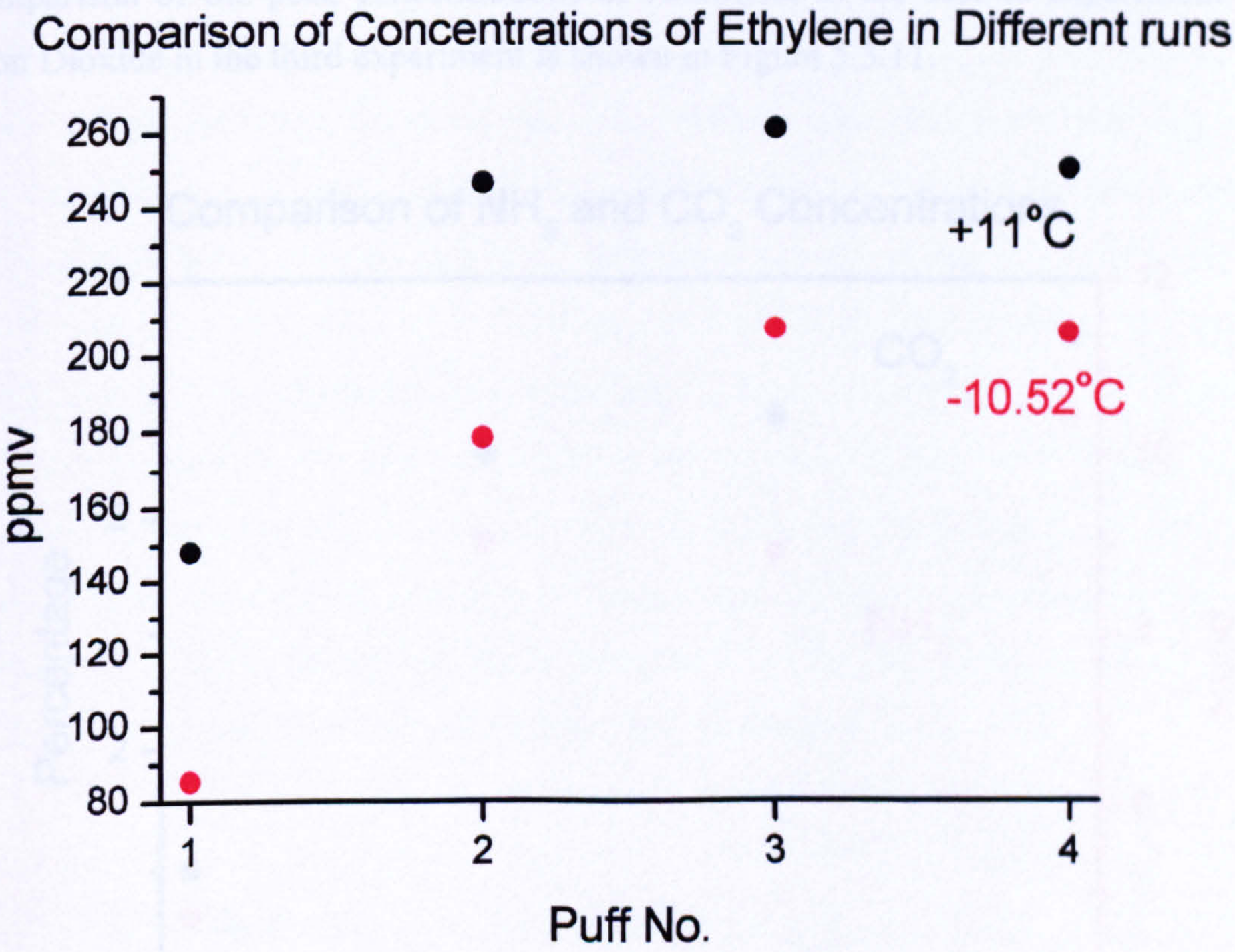

Figure 5.3.10 – *The Black dots show the peak Ethylene concentrations for the second experiment. The Red dots show the peak Ethylene concentrations for the third experiment.*

The results of the first experiment were not used due to the lower number of puffs in the first experiment compared to the subsequent two experiments. The substrate temperature

of the laser is used to identify the data from the two experiments. The pattern observed between the two experiments is almost identical. There is however an offset of approximately 50ppmv. This offset may be explained in a number of ways. The first is that there was a difference between the two cigarettes, which is unlikely given the mass manufacturing techniques used to produce these cigarettes. The second, and more likely explanation, is that the intensity of the smoking of the cigarettes differed between the two experiments. This would cause the final ratios of exhaust products to differ. With many thousands of exhaust products only a slight change in the smoking technique could produce a very large change in output products.

A comparison of the peak concentrations of Ammonia in the second experiment and Carbon Dioxide in the third experiment is shown in Figure 5.3.11.

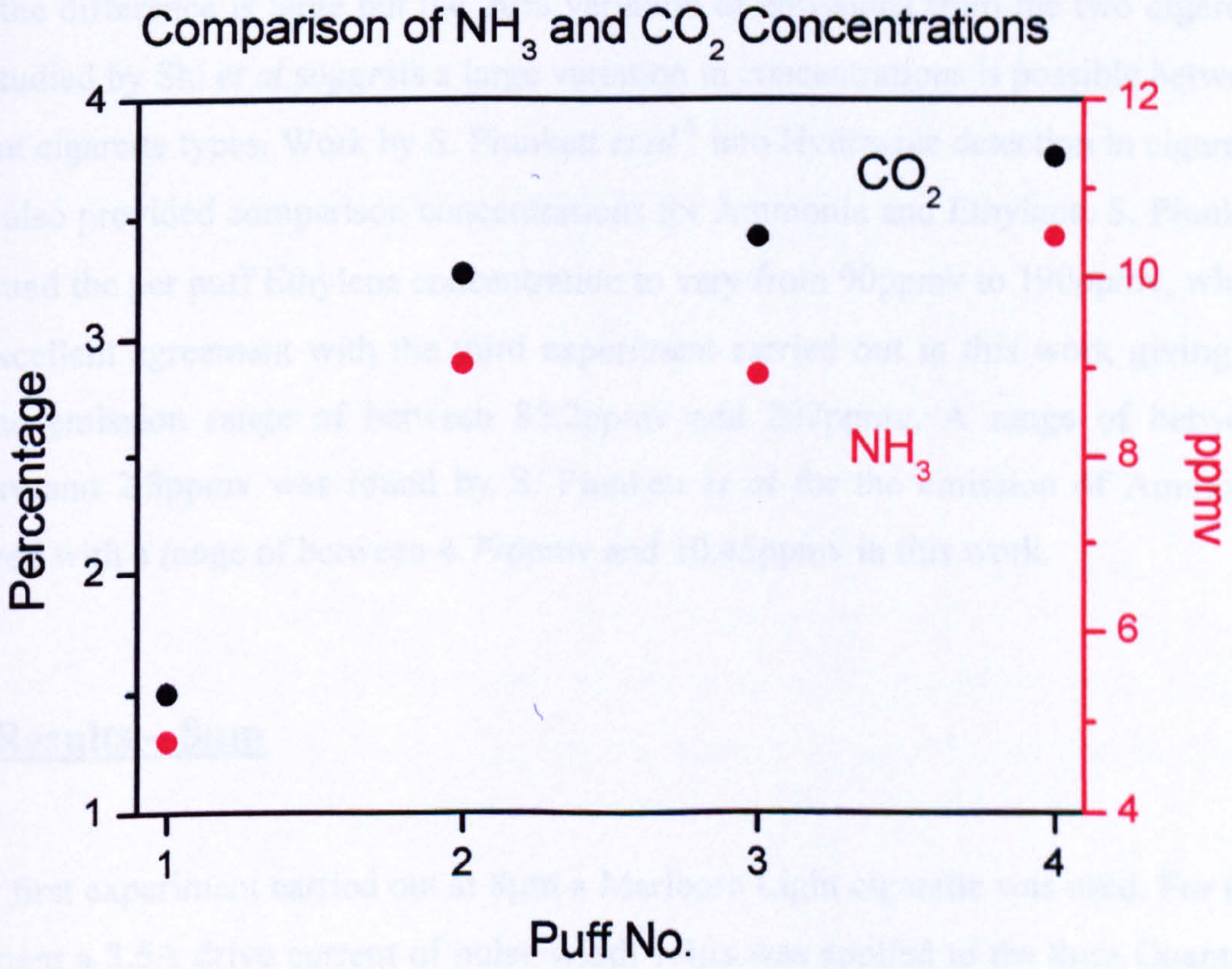

Figure 5.3.11 – *The Black dots show the peak Carbon Dioxide concentrations for the third experiment. The Red dots show the peak Ammonia concentrations for the second experiment.*

The Carbon Dioxide concentrations are plotted on the percentage scale and the Ammonia concentrations are plotted on the ppmv scale. A similar pattern of peak concentrations for the two gases is observed. This pattern is also similar to the pattern observed in the Ethylene concentrations. The comparison of the concentrations found in my study and previous work [6] is favourable. Two cigarette types were studied by Shi *et al.* giving an average per puff emission of Ammonia of 3ppmv and 10ppmv for the two cigarettes compared to 8.3ppmv in this work. Shi *et al* found an average puff emission of Carbon Dioxide of 7.3% and 9% for the two cigarette types studied compared to 3% in this work. The decreased levels of Carbon Dioxide in this work may be due to cigarette differences compared to the work of Shi *et al.* In this work an average puff emission of Ethylene of 200ppmv was found compared to 860ppmv and 1054ppmv from Shi *et al.* Again the difference is large but the 20% variation of emissions from the two cigarette types studied by Shi *et al* suggests a large variation in concentrations is possible between different cigarette types. Work by S. Plunkett *et al* [8] into Hydrazine detection in cigarette smoke also provided comparison concentrations for Ammonia and Ethylene. S. Plunkett *et al* found the per puff Ethylene concentration to vary from 90ppmv to 190ppmv, which is in excellent agreement with the third experiment carried out in this work giving an Ethylene emission range of between 85.2ppmv and 207ppmv. A range of between 0.5ppmv and 2.8ppmv was found by S. Plunkett *et al* for the emission of Ammonia compared with a range of between 4.79ppmv and 10.45ppmv in this work.

5.3.8 Results – 8μm

For the first experiment carried out at 8μm a Marlboro Light cigarette was used. For this experiment a 3.5A drive current of pulse width 1.4μs was applied to the 8μm Quantum Cascade laser. A pulse repetition rate of 20KHz was used. The substrate temperature of the laser was maintained at +3°C. Each of the spectra is an average of 20000 pulses. The

spectrum of the peak of the first puff is compared with the spectrum of Formaldehyde in Figure 5.3.12.

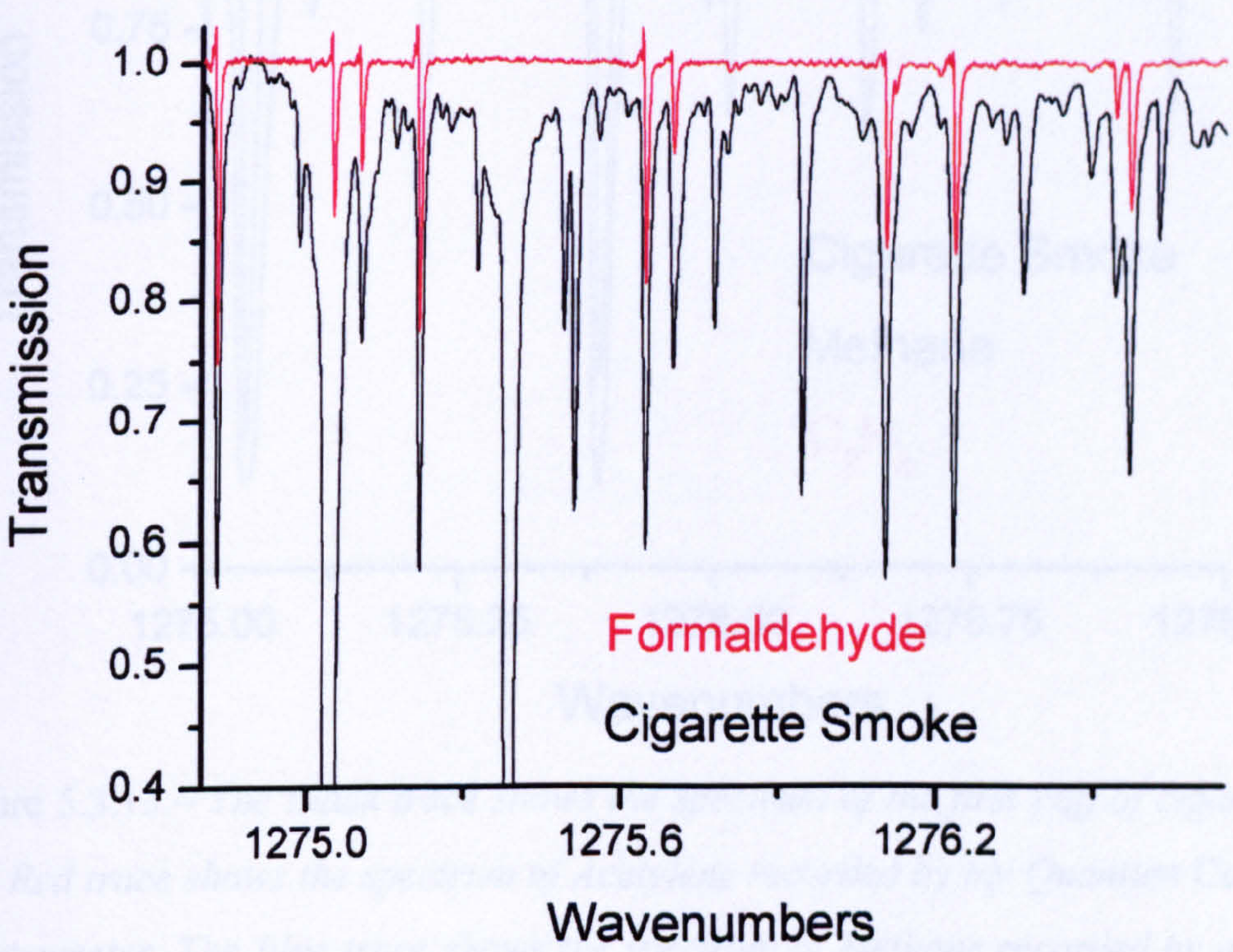

Figure 5.3.12 – *The Black trace shows the spectrum of the first puff of cigarette smoke. The Red trace shows the spectrum of Formaldehyde recorded by my Quantum Cascade laser spectrometer.*

The comparison spectrum was recorded with 0.2Torr of Formaldehyde in the 115m astigmatic Herriott cell. The same cigarette spectrum is compared with the spectra of Acetylene and Methane in Figure 5.3.13.

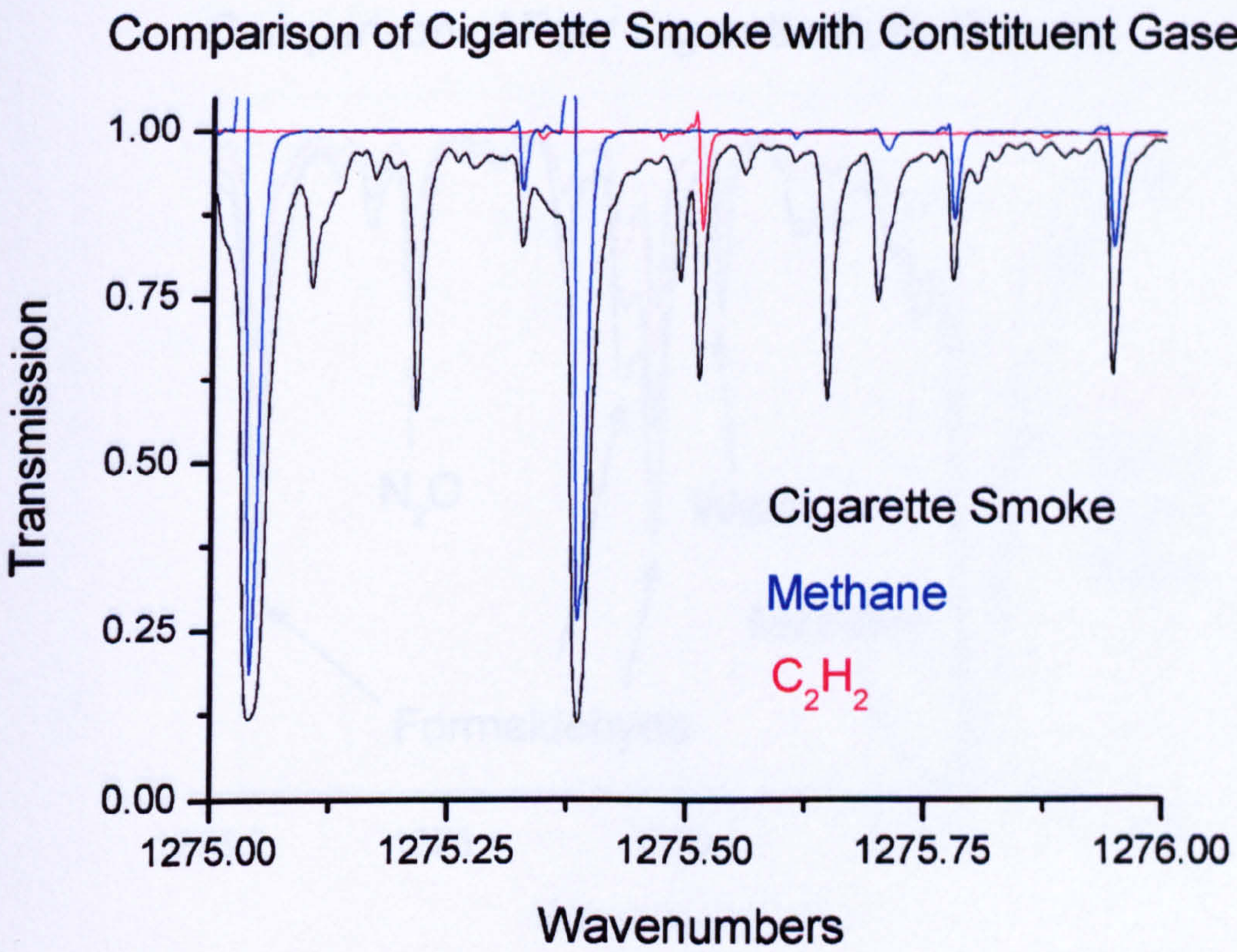

Figure 5.3.13 – *The Black trace shows the spectrum of the first puff of cigarette smoke. The Red trace shows the spectrum of Acetylene recorded by my Quantum Cascade laser spectrometer. The Blue trace shows the spectrum of Methane recorded by my Quantum Cascade laser spectrometer.*

The Methane comparison spectrum was recorded in the 115m astigmatic Herriott cell with 5milliTorr of pure gas. The Acetylene comparison spectrum was recorded in the 115m astigmatic Herriott cell with 8milliTorr of pure gas.

A comparison of the spectra from each of the first four puffs is shown in Figure 5.3.14.

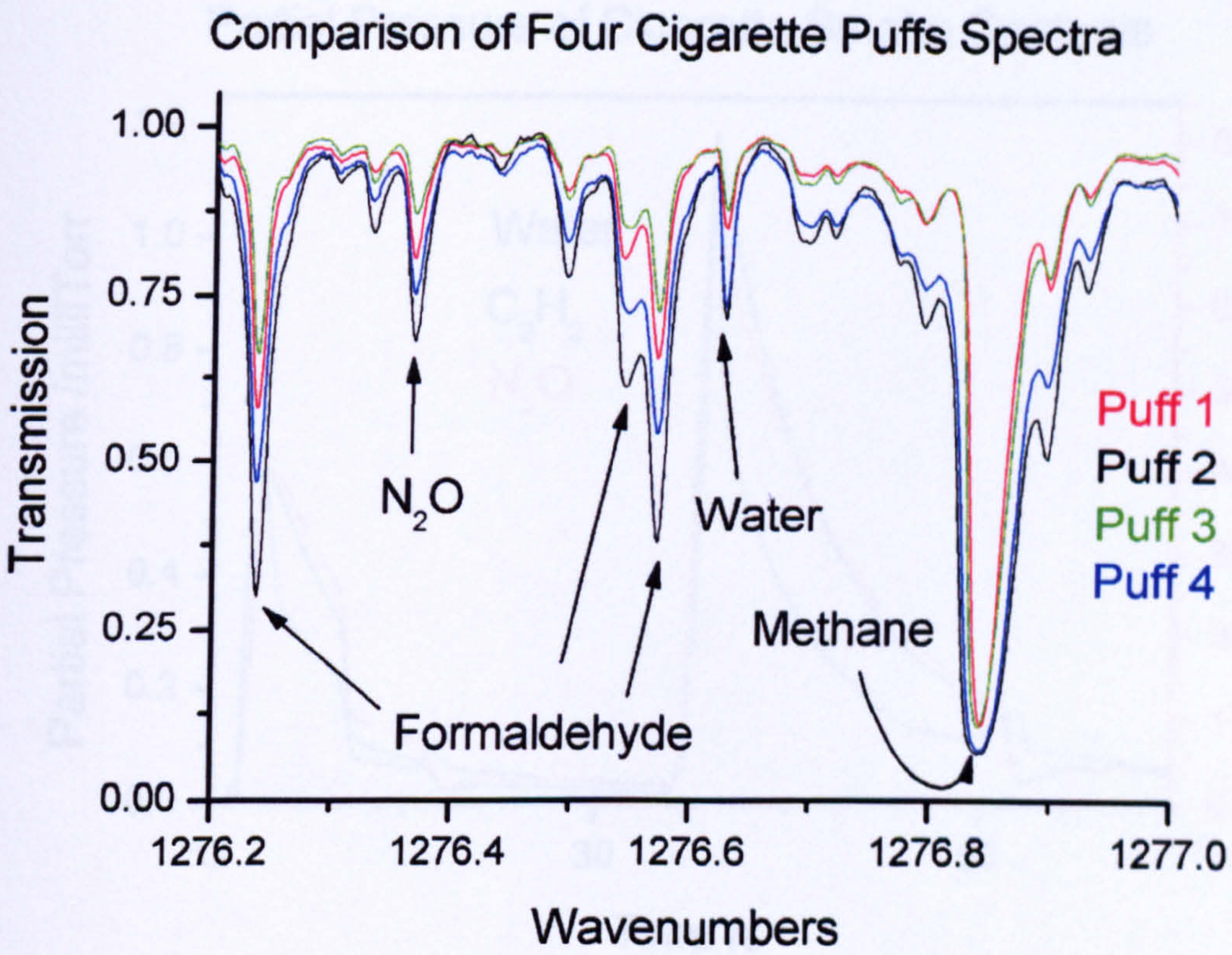

Figure 5.3.14 – *The Red trace shows the spectrum of the first puff. The Black trace shows the spectrum of the second puff. The Green trace shows the spectrum of the third puff. The Blue trace shows the spectrum of the fourth puff.*

The amount of general absorption is different in each of the first four puffs. The relative intensities of some of the absorption lines changes from the first puff to the fourth puff. The partial pressures of Water, Acetylene and Nitrous Oxide for the first two puffs of the cigarette are shown in Figure 5.3.15.

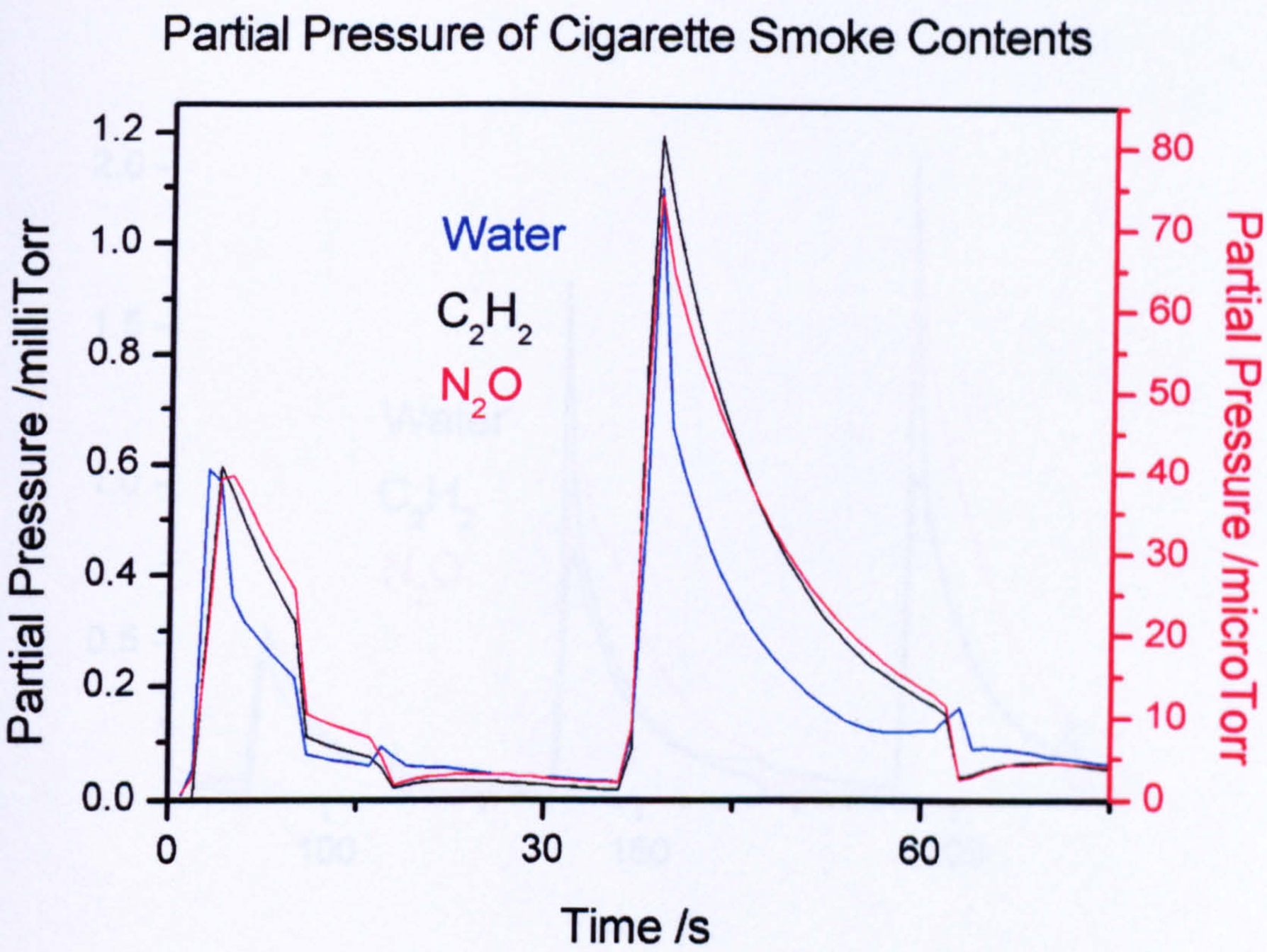

Figure 5.3.15 – *The Black trace shows the time evolution of Acetylene in cigarette smoke. The Red trace shows the time evolution of Nitrous Oxide in cigarette smoke. The Blue trace shows the time evolution of Water in cigarette smoke.*

The Acetylene and the Water traces are plotted on the milliTorr partial pressure scale and the Nitrous Oxide trace is plotted on the microTorr partial pressure scale.
The partial pressures of Water, Acetylene and Nitrous Oxide for the third, fourth and fifth puffs of the cigarette are shown in Figure 5.3.16.

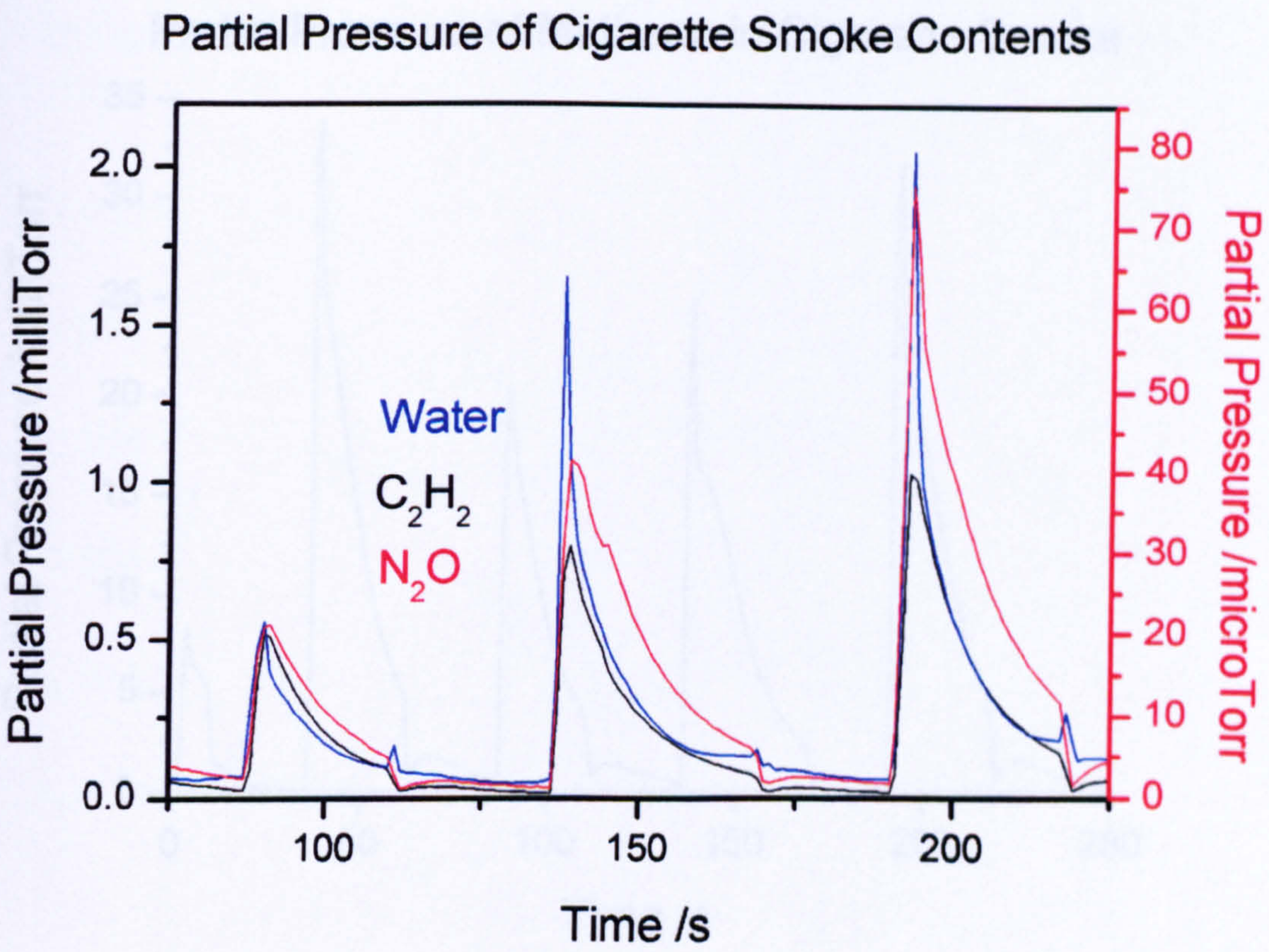

Figure 5.3.16 – *The Black trace shows the time evolution of Acetylene in cigarette smoke. The Red trace shows the time evolution of Nitrous Oxide in cigarette smoke. The Blue trace shows the time evolution of Water in cigarette smoke.*

The Nitrous Oxide trace is plotted on the microTorr partial pressure scale and the Acetylene and the Water traces are plotted on the milliTorr partial pressure scale. The pressures in the cell for the five puffs were 21Torr, 26.5Torr, 25.8Torr, 28Torr and 27Torr.

The partial pressure of Methane for the five puffs of the cigarette is shown in Figure 5.3.17.

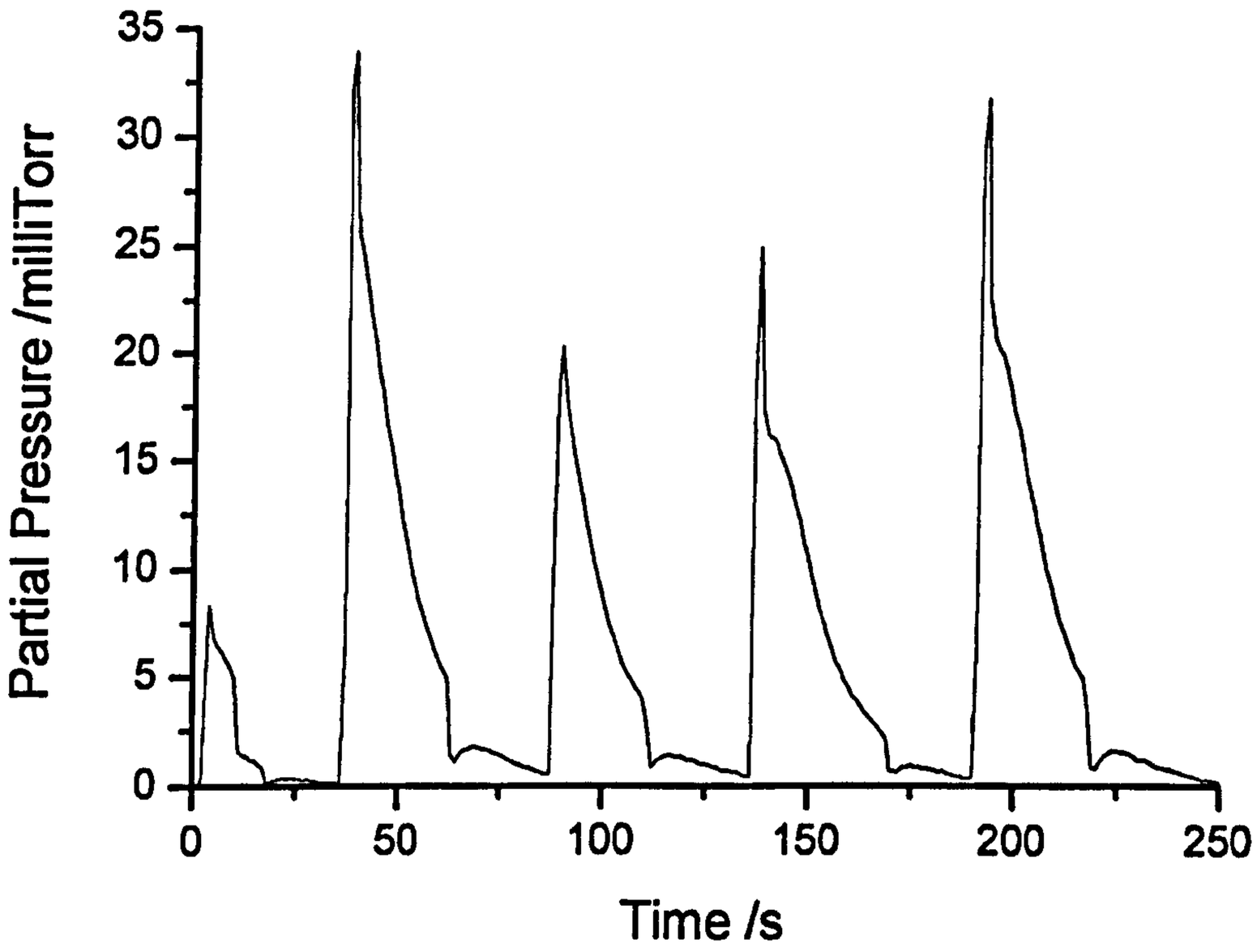

Figure 5.3.17 – *The time evolution of Methane in cigarette smoke.*

Using the peak pressures of the four puffs the maximum concentrations of the gases can be calculated. The peak concentrations of Water are 28.1ppmv, 41.58ppmv, 21.63ppmv, 59.14ppmv and 76.07ppmv. The peak concentrations of Nitrous Oxide for the five puffs are 1.85ppmv, 2.8ppmv, 0.82ppmv, 1.47ppmv and 2.79ppmv. For the five cigarette puffs the peak concentrations of Acetylene are 28.38ppmv, 45.15ppmv, 19.96ppmv, 28.38ppmv and 38.03ppmv. The peak concentrations of Methane are 394.7ppmv, 1281.5ppmv, 784.9ppmv, 890.4ppmv and 1180.7ppmv. As well as the four gases identified above Formaldehyde was also identified in the spectrum of cigarette smoke, however the integrated intensity for the lines in the region over which the laser emitted could not be found. The integrated absorption of the Formaldehyde is shown in Figure 5.3.18.

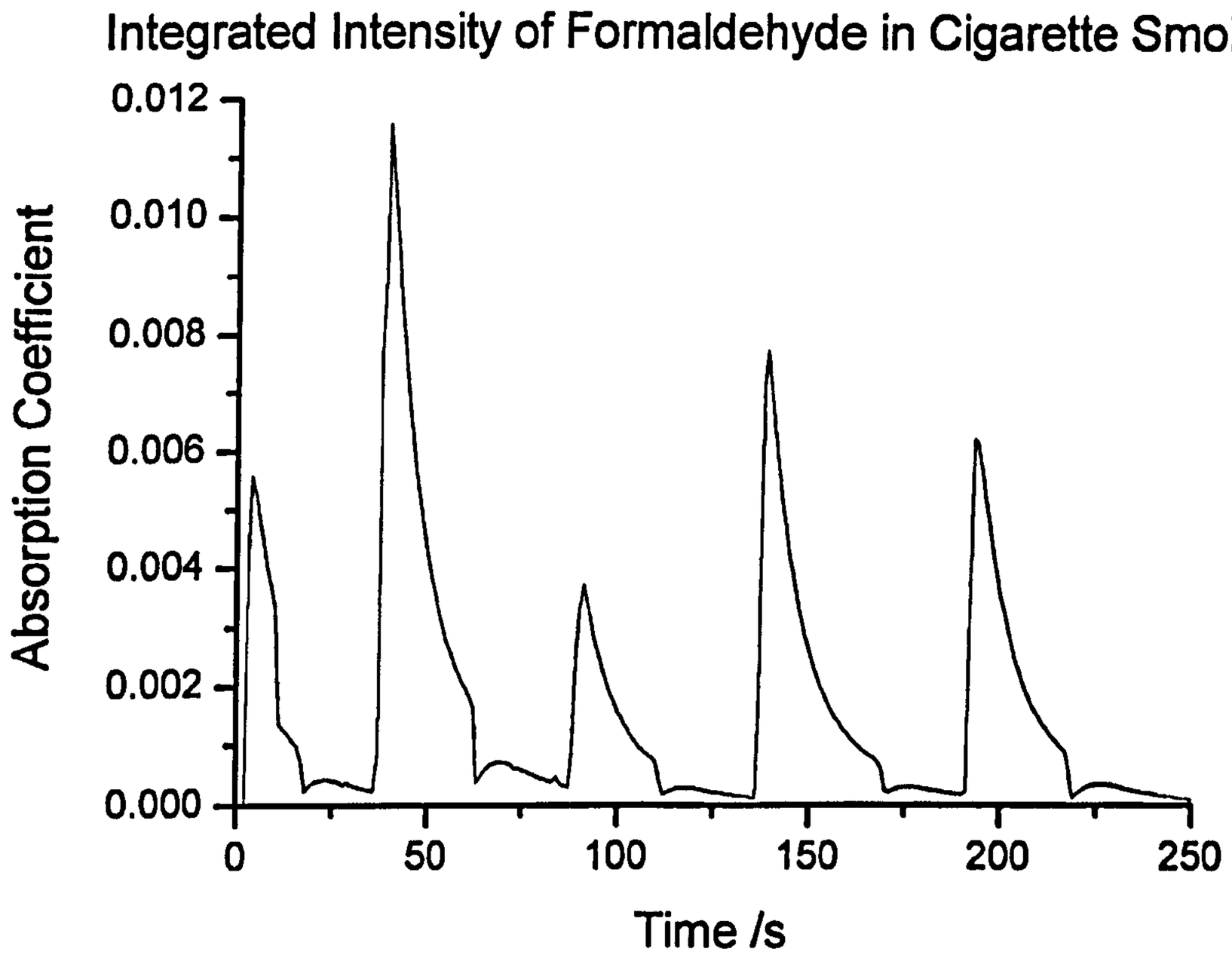

Figure 5.3.18 – *The integrated intensity of the Formaldehyde in cigarette smoke.*

It can be seen that the concentration of Formaldehyde is greatest in the second puff, which is not what would be expected [4] from previous work. The first puff was expected to contain the largest concentration of Formaldehyde. From a cigarette smoked using nine puffs M. E. Parrish [4] found that the first puff gave the largest Formaldehyde concentration and that the subsequent puffs showed a decreased Formaldehyde concentration until the Formaldehyde concentration increased for the last three puffs [5]. The first puff is the only puff that the material burned was not preheated. The preheating of the cigarette was found by S. Li *et al* to decrease the Formaldehyde concentration in a puff [5]. An increase in Formaldehyde concentration can be expected in the final puff compared to the previous puff due to the decreased length of the cigarette, which gives a shorter reaction zone for the Formaldehyde to react and form other products. An explanation of the increased second puff Formaldehyde concentration could be that there

is a difference in the cigarettes used in the two studies; also the smoking method may have an effect on the preheating of subsequent puffs.

A comparison of the peak concentrations of Water, Nitrous Oxide and Acetylene is shown in Figure 5.3.19.

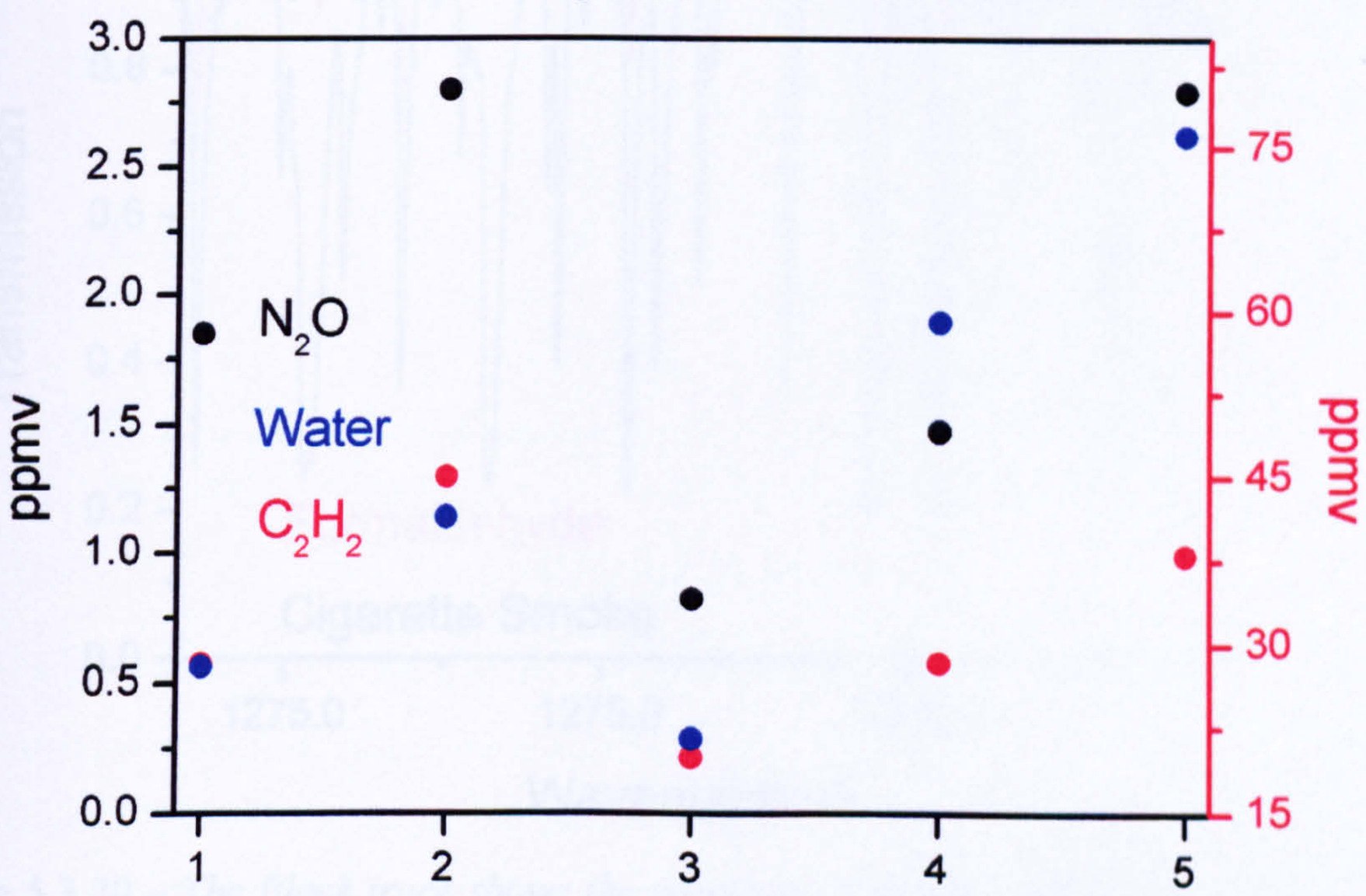

Figure 5.3.19 – *The Black dots show the concentration of Acetylene. The Blue dots show the concentration of Water. The Red dots show the concentration of Nitrous Oxide.*

The Nitrous Oxide concentrations are plotted on the black ppmv scale and the Water and Acetylene concentrations are plotted on the red ppmv scale.

The above experiment was repeated using a cigarette from the same packet; however the cigarettes filter was cut from 25mm to 10mm. This was to test the effect of the filter on cigarette emissions. The Quantum Cascade laser was driven using the same settings as

the above experiment. The spectrum of the peak of the first puff is compared to the spectrum of Formaldehyde in Figure 5.3.20.

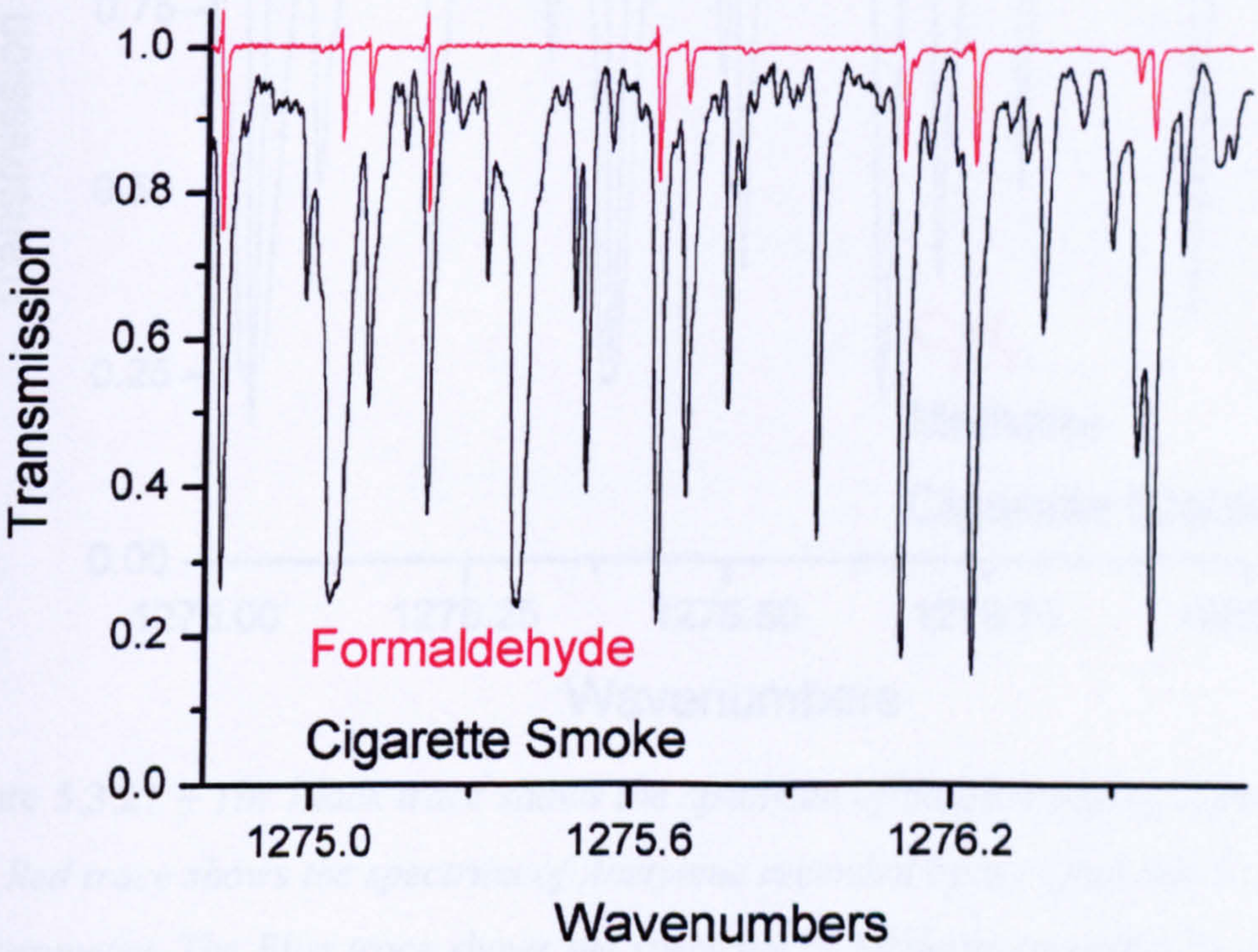

Figure 5.3.20 – *The Black trace shows the spectrum of the first puff of cigarette smoke. The Red trace shows the spectrum of Formaldehyde recorded by my Quantum Cascade laser spectrometer.*

The comparison spectrum was recorded with 0.2Torr of Formaldehyde in the 115m astigmatic Herriott cell. If Figure 5.3.12 is compared to Figure 5.3.20 the change in relative concentrations of the constituent gases of the cigarette smoke can be seen as the filter length is decreased. The same cigarette spectrum is compared with the spectra of Acetylene and Methane in Figure 5.3.21.

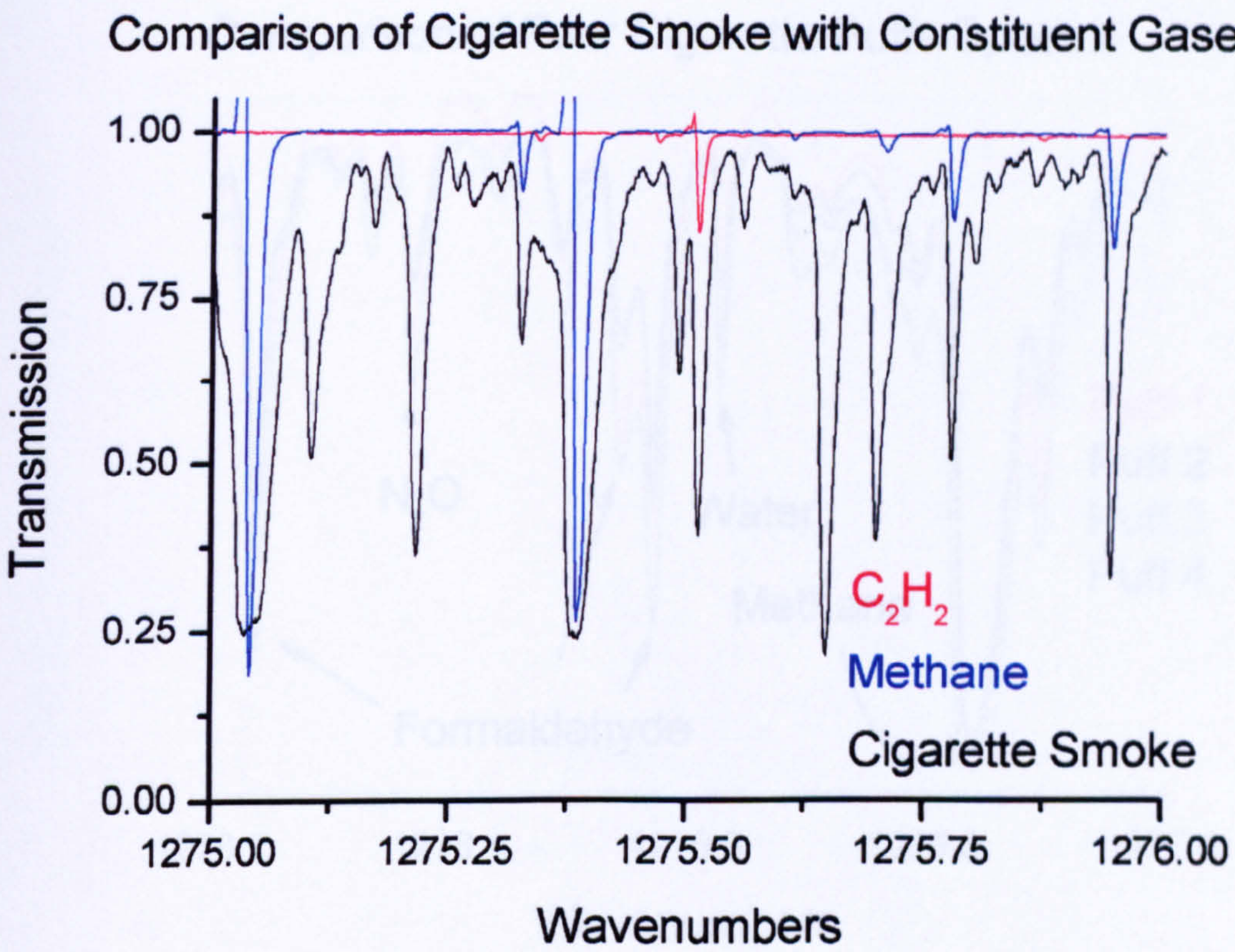

Figure 5.3.21 – *The Black trace shows the spectrum of the first puff of cigarette smoke. The Red trace shows the spectrum of Acetylene recorded by my Quantum Cascade laser spectrometer. The Blue trace shows the spectrum of Methane recorded by my Quantum Cascade laser spectrometer.*

The Methane comparison spectrum was recorded in the 115m astigmatic Herriott cell with 5milliTorr of pure gas. The Acetylene comparison spectrum was recorded in the 115m astigmatic Herriott cell with 8milliTorr of pure gas.

Figure 5.3.22 shows comparison of the spectra from each of the first four puffs recorded.

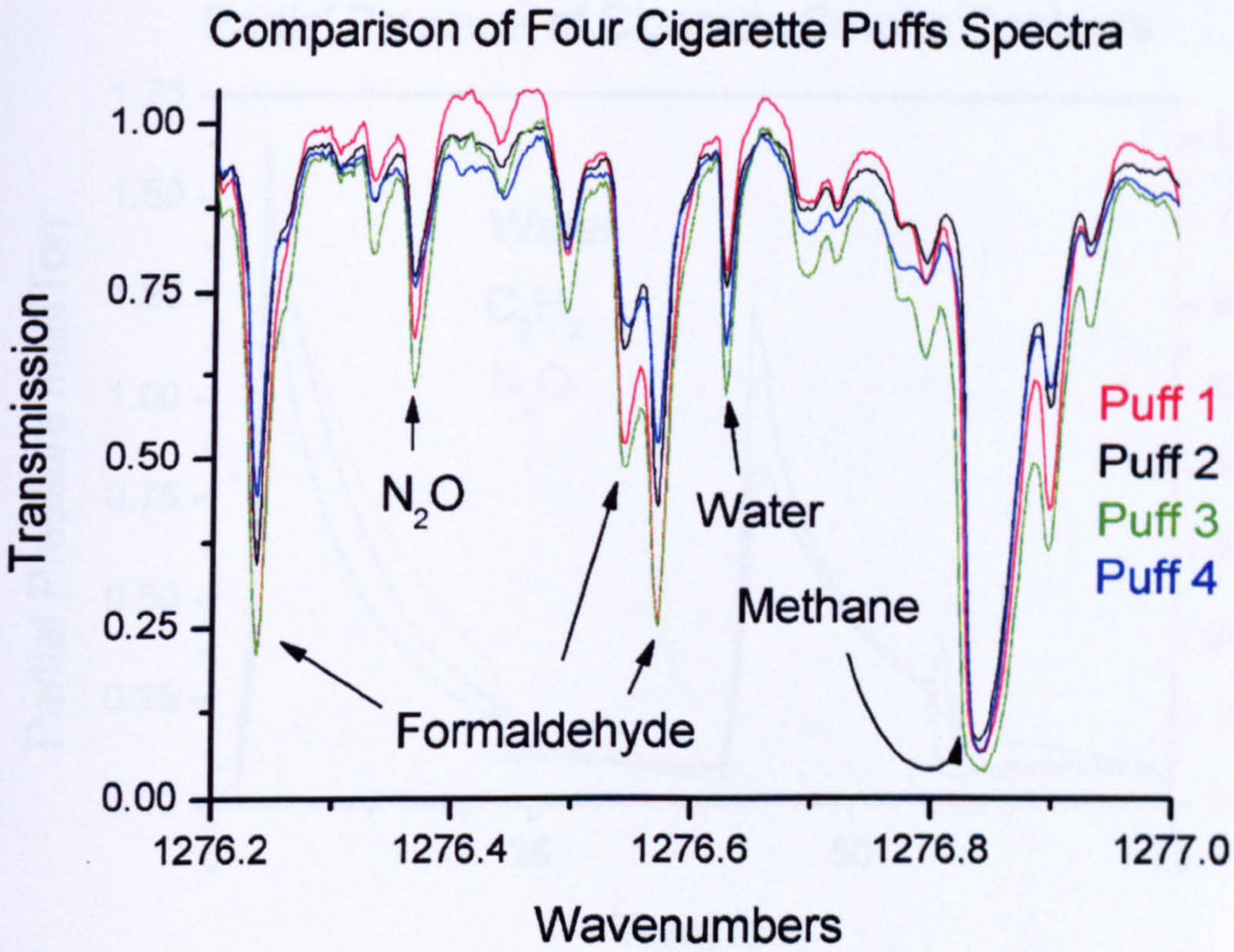

Figure 5.3.22 – *The Red trace shows the spectrum of the first puff. The Black trace shows the spectrum of the second puff. The Green trace shows the spectrum of the third puff. The Blue trace shows the spectrum of the fourth puff.*

The third puff appears to produce the largest amount of absorption quickly followed by the first puff. The second and fourth puffs appear to be similar to each other. The partial pressures of Water, Nitrous Oxide and Acetylene for the first two puffs of the cigarette are shown in Figure 5.3.23.

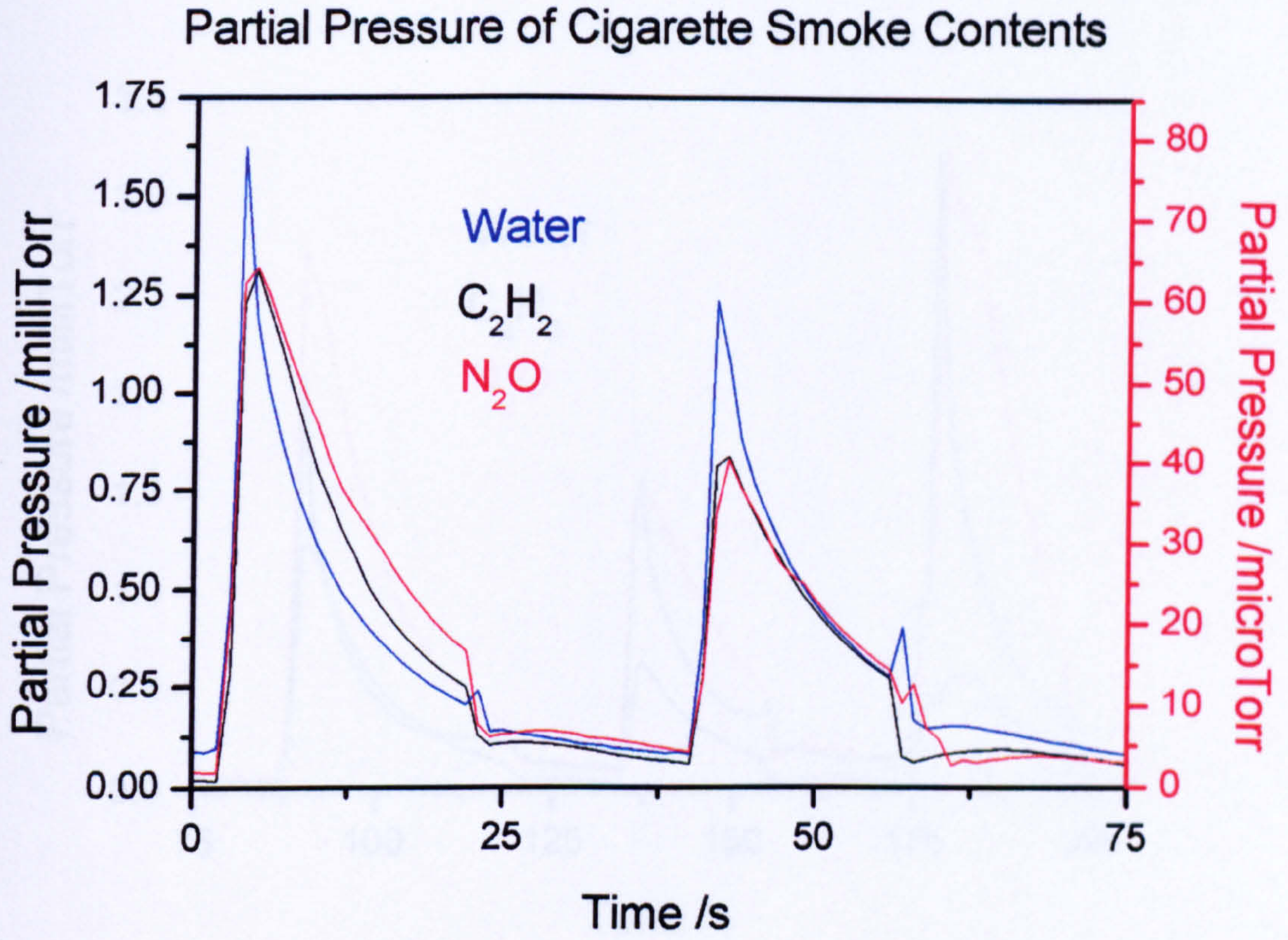

Figure 5.3.23 – *The Black trace shows the time evolution of Acetylene in cigarette smoke. The Red trace shows the time evolution of Nitrous Oxide in cigarette smoke. The Blue trace shows the time evolution of Water in cigarette smoke.*

The Nitrous Oxide pressures are plotted on the microTorr scale and the Acetylene and Water pressures are plotted on the milliTorr scale. The pressures in the cell for the five puffs were 22.2Torr, 18.4Torr, 22.5Torr, 19Torr and 20.1Torr. The partial pressures of Water, Acetylene and Nitrous Oxide for the third, fourth and fifth puffs of the cigarette are shown in Figure 5.3.24.

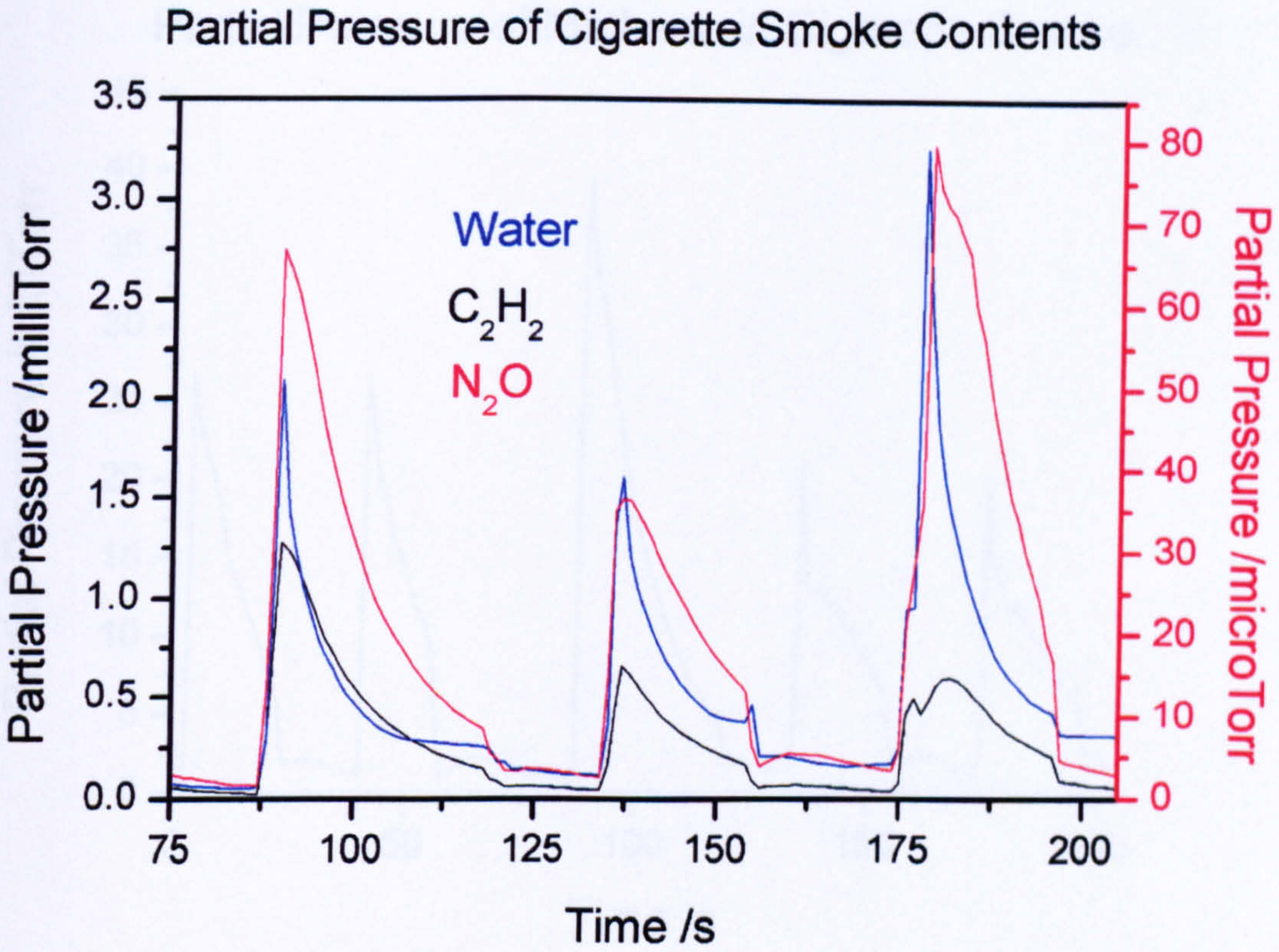

Figure 5.3.24 – *The Black trace shows the time evolution of Acetylene in cigarette smoke. The Red trace shows the time evolution of Nitrous Oxide in cigarette smoke. The Blue trace shows the time evolution of Water in cigarette smoke.*

The Nitrous Oxide pressures are plotted on the microTorr scale and the Acetylene and Water pressures are plotted on the milliTorr scale. By looking at the peak partial pressures of the gases the peak concentrations of the constituents can be found. The peak Water concentrations for the five puffs is 73.15ppmv, 67.31ppmv, 93.2ppmv, 84.53ppmv and 162.37ppmv. The peak concentrations of Nitrous Oxide are 2.89ppmv, 2.19ppmv, 2.97ppmv, 1.91ppmv and 3.96ppmv. The peak Acetylene concentrations are 59.1ppmv, 45.29ppmv, 56.84ppmv, 34.74ppmv and 30.05ppmv. Figure 5.3.25 shows the partial pressure of Methane during the smoking of the cigarette.

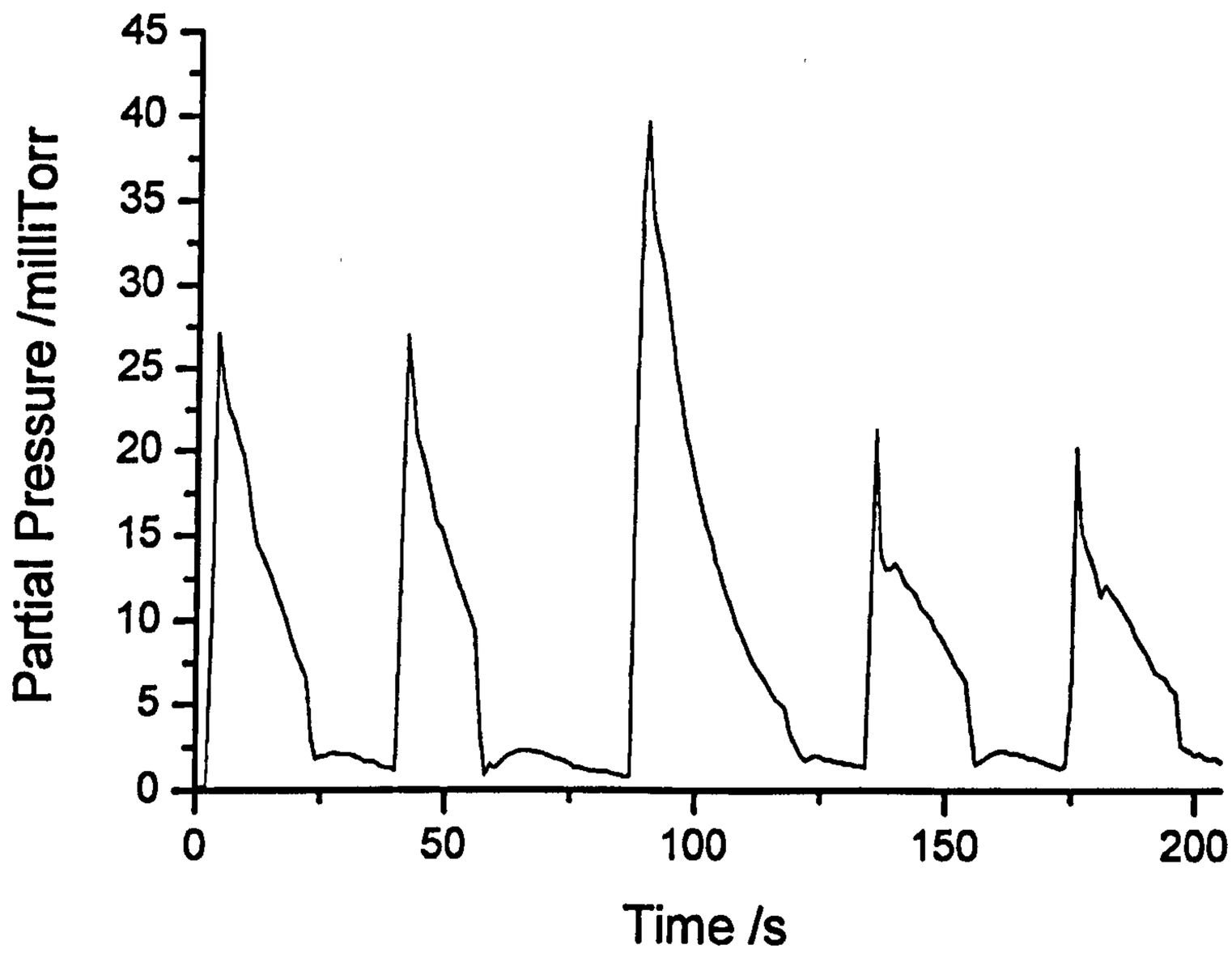

Figure 5.3.25 – *The time evolution of Methane in cigarette smoke.*

The peak concentrations of Methane are 1218.5ppmv, 1465.2ppmv, 1763.1ppmv, 1125.3ppmv and 1012.9ppmv. As with the previous experiment the integrated intensity of the Formaldehyde lines in the laser region could not be obtained. The integrated absorption of the Formaldehyde is shown in Figure 5.3.26.

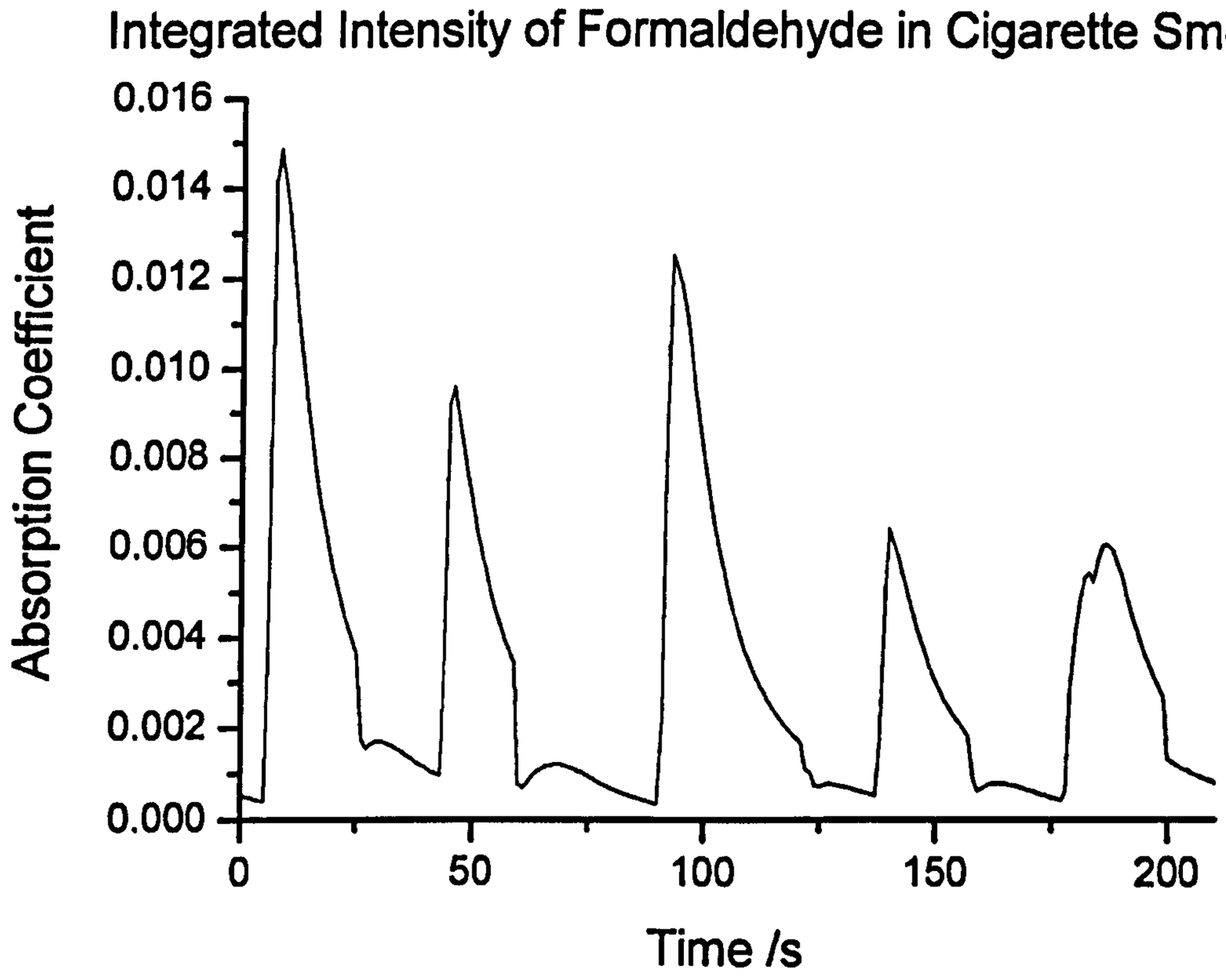

Figure 5.3.26 – *The integrated intensity of the Formaldehyde in cigarette smoke.*

The pattern of emission for the Formaldehyde is different to the emission pattern of Formaldehyde in the previous experiment with the full length filter. The largest absorption is in the first puff, which is what would be expected from other work [4]. A comparison of the peak concentrations of Water, Nitrous Oxide and Acetylene is shown in Figure 5.3.27.

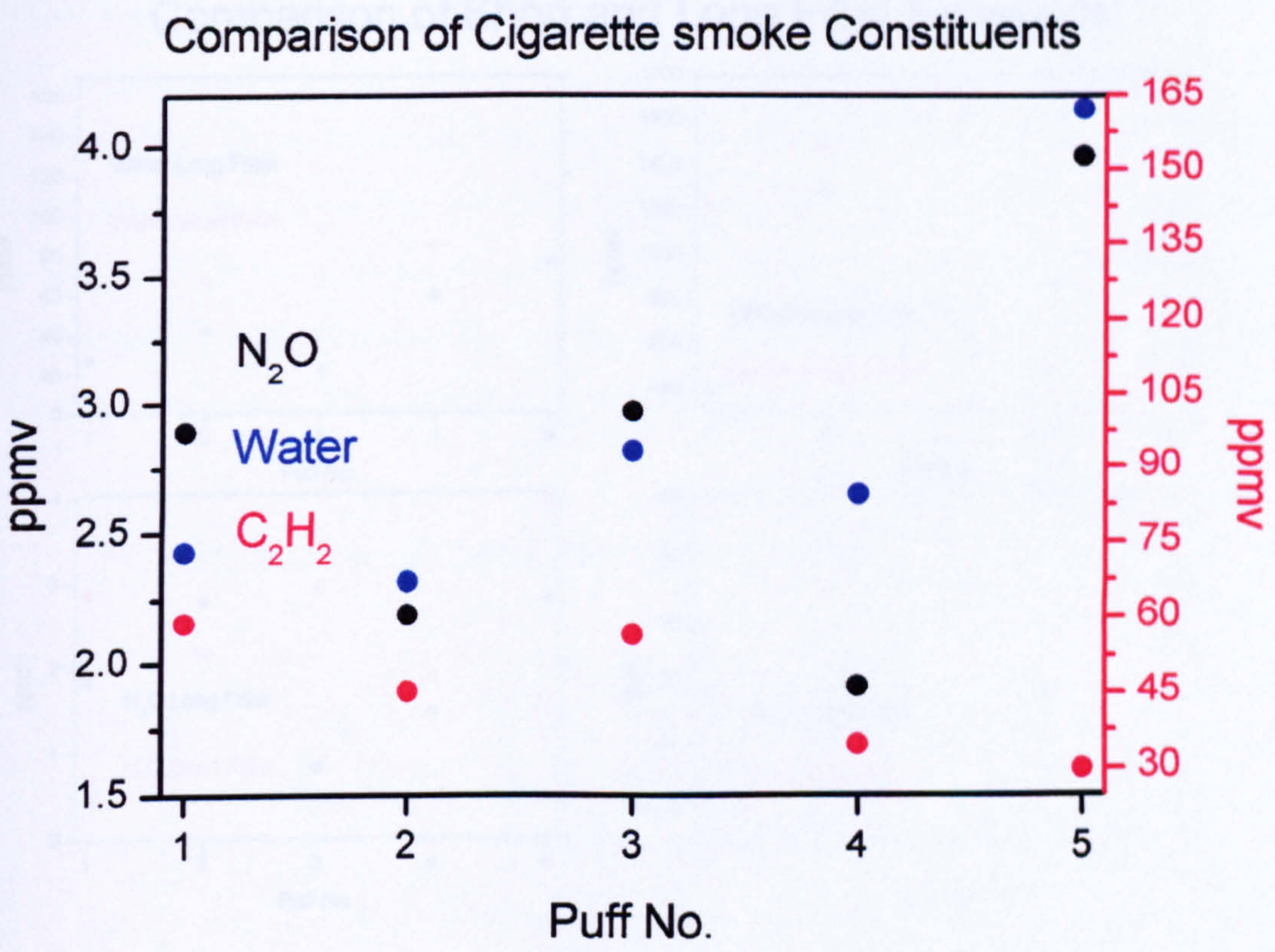

Figure 5.3.27 – *The Black dots show the concentration of Acetylene. The Blue dots show the concentration of Water. The Red dots show the concentration of Nitrous Oxide.*

The Nitrous Oxide concentrations are plotted on the black ppmv scale and the Water and Acetylene concentrations are plotted on the red ppmv scale. Using the concentration data from the two experiments, with the normal sized filter and the reduced filter, a comparison can be made. A comparison of the concentrations of Methane, Acetylene, Water and Nitrous Oxide in the two experiments is shown in Figure 5.3.28.

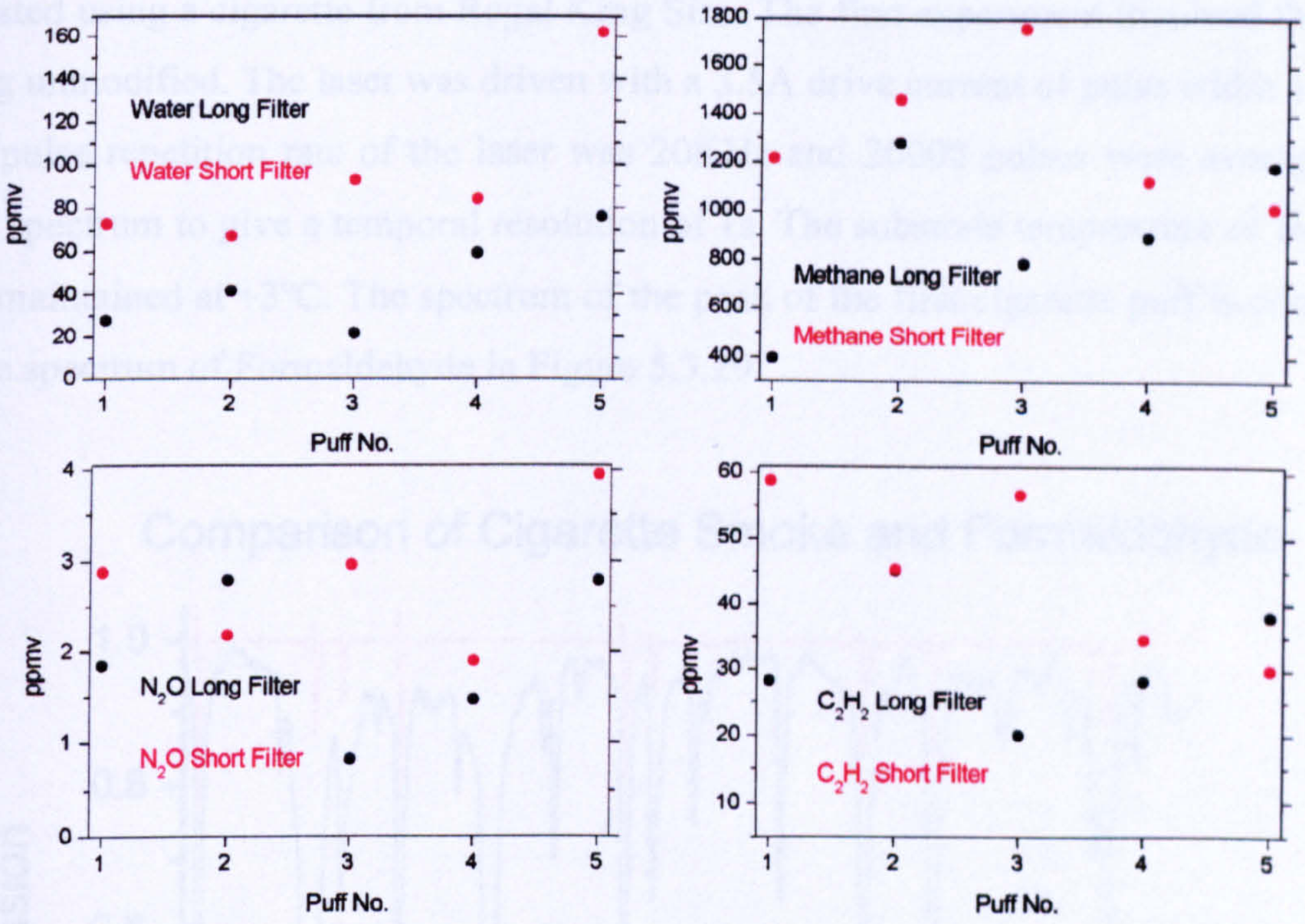

Figure 5.3.28 – *The Black dots show the emission in the long filter experiment. The Red dots show the emission in the short filter experiment.*

It can be seen that the levels of emission tend to be larger for the short filter experiment compared to the long filter experiment. For the first puff all of the gases are present in higher concentrations in the short filter experiment compared to the long filter experiment. For the second puff only the Nitrous Oxide concentration is larger in the long filter experiment compared to the short filter experiment. By the third and fourth puffs all of the gases are present at higher concentrations in the short filter experiment compared to the long filter experiment. In the final puff only the Methane concentration is higher in the long filter experiment than the short filter experiment. It would be expected that as the filter length was decreased the emission levels would increase. This is the case for most of the concentrations for the four gases.

In order to make a comparison with a different brand of cigarettes the experiments were repeated using a cigarette from Regal King Size. The first experiment involved the filter being unmodified. The laser was driven with a 3.5A drive current of pulse width 1400ns. The pulse repetition rate of the laser was 20KHz and 20000 pulses were averaged for each spectrum to give a temporal resolution of 1s. The substrate temperature of the laser was maintained at +3°C. The spectrum of the peak of the first cigarette puff is compared to the spectrum of Formaldehyde in Figure 5.3.29.

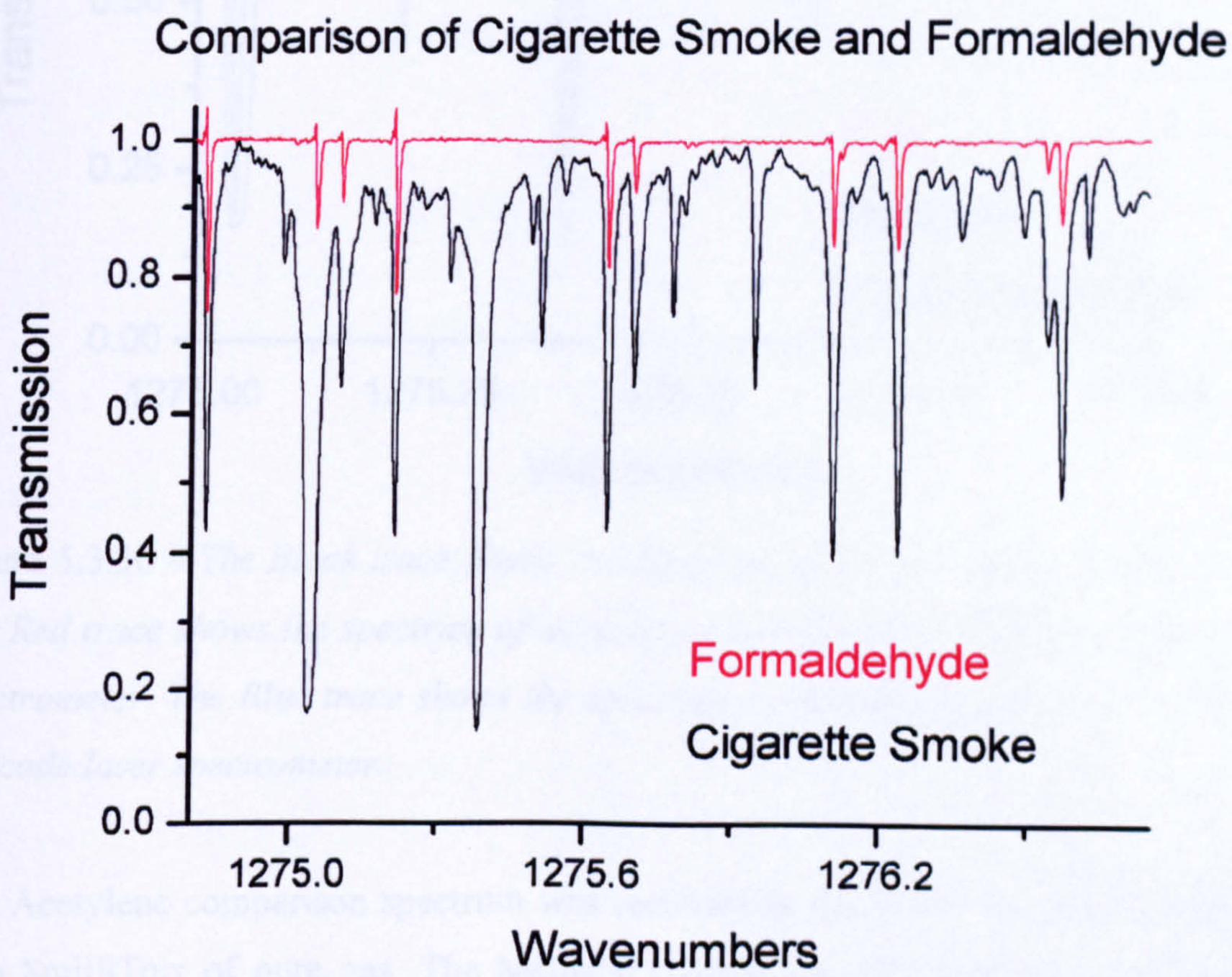

Figure 5.3.29 – *The Black trace shows the spectrum of the first puff of cigarette smoke. The Red trace shows the spectrum of Formaldehyde recorded by my Quantum Cascade laser spectrometer.*

The comparison spectrum was recorded with 0.2Torr of Formaldehyde in the 115m astigmatic Herriott cell. The same cigarette spectrum is compared with a spectrum of Methane and a spectrum of Acetylene in Figure 5.3.30.

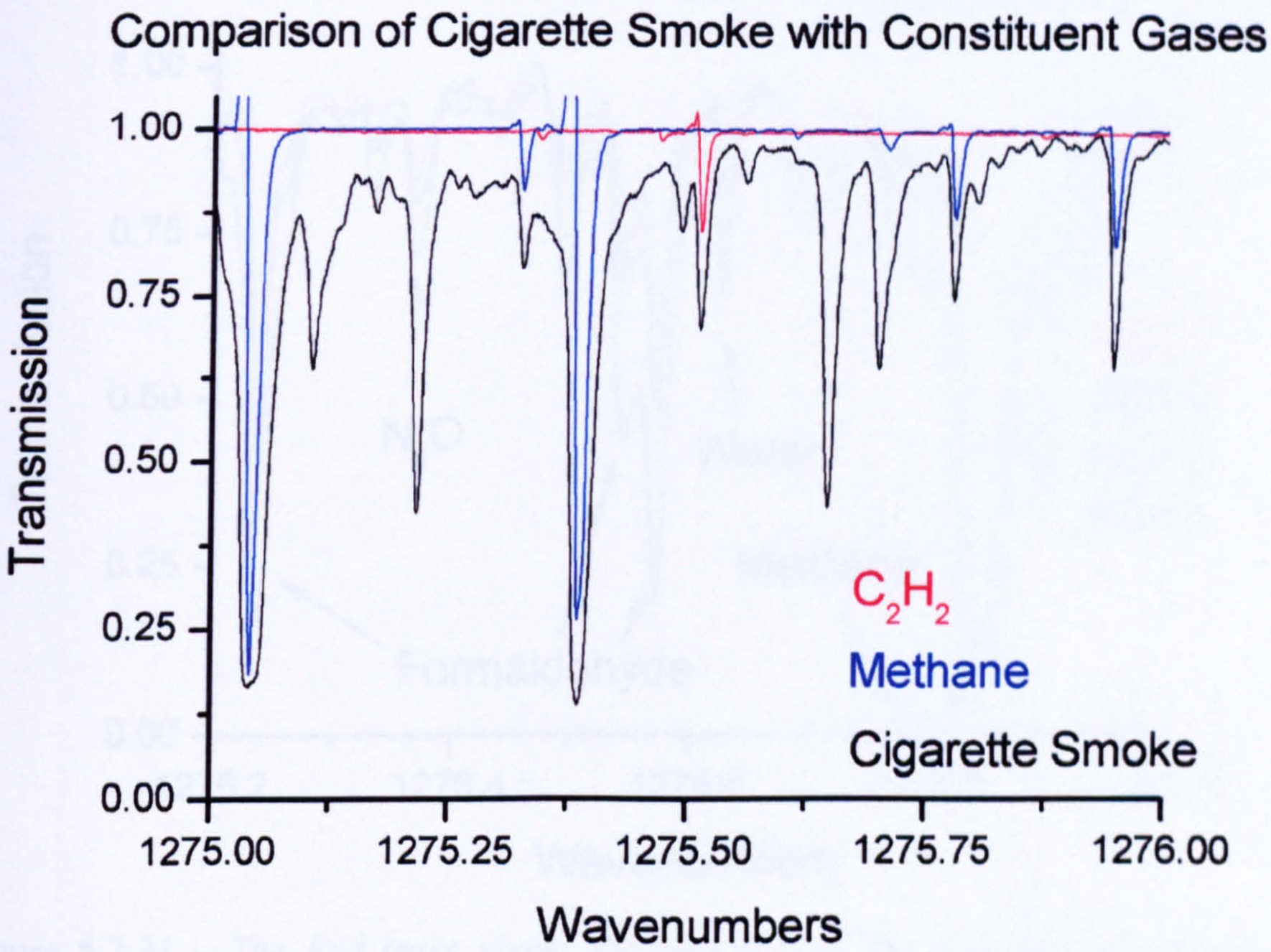

Figure 5.3.30 – *The Black trace shows the spectrum of the first puff of cigarette smoke. The Red trace shows the spectrum of Acetylene recorded by my Quantum Cascade laser spectrometer. The Blue trace shows the spectrum of Methane recorded by my Quantum Cascade laser spectrometer.*

The Acetylene comparison spectrum was recorded in the 115m astigmatic Herriott cell with 8milliTorr of pure gas. The Methane comparison spectrum was recorded in the 115m astigmatic Herriott cell with 5milliTorr of pure gas.

A comparison of the first four of the five cigarette puffs is made in Figure 5.3.31.

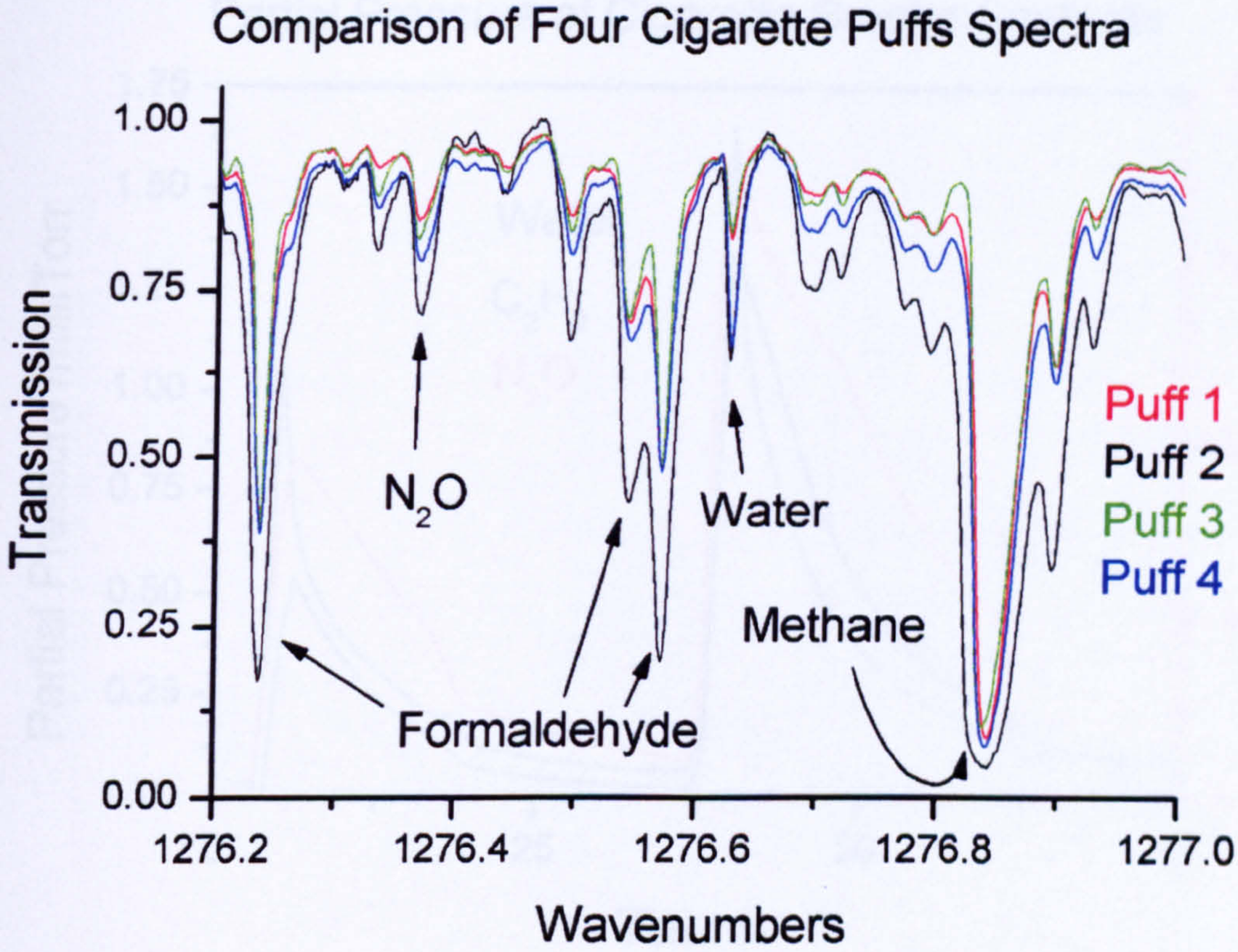

Figure 5.3.31 – *The Red trace shows the spectrum of the first puff. The Black trace shows the spectrum of the second puff. The Green trace shows the spectrum of the third puff. The Blue trace shows the spectrum of the fourth puff.*

From the three above diagrams comparing the cigarette smoke and some of the constituents of cigarette smoke it is clear that the level of absorption for the Regal King Size cigarette is larger than the level of absorption for the Marlboro Lights cigarette, which is what would be expected due to the lower tar levels in the Marlboro Light cigarette compared to the Regal King Size cigarette. The time evolution of Water, Nitrous Oxide and Acetylene in the first two puffs of the cigarette is shown in Figure 5.3.32.

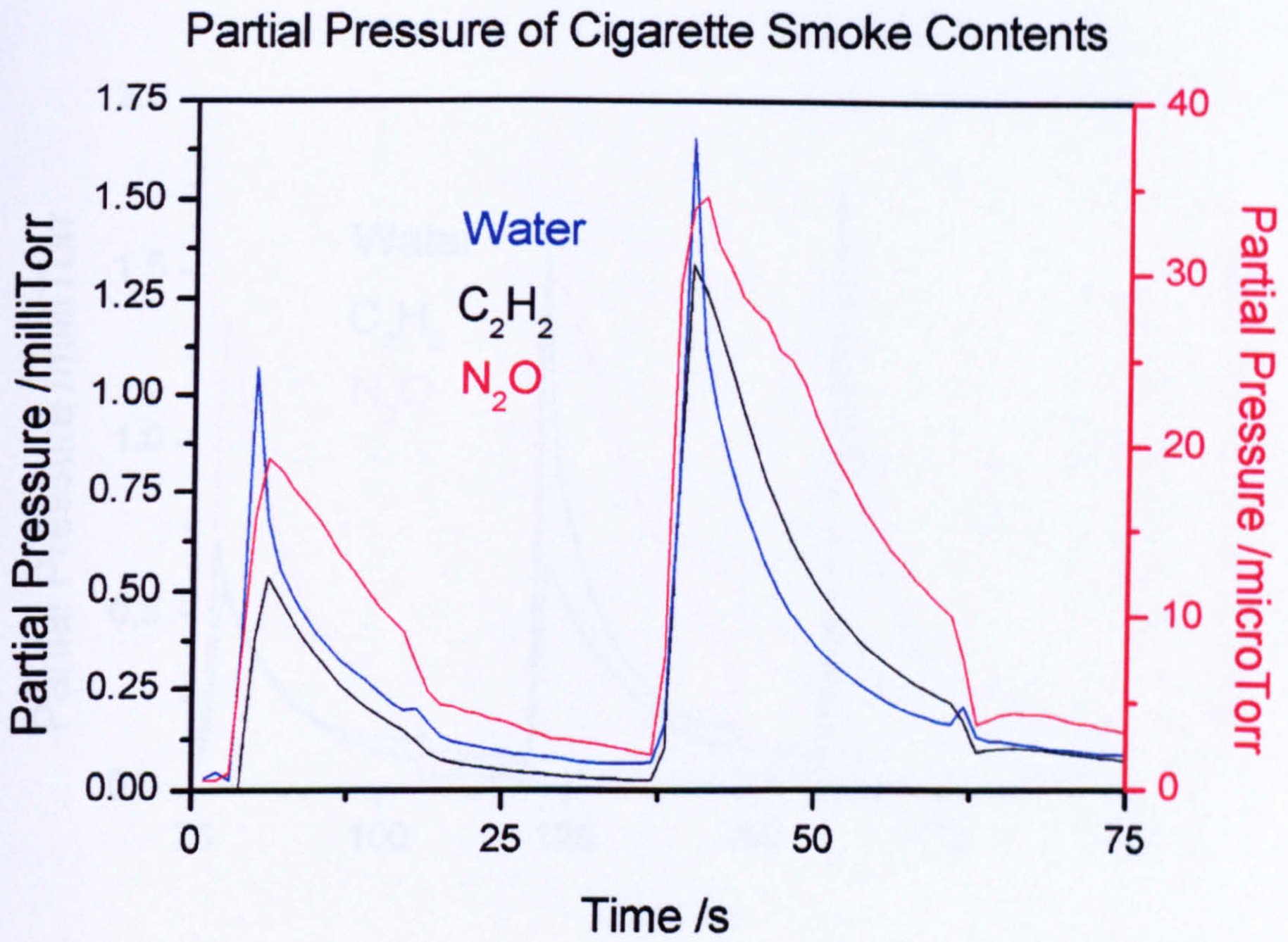

Figure 5.3.32 – *The Black trace shows the time evolution of Acetylene in cigarette smoke. The Red trace shows the time evolution of Nitrous Oxide in cigarette smoke. The Blue trace shows the time evolution of Water in cigarette smoke.*

The Water and Acetylene pressures are plotted on the milliTorr scale and the Nitrous Oxide pressure is plotted on the microTorr scale. The time evolution of Water, Nitrous Oxide and Acetylene in the third, fourth and fifth puffs of the cigarette are shown in Figure 5.3.33.

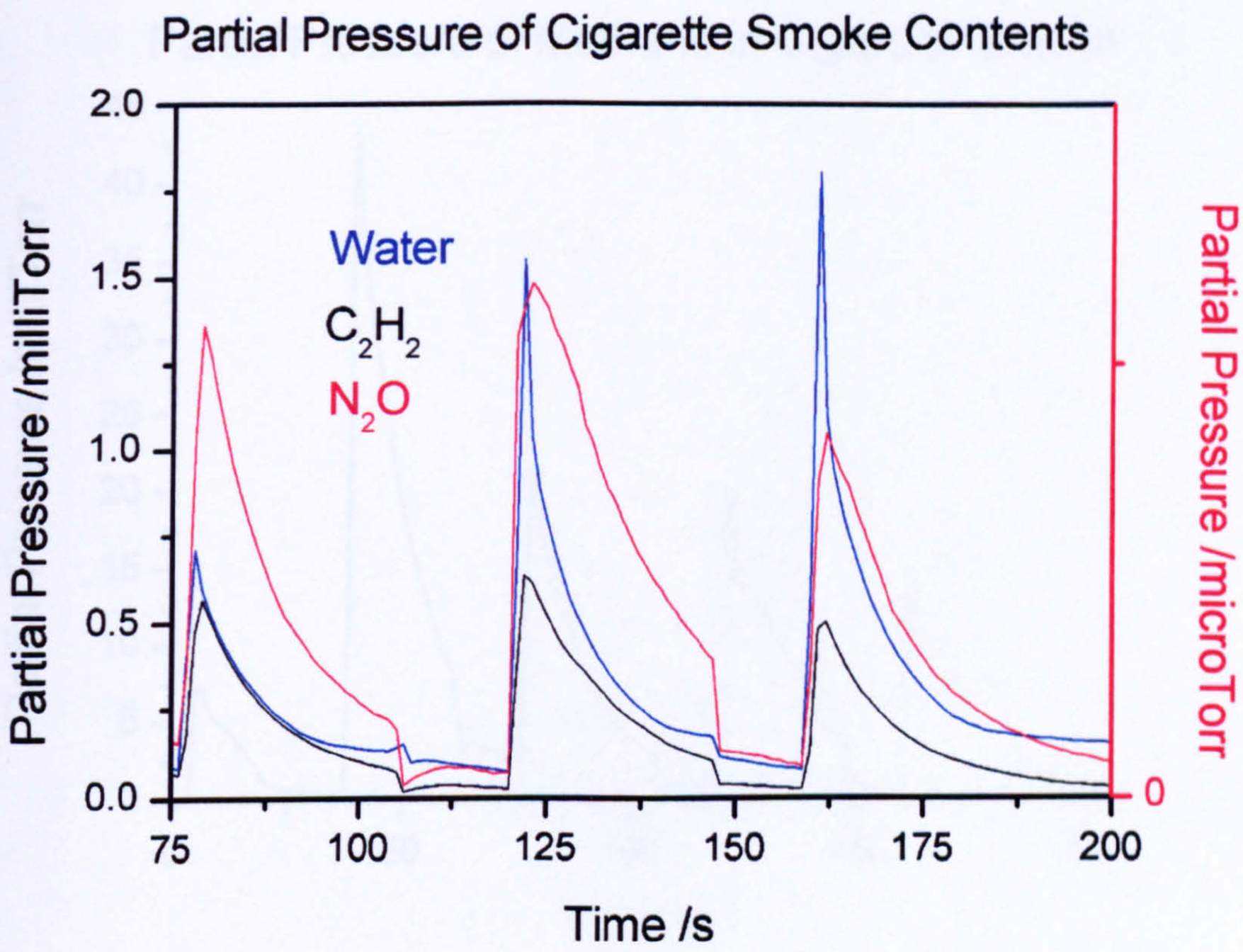

Figure 5.3.33 – *The Black trace shows the time evolution of Acetylene in cigarette smoke. The Red trace shows the time evolution of Nitrous Oxide in cigarette smoke. The Blue trace shows the time evolution of Water in cigarette smoke.*

The Nitrous Oxide pressure is plotted on the microTorr scale and the Water and Acetylene pressures are plotted on the milliTorr scale. The peak pressures for the five puffs are 30Torr, 24.2Torr, 21.5Torr, 26.5Torr and 24Torr. The peak concentrations of Nitrous Oxide are 0.637ppmv, 1.42ppmv, 1.27ppmv, 1.12ppmv and 0.87ppmv. For the five puffs the peak concentrations of Water are 35.77ppmv, 68.32ppmv, 33.07ppmv, 58.57ppmv and 75ppmv. For Acetylene the peak concentrations are 17.86ppmv, 55.1ppmv, 26.4ppmv, 23.92ppmv and 20.83ppmv. Figure 5.3.34 shows the partial pressure of Methane during the smoking of the cigarette.

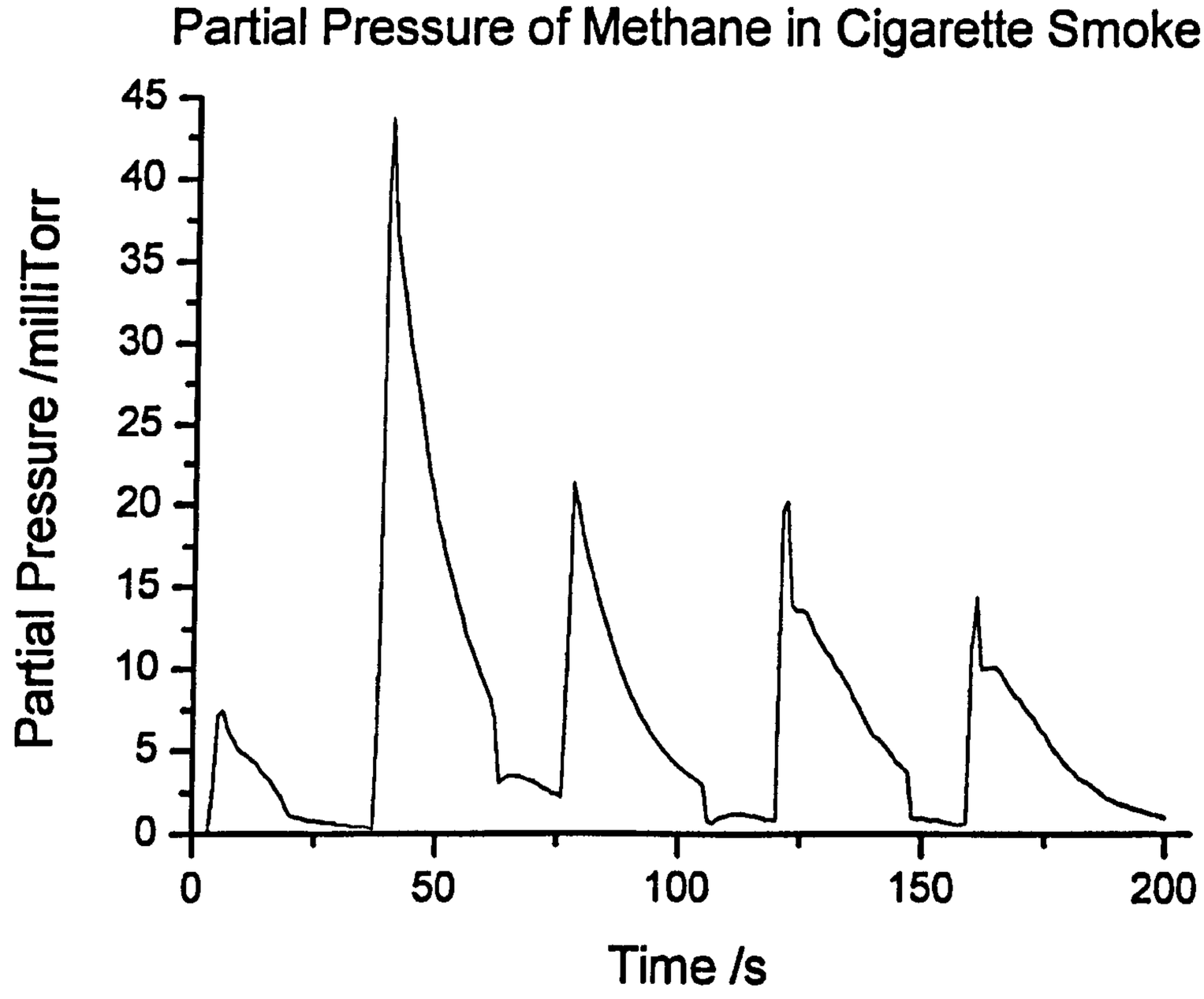

Figure 5.3.34 – *The time evolution of Methane in cigarette smoke.*

The peak concentrations of Methane are 247ppmv, 1808.3ppmv, 988.8ppmv, 761.9ppmv and 598.3ppmv. The integrated intensity of Formaldehyde is displayed as a function of time in Figure 5.3.35.

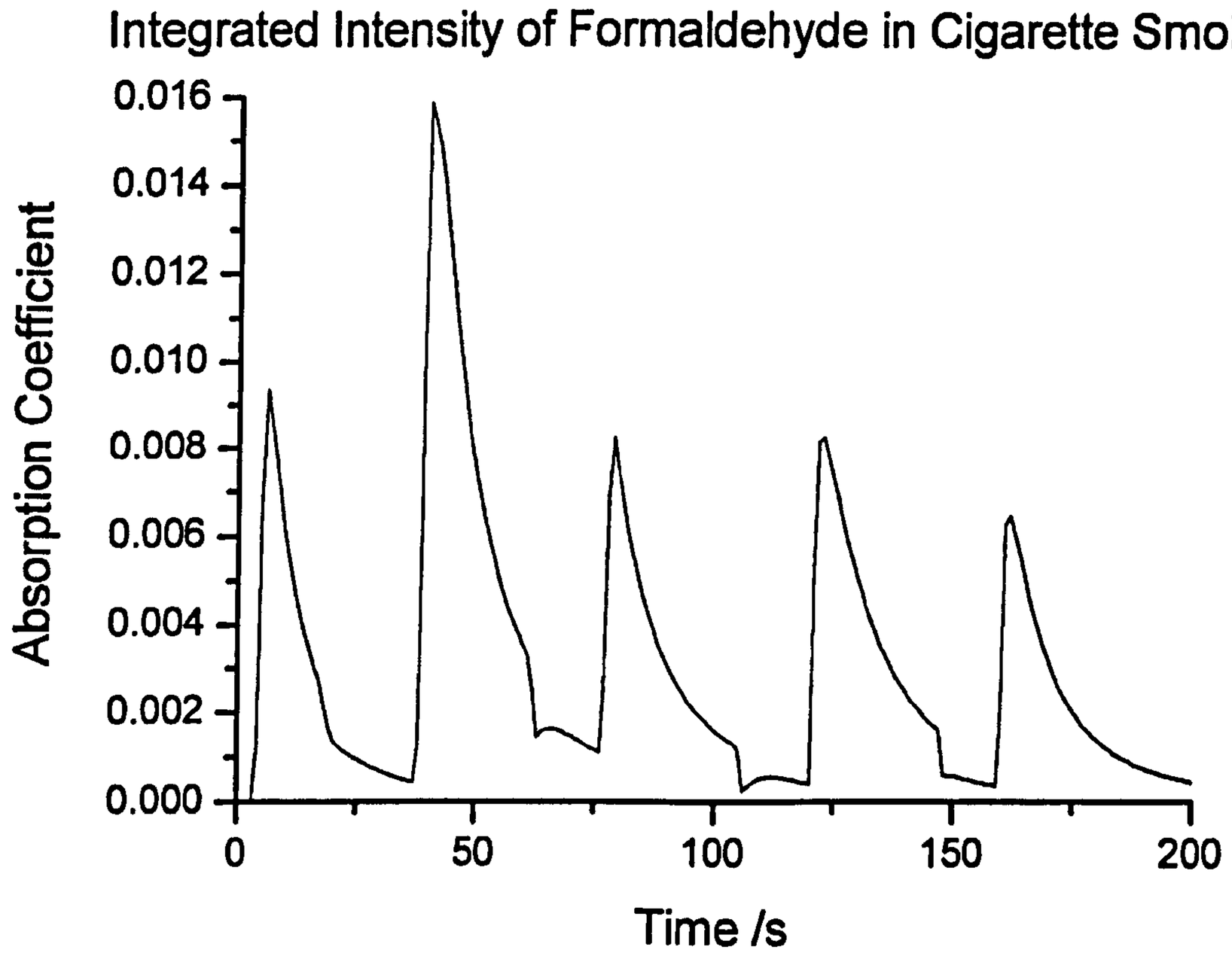

Figure 5.3.35 – *The integrated intensity of the Formaldehyde in cigarette smoke.*

The integrated intensity of Formaldehyde does not follow the expected pattern [4], however the pattern is similar to that of the Formaldehyde emission in the equivalent long filter experiment of the Marlboro Lights cigarette.

By plotting the peak concentrations of the Water, Acetylene and Nitrous Oxide as a function of puff number the relative emission patterns may be seen. This data is shown in Figure 5.3.36.

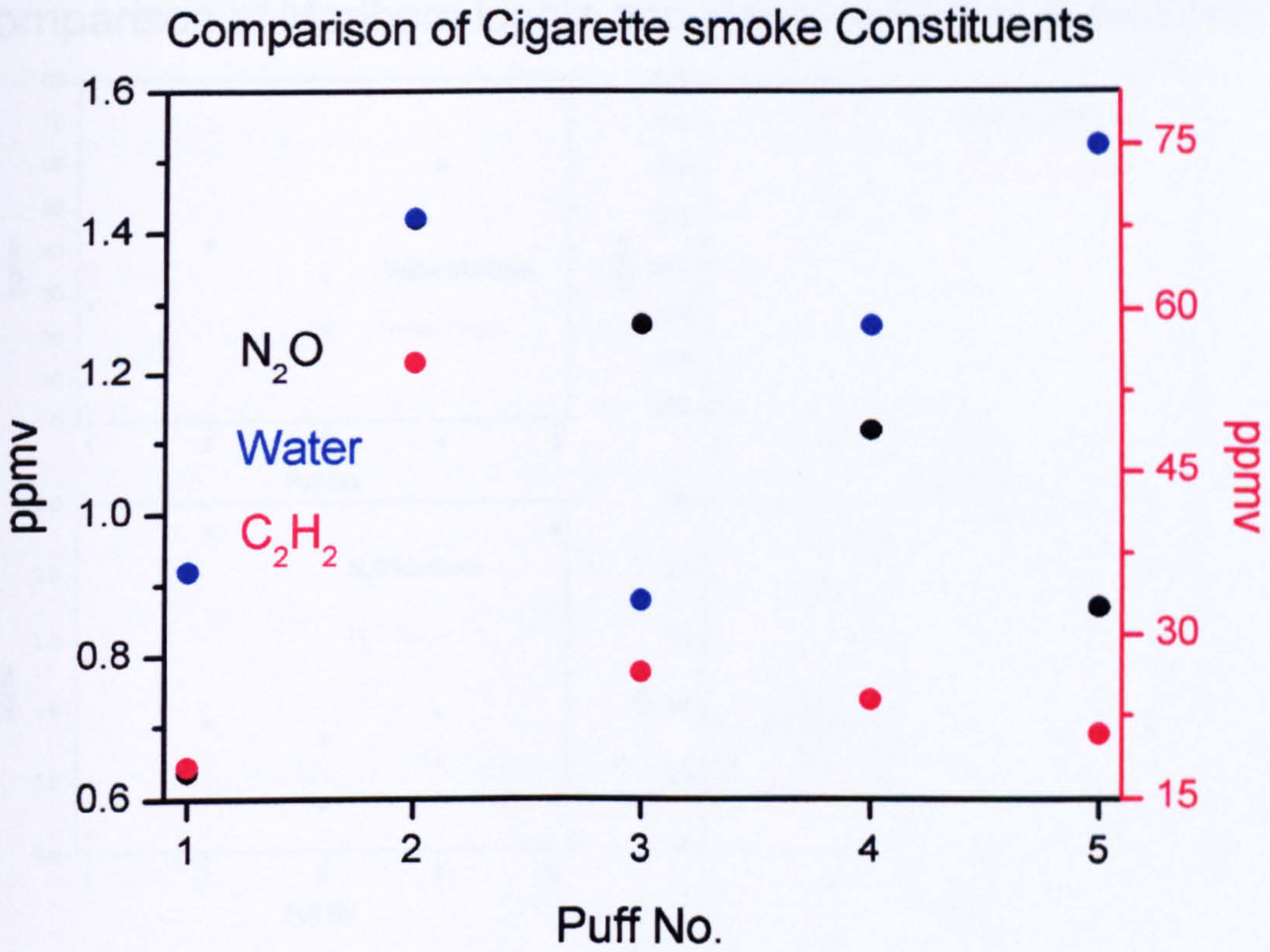

Figure 5.3.36 – *The Black dots show the concentration of Acetylene. The Blue dots show the concentration of Water. The Red dots show the concentration of Nitrous Oxide.*

The Nitrous Oxide concentrations are plotted on the black ppmv scale and the Water and Acetylene concentrations are plotted on the red ppmv scale. The dot corresponding to the Nitrous Oxide concentration for puff two lies under the Water dot for that puff. The emissions for Water, Nitrous Oxide, Acetylene and Methane for the Marlboro Lights cigarette with an unmodified filter and the Regal King size cigarette with an unmodified filter are compared in Figure 5.3.37.

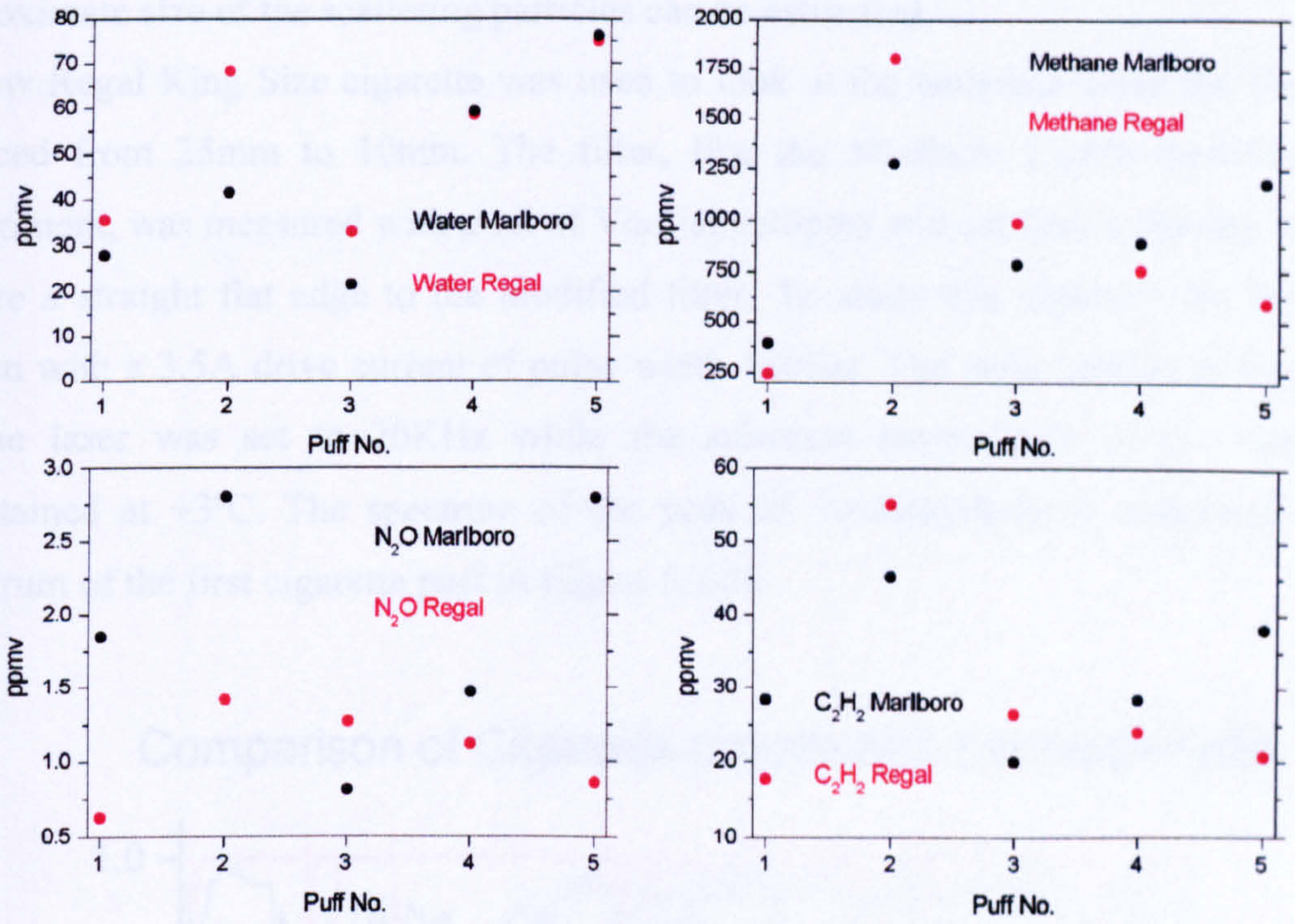

Figure 5.3.37 – *The Black dots show the emission in the Marlboro Lights experiment. The Red dots show the emission in the Regal King Size experiment.*

For the majority of the data the identifiable emissions from the Marlboro Lights cigarette is larger than the Regal King Size cigarette. However some of the largest emissions are from the Regal King Size cigarette, such as the second puff Acetylene emission and the second puff Methane emission. The other difference between the two cigarettes is the amount of larger molecules in the smoke stream. These large molecules cause the laser beam to be scattered. The scattering in the Regal King Size experiment was larger than the scattering in the Marlboro Lights experiment, which suggests a larger number density of larger molecules in the Regal King Size cigarette smoke. However the exact density of large molecules or the size of the large molecules cannot be identified from the simple scattering process observed in the two experiments. As the optical cell used was glass the scattered laser light could not penetrate the cell for the scattering angles to

be studied, however if we assume that the scattering is a function of λ then the approximate size of the scattering particles can be estimated.

A new Regal King Size cigarette was used to look at the emission when the filter was reduced from 25mm to 10mm. The filter, like the Marlboro Lights modified filter experiment, was measured with a set of Vernier callipers and cut with a Stanley blade to ensure a straight flat edge to the modified filter. To study this cigarette the laser was driven with a 3.5A drive current of pulse width 1400ns. The pulse repetition frequency of the laser was set to 20KHz while the substrate temperature of the laser was maintained at +3°C. The spectrum of the peak of Formaldehyde is compared to the spectrum of the first cigarette puff in Figure 5.3.38.

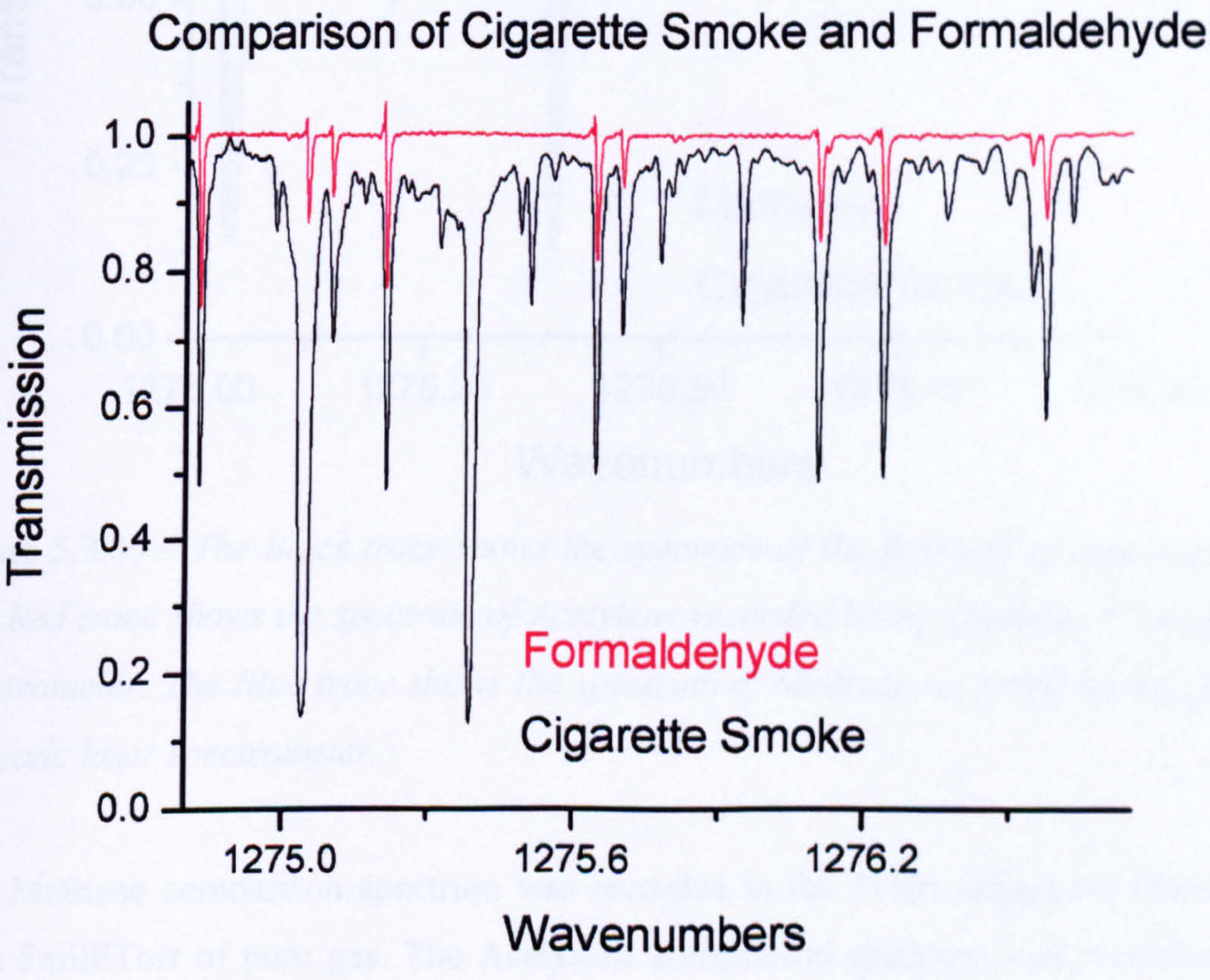

Figure 5.3.38 – *The Black trace shows the spectrum of the first puff of cigarette smoke. The Red trace shows the spectrum of Formaldehyde recorded by my Quantum Cascade laser spectrometer.*

The comparison spectrum was recorded with 0.2Torr of Formaldehyde in the 115m astigmatic Herriott cell. A spectrum of Methane and a spectrum of Acetylene are compared with the same cigarette spectrum in Figure 5.3.39.

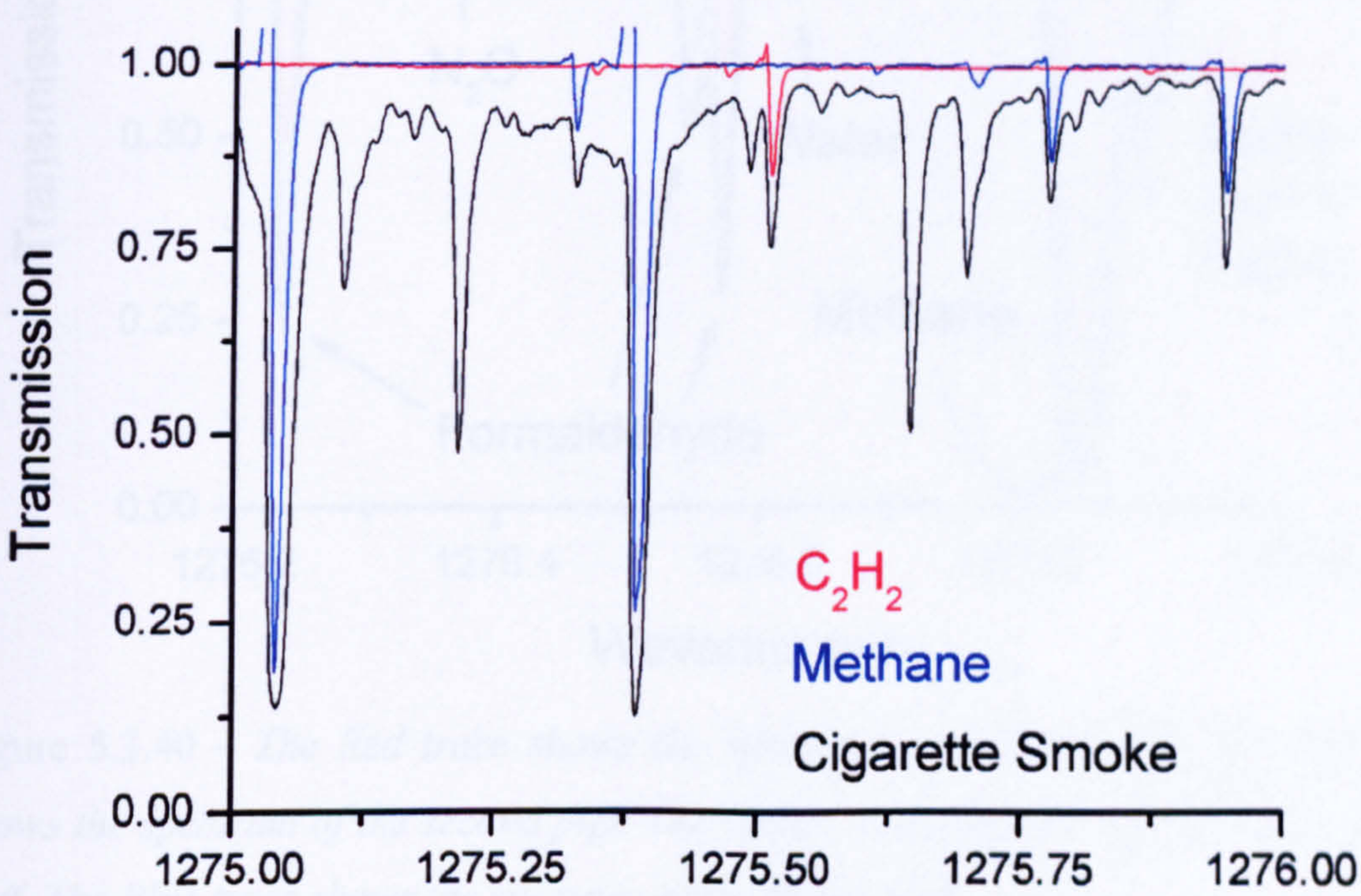

Figure 5.3.39 – *The Black trace shows the spectrum of the first puff of cigarette smoke. The Red trace shows the spectrum of Acetylene recorded by my Quantum Cascade laser spectrometer. The Blue trace shows the spectrum of Methane recorded by my Quantum Cascade laser spectrometer.*

The Methane comparison spectrum was recorded in the 115m astigmatic Herriott cell with 5milliTorr of pure gas. The Acetylene comparison spectrum was recorded in the 115m astigmatic Herriott cell with 8milliTorr of pure gas.

A graph of the comparison of the first four of the five cigarette puffs is made in Figure 5.3.40.

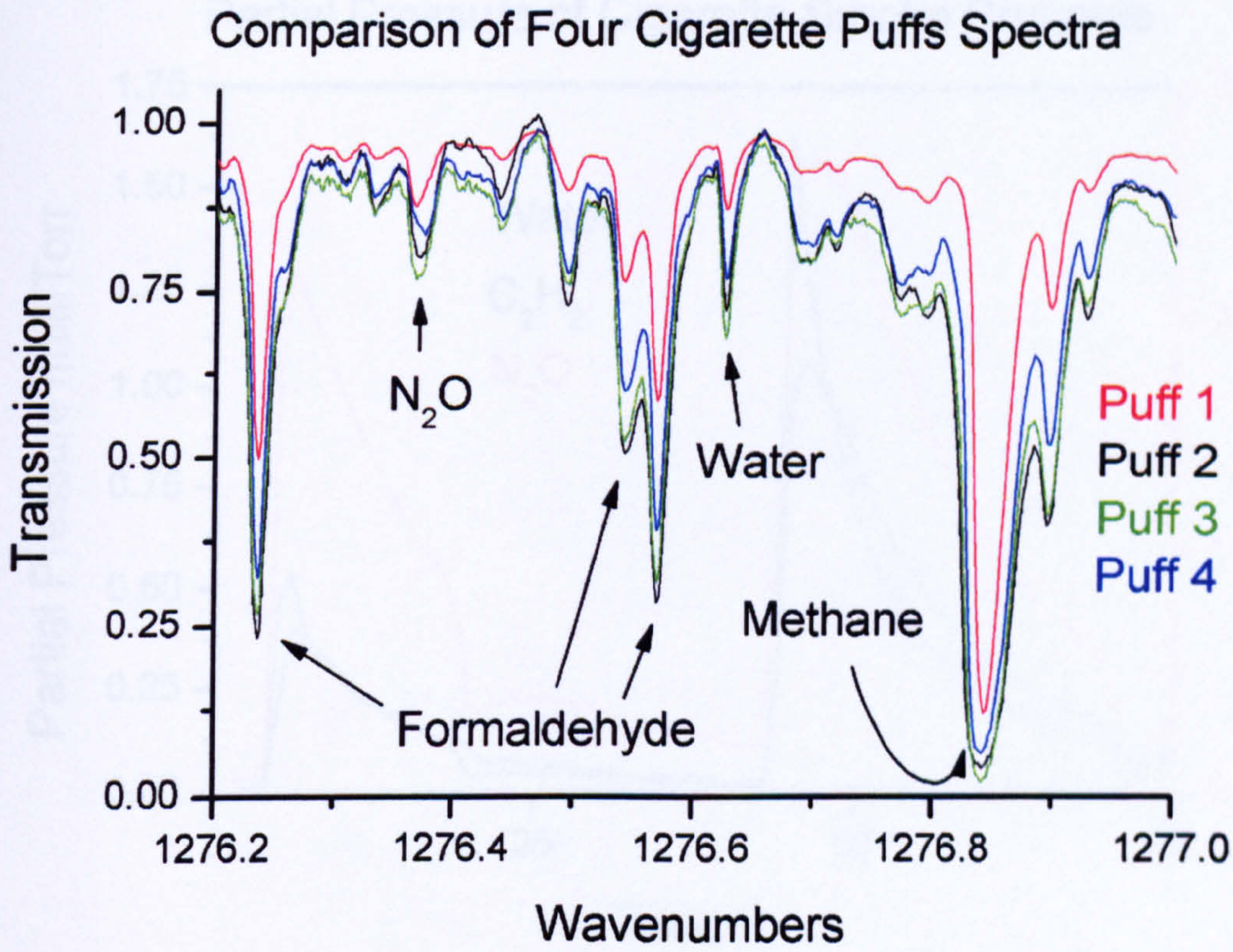

Figure 5.3.40 – *The Red trace shows the spectrum of the first puff. The Black trace shows the spectrum of the second puff. The Green trace shows the spectrum of the third puff. The Blue trace shows the spectrum of the fourth puff.*

The general amount of absorption in the four puffs compared to the second puff of previous experiment where the filter of the Regal King Size cigarette was unmodified is similar. The other three puffs from the previous experiment show less absorption than in the current experiment. The scattering from large molecules was greater in this experiment than in the unmodified filter experiment. The time evolution of Nitrous Oxide, Water and Acetylene in the first two puffs of the Regal King Size cigarette is shown in Figure 5.3.41.

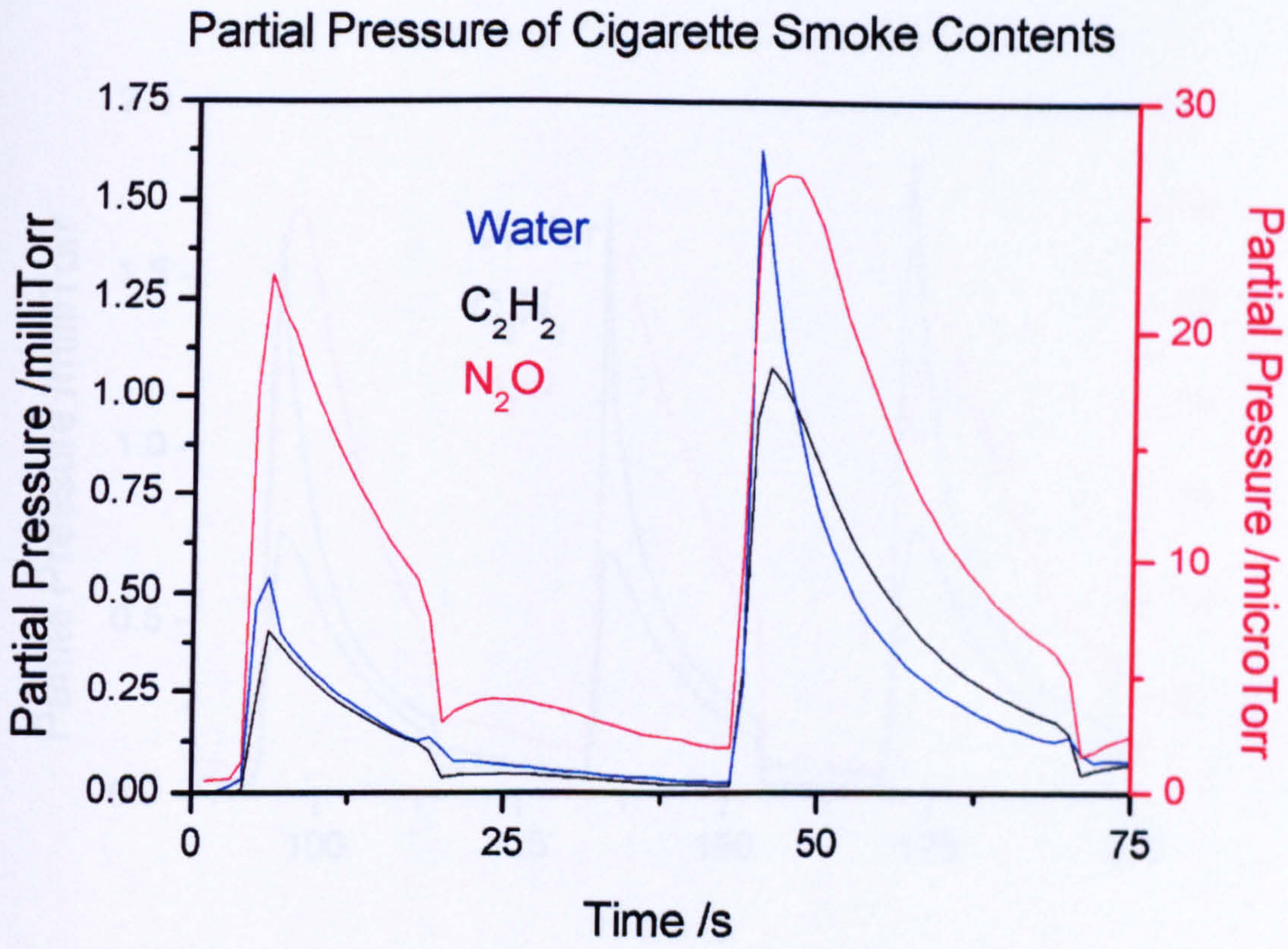

Figure 5.3.41 – *The Black trace shows the time evolution of Acetylene in cigarette smoke. The Red trace shows the time evolution of Nitrous Oxide in cigarette smoke. The Blue trace shows the time evolution of Water in cigarette smoke.*

The Nitrous Oxide pressure is plotted on the microTorr scale and the Water and Acetylene pressures are plotted on the milliTorr scale. The peak pressures for the five puffs of the cigarette are 24.2Torr, 28.1Torr, 27.5Torr, 21.7Torr and 28.2Torr. The time evolution of Water, Nitrous Oxide and Acetylene in the third, fourth and fifth puffs of the cigarette are shown in Figure 5.3.42.

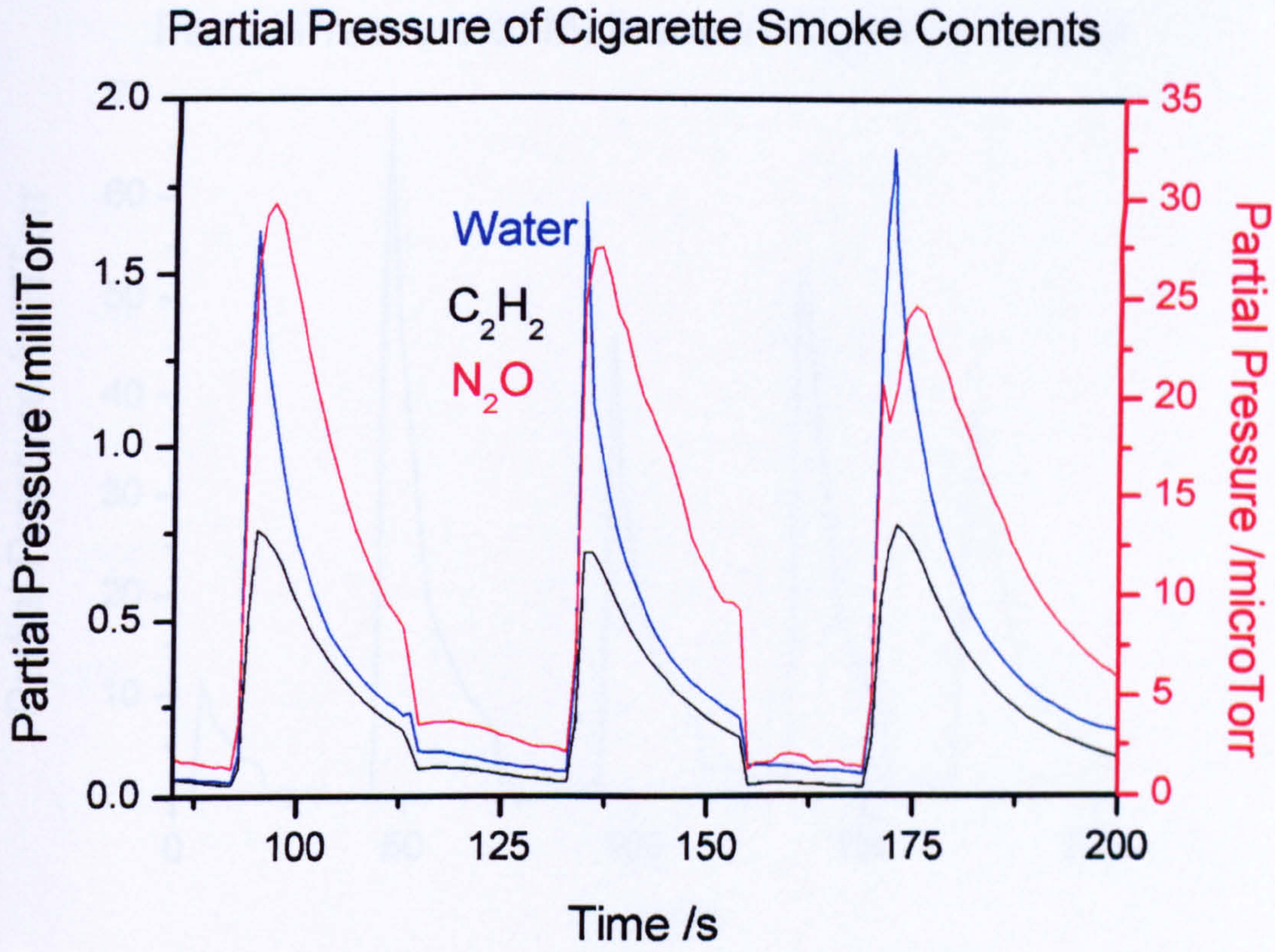

Figure 5.3.42 – *The Black trace shows the time evolution of Acetylene in cigarette smoke. The Red trace shows the time evolution of Nitrous Oxide in cigarette smoke. The Blue trace shows the time evolution of Water in cigarette smoke.*

The Nitrous Oxide partial pressure is plotted on the microTorr scale and the Water and Acetylene partial pressures are plotted on the milliTorr scale. For the five puffs the peak concentrations of Water are 22.19ppmv, 57.83ppmv, 59.12ppmv, 78.57ppmv and 65.94ppmv. The peak concentrations of Nitrous Oxide are 0.93ppmv, 0.95ppmv, 1.08ppmv, 1.27ppmv and 0.87ppmv. For Acetylene the peak concentrations are 16.73ppmv, 38.2ppmv, 27.53ppmv, 31.84ppmv and 27.41ppmv. Figure 5.3.43 shows the partial pressure of Methane during the smoking of the cigarette.

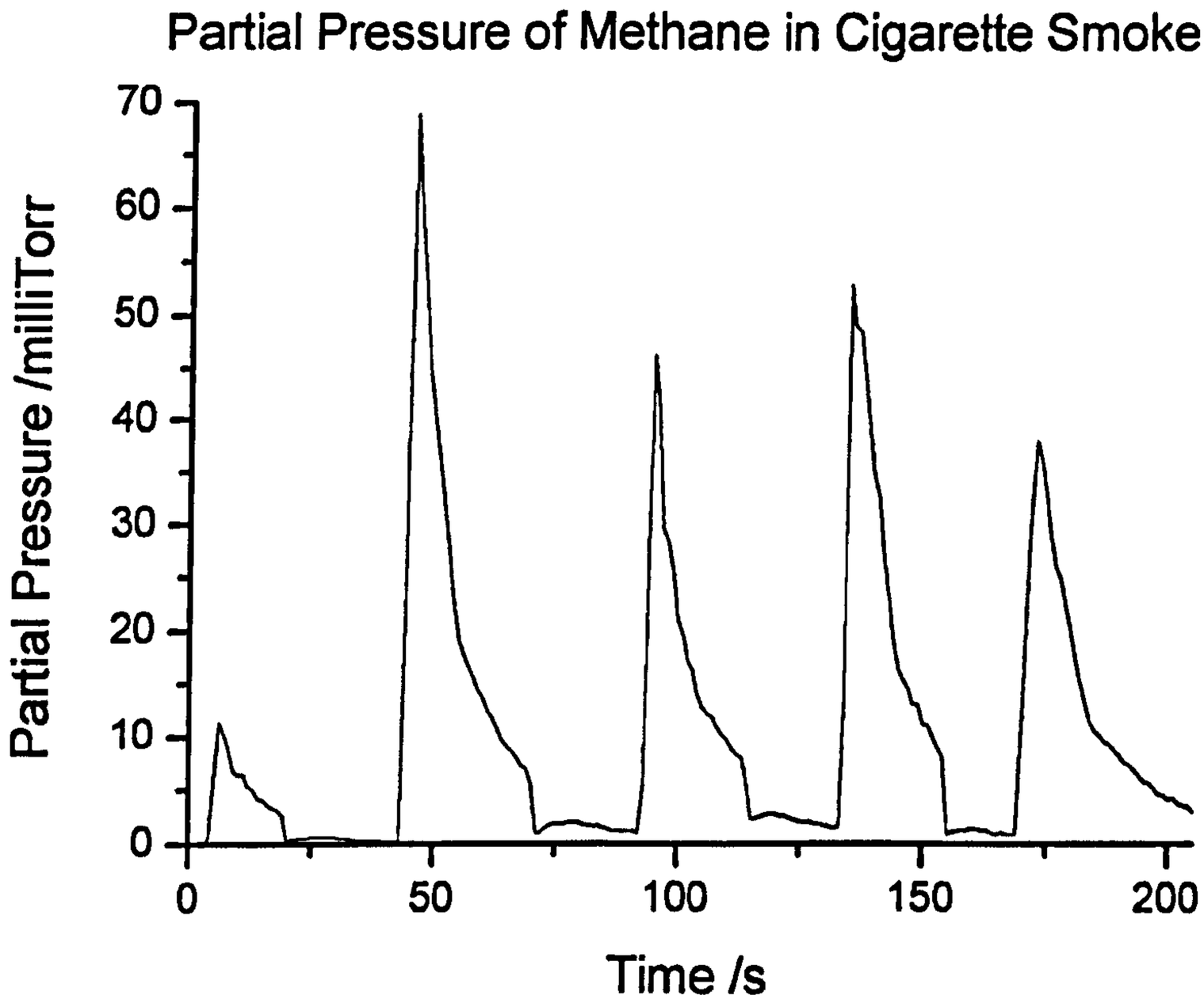

Figure 5.3.43 – *The time evolution of Methane in cigarette smoke.*

The emission pattern of Methane in the shortened filter experiment is similar to the emission pattern of Methane in the long filter experiment with a large emission during the second puff. The other four puffs are closer to the large second puff emission in the shortened filter experiment than in the long filter experiment. The peak concentrations of Methane are 462.1ppmv, 2452.7ppmv, 1673.8ppmv, 2453.9ppmv and 1353ppmv. The integrated intensity of Formaldehyde is displayed as a function of time in Figure 5.3.44.

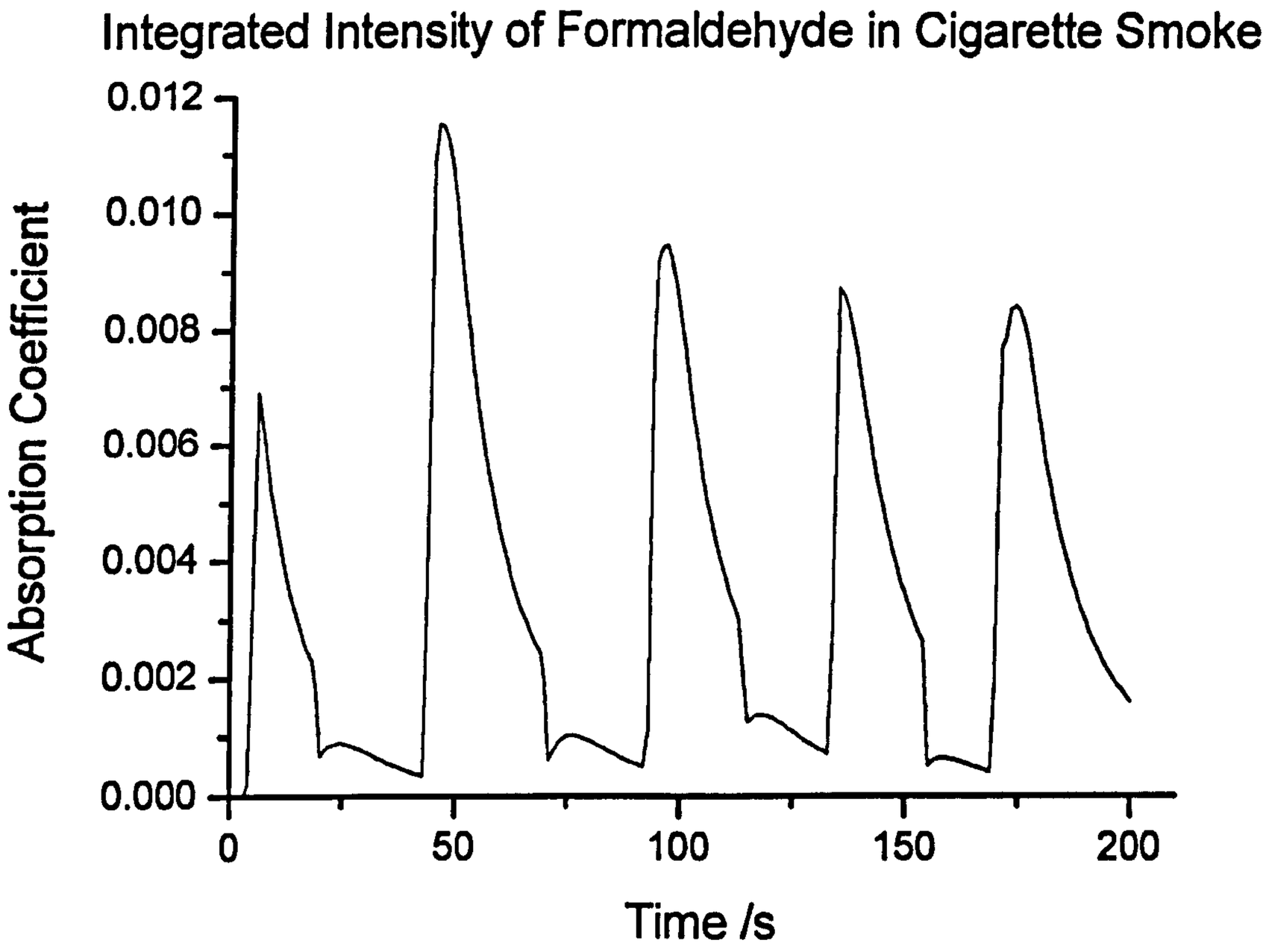

Figure 5.3.44 – *The integrated intensity of the Formaldehyde in cigarette smoke.*

The integrated intensity of Formaldehyde does not follow the expected pattern [4], however the pattern is similar to that of the Formaldehyde emission in the previous unmodified filter Regal King Size experiment. And like the Methane emission the second puff of the Formaldehyde is larger than the other four puffs in the two experiments. The second puff is not so much bigger than the others in this experiment than in the previous experiment. The peak concentrations of Water, Nitrous Oxide and Acetylene are shown for all five cigarette puffs in Figure 5.3.45.

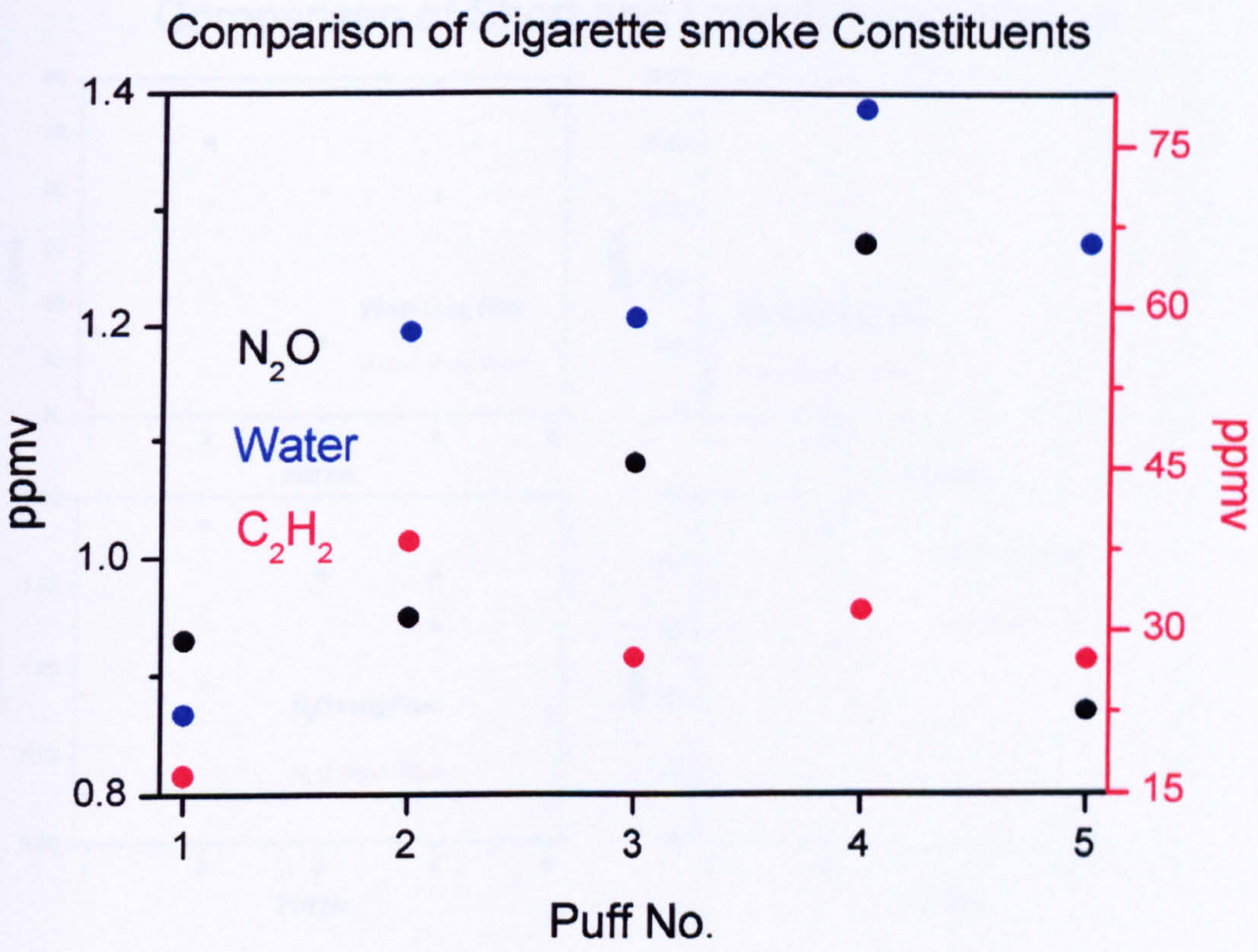

Figure 5.3.45 – *The Black dots show the concentration of Acetylene. The Blue dots show the concentration of Water. The Red dots show the concentration of Nitrous Oxide.*

The concentrations of Water and Acetylene are shown on the red ppmv scale and the concentrations of Nitrous Oxide are shown on the black ppmv scale. These concentrations, along with the concentrations of Methane for the five puffs, can be compared with the data for the unmodified filter experiment. This is plotted in Figure 5.3.46.

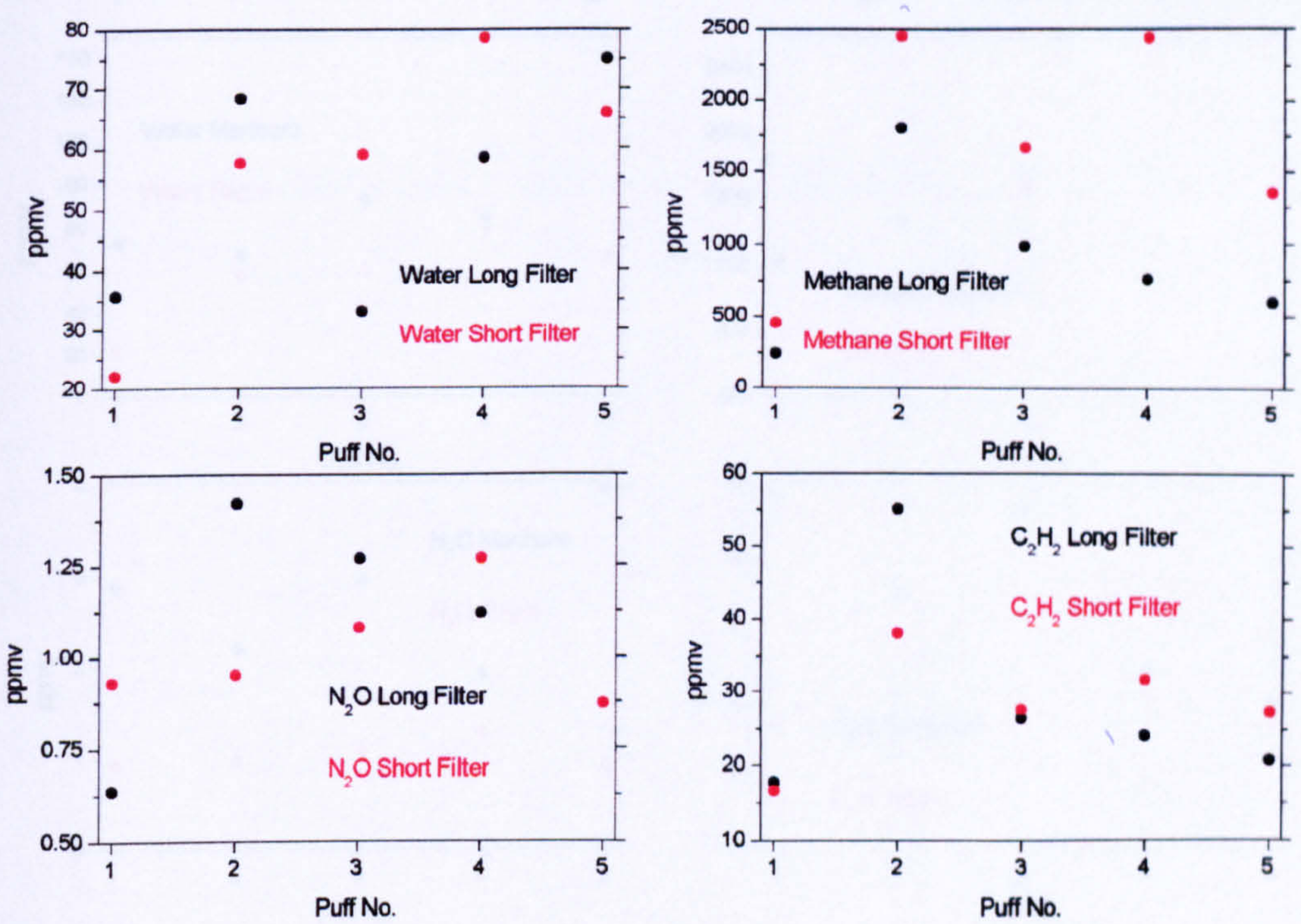

Figure 5.3.46 – *The Black dots show the emission in the long filter experiment. The Red dots show the emission in the short filter experiment.*

The concentration of Methane for all of the five puffs is larger in the short filter experiment compared to the appropriate puff in the long filter experiment. The other three gases show similar emissions when averaged over all five puffs. This suggests that the cigarette filter preferentially filters some gases more than other gases. The short filter data for the Regal King Size cigarette is compared to the short filter cigarette data for the Marlboro Lights in Figure 5.3.47.

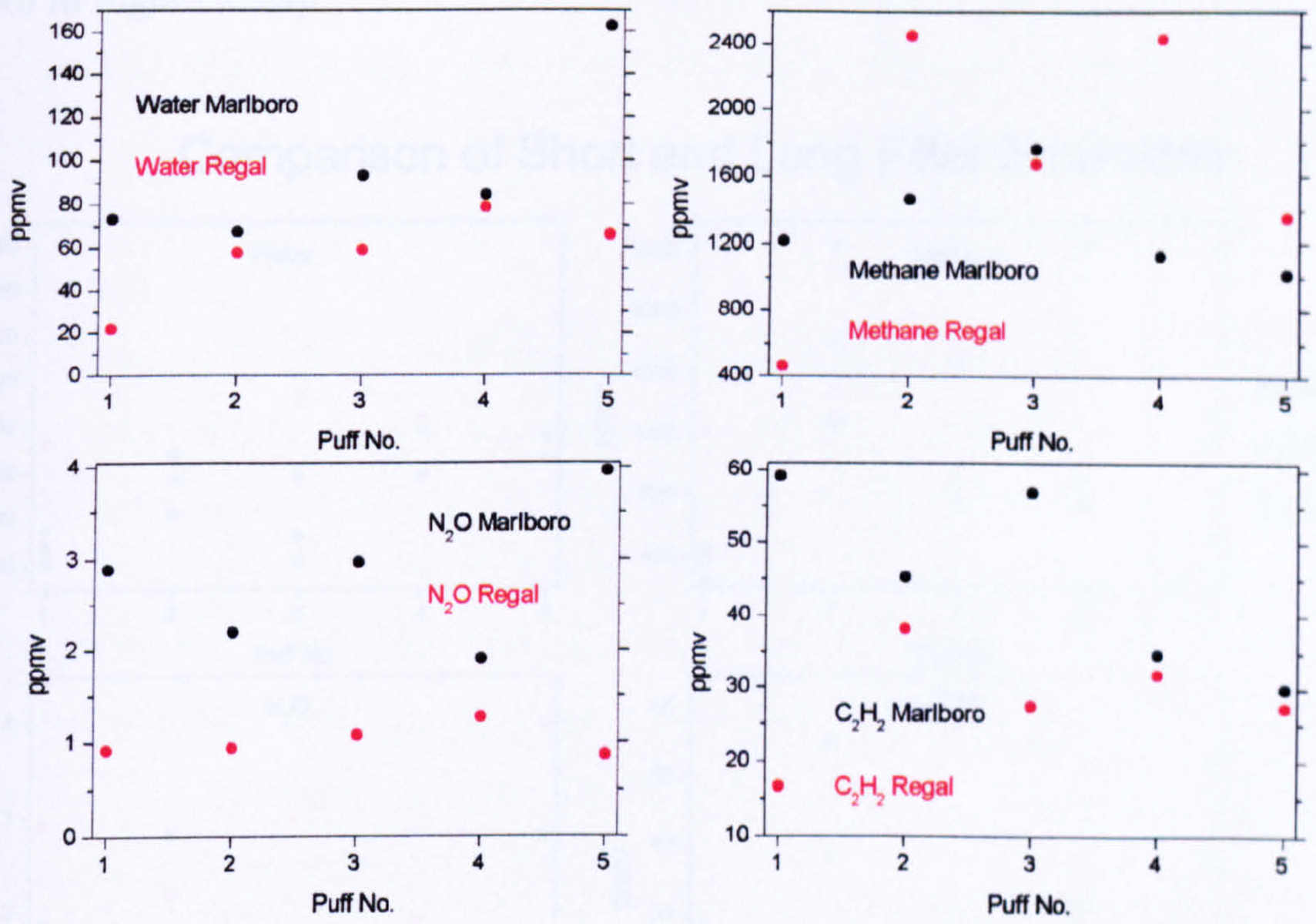

Figure 5.3.47 – *The Black dots show the emission in the Marlboro Lights experiment. The Red dots show the emission in the Regal King Size experiment.*

For the Water, Nitrous Oxide and Acetylene emissions all of the Marlboro Lights cigarette puffs contain more of the gases than the equivalent Regal King Size puff. Only the second and fourth puffs Methane emissions are larger in the Regal King Size cigarettes than the Marlboro Lights cigarettes.

5.3.9 Discussion – 8μm

From the work done at 8μm there appears to be less of a standard emission pattern during the puffs of the cigarette for most of the gases identifiable at 8μm. However three of the four experiments show very similar Formaldehyde emission patterns, the exception being the shortened filter Marlboro Lights cigarette. A comparison of the

emission of Methane, Acetylene, Nitrous Oxide and Water for the four experiments is shown in Figure 5.3.48.

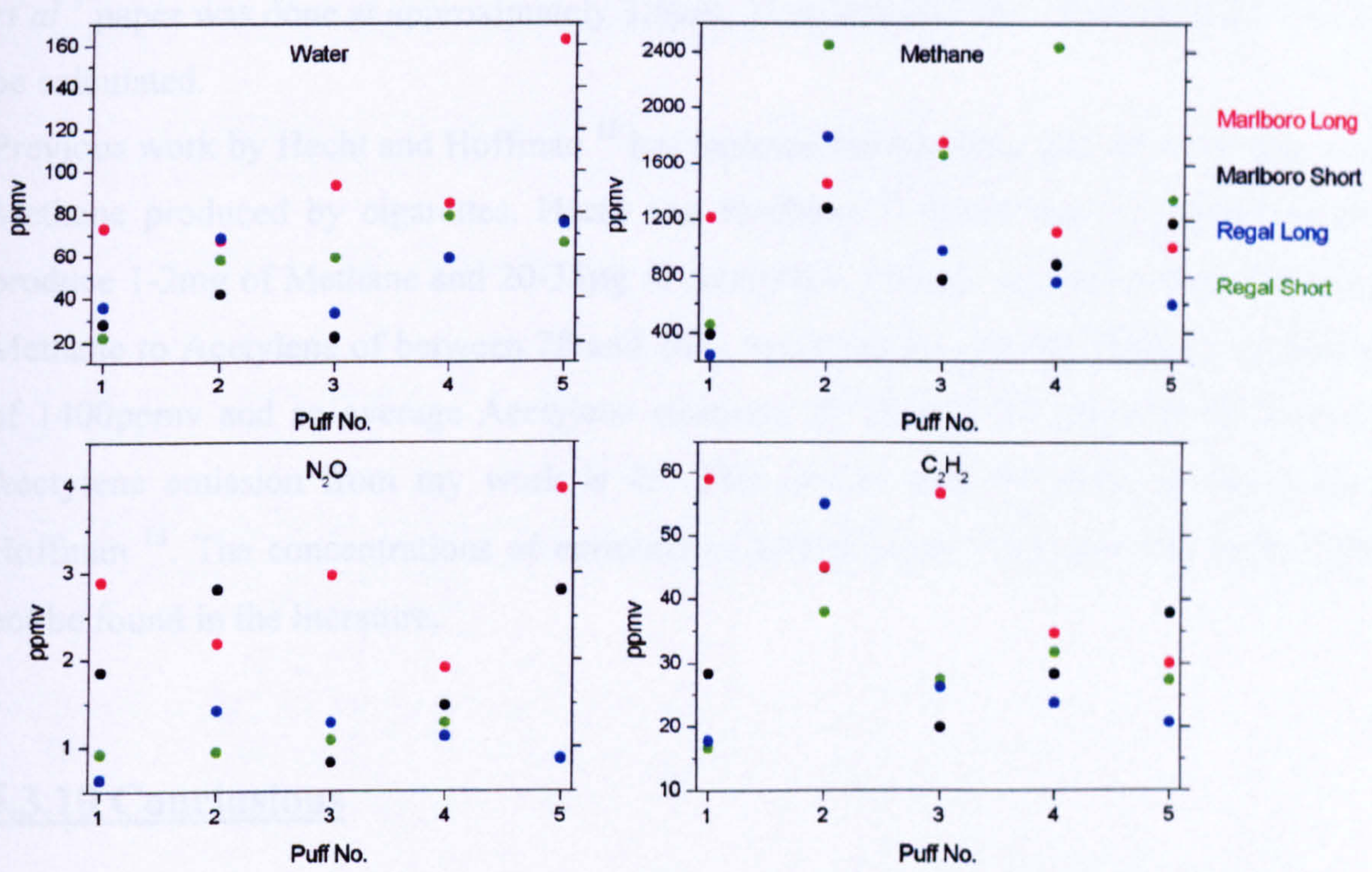

Figure 5.3.48 – *The Black dots in the four graphs show the emission in the Marlboro Lights short filter experiment. The Red dots in the four graphs show the emission in the Marlboro Lights long filter experiment. The Blue dots in the four graphs show the emission in the Regal King Size short filter experiment. The Green dots in the four graphs show the emission in the Regal King Size Long filter experiment.*

From the above data and the scattering by large molecules, in general the longer filter reduces the emissions from the cigarette and the higher tar cigarette, which is the Regal King Size cigarette, produces more emissions. The only reference found on the concentration of Nitrous Oxide in cigarette smoke was by R. E. Barren *et al.* [12]. R. E. Barren *et al* observed Nitrous Oxide at approximately 4.5μm, giving a per puff range of 2-20ppmv. This compares to the range of 0.6-2.8ppmv from this work. In the paper by

R. E. Barren *et al* they could not narrow the range down and reported that further work would be done to better estimate the Nitrous Oxide range.

The line intensities for the observed Formaldehyde lines could not be found in the literature. The cigarette Formaldehyde work reported by other researchers such as the Li *et al* [5] paper was done at approximately 3.6μm. Time did not allow for line intensities to be calculated.

Previous work by Hecht and Hoffman [13] has reported the mass per puff of Acetylene and Methane produced by cigarettes. Hecht and Hoffman [13] found that a cigarette could produce 1-2mg of Methane and 20-35μg of Acetylene. This gives a ratio of emission of Methane to Acetylene of between 28 and 100. Assuming an average Methane emission of 1400ppmv and an average Acetylene emission of 35ppmv the ratio of Methane to Acetylene emission from my work is 40. This ties in with the work of Hecht and Hoffman [13]. The concentrations of emission of Methane and Acetylene per puff could not be found in the literature.

5.3.10 Conclusions

I have shown that by using my Quantum Cascade laser based spectrometer several gases, such as Methane, Nitrous Oxide, Water and others, can be detected in the exhaust smoke of cigarettes. Cigarettes have been studied at 8μm and 10μm. The puff by puff analysis of different cigarette types has been conducted to look at the concentrations of the identifiable gases in each of the puffs. By looking at the amount of scatter an indication of the amount of larger molecules produced by the cigarettes has been identified. The effect of altering the filter system of a cigarette has been looked at for two different types of cigarette. The results of the work carried out are interesting enough that a further study could be carried out using a standard smoke sampling technique in order to improve the reproducibility of the results.

5.3.11 References

1) Chemical composition of tobacco and cigarette smoke in two brands of New Zealand cigarettes, J. Fowles, New Zealand ministry of health report, 25th August 2003

2) Chemical components of cigarette smoke and biological activity, A. D. Little, British American Tobacco, report C-69157, 6th February 1968

3) All about asthma, http://www.asthma.org.uk/about/an035.php

4) Measurement of formaldehyde in a single puff of cigarette smoke using tunable diode laser infrared spectroscopy, M. E. Parrish and C. N. Harward, App. Spec., **54**, 11, 1665-1677, (2000)

5) Formaldehyde in the gas phase of mainstream cigarette smoke, S. Li, J. L. Banyasz, M. E. Parrish, J. Lyons-Hart and K. H. Shafer, Journal of Analytical and Applied Pyrolysis, **65**, 137-145, (2002)

6) Quantum cascade infrared laser spectroscopy for real-time cigarette smoke analysis, Q. Shi, D. D. Nelson, J. B. McManus, M. S. Zahniser, M. E. Parrish, R. E. Baren, K. H. Shafer and C. N. Harward, Anal. Chem., **75**, 5180-5190, (2003)

7) Hydrazine detection limits in the cigarette smoke matrix using infrared tunable diode laser absorption spectroscopy, S. Plunkett, M. E. Parrish, K. H. Shafer, J. H. Shorter, D. D. Nelson and M. S. Zahniser, Spectrochimica Acta A, **58**, 2505-2517, (2002)

8) Puff-by-puff and intrapuff analysis of cigarette smoke using infrared spectroscopy, M. E. Parrish, J. L. Lyons-Hart and K. H. Shafer, Vibrational Spectroscopy, **27**, 29-42, (2001)

9) Astigmatic mirror multipass absorption cells for long-path-length spectroscopy, J. B. McManus, P. L. Kebabian and M. S. Zahniser, App. Opts., **34**, 18, 3336-3348, (1995)

10) Determination of ammonia in mainstream tobacco smoke, Canadian Health board, Health Canada official method, December 1999

11) Private communication, T. A. Blake, R. L. Sams and S. W. Sharpe, Enviromental Molecular science laboratory, Pacific Northwest National Laboratory

12) Quad quantum cascade laser spectrometer with dual gas cells for the simultaneous analysis of mainstream and sidestream cigarette smoke, R. E. Baren, M. E. Parrish. K.

H. Shafer, C. N. Harward, Q. Shi, D. D. Nelson, J. B. McManus and M. S. Zahniser, Spectrochimica Acta A, **60**, 3437-3447, (2004)

13) The relevance of tobacco-specific nitrosamines to human cancer, S.S. Hecht and D. Hoffmann, Cancer Surveys *8*: 273-294, (1989)

5.4 Vehicle Emissions Experiments

5.4.1 Introduction

In this chapter I will discuss the work that I have carried out studying the exhaust emissions of Cars and Motorbikes. The monitoring of emissions from vehicles has become important in recent years due to public concern and changes in legislation limiting emissions. The introduction of new car emission rules in the UK in April 2002 [1] paved the way for taxing cars on the amount of carbon dioxide emissions produced. Vehicle exhaust pollution is thought to be the single largest source of gaseous pollutants in urban areas [2]. In the first section of this chapter I will discuss the technologies associated with the reduction and control of vehicle emissions. I will also discuss the motivation for measuring some of the gases monitored during this work. I will describe experiments carried out at 8μm and 10μm to monitor several gaseous species in different vehicle exhausts, including Methane, Nitrous Oxide, Carbon Dioxide, Ethylene, Water and Acetylene. The concentrations of these gases have between worked out as a function of time relative to the start of the vehicle engines. The relationship between the exhaust constituents will be discussed.

5.4.2 Vehicle Exhaust Components

A standard petrol combustion vehicle exhaust plume contains hundreds of different compounds. Some of the chemicals released are described below. Particulates are formed in the exhausts of vehicles. These particulates are made up of a carbon core with other chemicals such as acids, organic compounds and metals. NOx is also produced in vehicle emissions, which reacts in the atmosphere to form other compounds. Other compounds released include volatile organic compounds (VOC), which include Acrolein, Benzene and other aromatic compounds.

The gases, which were measured during this work, include Methane, Nitrous Oxide, Carbon Dioxide, Ethylene, Water and Acetylene. These gases were chosen because the lasers available to me lased at wavelengths that were advantageous to the detection of

these gases. The 10μm laser detected Ethylene, Water and Carbon Dioxide. The 8μm laser detected Methane, Nitrous Oxide, Carbon Dioxide, Water and Acetylene.

5.4.3 Other Vehicle Exhaust Monitoring

A great deal of research has been done into the emissions of vehicles. With new technological breakthroughs in catalytic converters and engine management systems comes more studies to test their effectiveness. I will highlight some of this work that is relevant to the work that I have done. Laser based spectroscopy has been used extensively to study exhaust emissions under several different conditions. E. D. Hinkley and A. R. Calawa looked at the ethylene concentrations above a car park using a double pass tunable diode laser spectrometer [2]. A tunable diode laser system was used by D. D. Nelson et al to look at several small molecules in the exhausts of vehicles by a cross road remote sensing technique [3]. A study of over 1000 vehicles was made by J. L. Jimenez et al which looked at the Nitrous Oxide levels in car exhausts as the vehicle crosses the laser beam [4]. Work has been done by M. Tanaka et al to look at the effects of different types of fuel on the emissions produced by motor vehicles [5]. The cold start emissions of Methane, Benzene and Alkyl Benzene were studied by N. V. Heeb et al [6]. A review of the advances in catalytic converter technology over the last quarter century has been made by J. Kašpar et al [7].

5.4.4 Catalytic Converter

Three way catalysts (TWC) have been developed over the last decades to convert harmful emission gases into less harmful products before release into the atmosphere. The components of the vehicle exhaust require reduction and oxidisation reactions to be performed simultaneously in the converter. The effectiveness of a catalytic converter varies with several parameters. The age and condition of the vehicle effect the emissions produced. Poorly maintained vehicles and wear and tear lead to greater emissions of Carbon Monoxide and Hydrocarbons [2]. The different gases, and their relative

concentrations, tell us about the health of a vehicle. The temperature of the catalytic converter and the temperature of the engine effect the emissions from a vehicle. A typical catalytic converter has an optimum operating temperature of approximately 900°C [7]. This means that the emissions of a vehicle will change from start up to running temperature, which will be shown in this chapter. The air/fuel ratio has a major influence on vehicles emissions. When the air/fuel ratio is greater than 1 the engine is said to be running rich, which causes more unburned Hydrocarbons and Carbon Monoxide to be produced. This situation is most common at start up. When the air/fuel ratio is less than 1 the engine is said to be running lean, which causes low Hydrocarbon and Carbon Monoxide emission. The amount of NOx produced is increased because of the lack of a reducing agent such as Carbon Monoxide or a Hydrocarbon. When the air/fuel ratio equals 1 the engine is said to be running stoichiometrically, which is the optimum operating condition. The conversion efficiency for the removal of harmful species is at its maximum. In order to maintain the air/fuel ratio at the stoichiometrical level a control loop is used. The Oxygen concentrations before and after the converter are compared to monitor fluctuations in the air/fuel ratio.

5.4.5 Vehicles Studied

Several different vehicles were studied during this work. The first set of vehicles was studied using the 10μm laser. The first of these vehicles was a year 2003 Renault Clio 1.2 16V automatic, which was also studied using the 8μm laser. The second vehicle was a year 2001 Peugeot 406 2.0HDi manual. The other vehicles were a year 1990 1.8D Ford Cargo van manual, a year 2000 BMW 318i automatic, a 1999 Toyota Avensis 2.0 manual and a year 2000 Honda S2000 manual. As well as the Renault Clio a 2003 Toyota Avensis 2.0 manual and a 2003 Yamaha R6 600cc motor bike were studied at 8μm.

5.4.6 Experimental Setup

A full description of the spectrometer can be found in section 3.1. The lasers were mounted in temperature controlled enclosures. The temperature of the laser substrate could be varied between -40°C and +40°C, however most of the experiments were carried out at around 0°C. Both lasers were excited by top hat shaped current pulses from the in house designed power supply [8]. The pulses used to drive the 10μm laser varied from 150ns to 300ns. In section 3.2 I showed that the chirp rate of the 10μm laser at 5A drive current is approximately linear over a 200ns pulse. The pulses used to drive the 8μm laser varied from 1000ns to 1500ns. The chirp rate of the 8μm laser is extremely nonlinear when pulsed at 1270ns with a 3.5A drive current. An order of magnitude change in chirp rate from the start to the end of the pulse is possible. Only one laser was used during any one experiment. The light from the laser in use was directed into the astigmatic Herriott cell [9] using steering mirrors. For the 10μm experiments the astigmatic Herriott cell was setup for 66m of optical path. For the 8μm experiments the astigmatic Herriott cell was configured for 115m of optical path. The astigmatic Herriott cell and both of these solutions are described in detail in section 2.3. Some of the earlier 10μm experiments were carried out using bagged samples. These samples were collected from the exhaust pipe of the vehicle and then studied one bag at a time. This method had the disadvantage of very poor time resolution. Bags could only be collected about once every two minutes. The time taken to get the bags bag to the spectrometer and then analyse them was at least ten minutes, which meant that any short lived species in the exhaust would have no longer been present when the sample were analysed. The rest of the 10μm experiments and the 8μm experiments were carried out using flowing samples. The car exhaust was connected to the input port of the cell using a 50m long 12mm diameter hose. Flow rate experiments with the hose found that the dwell time in the cell was approximately 2s and the flow in the hose was approximately plug flow. The output port of the cell was connected to the vacuum system. The pressure in the cell was maintained at a constant level of between 35Torr and 50Torr using a manual valve in the 10μm experiments and a pressure controller in the 8μm experiments. After exiting

the astigmatic Herriott cell the laser beam was focussed onto the fast MCT detector and digitised using an Acqiris averager card. The rest of the 8μm experiments looked at the exhaust plume outside of the exhaust pipe. The hose was placed a distance away from the pipe so that the exhaust gases were diluted by the atmosphere. This allows the sensitivity of the instrument and the dispersion of exhaust gases in the atmosphere to be looked at. The vehicles were started from cold and left to idle during the experiment. The vehicles tested used automatic chokes on start up so the engine revving and air/fuel ratios were set by the engines timing belt or engine management system.

5.4.7 Results - 10μm

The first set of results I will discuss relate to the working involving bagged samples. The car tested for these measurements was the 1999 Toyota Avensis. A drive current of 5A was used to drive the 10μm laser with 300ns pulses and a repetition rate of 5KHz. The substrate temperature of the laser was maintained at -1.52°C. Each of the spectra recorded was an average of 5000 pulses, which gives a one second recording time. Figure 5.4.1 below shows the spectrum of the car exhaust at start up.

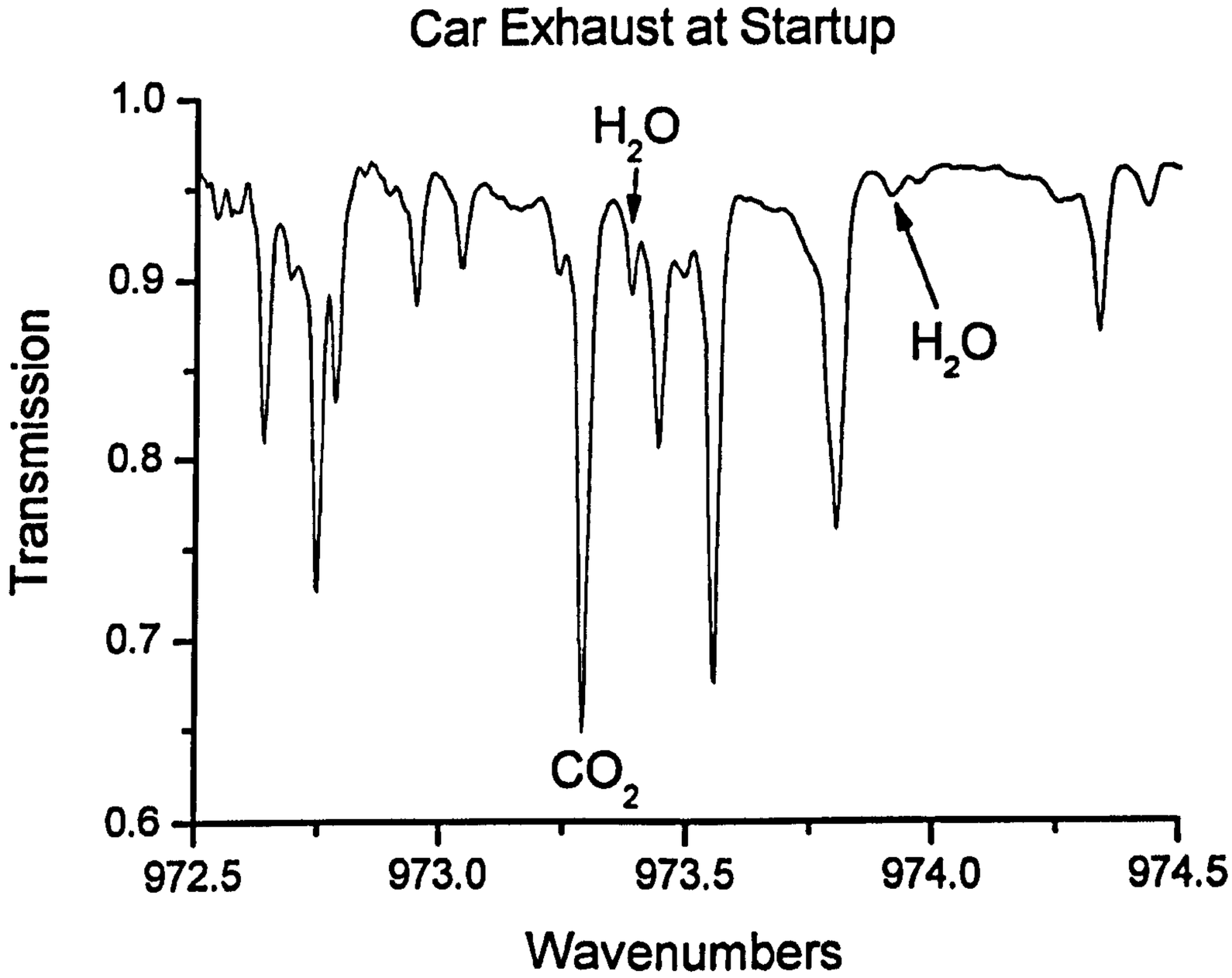

Figure 5.4.1 – *Car exhaust at start up*

This spectrum consists of mainly Ethylene and Carbon Dioxide. The strongest Carbon Dioxide line in the lasing region is indicated on the figure. The rest of the strong lines are Ethylene absorption lines. There are two weak water lines in the region at about 973.45cm^{-1} and 974cm^{-1}, which are also marked on the spectrum. The second bagged sample was taken five minutes after the car had started up. Figure 5.4.2 below shows the car exhaust spectrum taken after five minutes of the engine running.

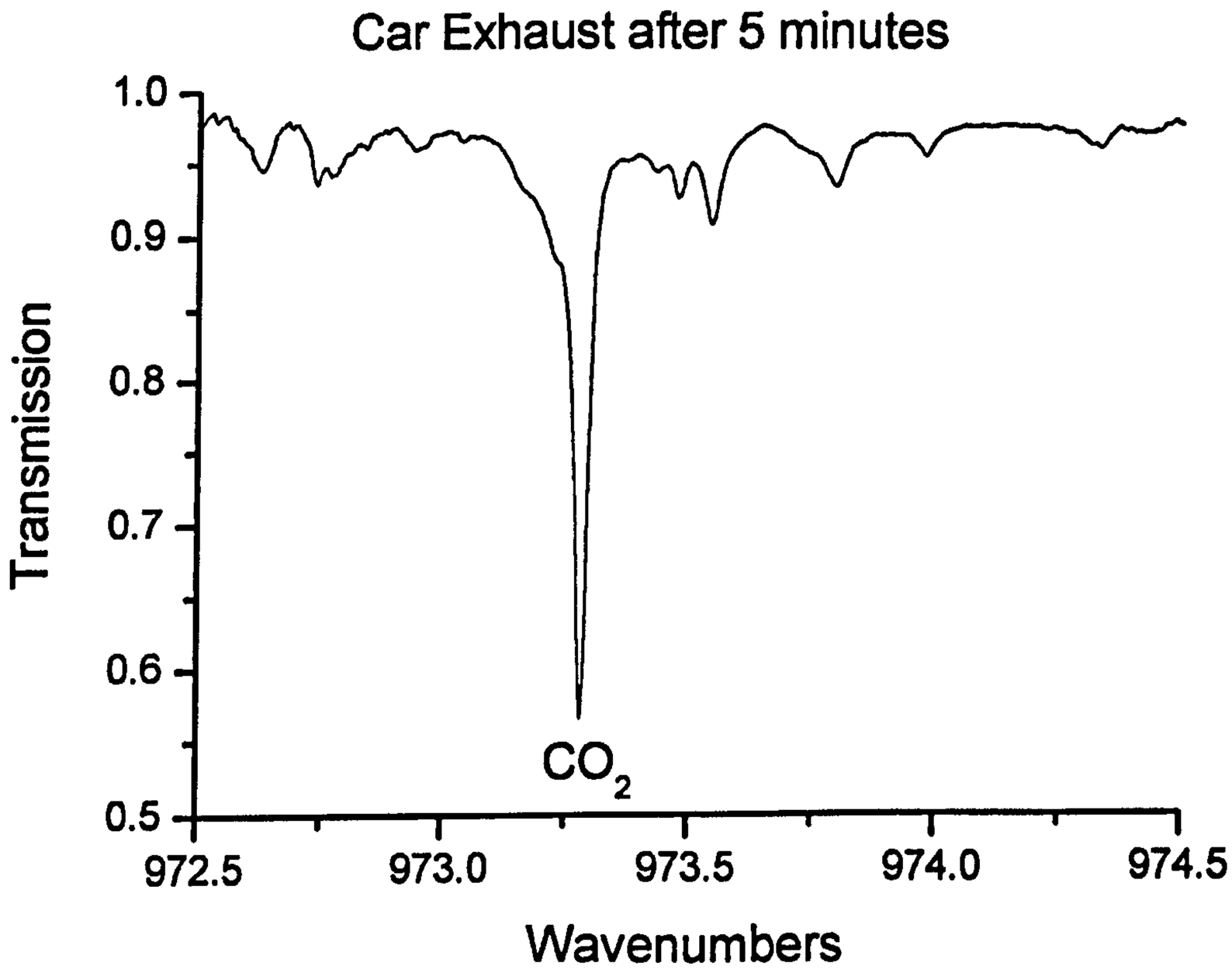

Figure 5.4.2 – *Car exhaust after five minutes of running*

It can be seen that after five minutes of the engine running the majority of absorption in the lasing region is done by Carbon Dioxide. This is what would be expected as the cars catalytic converter warmed to operating temperature. The Ethylene spectrum can still be seen so after five minutes there is still a residual Ethylene emission. It is also still possible to detect the water in the exhaust, which is also expected because Water is one of the end products in the catalytic converter reactions. The change in spectral features from start up to five minutes is enormous. Bagging the exhaust every five minutes does not provide the temporal resolution to study the changing emissions from a car exhaust. Speeding up the bagging process still leads to a temporal response of, at best, two minutes. The solution is too continuously sample the exhaust fumes, which is what lead me to the results I will discuss now. The first vehicle I tested using the continual sampling method was the 2003 Renault Clio. For this experiment the 10μm laser was driven with a 5A drive current using pulses of 140ns length and a repetition rate of

5KHz. The laser substrate was maintained at a temperature of +1°C. Each spectrum is the average of 5000 pulses, giving a time resolution of 1s. Figure 5.4.3 below shows the raw background and spectrum traces plotted on top of each other.

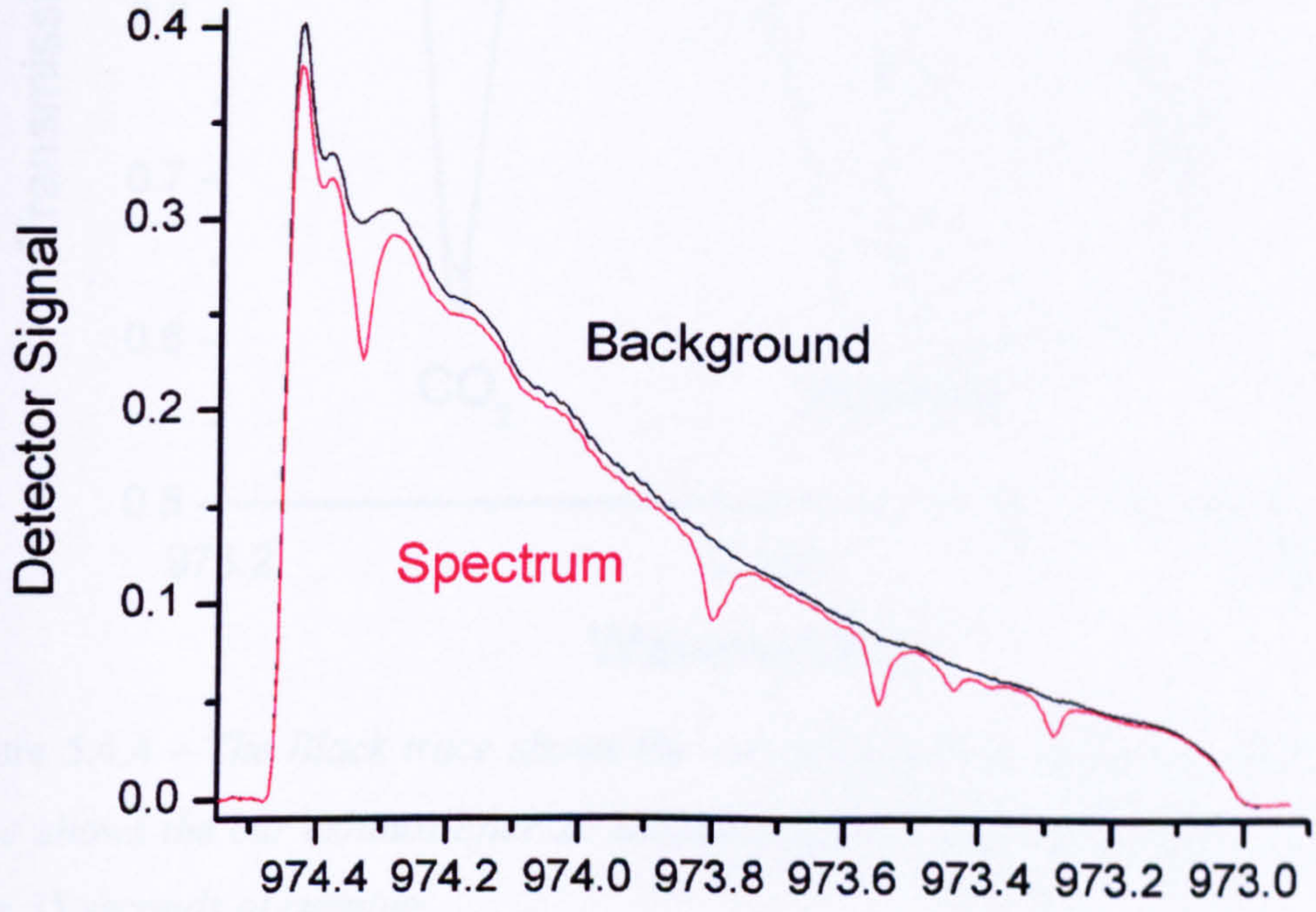

Figure 5.4.3 – *The Black trace shows the raw background pulse. The Red trace shows the raw spectrum pulse.*

The wavenumbers scale is reversed to show the start of the pulse in time at the left of the figure and the end of the pulse in time at the right of the figure. The detector signal has been inverted to show the data as positive values rather than the negative values returned from the inverting amplifier. Figure 5.4.4 below shows the changing absorption of Carbon Dioxide and Ethylene in the exhaust fumes.

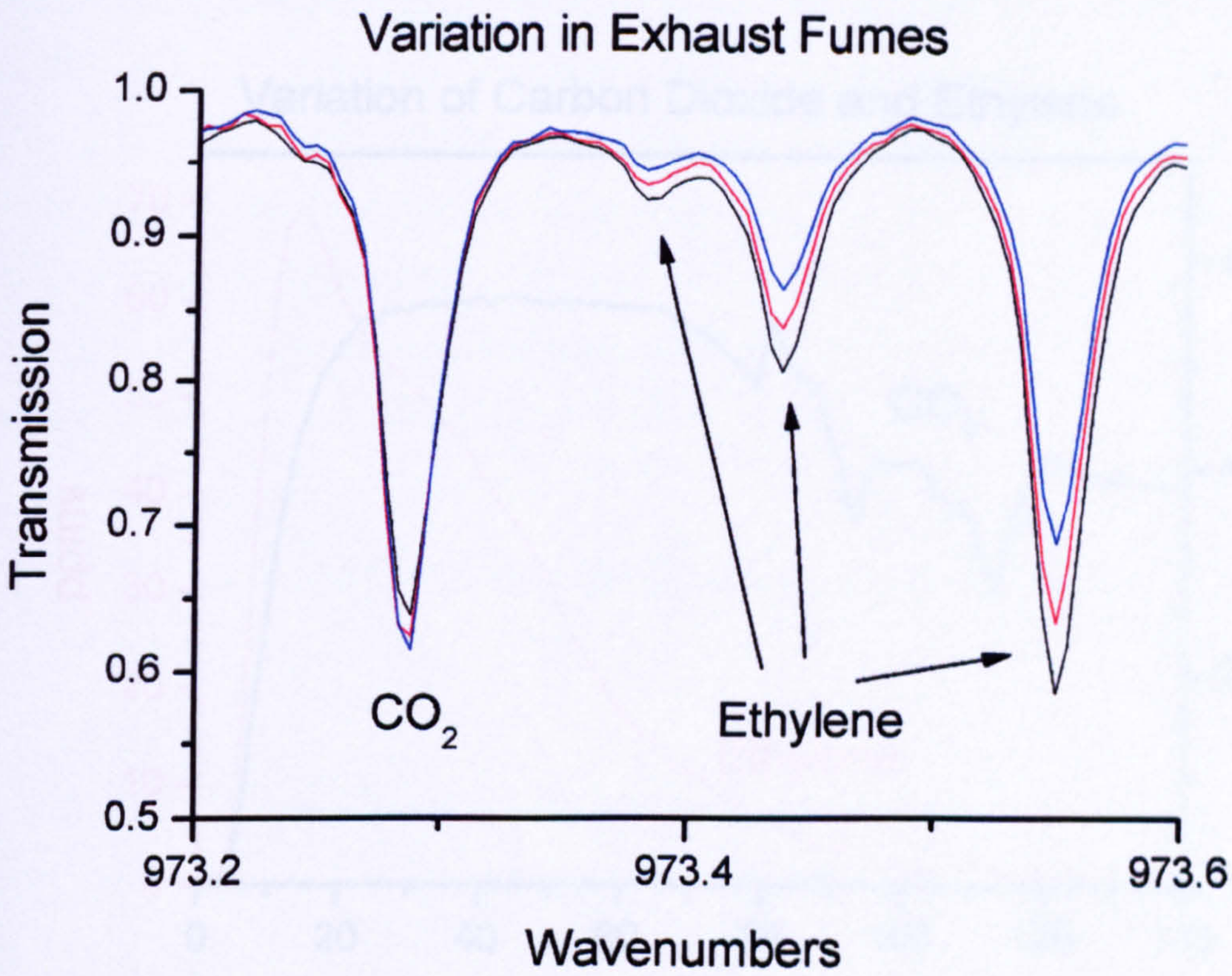

Figure 5.4.4 – *The Black trace shows the car exhaust fumes after 15 seconds. The Red trace shows the car exhaust after 25 seconds and the Blue trace shows the car exhaust after 35 seconds of running.*

It can be seen that in the 20s window from 15s after start up to 35s after start up that the Ethylene concentration has steadily dropped, whereas the Carbon Dioxide concentration has increased before levelling off. As the concentrations of the absorbing gases are directly linked to the area under the absorption line (after the natural logarithm of the transmission has been taken), the retrieval of the concentrations is relatively straight forward assuming there is no power saturation present. Power saturation and other nonlinear effects which may lead to asymmetric lineshapes are discussed in section 4.1. The retrieval process is described in section 3.1. Using this method the concentrations of Ethylene and Carbon Dioxide have been calculated as a function of time relative to the engine start up. Figure 5.4.5 below shows the variation in the concentrations of the Carbon Dioxide and Ethylene.

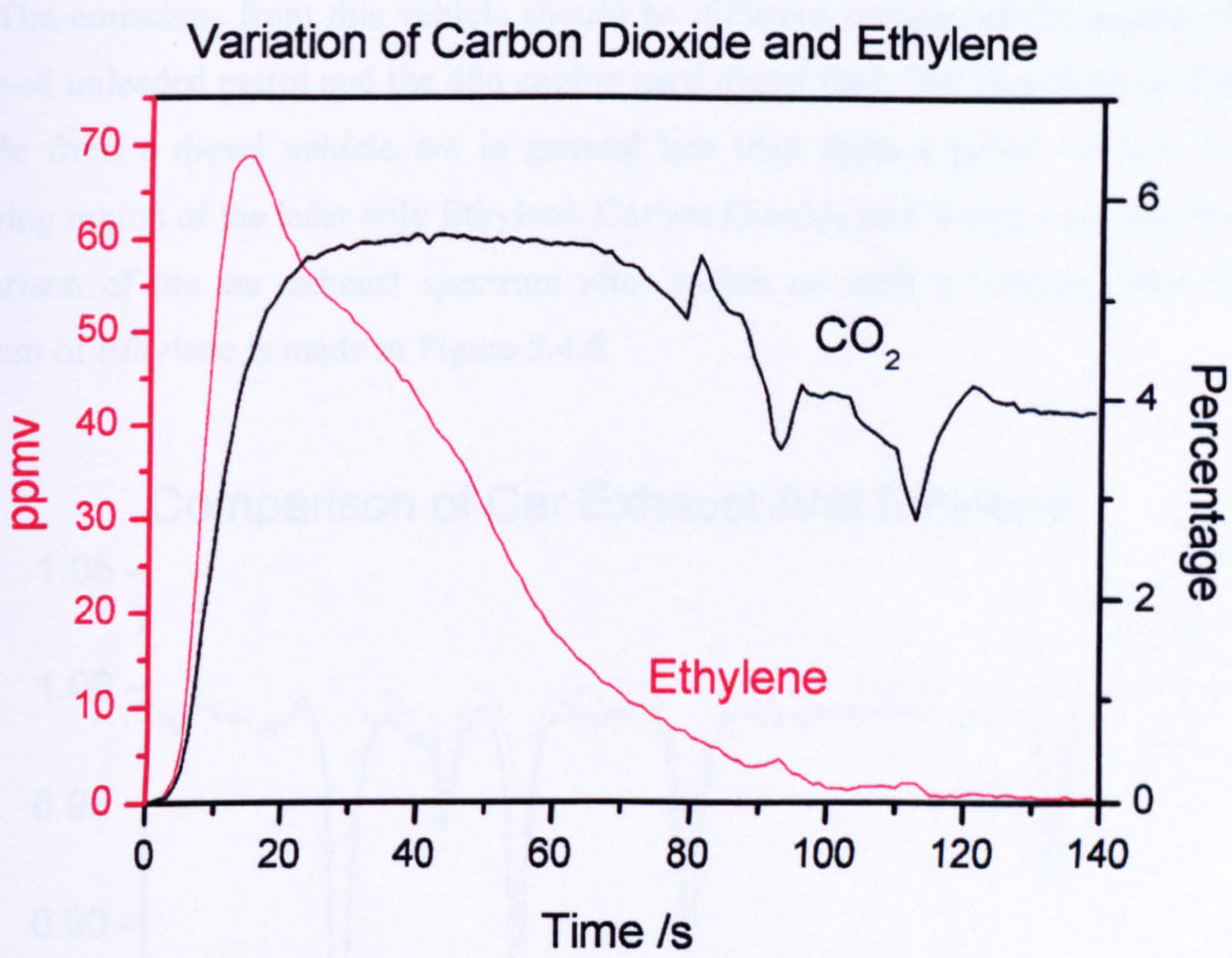

Figure 5.4.5 – *The Red trace shows the variation of Ethylene in the car exhaust and the Black trace shows the variation of Carbon Dioxide in the car exhaust.*

The Ethylene is plotted on a ppmv scale, which represents the number of parts per million by volume. The Carbon Dioxide is plotted on a simple percentage scale. Even though the amount of absorption from the Carbon Dioxide line is similar to the amount of absorption from one of the strong Ethylene lines the actual concentrations of the two gases are orders of magnitude different. This is due to the difference in the integrated intensities of the lines, which is discussed in section 4.1. From the data it seems as though the Ethylene emission is trailing off and the Carbon Dioxide emission is heading towards an asymptotic limit. This is in good agreement with the observations of the bagged emission experiment. The anti correlated events in the time evolution that occur at approximately 90s and 110s are probably due to the automatic choke adjusting the air/fuel ratio.

Using the same laser settings as above the second vehicle studied was the Peugeot 406 HDi. The emissions from this vehicle should be different because of the engine of the Clio used unleaded petrol and the 406 engine used diesel fuel. The emissions of Carbon Dioxide from a diesel vehicle are in general less than from a petrol vehicle. In the absorbing region of the laser only Ethylene, Carbon Dioxide and Water were detected. A comparison of the car exhaust spectrum after switch on with a Nitrogen Broadened spectrum of Ethylene is made in Figure 5.4.6.

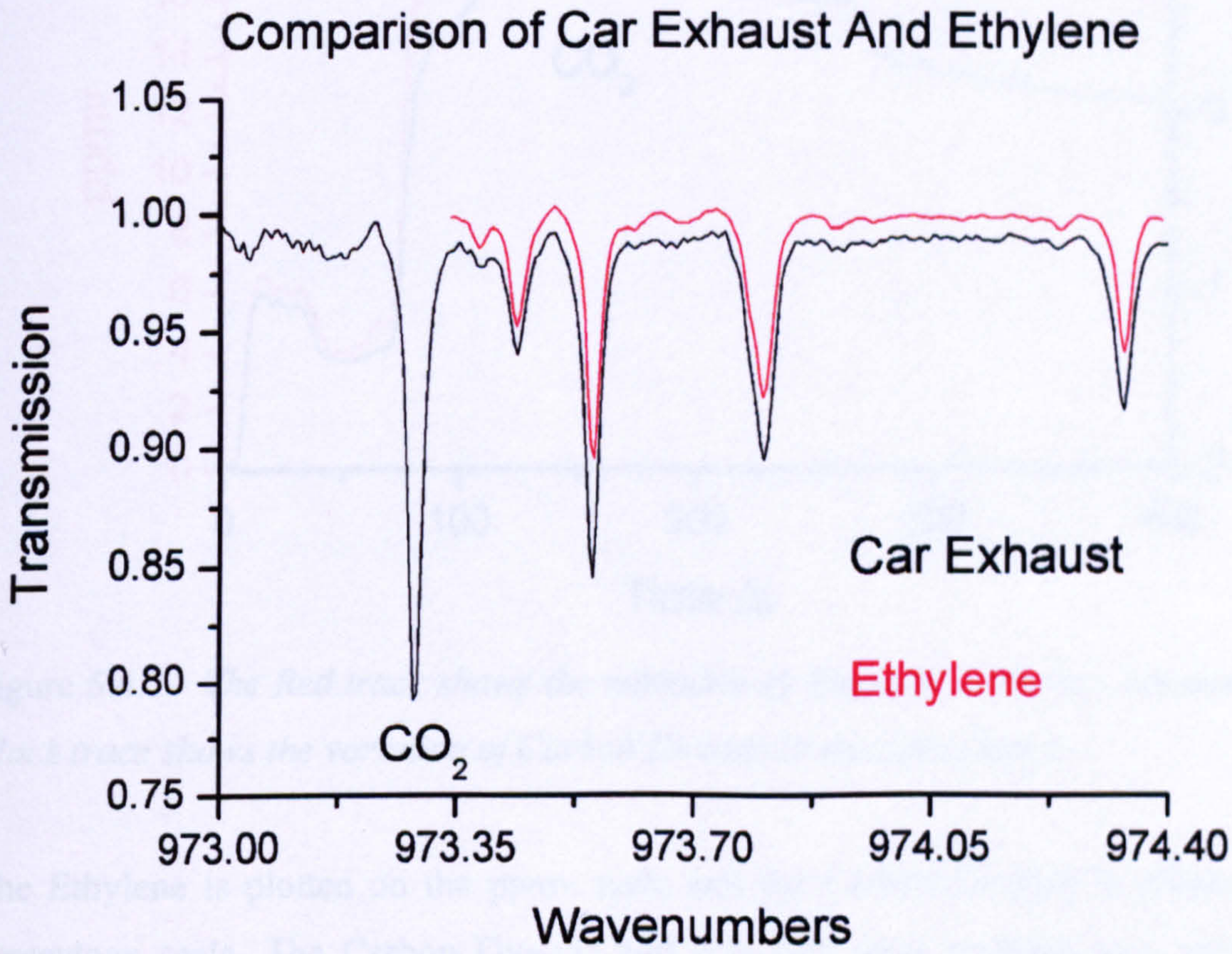

Figure 5.4.6 – *The Black trace shows the spectrum of the car exhaust. The Red trace shows the spectrum of Nitrogen broadened Ethylene.*

The car exhaust spectrum was recorded 90s after start up. The Ethylene spectrum was recorded with a Total cell pressure of 30Torr in which approximately 3milliTorr of Ethylene was present and the balance was Nitrogen.

Figure 5.4.7 shows the variation of Ethylene and Carbon Dioxide in the car exhaust as a function of time.

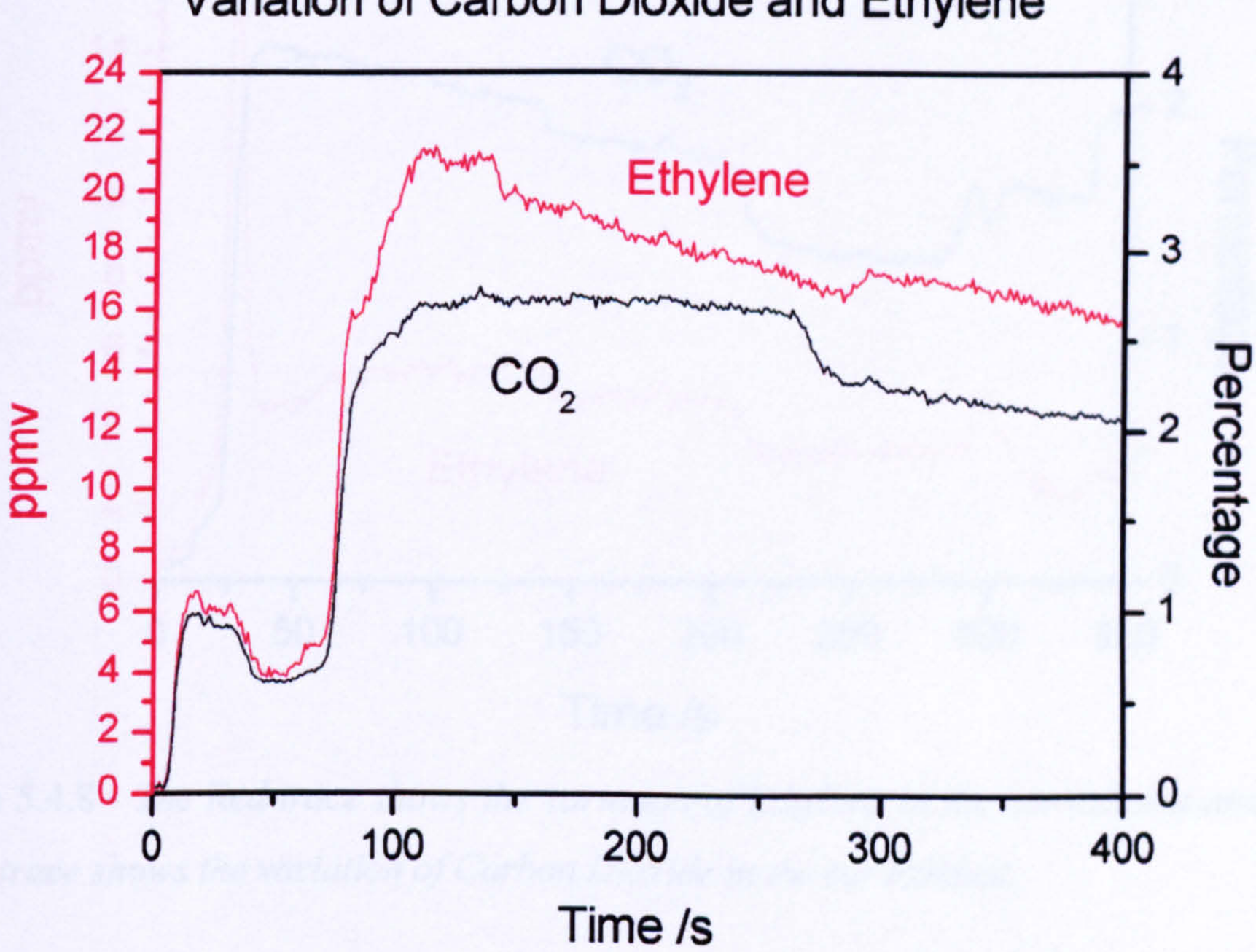

Figure 5.4.7 - *The Red trace shows the variation of Ethylene in the car exhaust and the Black trace shows the variation of Carbon Dioxide in the car exhaust.*

The Ethylene is plotted on the ppmv scale and the Carbon Dioxide is plotted on the percentage scale. The Carbon Dioxide and Ethylene seem to track each other much better than in the exhaust of the Clio.

The third vehicle studied was the Ford Van. This vehicle was also powered by a diesel engine. The laser settings were the same as the previous experiments. Figure 5.4.8 below shows the variation of Carbon Dioxide and Ethylene in the exhaust of the van.

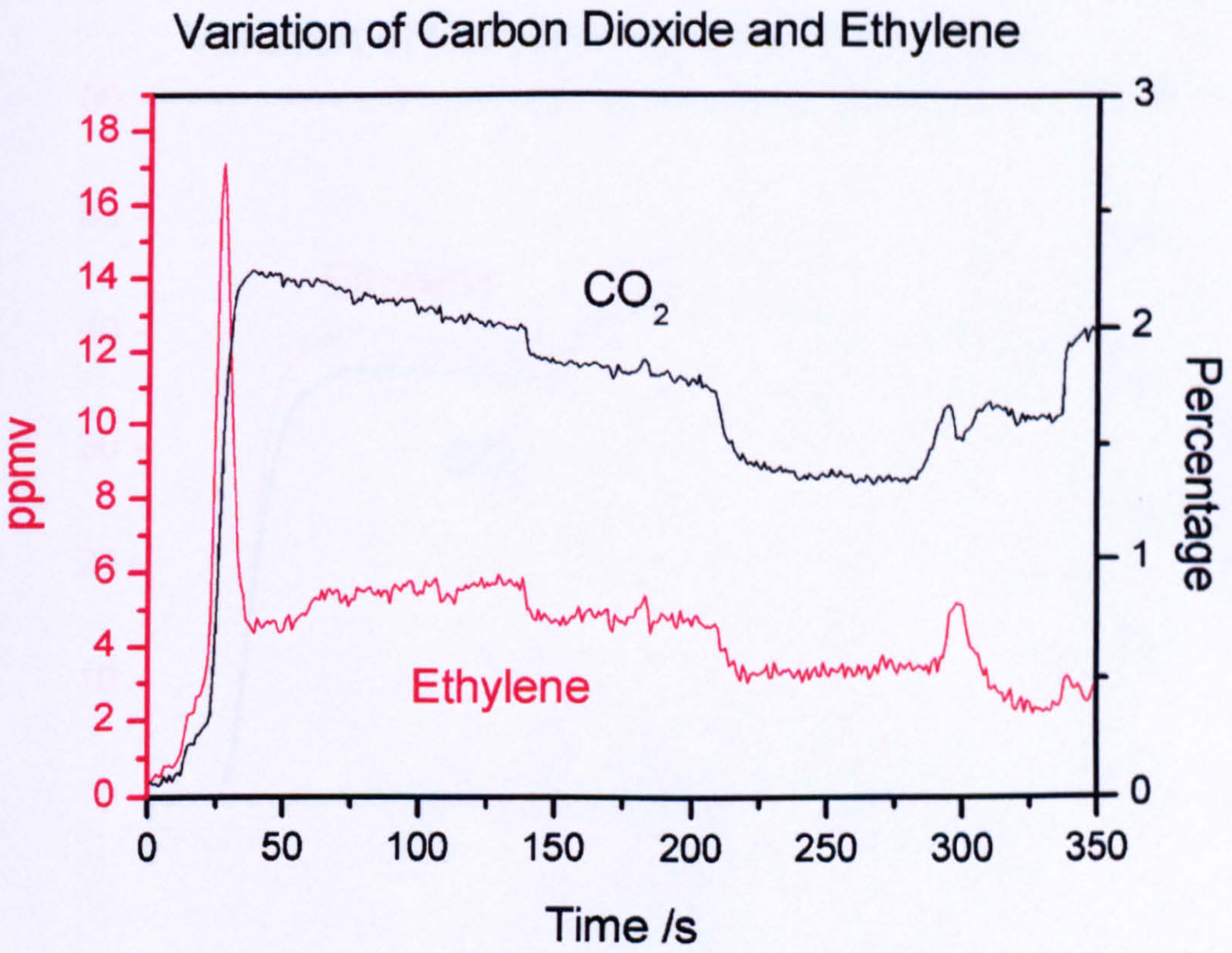

Figure 5.4.8 - *The Red trace shows the variation of Ethylene in the car exhaust and the Black trace shows the variation of Carbon Dioxide in the car exhaust.*

The Ethylene is plotted on the ppmv scale and the Carbon Dioxide is plotted on the percentage scale. Apart from the initial spike of Ethylene the two gases seem to track each other well.

The fourth vehicle to be studied was the BMW 318i. The laser settings were left unchanged from the previous measurements. This vehicle used unleaded fuel and should therefore be more like the Clio than the 406 of the Van. The variation of Ethylene and Carbon Dioxide in the BMWs exhaust is shown below in Figure 5.4.9.

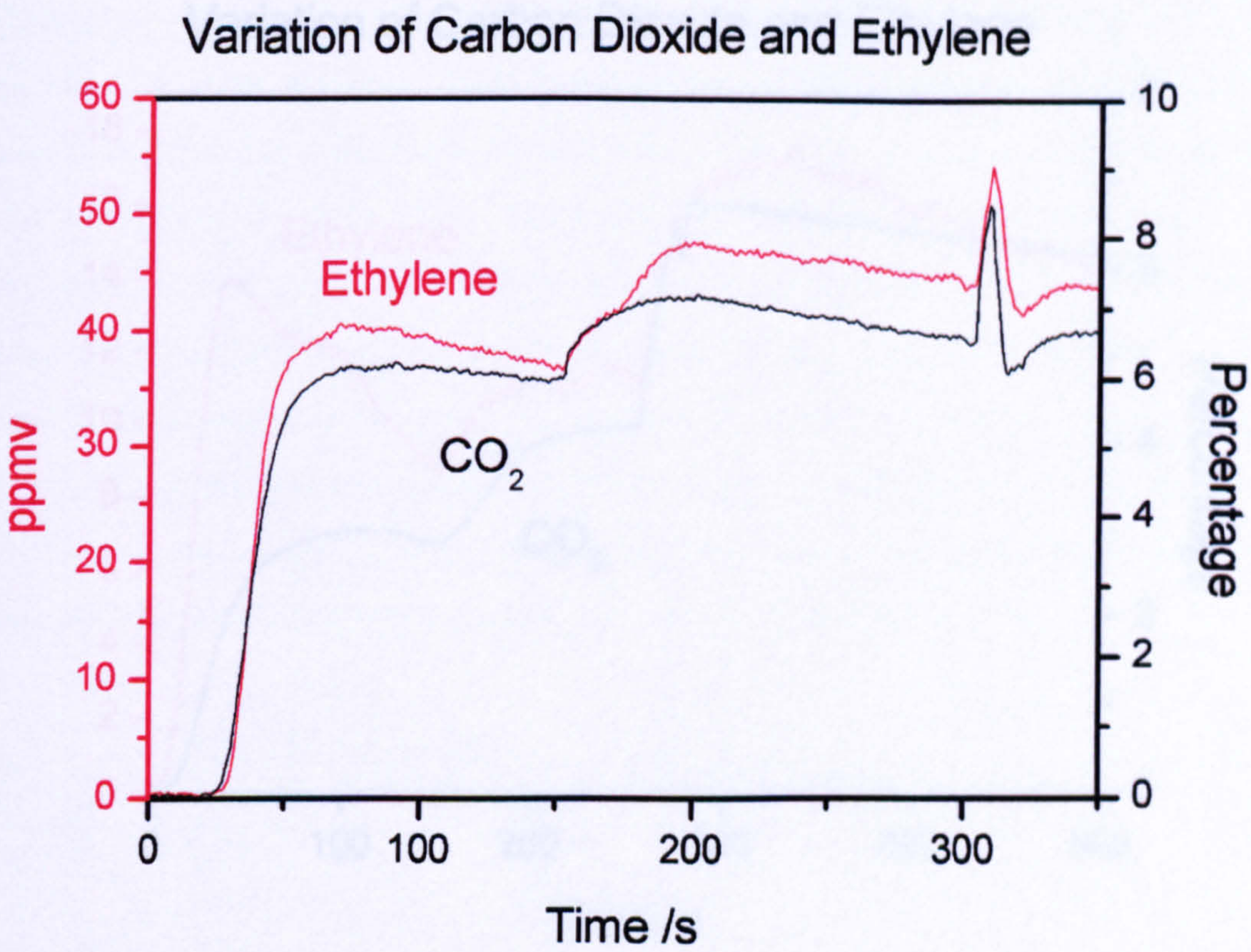

Figure 5.4.9 – *The Red trace shows the variation of Ethylene in the car exhaust and the Black trace shows the variation of Carbon Dioxide in the car exhaust.*

The Carbon Dioxide is plotted on the percentage scale and the Ethylene is plotted on the ppmv scale. The two gases again seem to track each other very well. The correlated spike in the two traces that occurs at about 300s after start up is probably due to the engine management system altering the automatic choke setting.

The final vehicle to be tested using this method was the Honda S2000. Figure 5.4.10 below shows the variation in the concentrations of Ethylene and Carbon Dioxide in the exhaust of the S2000.

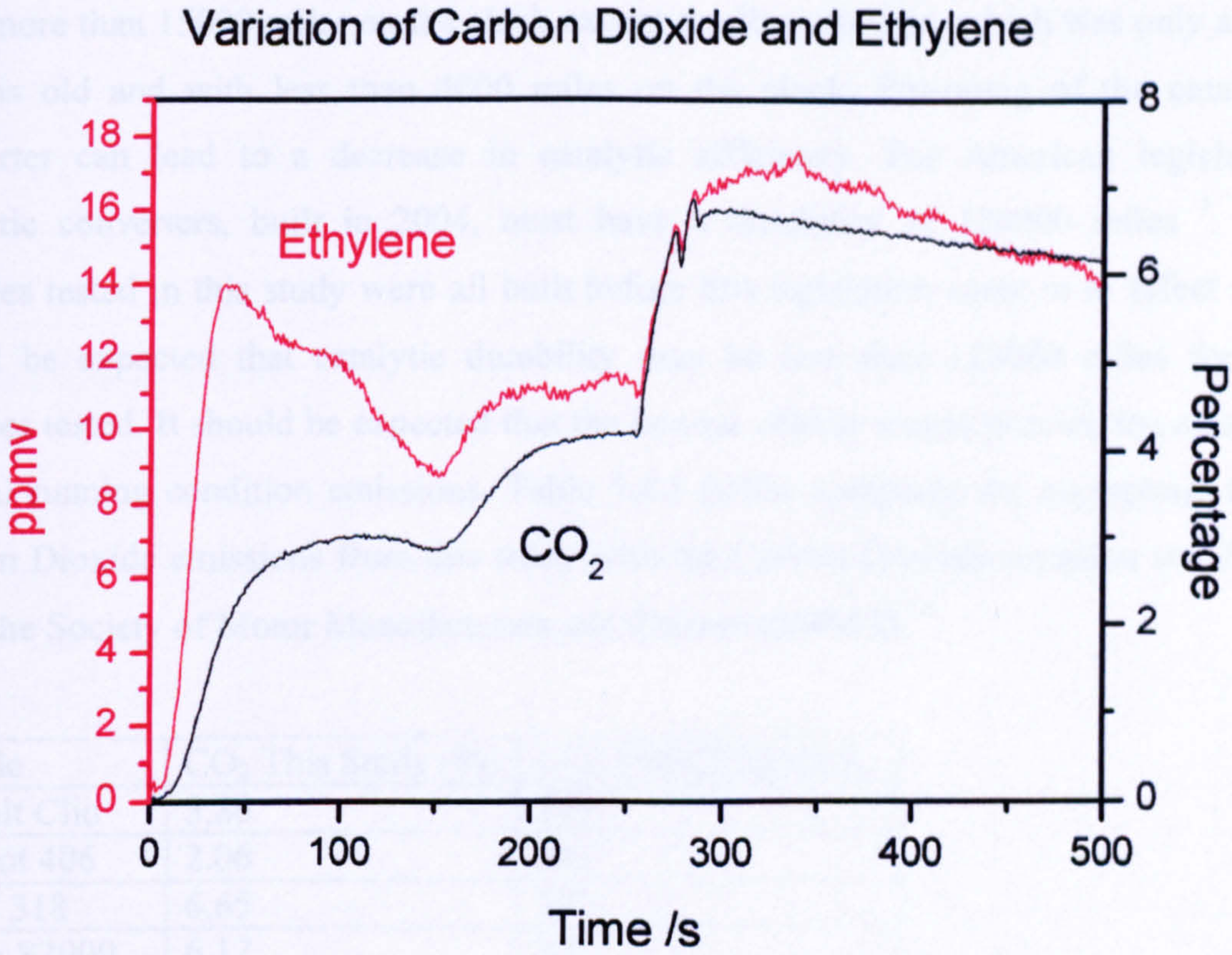

Figure 5.4.10 – *The Red trace shows the variation of Ethylene in the car exhaust and the Black trace shows the variation of Carbon Dioxide in the car exhaust.*

The Ethylene is plotted on the ppmv scale and the Carbon Dioxide is plotted on the percentage scale. Again the Ethylene and the Carbon Dioxide emissions are partly correlated.

5.4.8 Discussion - 10µm

From the work carried out it is apparent that no two vehicles emissions are the same when studied under similar conditions. The Carbon Dioxide emissions in all of the vehicles tend towards an asymptotic limit after the engine and catalytic converter have warmed to operating temperature. The Ethylene also tends towards an asymptotic limit for all of the vehicles, except in the Renault Clio the limit is zero. This could be to do with the age of the vehicles tested. All of the vehicles tested were at least one year old

with more than 15000 miles on the clock except the Renault Clio, which was only a few months old and with less than 4000 miles on the clock. Poisoning of the catalytic converter can lead to a decrease in catalytic efficiency. For American legislation catalytic converters, built in 2004, must have a durability of 120000 miles [7]. The vehicles tested in this study were all built before this legislation came in to effect so it would be expected that catalytic durability may be less than 120000 miles for the vehicles tested. It should be expected that the newest vehicle would provide the cleanest normal running condition emissions. Table 5.4.1 below compares the asymptotic limit Carbon Dioxide emissions from this study with the Carbon Dioxide emission standards from the Society of Motor Manufacturers and Traders (SMMT) [10].

Vehicle	CO_2 This Study (%)	CO_2 SMMT (g/Km)
Renault Clio	3.86	149
Peugeot 406	2.06	147
BMW 318	6.65	190
Honda S2000	6.17	237

The SMMT figures are produced from vehicles that are nearly new, which is not the case with some of the vehicles tested in this work. The Carbon Dioxide emissions from vehicles built before March 2001 are provided to the SMMT by the vehicle manufacturer and not by an independent test. The data from after March 2001 is taken from vehicles studied on a rolling road. This means that the comparison between this work and SMMT data may not be perfect. This is because the emissions will vary depending on the amount of revs the engine is experiencing; all of the engines idle at a similar rate, but travelling at the same speed on the rolling road will produce a wider range of revs. This will cause the fuel consumption, and therefore exhaust emissions, to be much more varied across the sample of vehicles. Another factor that could affect the comparison is the condition of the vehicles. If the any of the vehicles tested during this study had undergone significant catalytic poisoning then the emissions from these vehicles would be different to when they were new. Having said that the two sets of data are in general agreement such that a vehicle with a low percentage of Carbon Dioxide

emissions in my study will have a low Carbon Dioxide emission in the SMMT data. The effect of Ethylene and other hydrocarbons on the formation of Ozone has been studied by Derwent et al [11]. Ethylene is one of the most effective Ozone producers and as such is an interesting gas to monitor in the exhausts of cars.

5.4.9 Results - 8μm

I will discuss the results from the two different experiments carried out using the 8μm laser. In the first experiment three different vehicles were studied. The first vehicle studied was the same Renault Clio as studied in the 10μm region. This experiment was conducted using the 8μm laser driven with a 3.5A drive current. The pulse width of the laser was 1270ns and the pulse repetition rate was 20KHz. The substrate temperature of the laser was maintained at +3°C. Each of the spectra recorded is an average of 20000 pulses, giving a temporal resolution of 1s. Figure 5.4.11 below shows the comparison of the background pulse with the spectrum pulse recorded 50s after start up.

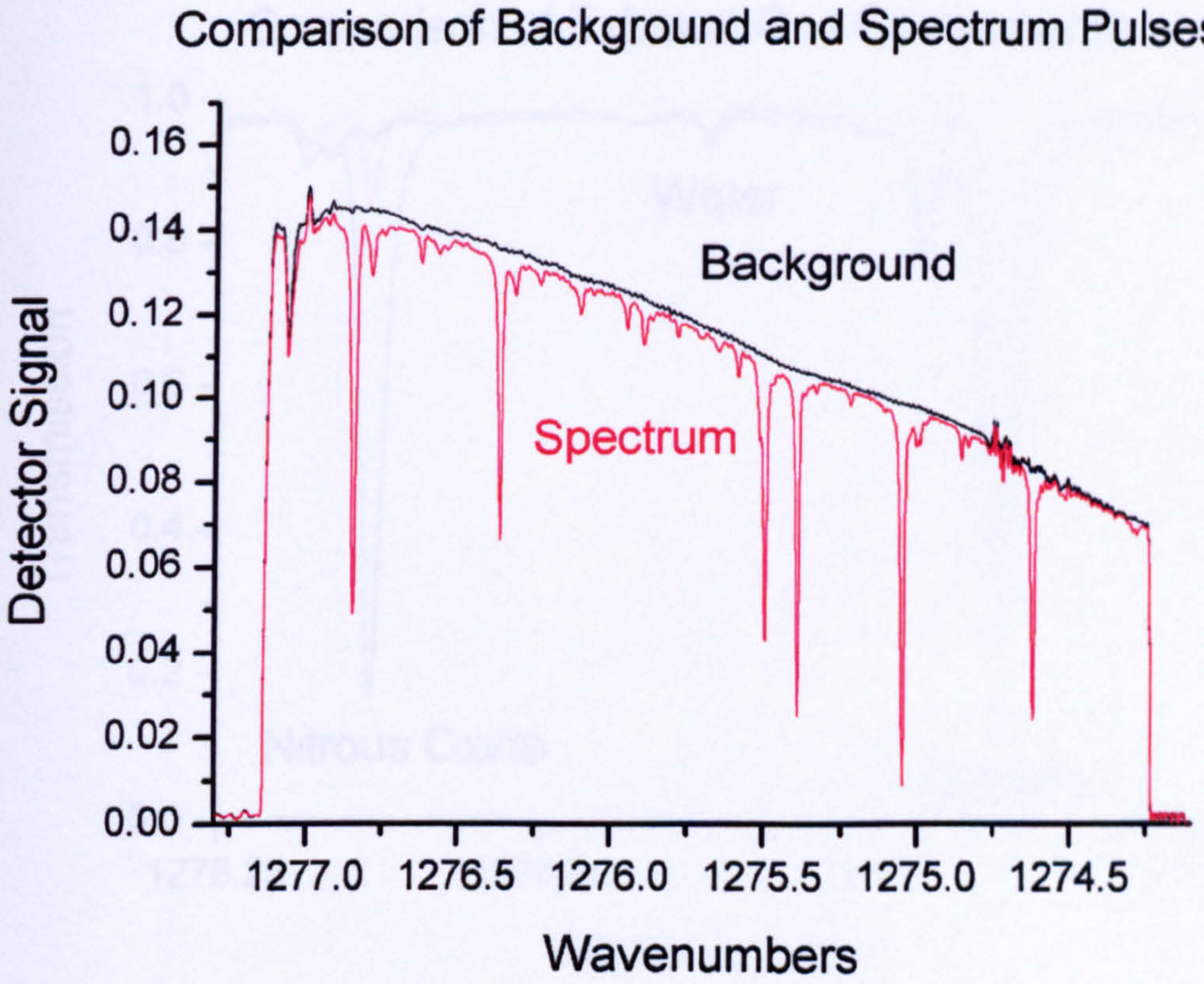

Figure 5.4.11 – *The Black trace shows the raw background pulse. The Red trace shows the raw spectrum pulse.*

The wavenumbers scale is reversed to show the start of the pulse in time at the left of the figure and the end of the pulse in time at the right of the figure. The detector signal has been inverted to show the data as positive values rather than the negative values returned from the inverting amplifier. Due to a larger micro window when using the 8μm laser compared to the 10μm laser more absorbing gases can be detected by my system in a vehicles exhaust at 8μm. The variation of three different absorbing species with time is shown in Figure 5.4.12 below.

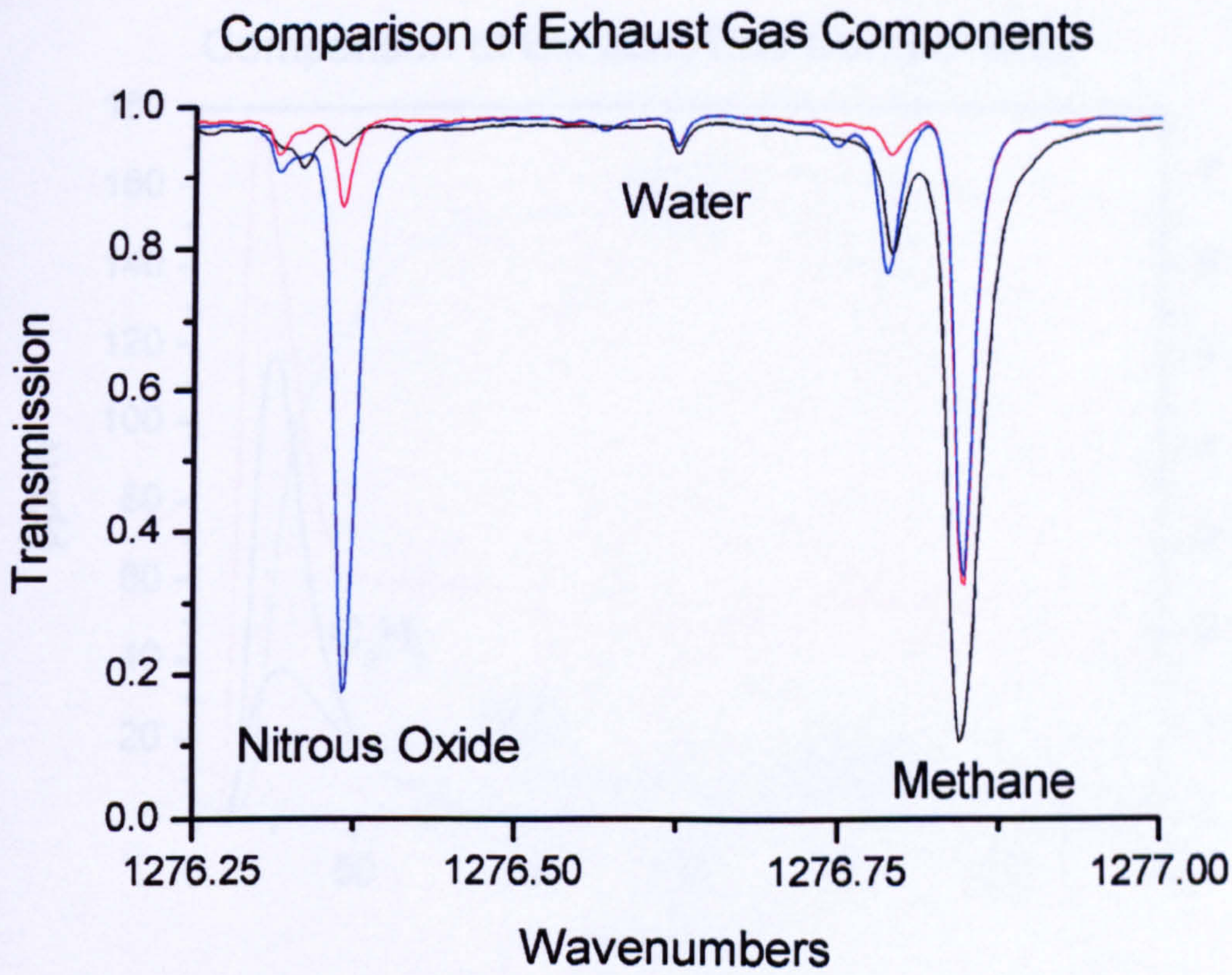

Figure 5.4.12 – *The Black trace shows the spectrum of the car exhaust 5s after start up. The Red trace shows the spectrum of the car exhaust 39s after start up. The Blue trace shows the spectrum of the car exhaust 74s after start up.*

It can be seen from these spectra that the concentration of Methane in the car exhaust quickly reaches a peak and then decays towards a steady limit. The concentration of Nitrous Oxide in the first spectrum is small, but the concentration steadily builds up in the next two spectra. However the Water in the three spectra does not appear to change very much. The asymmetry of the strong absorption lines may be an indication of power saturation, which is an effect described in section 4.1. As a result the concentrations retrieved may be underestimating the true concentrations of the exhaust gases. The variation of the major components of the vehicle exhaust emissions detected in the micro window is shown below in Figure 5.4.13.

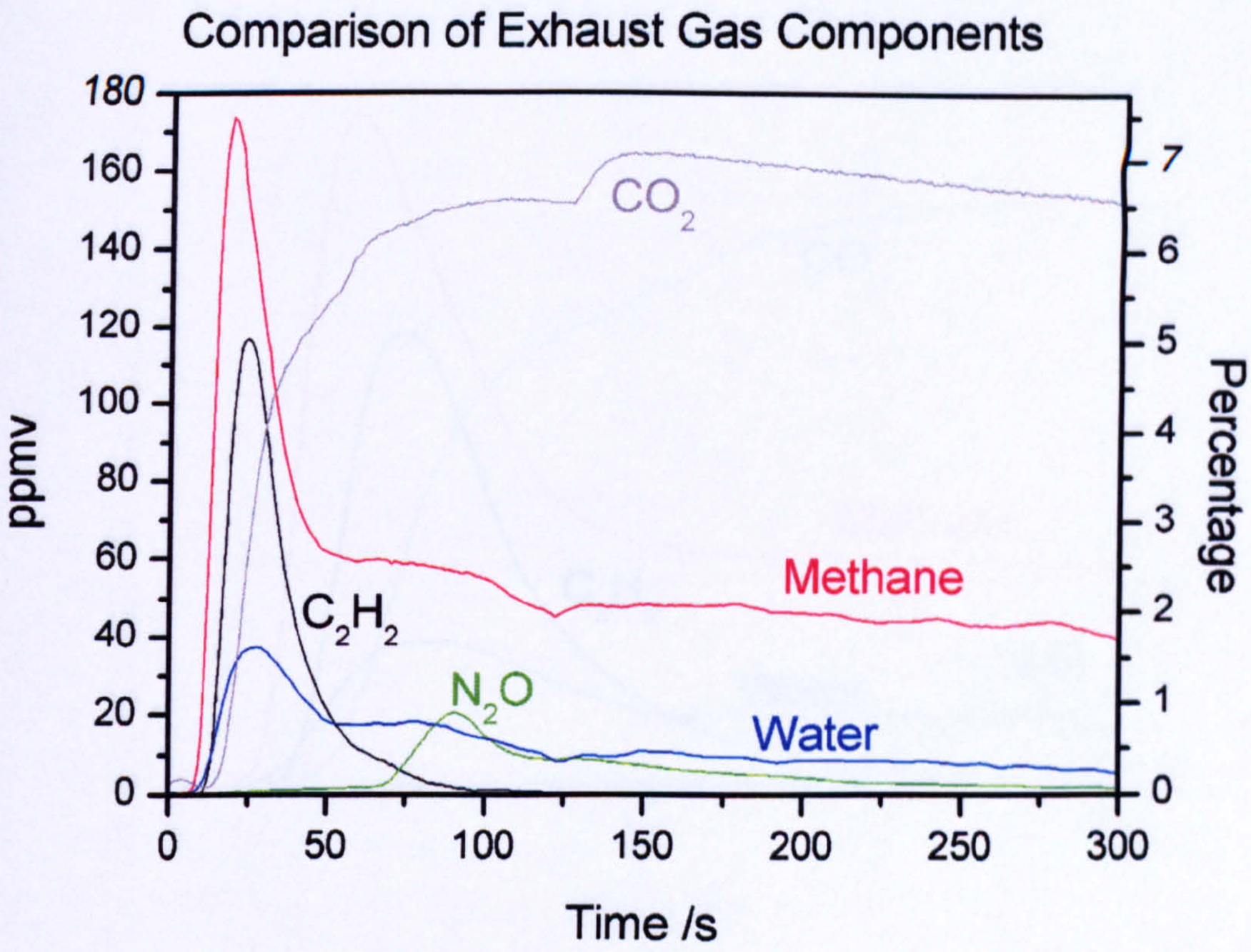

Figure 5.4.13 – *The Red trace shows the variation of Methane as a function of time. The Black trace shows the variation of Acetylene as a function of time. The Green trace shows the variation of Nitrous Oxide as a function of time. The Blue trace shows the variation of Water as a function of time. The Grey trace shows the variation of Carbon Dioxide as a function of time.*

The Water and Carbon Dioxide traces are plotted on the percentage scale. The Methane, Nitrous Oxide and Acetylene traces are plotted on the ppmv scale. The Water, Methane and Acetylene all have an initial peak of emission which is followed by a decay. The Acetylene decays below the detection capabilities of the spectrometer; however the Methane and Water emissions are still detected at the end of the experiment. The Nitrous Oxide peak appears about one minute after the first set of peaks, but it also decays to detectable limit. For clarity of zoom of Figure 5.4.13 is shown below in Figure 5.4.14.

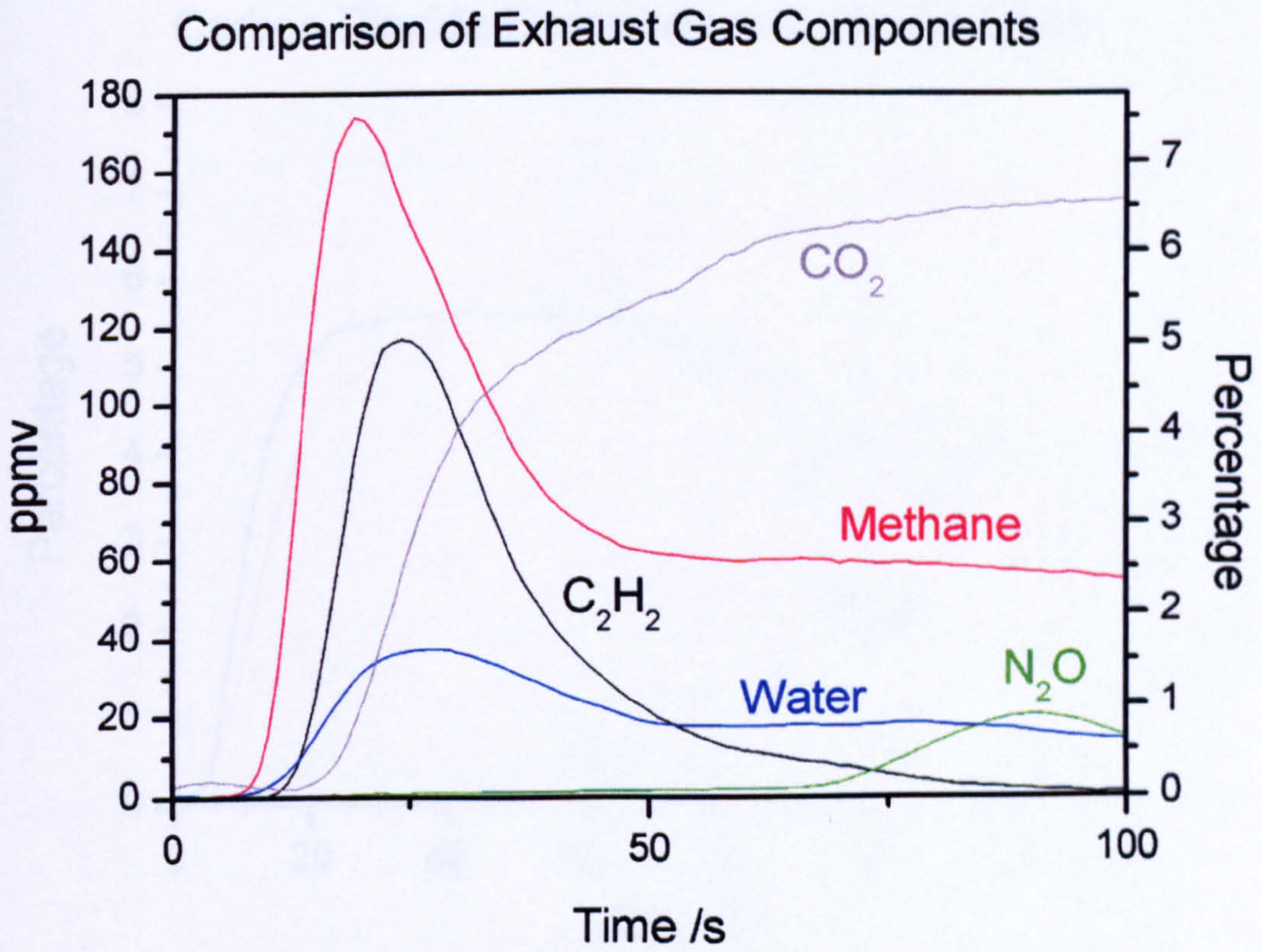

Figure 5.4.14 – *A zoom of Figure 5.4.13*

The Carbon Dioxide emissions from the Renault Clio can be compared using the 10μm data and the 8μm data. The two experiments were carried out one year apart so a change in the emission pattern of the vehicle should be expected. Figure 5.4.15 below shows the comparison of Carbon Dioxide emissions at 8μm and 10μm.

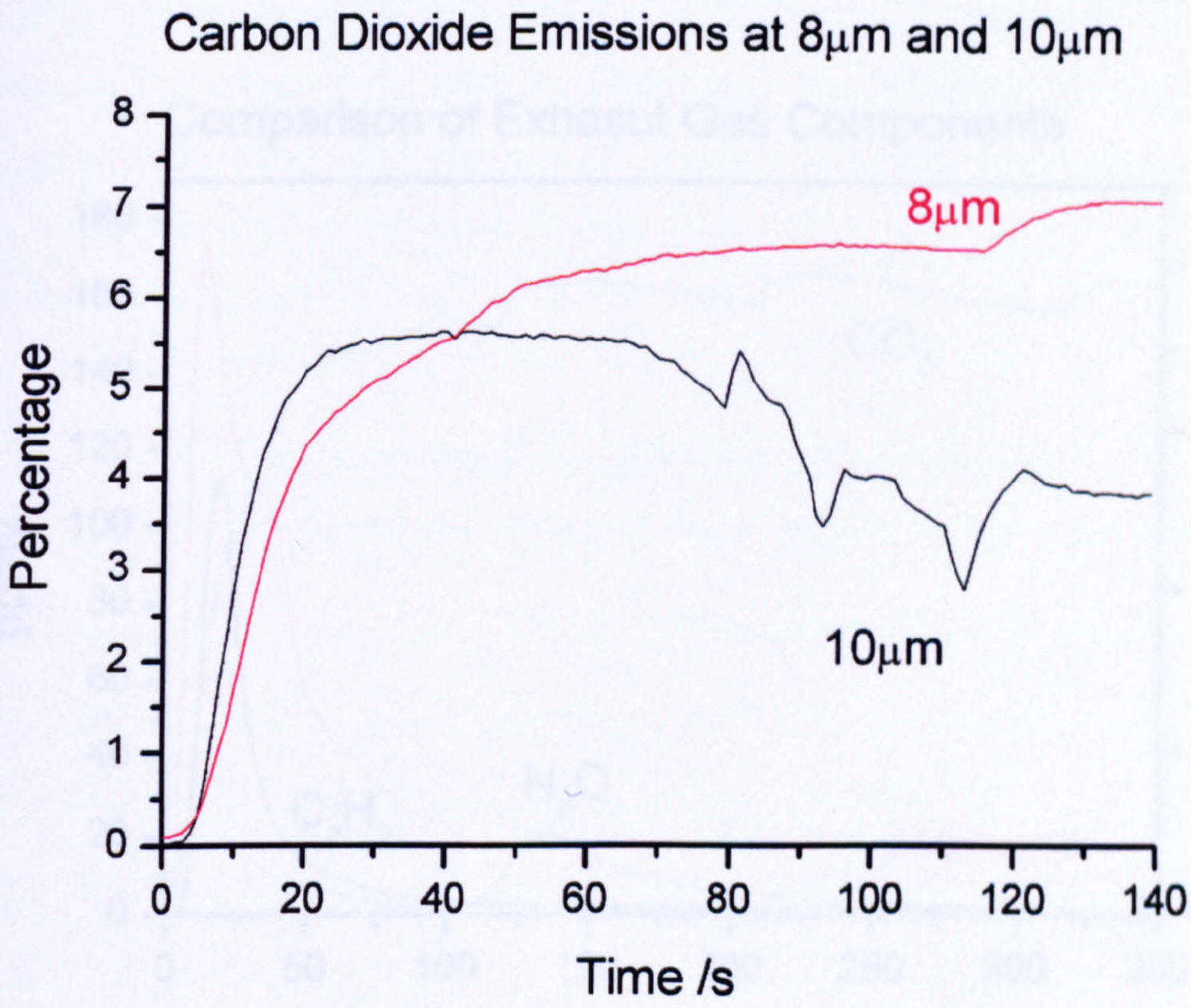

Figure 5.4.15 – *The Black trace shows the Carbon Dioxide emission as a function of time using the 10μm laser. The Red trace shows the Carbon Dioxide emission as a function of time using the 8μm laser.*

The two traces follow each other over the first 40s, but after that there is a distinct difference in the two traces. This could be down to several factors. When the first measurements were made the vehicle was new and was being run in, however at the second set of measurements the vehicle was over a year old. Other things that will effect the emissions include the fuel used, the weather conditions and the condition of the engine.

The second vehicle studied at 8μm was the Toyota Avensis. The laser was driven using the same settings as the first 8μm experiment. Due to the rainy conditions on the day of the experiment the Water content of the exhaust spectra could not be extracted from the background atmospheric Water level. Figure 5.4.16 below shows the time evolution of Methane, Nitrous Oxide, Carbon Dioxide and Acetylene in the exhaust fumes.

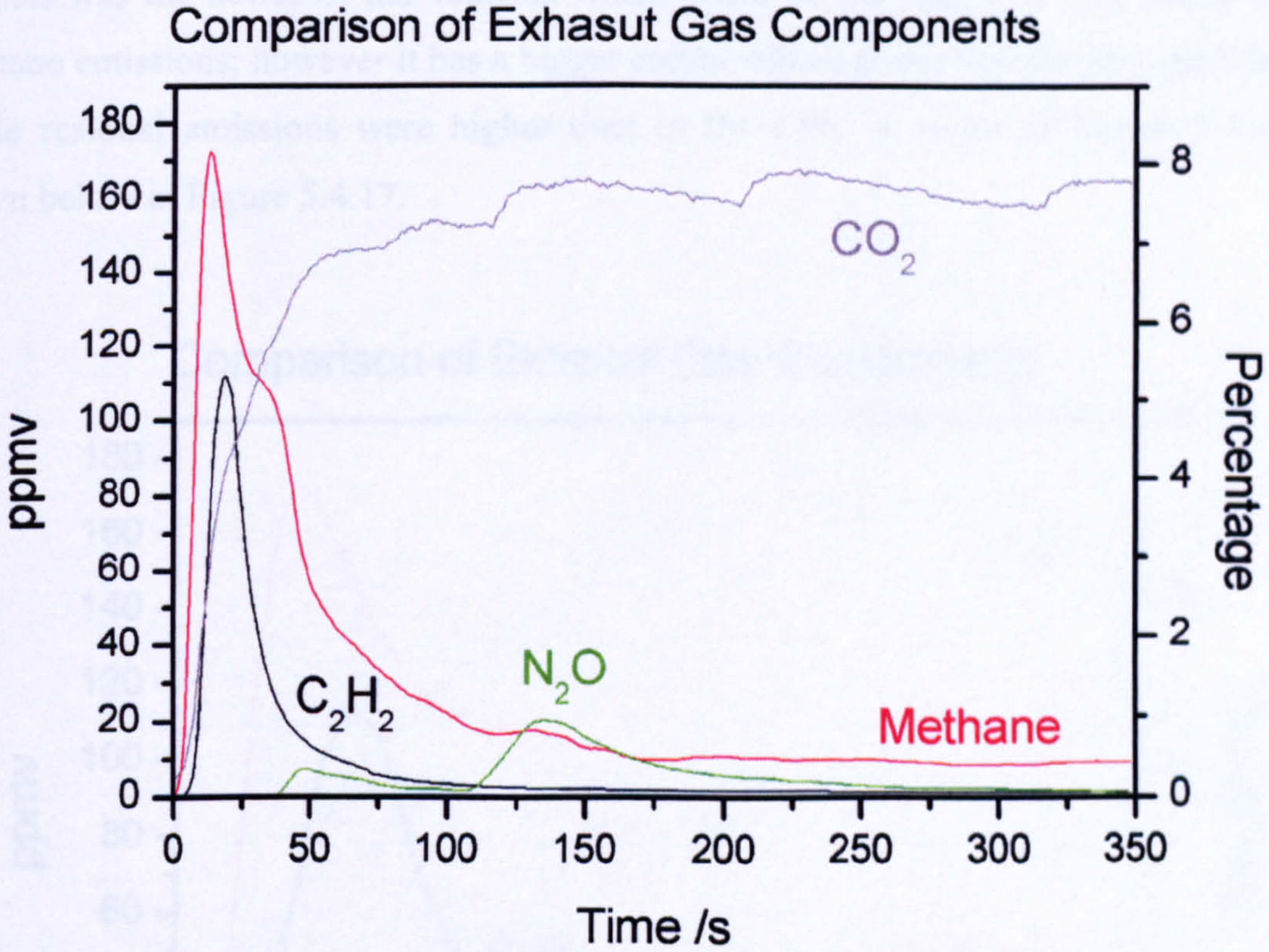

Figure 5.4.16 – *The Red trace shows the variation of Methane as a function of time. The Black trace shows the variation of Acetylene as a function of time. The Green trace shows the variation of Nitrous Oxide as a function of time. The Grey trace shows the variation of Carbon Dioxide as a function of time.*

The Carbon Dioxide trace is plotted on the percentage scale. The Methane, Nitrous Oxide and Acetylene traces are plotted on the ppmv scale. The exhaust emission pattern for the Avensis and the Clio appear similar. The peak emission values of Methane, Acetylene and Nitrous Oxide are all comparable. The Methane peak emission is 172ppmv from the Avensis and 173ppmv from the Clio. The Acetylene peak emission is 112ppmv in the Avensis compared with 117ppmv in the Clio. The Nitrous Oxide peak emission is 20.1ppmv in the Avensis and 20.3ppmv in the Clio. The residual levels of Methane are almost an order of magnitude different. After 300s the Methane emission from the Avensis is 8.33ppmv compared to 44ppmv from the Clio. The residual levels of

the Nitrous Oxide were 2.26ppmv for the Avensis and 2.1ppmv for the Clio. The Avensis was the newer of the vehicles which could be the reason for the much lower Methane emissions; however it has a bigger engine which could explain why the Nitrous Oxide residual emissions were higher than in the Clio. A zoom of Figure 5.4.16 is shown below in Figure 5.4.17.

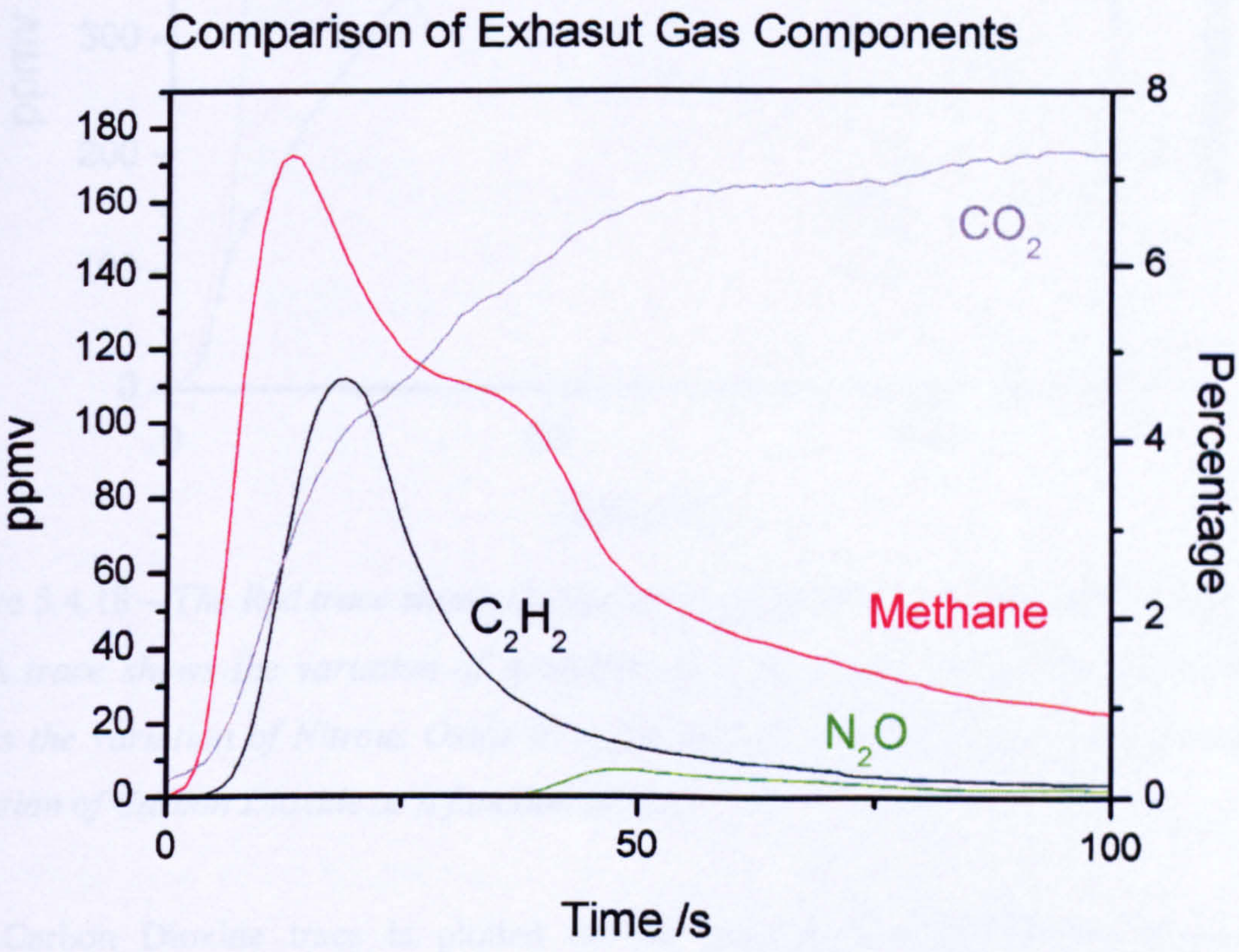

Figure 5.4.17 – *A zoom of Figure 5.4.16*

The third vehicle studied at 8μm was the Yamaha R6 motorbike. The laser settings were unchanged from the previous measurements. The Water and Nitrous Oxide emissions could not be detected above the ambient levels in the atmosphere. The time evolution of Methane, Acetylene and Carbon Dioxide in the exhaust fumes are shown below in Figure 5.4.18.

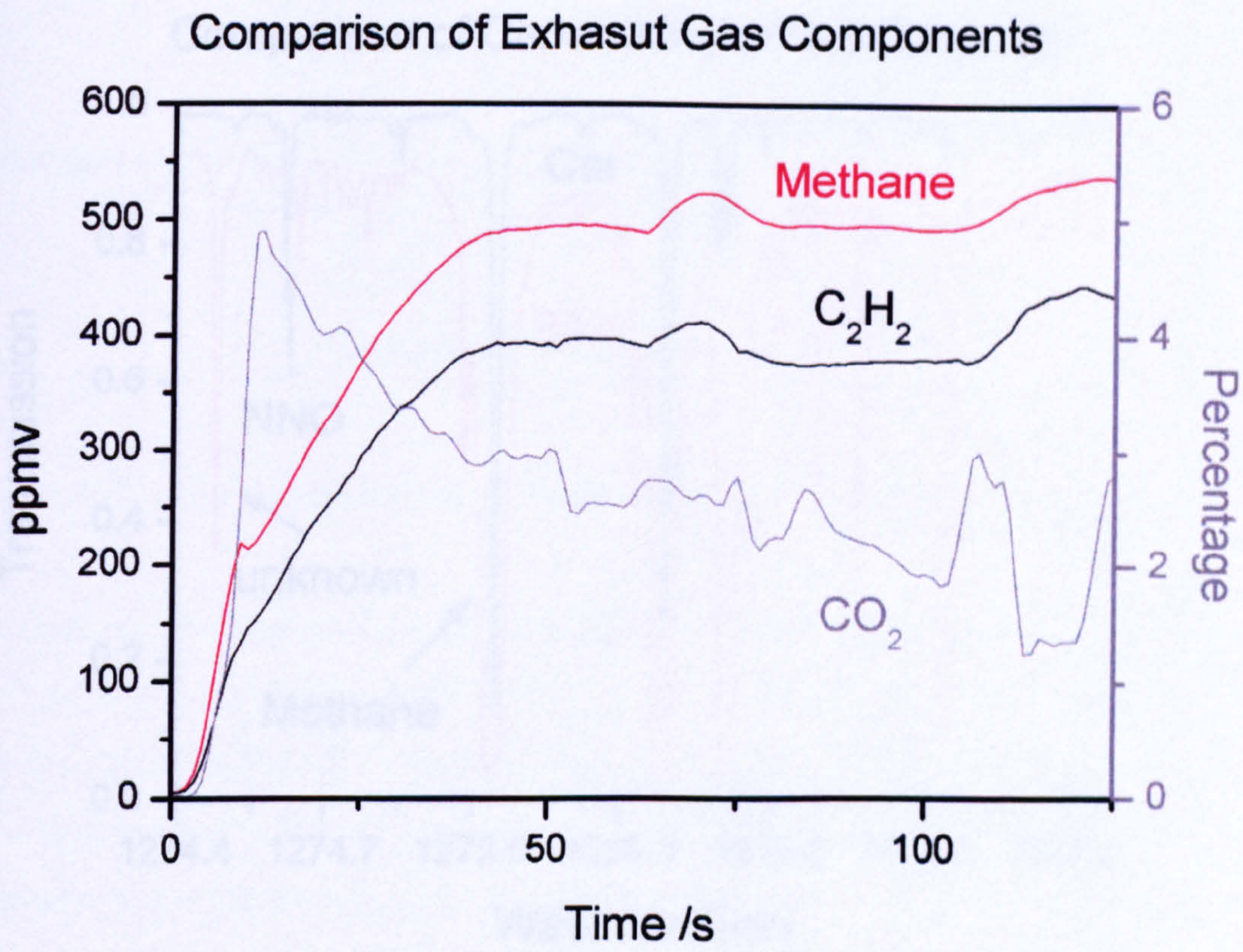

Figure 5.4.18 – *The Red trace shows the variation of Methane as a function of time. The Black trace shows the variation of Acetylene as a function of time. The Green trace shows the variation of Nitrous Oxide as a function of time. The Grey trace shows the variation of Carbon Dioxide as a function of time.*

The Carbon Dioxide trace is plotted on the percentage scale. The Methane and Acetylene traces are plotted on the ppmv scale. The peaks in emission of Acetylene and Methane are much larger in the R6 than in the two cars tested at 8µm. The Methane emission peak is 538ppmv for the R6 compared to 173ppmv for the Clio. The Acetylene emission peak is 443ppmv for the R6 and is 117ppmv for the Clio. The exhaust spectra of the R6 also contained the absorption fingerprint of other unknown gas/gases. Figure 5.4.19 below shows the comparison between a spectrum recorded of the R6 exhaust and a spectrum recorded of the Clio exhaust.

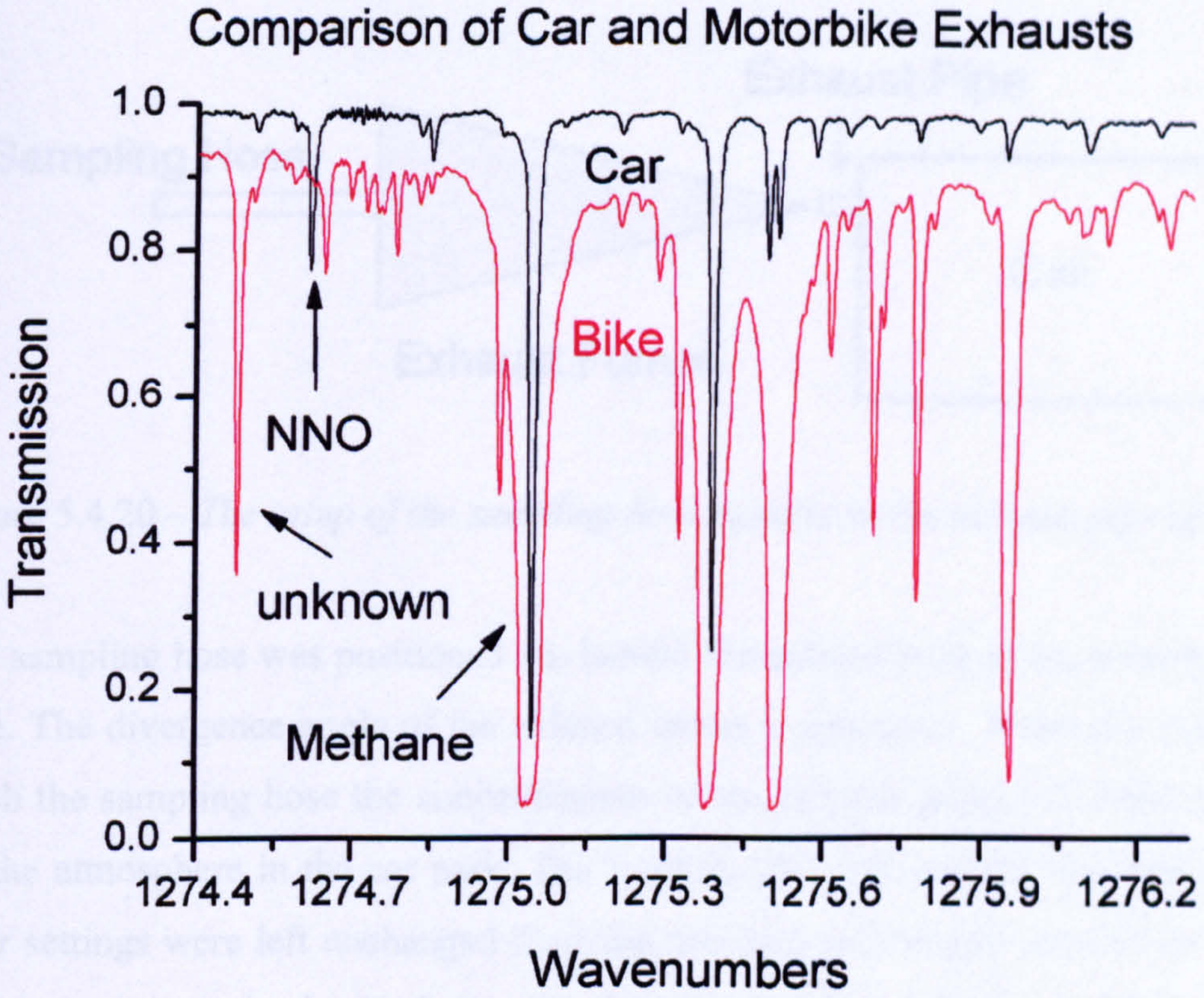

Figure 5.4.19 – *The Black trace shows the spectrum of the car exhaust. The Red trace shows the spectrum of the bike exhaust.*

Both of the spectra represent 50s after switch on of both vehicles. Several absorption lines can be seen in the R6 spectrum that are not present in the Clio spectrum. These lines have at present not been identified.

All of the above 8μm experiments sampled the exhaust gases inside the exhaust pipe of the vehicle. This gave the strongest signals possible for all of the gases detected. In order to make real world measurements of exhaust gases either cross exhaust path measurements need to be made, or the gases can be sampled a distance from the exhaust pipe. To make cross exhaust path measurements the spectrometer would require significant alterations so the second technique was used. The setup of the sampling hose and car exhaust is shown below in Figure 5.4.20.

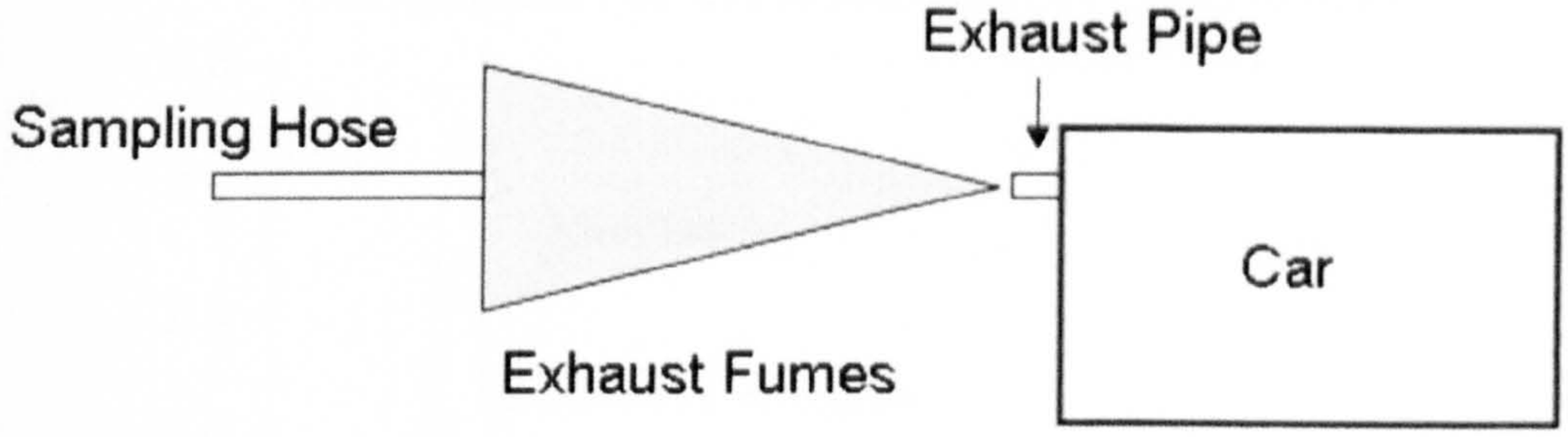

Figure 5.4.20 – *The setup of the sampling hose relative to the exhaust pipe of the car.*

The sampling hose was positioned 1m behind the exhaust pipe at the same height as the pipe. The divergence angle of the exhaust fumes is unknown. When the exhaust fumes reach the sampling hose the concentrations of the exhaust gases will have been diluted by the atmosphere in the car park. The Renault Clio was used in this experiment. The laser settings were left unchanged from the previous experiment. Due to the dilution of the atmosphere only the Methane and Acetylene could be detected above atmospheric levels. The time evolution of Acetylene and Methane in the car exhaust fumes are shown below in Figure 5.4.21.

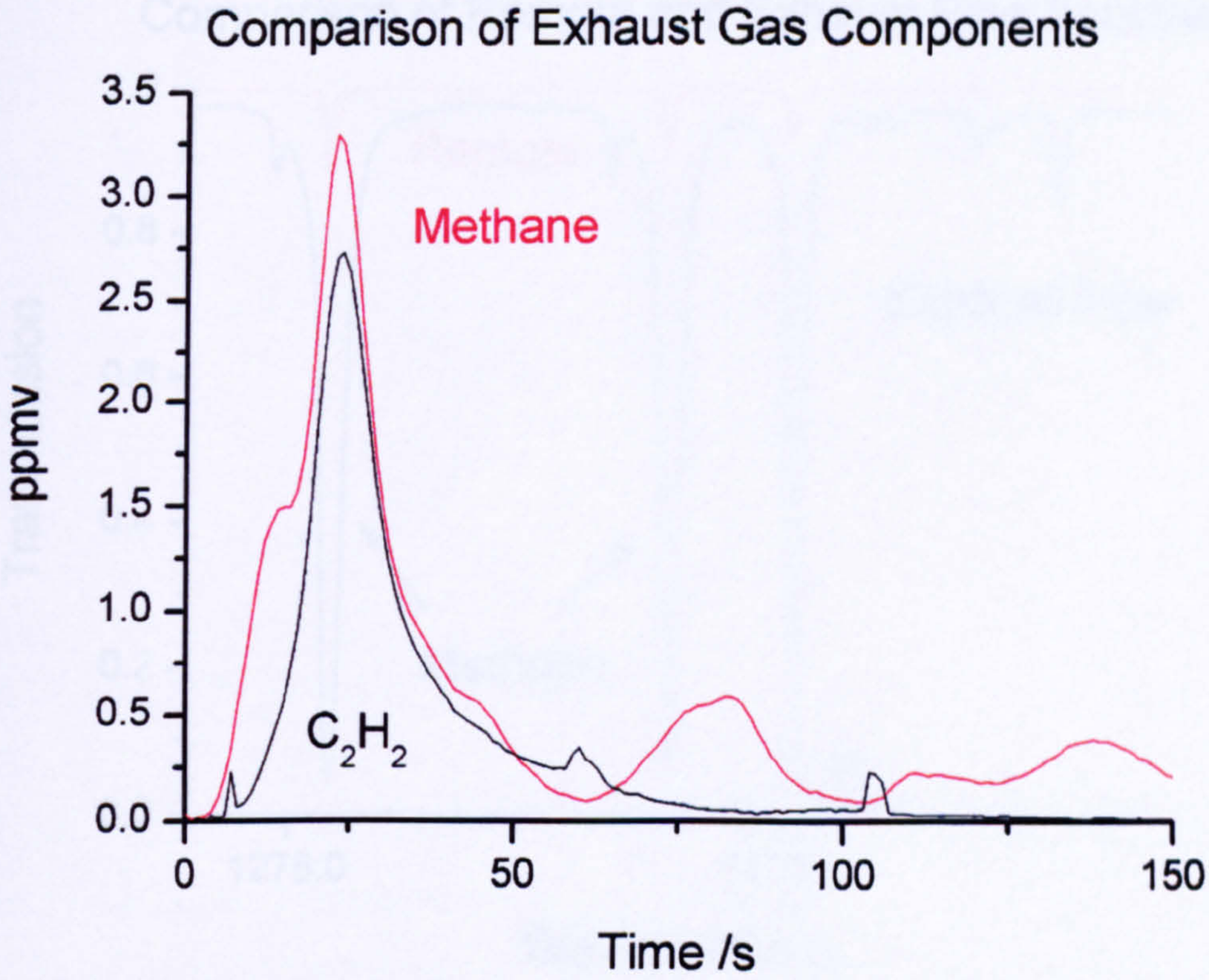

Figure 5.4.21 – *The Black trace shows the time evolution of Acetylene and the Red trace shows the time evolution of Methane.*

The general shape of the two traces follows well the time evolution of the Acetylene and Methane in the direct exhaust pipe sampling experiment. The background Methane level was removed from the measurement.

Figure 5.4.22 below shows a comparison of two spectra. The first spectrum was recorded using the direct exhaust pipe sampling technique and the second spectrum was recorded using the remote sampling technique. Both spectra are of the Renault Clio's exhaust fumes recorded s after start up.

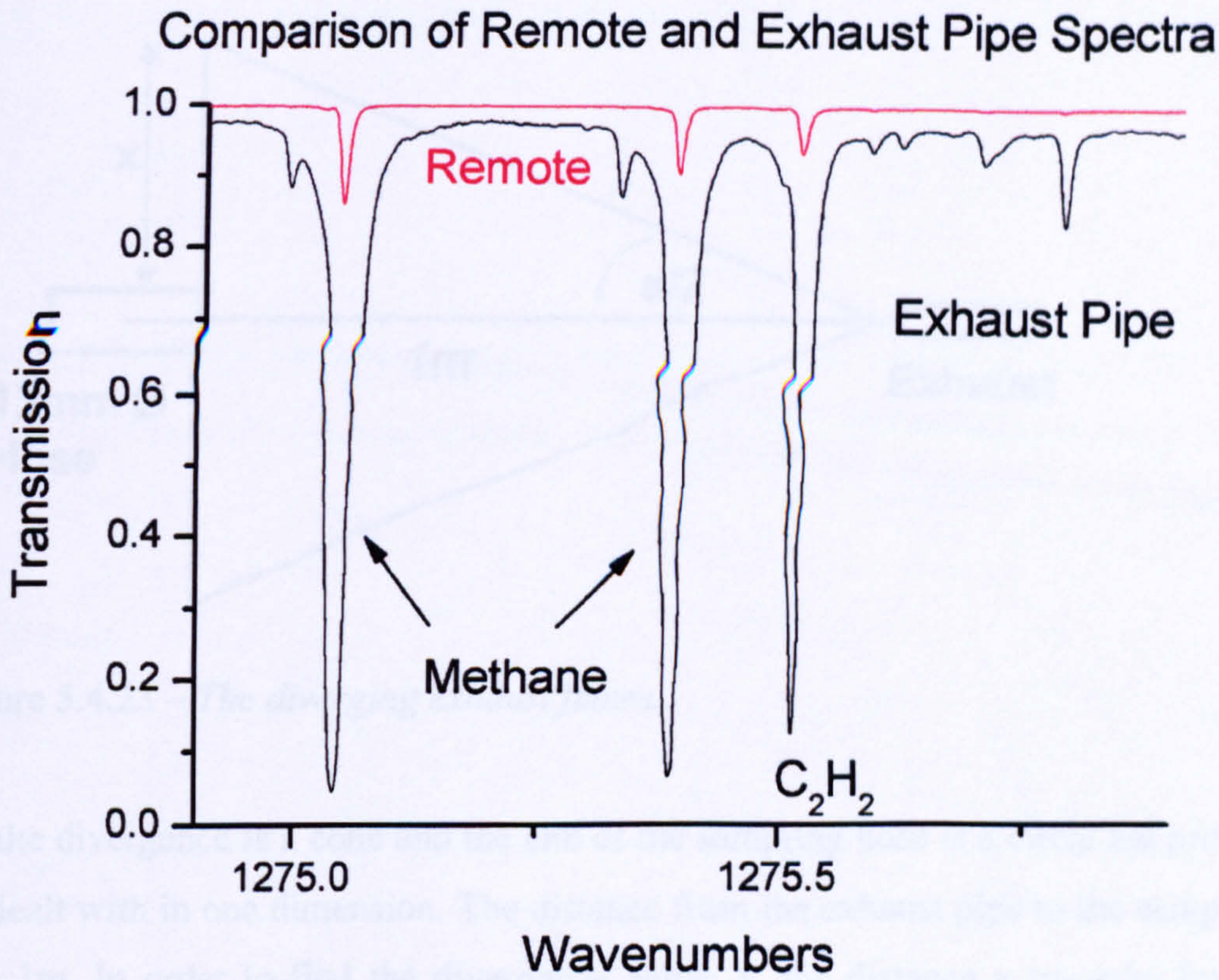

Figure 5.4.22 – *The Black trace shows the direct exhaust pipe sampled spectrum and the Red trace shows the remote sampled spectrum.*

From the relative concentrations of the exhaust gas components Acetylene and Methane the divergence angle of the exhaust fumes can be calculated, assuming the exhaust fumes expand from a point source uniformly in a cone shape. Figure 5.4.23 shows the problem.

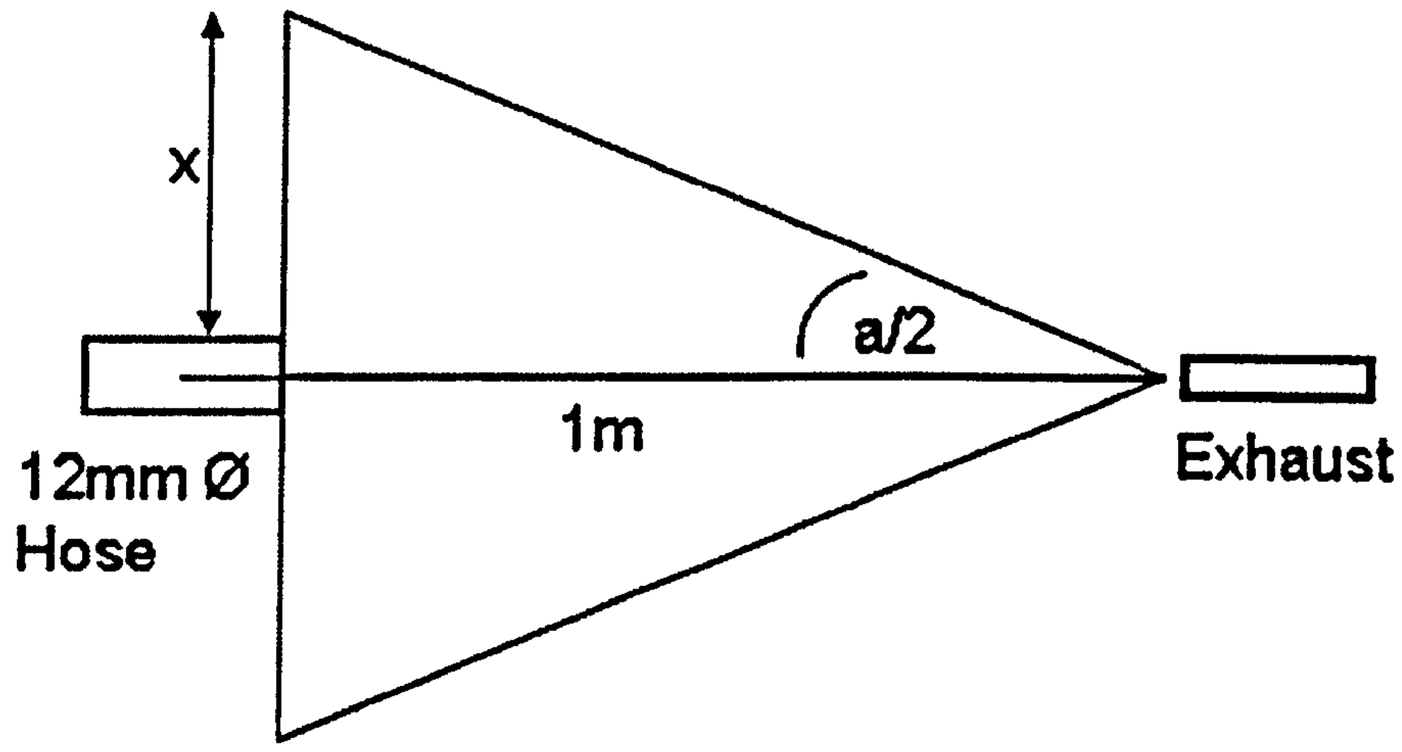

Figure 5.4.23 – *The diverging exhaust fumes.*

As the divergence is a cone and the end of the sampling hose is a circle the problem can be dealt with in one dimension. The distance from the exhaust pipe to the sampling hose was 1m. In order to find the divergence angle, a, the distance x must be found. X is found by ratioing the peak concentrations of Methane and Acetylene using the direct exhaust pipe sampling technique and the remote sampling technique. For Methane:

$$\frac{x}{Conc_{Direct}} = \frac{\text{Hose Radius}}{Conc_{Remote}}$$

Where $Conc_{Direct}$ is the peak concentration of Methane in the direct sampling technique which is 173.98ppmv, $Conc_{Remote}$ is the peak concentration of Methane in the remote sampling technique which is 3.28ppmv and the Hose Radius is 6mm.

$$\frac{x}{173.98ppmv} = \frac{0.6cm}{3.28ppmv}$$

$$\therefore x = \frac{173.98}{3.28} \cdot 0.6cm = 32cm$$

From this the divergence angle, a, can be calculated:

$$a=2\cdot\tan\left(\frac{32\text{cm}}{100}\right)=35.5^{\circ}$$

Using Methane the divergence angle of the exhaust fumes is 35.5°. The same calculation can be made using the Acetylene data, where $Conc_{Direct}$ is 116.77ppmv and $Conc_{Remote}$ is 2.71ppmv:

x=25.9cm

a=29°

This gives a divergence angle of 29°.

5.4.10 Discussion - 8µm

The emissions from the two cars studied at 8µm seem to follow a similar pattern. The peak values for the gases in the two exhausts are comparable. There are differences though. The newer car, the Toyota Avensis, emits less Methane (8.33ppmv) when at running temperature than the Renault Clio (44ppmv). This is compared to the peak emission levels of Methane when the engines are cold of 173ppmv for the Renault Clio and 172ppmv for the Toyota Avensis. This could be a sign of slight catalytic poisoning of the Renault Clio's catalytic converter. The Nitrous Oxide emission for both of these vehicles is almost identical. The peak emission is 20.3ppmv from the Clio and 20.1ppmv for the Avensis. The running temperature emission is 2.1ppmv for the Clio and 2.26ppmv from the Avensis. The Clio would be expected to produce lower emissions due to its smaller engine; however the running temperature Nitrous Oxide emission is only 7% less than from the Avensis compared to the Clio's 40% smaller engine. From the Methane and Nitrous Oxide data I would say that the Toyota Avensis' catalytic

converter is less poisoned than the Renault Clio's and that the two converters are designed to reduce the emissions from the exhaust in different ways.

The motor bike tested produced much larger emissions of detectable unburnt hydrocarbons than the two cars tested. The emission pattern was also different; there was no peak in emissions of the unburnt hydrocarbons. The Nitrous Oxide emissions from the R6 could not be detected above the other absorption lines in the spectrum, nor could the Water. The Carbon Dioxide emissions were comparable with the cars though.

5.4.11 Conclusions

I have demonstrated the high sensitivity coupled with the high selectivity of my spectrometer for the detection of gases in vehicle exhaust emissions. I have shown that the instrument is capable of detecting Methane, Acetylene, Carbon Dioxide, Water and Nitrous Oxide simultaneously. The concentrations of these gases have been looked at as a function of time relative to the start up of the vehicle being tested. The concentrations of the unburnt hydrocarbons, Acetylene and Methane at 8μm and Ethylene at 10μm, for most of the cars tested peaks near the switch on and decreases towards an asymptotic limit at longer times. This poses a problem for car manufacturers as legislation limiting start up emissions comes into force. New catalytic converter technology will be needed to reduce the time taken for a converter to reach operating temperature as well as improving filters and engine management systems. I have also shown that a car start up can be detected by the system using a remote sampling technique. Comparing the directly sampled exhaust gas spectra with the remotely sampled spectra information about the shape and size of the exhaust fumes can be recovered.

5.4.12 References

1) The Automobile Association, www.theaa.com

2) Infrared Laser absorption: Theory and applications, C. R. Webster, R. T. Menzies and E. D. Hinkley, Chapter 3: Diode lasers for pollutant monitoring, Wiley, (1988)

3) A tunable diode laser system for the remote sensing of on-road vehicle emissions, D. D. Nelson, M. S. Zahniser, J. B. McManus, C. E. Kolb and J. L. Jiménez, App. Phys. B, **67**, 433-441, (1998)

4) Cross road and mobile tunable infrared laser measurements of nitrous oxide emissions from motor vehicles, J. L. Jiménez, J. B. McManus, J. H. Shorter, D. D. Nelson, M. S. Zahniser, M. Koplow, G. J. McRae and C. E. Kolb, Chemosphere – Global change Science, **2**, 397-412, (2000)

5) Effects of super-light-duty gasoline and LPG-fueled cars on 16 ambient hydrocarbons at roadsides in Japan, M. Tanaka, M. Warashina, Y. Itano, Y. Tsujimoto and S. Wakamatsu, Chemosphere – Global change Science, **3**, 199-207, (2001)

6) Methane, benzene and alkyl benzene cold start emission data of gasoline-driven passenger cars representing the vehicle technology of the last two decades, N. V. Heeb, A.-M. Forss, C. J. Saxer and P. Wilhelm, Atmospheric Environment, **37**, 5185-5195, (2003)

7) Automotive catalytic converters: current status and some perspectives, J. Kašpar, P. Fornasiero and N. Hickey, Catalysis Today, **77**, 419-449, (2003)

8) Fast ultra-sensitive real time quantum cascade laser spectrometer, E. L. Normand, PhD Thesis, Department of Physics, University of Strathclyde, (2004)

9) Astigmatic mirror multipass absorption cells for long-path-length spectroscopy, J. B. McManus, P. L. Kebabian and M. S. Zahniser, App. Opts., 34, 18, 3336-3348, (1995)

10) The Society of Motor Manufacturers and Traders (SMMT), www.smmt.co.uk

11) Photochemical ozone creation potentials for a large number of reactive hydrocarbons under European conditions, R. G. Derwent, H. E. Jenkins and S. M. Saunders, Atmospheric Enviroment, **30**, 2, 181-199, (1996)

6 Future Work and Conclusions

6.1 An Airplane based Instrument

Part of the funding for my research was provided by NERC. This funding was provided with a studentship so that the laboratory based instrument developed during the first 2 years of my PhD could be developed further into an airplane based instrument. The majority of this work will be carried out by Stephen Wright.

In order for the laboratory based sensor to be operated in an airplane several stages must be completed. The size of the instrument at present is too large and heavy to be used on an airplane and therefore must be reduced. This can be done by using a more compact beam path on a smaller optical breadboard. As the pressure in the cell will be maintained at a constant level for the flights the size and weight of the pumping system can be reduced as the instrument does not require a very low base pressure. The current control electronics allow a large degree of freedom for using different settings to drive the laser system. For the airplane instrument this large degree of freedom is not required as the settings to be used should not change from flight to flight, which allows some of the electronics to be reduced. As well as reducing the size of the instrument the optical components of the instrument must be made more rugged. This can be done in a couple of ways. Firstly the height of the beam must be moved closer to the breadboard. The mounts could be replaced by commercially available rugged industrial mounts. In order for the instrument to perform unattended the software used to control the instrument and record the data must be upgraded. The current software allows for the automation of operation but does not have any self checking routines that would detect problems in the system. Routines for fully automating the concentration retrieval must also be developed. As the detector is a liquid nitrogen cooled device the dwell time of the dewer determines the length of unattended flight that the instrument is capable of making. This problem can be solved by either using a thermoelectrically cooled detector or by using liquid nitrogen auto filler. Both methods have advantages and disadvantages. Thermoelectrically cooled detectors tend to have lower responsivities than liquid nitrogen cooled devices but they are no bigger than liquid nitrogen cooled detectors. An

auto filler allows the high sensitivity liquid nitrogen detector to be used for a longer period of time, however the size and weight of the auto filler is a disadvantage and it is another component that may go wrong.

6.2 An Open path Sensor

As well as gas cell based sensor the laboratory based sensor technology could easily be applied to an open path. This type of sensor removes the need for the large and costly gas cell and vacuum system. An open path sensor has several applications such as exhaust measurements, atmospheric monitoring and health and safety applications. In order to convert the laboratory sensor into an effective open path sensor much of the work done for the airplane sensor could be used, such as the reduction in the complexity of the electronics and the software upgrade. By removing the gas cell the sensitivity of the open path sensor can be increased by increasing the separation of the laser and the detector or the laser/detector from a retro reflector. This assumes that the gases of interest are present along the whole of the beam path, which in the case of atmospheric monitoring of Methane or Nitrous Oxide is a good assumption. However for health and safety applications or exhaust measurements the gases of interest tend to be localised and increasing the optical path will not increase the sensitivity of the instrument. This type of sensor could be made very compact and could be easily deployed in many different environments.

6.3 Nonlinear Optics

In order to more fully understand the results from this work more experiments must be carried out. By using a pulsed Quantum Cascade Laser the direction of the chirp cannot be easily changed. Also the speed of the chirp can only be altered by at most 1 order of magnitude. If a continuous wave device was available the chirp direction could be

changed. The chirp rate could also be tuned over the larger range. This would allow different experiments to be carried out. If other wavelength QCLs could be obtained the number of gases studied could be increased allowing different types of molecules to be examined.

6.4 Conclusions

During my research I developed a Quantum Cascade Laser based absorption spectrometer. I used this spectrometer to perform trace gas detection and to observe non linear optical phenomena.

I have presented the design of this spectrometer and the further development made during my research.

I have shown that this simple design of spectrometer can be used for real time multi species analysis in different monitoring environments such as car exhausts, human breath, cigarette smoke and the Earths atmosphere. I have observed the emission of several gases from different motor vehicles in real time. The results I obtained were compared to work carried out by other research groups.

As ground work for the airplane based instrument I recorded the low temperature spectra of several important atmospheric gases such as Methane and Nitrous Oxide at the Rutherford Appleton Laboratory. I have also studied the atmosphere of Glasgow at ground level as a basis for the airplane measurements to be carried out after my research.

It has been shown that the spectrometer developed during my research is capable of producing non linear effects in low pressure gases such as power saturation, rapid passage and Dicke narrowing. These effects were caused by the chirp rate and intensity of the lasers used. I have shown the results of an initial study into these phenomena.